

PREDICTIVE MODELS FOR STRONTIUM ISOTOPE DISTRIBUTIONS IN BEDROCK,
WATER AND ENVIRONMENTAL MATERIALS FOR REGIONAL PROVENANCE
STUDIES

by

Clément Pierre Bataille

A dissertation submitted to the faculty of
The University of Utah
in partial fulfillment of the requirements for the degree of

Doctor of Philosophy

in

Geology

Department of Geology and Geophysics

The University of Utah

December 2014

Copyright © Clément Pierre Bataille 2014

All Rights Reserved

The University of Utah Graduate School

STATEMENT OF DISSERTATION APPROVAL

The dissertation of Clement Pierre Bataille

has been approved by the following supervisory committee members:

Gabriel J. Bowen	, Chair	06/02/14
_____		_____
		Date Approved
Diego P. Fernandez	, Member	06/02/14
_____		_____
		Date Approved
Lisa Stright	, Member	06/02/14
_____		_____
		Date Approved
Thure E. Cerling	, Member	06/02/14
_____		_____
		Date Approved
Brett J. Tipple	, Member	06/17/14
_____		_____
		Date Approved

and by **John Bartley**, Chair/Dean of

the Department/College/School of **Geology and Geophysics**

and by David B. Kieda, Dean of The Graduate School.

ABSTRACT

Strontium isotope ratio ($^{87}\text{Sr}/^{86}\text{Sr}$) has a strong potential to complement atmospherically-derived traditional stable isotopes in geochemical provenance studies because strontium (Sr) in Earth surface reservoirs is sourced from local bedrock. As such, $^{87}\text{Sr}/^{86}\text{Sr}$ variations are discrete and differ drastically from the large scale smoothed variations of atmospherically-derived stable isotopes. Among the most successful recent applications, $^{87}\text{Sr}/^{86}\text{Sr}$ has been used to interpret provenance of individuals in archeology, to identify the origin of dust aerosols, to reconstruct cation source and mobility in rivers, and to reconstruct animal or material movement pathways. However, extending the applications of $^{87}\text{Sr}/^{86}\text{Sr}$ for provenance to larger spatial scales is currently hampered by the absence of methods to predict the $^{87}\text{Sr}/^{86}\text{Sr}$ of Sr sources at the regional scale. In this dissertation, a flexible geostatistical framework is established to predict $^{87}\text{Sr}/^{86}\text{Sr}$ distributions in bedrock, river water and soil water at regional scale. This approach leverages publically-available geospatial data on rock geochemistry, surficial and bedrock geology, climate, hydrology, and aerosols to model the input and propagation of Sr from multiple geological sources through hydrosystems and ecosystems. In a first step, we develop predictive models for $^{87}\text{Sr}/^{86}\text{Sr}$ in bedrock as a function of variations in rock age and rock type. In a second step, we model the Sr release from different rock units, its transport as dissolved Sr or in aerosols, and its accumulation and mixing in ecosystems. The model was tested for the contiguous USA and circum-Caribbean region and the

model showed promising results but the predictive power remained too low for routine provenance interpretations. In a final step, we develop a flexible geochemical framework that explicitly accounts for prediction uncertainty and local variability of $^{87}\text{Sr}/^{86}\text{Sr}$ and includes a Sr-specific process-based chemical weathering model. This improved model version is applied to predict $^{87}\text{Sr}/^{86}\text{Sr}$ in bedrock and rivers over Alaska and explain 82% of $^{87}\text{Sr}/^{86}\text{Sr}$ variance in Alaska Rivers. Integrated into a multi-isotopes framework, $^{87}\text{Sr}/^{86}\text{Sr}$ could dramatically improve the spatial resolution of provenance assignments. Predictive $^{87}\text{Sr}/^{86}\text{Sr}$ models are also a powerful standalone tool to visualize, identify and model mechanistic processes influencing local to global $^{87}\text{Sr}/^{86}\text{Sr}$ in Earth surface reservoirs.

To my parents and my wife for their loving support throughout the years, to anonymous French and American taxpayers who generously supported my education, to Yves Godderis and Emmanuel Brochier for transmitting to me their passion of natural sciences and metaphysics, and to God for creating strontium isotopes and making the Universe so fascinating.

TABLE OF CONTENTS

ABSTRACT	iii
LIST OF TABLES	viii
LIST OF FIGURES	x
ACKNOWLEDGMENTS	xii
CHAPTER	
I. INTRODUCTION.....	1
Isotope geochemistry in provenance studies	2
Strontium isotope geochemistry for provenance studies	4
Sr isotope systematics.....	5
Strontium cycle	6
⁸⁷ Sr/ ⁸⁶ Sr variations in the Earth throughout geological time	7
Application of ⁸⁷ Sr/ ⁸⁶ Sr in low temperature geochemistry	8
Modeling ⁸⁷ Sr/ ⁸⁶ Sr variations	11
Objectives and outline	13
References.....	14
II. MAPPING ⁸⁷ Sr/ ⁸⁶ Sr VARIATIONS IN BEDROCK AND WATER FOR LARGE SCALE PROVENANCE STUDIES.....	21
Abstract.....	22
Introduction	22
Bedrock models	23
Water models	25
Results and discussion	26
Conclusion and perspectives	32
Acknowledgements	33
References.....	33
Supplementary methods and tables	36
III. MAPPING MULTIPLE SOURCE EFFECTS ON THE STRONTIUM ISOTOPIC SIGNATURES OF ECOSYSTEMS FROM THE CIRCUM-CARRIBBEAN	

REGION	85
Abstract	86
Introduction	86
Material and methods	88
Discussion	100
Acknowledgements	102
Literature cited	102
Appendix A	106
IV. A GEOSTATISTICAL FRAMEWORK TO PREDICT STRONTIUM ISOTOPES VARIATIONS IN ALASKA RIVERS	110
Abstract	111
Introduction	112
Material and methods	115
Results and discussion	132
Conclusion	143
Acknowledgements	144
References	144
Supplementary material	165
Supplementary dataset 1: Bedrock model validation dataset	203
Supplementary dataset 2: Chemical weathering model calibration dataset	204
References	205
V. CONCLUSION	207
Summary	208
Perspectives	209
Limitations and future improvements	211
References	214

LIST OF TABLES

2.1 Geology and measured and modeled $^{87}\text{Sr}/^{86}\text{Sr}$ values for bedrock in the catchment water model validation catchments	29
2S.1 Values of $(Rb/Sr)_{parent}$ and $(Rb/Sr)_{lithology}$ used in equations 2 and 3 for each unique lithologic descriptor (rocktype1 and rocktype2) present in the USGS geodatabases (U.S. Geological Survey, 2005, State Geologic Map Compilation, online at http://tin.er.usgs.gov/geology/state/)	44
2S.2 Assigned numerical age for each unique age descriptor present in the composite geodatabase.....	49
2S.3 Estimated values of $(^{87}\text{Sr}/^{86}\text{Sr})_{seawater}$ throughout Earth history as used in equation 3.....	75
2S.4 Values of $Sr\ content$ and W used in equations 5 and 6 for each unique lithologic descriptor (rocktype1 and rocktype2) present in the composite geodatabase.....	79
2S.5 Bulk dissolution rates of common minerals in laboratory as found by Franke (2009)	84
3.1 Chemical weathering model validation	94
3.2 Mixing model validation	95
3.A1 Parameterization of Eqs. 5 and 7 for each lithological descriptor present in the Caribbean geodatabase (French et al. 2004)	106
4.1 Summary statistics of the chemical weathering model calibration steps	152
4.2 Summary of goodness of fit measures for the bedrock model over Alaska	153
4.3 Summary of goodness of fit measures for the chemical weathering model for Alaska River	154
4.4 Summary of goodness of fit measures for the catchment water model	155
4.5 Summary of lithological proportion across Alaska and their corresponding mean	

slope and mean permafrost zonation index (pfi)	156
4.S1 Summary of power-transformation for $(^{87}\text{Rb}/^{86}\text{Sr})_{\text{parent}}$ dataset of each major GLiM lithological class	174
4.S2 Q-Q plots and histograms of $(^{87}\text{Rb}/^{86}\text{Sr})_{\text{parent}}$ dataset of each major GLiM lithological class after power-transformation and outliers removal	175
4.S3 Summary of power-transformation for $(^{87}\text{Rb}/^{86}\text{Sr})_{\text{rock}}$ for each major GLiM lithological class	177
4.S4 Q-Q plots and histograms of $(^{87}\text{Rb}/^{86}\text{Sr})_{\text{rock}}$ datasets for each major GLiM lithological class after power-transformation.....	178
4.S5 Summary of variogram model proprieties used in ordinary krigging of power-transformed $(^{87}\text{Rb}/^{86}\text{Sr})_{\text{rock}}$ of each GLiM class dataset.....	181
4.S6 Plot of empirical variograms and fitted variogram models for each GLiM major lithological class	182
4.S7 Scatterplot of predicted vs. observed power-transformed $(^{87}\text{Rb}/^{86}\text{Sr})_{\text{rock}}$ for each lithological class and summary statistic of model prediction	185
4.S8 Attribute table of the digital Atlas of Terranes from the Northern Cordillera (Colpron and Nelson, 2010) with additional lithological description, min age and max age field based on Nelson et al., 2013	189

LIST OF FIGURES

2.1 Three-stage model for the evolution of the $^{87}\text{Sr}/^{86}\text{Sr}$ in Earth materials through geological time	23
2.2 Location of the samples used for the water model verification: Green: $^{87}\text{Sr}/^{86}\text{Sr}$ measurement in stream water from 1: Clarks Fork of the Yellowstone Basin (Horton et al., 1999); 2: Owens River Lake Basin (Pretti and Stewart, 2002); 3: Scioto River watershed (Stueber et al., 1975); 4: Susquehanna River Basin (Fisher and Stueber, 1976); Red: $^{87}\text{Sr}/^{86}\text{Sr}$ measurements of marijuana from 79 counties across the USA (West et al., 2009).....	27
2.3 Validation of silicate Sr isotope model.....	27
2.4 Validation of carbonate Sr isotope model, showing linear correlations between 246 worldwide $^{87}\text{Sr}/^{86}\text{Sr}$ measurements for carbonate rocks and the $^{87}\text{Sr}/^{86}\text{Sr}$ predicted by the bedrock model and age-only models	28
2.5 Validation of silicate Sr isotope model by lithology	28
2.6 Modeled bedrock Sr isotope ratios for the contiguous USA	28
2.7 Catchment water model validation results	29
2.8 Validation of the catchment water Sr isotope model across all study catchments, showing linear regressions between measured $^{87}\text{Sr}/^{86}\text{Sr}$ and flux-weighted catchment water and age-only water model predictions for 68 streams of the USA (celestite-corrected values are used for the Scioto River).....	31
2.9 Modeled Sr isotope ratios for (A) local water, (B) flux-weighted catchment water, (C) flux-weighted catchment water model values averaged within watersheds of the Watershed Boundary Dataset (http://www.nrcs.usda.gov/wps/portal/nrcs/main/national/water/watershed/dataset) and (D) residual between major bedrock (Fig. 6B) and average flux-weighted catchment water (Fig. 9C)	32
2.10 Linear regression between $^{87}\text{Sr}/^{86}\text{Sr}$ in marijuana and the mean values of the modeled water in the country of sample origin.....	33

3.1 Representation of the box model with fluxes of dissolved Sr mixing in the soluble bioavailable Sr pool	88
3.2 Bedrock-only model $^{87}\text{Sr}/^{86}\text{Sr}$ variations calculated using equations from Bataille and Bowen (2012)	91
3.3 Sample locations for data included in the validation datasets.....	96
3.4 Bioavailable Sr isotope model validation results.....	97
3.5 (A) Contribution of bedrock weathering to the bioavailable Sr pool calculated as $F(\text{Sr})_{w \rightarrow \text{bio}} / (F(\text{Sr})_{w \rightarrow \text{bio}} + F(\text{Sr})_{\text{ss} \rightarrow \text{bio}} + F(\text{Sr})_{d \rightarrow \text{bio}})$	98
3.6 (A) Difference between predicted $^{87}\text{Sr}/^{86}\text{Sr}$ from the bedrock-only model and $^{87}\text{Sr}/^{86}\text{Sr}$ from the two source mixing model including sea salt and bedrock weathering	99
4.1 Flowchart summarizing the input data, parameterization steps and parameter estimation methods for the igneous submodel	157
4.2 Terrane ages and boundaries across Alaska	158
4.3 Predicted $^{87}\text{Sr}/^{86}\text{Sr}$ in bedrock across Alaska	159
4.4 Bedrock model validation.....	160
4.5 Calibration of the Sr chemical weathering model.....	161
4.6 Map of sampling sites (with ID numbers) and their associated observed $^{87}\text{Sr}/^{86}\text{Sr}$ (color scale) for the catchment water model validation dataset modified from Brennan et al. (in press).....	162
4.7 Catchment model validation for Alaska Rivers.....	163
4.8 Predicted $^{87}\text{Sr}/^{86}\text{Sr}$ from the catchment water model applied across Alaska	164

ACKNOWLEDGMENTS

I am greatly indebted to my advisor, Gabriel Bowen, who, through his example, his constructive reviews, his advice and his support has helped me to accomplish this work. He has been an incredibly devoted advisor and has helped me to enjoy my research and to more broadly love science. It could have been easy for such a brilliant young professor to give me little independence and to force his research interests on me, but instead, Gabe helped me to develop my own thinking in a friendly but efficient advising style. Gabe is a great example of what a good advisor should be for doctoral students. He has enough patience to let me think on my own and he fully accepted the mistakes and detours that came from leaving me so much room. I believe he gave me a solid background to face the challenges of the professional academic world. At a personal level, Gabe also gives an invaluable example of a balanced and happy man. He manages to be an amazing and hard-working scientist, a sociable man caring for others and a good father. His example and personal accomplishment were at least as valuable in my eyes as his professional career and I greatly admire the person he is. Finally, he and his wife, Brenda, were always supportive of my personal choices and of my family and contributed to make my PhD peaceful, happy and balanced.

I thank my previous committee members from Purdue University (Matt Huber, Timothy Filley and Chi-Hua Huang) and my current committee members from the University of Utah: Lisa Stright, Thure Cerling, Brett Tipple and Diego Fernandez, who

help me to think critically about this work and were always available for talking about science. I particularly thank Thure for his fascinating point of view on many science topics. I particularly thank Lisa for her inputs in geostatistics, her incredible teaching skills and her great example of raising young kids while being an accomplished scientist. I particularly thank Brett for teaching me gas chromatography methods and for fun discussions in the lab. I particularly thank Diego for initiating me into ICP-MS methods.

I thank all the collaborators who made this work possible, particularly Jens Hartmann, Casey Kennedy, Sean Brennan, Jason Laffoon, Nils Moosdorf, Matthew Wooller and Justin Vandavelde as well as all the institutions who manage and made available the various data I have used throughout this PhD (Earthchem, GEOROC, USGS). I also thank all the staff, and lab technicians at Purdue and University and at the University of Utah for helping me in my work. I thank all the members of the IREH and SPATIAL laboratories for their friendship and help throughout this PhD, particularly Justin Vandavelde, Bianca Maibauer, Alex Lowe and Stephen Ruegg.

I want to thank my parents in France for giving me such a wonderful education and encouraging my scientific curiosity, my brother and sisters for supporting me through those years away from my homeland and my family-in-law for adopting me and always making me feel at home in America. I mostly want to thank my wife, Hilary, who has been incredibly patient and helpful throughout those years of hardwork. Finally I want to thank my kids for making my PhD much more fun and challenging and for keeping my feet on the ground.

Funding sources for this work are acknowledged at the end of each chapter.

CHAPTER I

INTRODUCTION

Isotope geochemistry in provenance studies

In a globalized world, where movements of materials and individuals are accelerating and where consumers are increasingly concerned about product quality and provenance, tracing the origin of natural materials and human products is of great relevance. A growing number of international and/or local legislative initiatives in a variety of domains have helped to improve the traceability of human and natural products (e.g., food, endangered species) by introducing programs and labels to track provenance (e.g., United States “Country of Origin Labeling for Food Products”). The proliferation of those labels in recent years has increased the demand for new techniques able to resolve provenance at different spatial scales. Stable isotopes have gained considerable interest as a tool for provenance studies and have been successfully applied in a variety of fields to determine product authenticity for regulating trade practices (Kelly et al., 2005), to track the travel histories of individuals in criminal and/or archeological cases (Bentley, 2006), and to follow migration pathways of endangered and exploited animal populations (Hobson et al., 2010). The application of stable isotope geochemistry for resolving provenance relies on comparing the isotopic signature of a sample of unknown origin to that of baseline maps characterizing the isotopic signature of the potential isotope source(s) of the sample. Consequently, the application of stable isotopes as a tool of provenance requires mature and cost-effective analytical capabilities to analyze stable isotope ratio in the sample of interest, as well as mechanistic models able to predict the isotopic signatures of elemental sources at varied spatiotemporal scales.

Oxygen (O) and hydrogen (H) isotope ratios are the most commonly applied isotope systems to resolve provenance in terrestrial environments (Bowen, 2010b). The

main advantages of applying O and H isotope ratios for provenance studies is that H and O stable isotope ratio analyses are precise, rapid and cost-effective and that the processes controlling the spatial isotopic variations of H and O on the Earth's surface are well-understood and can be used to develop accurate predictive models (Bowen, 2010b). The spatial variability of O and H isotope ratios in reservoirs of the Earth surface originates primarily from isotopic fractionation in biogeochemical processes as water cycles through different reservoirs (Bowen, 2010b). Isotopic fractionation imparts a unique spatiotemporal "isotopic label" or fingerprint to a given reservoir and/or material, and this unique fingerprint coupled with predictive models of isotope variations can be used to model the probability of geographic origin (Wunder, 2010). Decades of work have led to the development of models to predict the O and H isotope ratio variations in ocean water (LeGrande and Schmidt, 2006), rainfall (Bowen, 2010a), surface water (Bowen et al., 2011), tap water (Bowen et al., 2007) or animal tissues (West et al., 2007). Maps derived from those predictive models are widely distributed (Bowen et al., 2014) and routinely integrated to interpret provenance in fields as varied as forensics, archeology, atmospheric sciences, ecology, and paleoclimate. However, one fundamental limitation in applying O and H isotope in provenance studies is the generally broad scale of O and H isotope ratio variations. H and O isotope variations are primarily controlled by large scale (10 to 100 km) atmospheric processes that produce a continuous gradient in isotope variations and make geographic assignment nonunique (Bowen, 2010a; Farmer et al., 2008).

Strontium isotope geochemistry for provenance studies

Strontium isotope ratio ($^{87}\text{Sr}/^{86}\text{Sr}$) constitutes an alternative and complementary tool to enhance the spatial resolution for provenance studies because strontium (Sr) in soils, waters, plants, and animals is sourced primarily from local bedrock. As such, $^{87}\text{Sr}/^{86}\text{Sr}$ patterns follow discrete variations of geological regimes with relatively constant $^{87}\text{Sr}/^{86}\text{Sr}$ within geological units of known age and lithology (Capo et al., 1998). This discrete patterning is superimposed by $^{87}\text{Sr}/^{86}\text{Sr}$ variability associated with local and regional geological processes. Local $^{87}\text{Sr}/^{86}\text{Sr}$ heterogeneity originates from variations in petrology, sedimentary provenance, bulk composition, or postburial alteration processes, whereas larger-scale $^{87}\text{Sr}/^{86}\text{Sr}$ heterogeneity are a function of regional tectonic or sedimentary basin processes. This multiscale and discrete patterning of $^{87}\text{Sr}/^{86}\text{Sr}$ variability is drastically different from the continuous patterns of O and H isotopes, providing complementary information to those isotopes for resolving provenance at multiple scales. Another critical advantage of the Sr isotope systems in comparison with traditional stable isotopes used in geoprofiling studies is that interpretation of $^{87}\text{Sr}/^{86}\text{Sr}$ variations are not complicated by isotopic fractionation (Capo et al., 1998). Small mass-dependent isotopic fractionation of Sr isotopes can occur in geologic and biological processes, but this isotopic fractionation is corrected for during mass spectrometric measurement by normalization of the nonradiogenic isotopes to known values (Capo et al., 1998). As a result, the measured $^{87}\text{Sr}/^{86}\text{Sr}$ reflects only variations in the amount of radiogenic ^{87}Sr present in the sample, which ultimately is a function of its Sr source. Sr has also a long residence time in most reservoirs, which, combined with the absence of isotopic fractionation, leads to relatively constant $^{87}\text{Sr}/^{86}\text{Sr}$ signatures in bedrock and soils

at human timescales. These properties make $^{87}\text{Sr}/^{86}\text{Sr}$ a conservative tracer in Earth surface reservoirs, thus greatly simplifying interpretation of $^{87}\text{Sr}/^{86}\text{Sr}$ data.

Sr isotope systematics

Sr (atomic number 38) is a divalent alkaline Earth trace element which can substitute for Ca in Ca-bearing minerals such as plagioclase feldspar, apatite, sulfates (gypsum and anhydrite), and carbonates. Sr is one of the most abundant trace elements and is ubiquitous on the Earth's surface, making isotopic analysis relatively easy in comparison with other radiogenic isotopes. Sr has four naturally occurring stable isotopes ^{84}Sr (0.56%), ^{86}Sr (9.87%), ^{87}Sr (7.04%) and ^{88}Sr (82.53%) with ^{87}Sr originating from the β -decay of rubidium 87 (^{87}Rb) (decay constant $\lambda=1.42\times 10^{-11}$ year $^{-1}$) (Faure, 1977). ^{87}Sr (daughter of ^{87}Rb) is not concentrated in the same rock types as the other stable Sr isotopes because rubidium (Rb; atomic number 37) is an alkali metal and substitutes for K in K-bearing minerals such as muscovite, biotite, alkali feldspars (orthoclase and microcline), clays (illite) and evaporites (sylvite, carnallite). As a result, the present day quantity of ^{87}Sr normalized to the naturally occurring and invariant ^{86}Sr ($^{87}\text{Sr}/^{86}\text{Sr}$) in a given rock can be expressed using the radiogenic production equation as:

$$\left(\frac{^{87}\text{Sr}}{^{86}\text{Sr}}\right)_{\text{rock}} = \left(\frac{^{87}\text{Sr}}{^{86}\text{Sr}}\right)_i + \left(\frac{^{87}\text{Rb}}{^{86}\text{Sr}}\right)_{\text{rock}} (e^{\lambda t} - 1), \quad (1.1)$$

where $^{87}\text{Sr}/^{86}\text{Sr}$ variations in rocks ($(^{87}\text{Sr}/^{86}\text{Sr})_{\text{rock}}$) are a function of: 1) the initial $^{87}\text{Sr}/^{86}\text{Sr}$ ($(^{87}\text{Sr}/^{86}\text{Sr})_i$) which depends on the geological history of the parent rock, 2) bedrock age (t) which controls the fraction of ^{87}Rb that decayed into ^{87}Sr , and 3) the $^{87}\text{Rb}/^{86}\text{Sr}$ of the

rock ($(^{87}\text{Rb}/^{86}\text{Sr})_{\text{rock}}$) which varies with lithology because of the specific affinity of Rb and Sr with different minerals. This radiogenic equation is the basis for the rubidium-strontium dating method, used to determine the time of crystallization of igneous rocks such as granites (Faure, 1977).

$^{87}\text{Rb}/^{86}\text{Sr}$ is directly proportional to the Rb/Sr and can be expressed as:

$$\frac{^{87}\text{Rb}}{^{86}\text{Sr}} = \frac{\text{Rb}(w^{87}\text{Rb})(m\text{Sr})}{\text{Sr}(w^{86}\text{Sr})(m\text{Rb})} \approx 2.8936 \frac{\text{Rb}}{\text{Sr}}, \quad (1.2)$$

where m refers to the atomic mass of an element and w to the abundance (%) of an isotope.

Strontium cycle

Sr is a relatively lithophilic element and has become increasingly concentrated on the more surficial layers of the Earth (Mantle and Crust) as geochemical differentiation processes (e.g., fractional crystallization) occurred during Earth's history. Sr is particularly concentrated in Ca-rich rock types such as carbonates, evaporites or intermediate igneous rock and is relatively less concentrated in felsic igneous rocks and siliciclastic sediments. Bedrock is the principal source of Sr to the Earth surface and Sr is exported from rocks to other reservoirs through erosion, weathering, and biological uptake (Capo et al., 1998). Erosion and weathering of bedrock and soils transfer Sr to the hydrosphere and the atmosphere in dissolved form or bounded to other particulates (Capo et al., 1998). During the cycling of Sr on the Earth surface, part of this Sr is uptaken by the biosphere and is concentrated in certain Ca-rich biological tissues (e.g., bones).

Ultimately, Sr is transported to the ocean where it is deposited in carbonates on the ocean floor and recycled back into the Earth's interior through subduction (Capo et al., 1998).

$^{87}\text{Sr}/^{86}\text{Sr}$ variations in the Earth throughout geological time

All rock reservoirs inherited an identical initial $^{87}\text{Sr}/^{86}\text{Sr}$ signature (0.699) from the well-mixed primordial Earth (Wetherill et al., 1973). $^{87}\text{Sr}/^{86}\text{Sr}$ evolution of distinct geological reservoirs was induced by geochemical differentiation associated with fractional crystallization and the formation of different Earth layers and rock reservoirs (Faure, 1977). As geochemical differentiation progressed, Sr and even more so, Rb, concentrated into melts, resulting in high Rb/Sr ratios in the continental crust and its progressive diminution in the residual mantle (Faure, 1977). The $^{87}\text{Sr}/^{86}\text{Sr}$ of the bulk Earth increased as ^{87}Rb decayed into ^{87}Sr and this increase was enhanced in the crust as ^{87}Rb became concentrated by recycling. As new rock reservoirs were formed from crustal or mantle precursors, they inherited the $^{87}\text{Sr}/^{86}\text{Sr}$ of their parent, but in most cases fractional crystallization led to dissimilar Rb/Sr, causing their $^{87}\text{Sr}/^{86}\text{Sr}$ to evolve along a different Rb/Sr slope than the parent material. Rocks with higher (lower) Rb/Sr than their parent evolved along a steeper (flatter) slope. The $^{87}\text{Sr}/^{86}\text{Sr}$ signatures of the parent and new rock reservoirs further diverged as time progressed because of the different ^{87}Rb content of each reservoir. At equal Rb/Sr ratio, older rocks have higher $^{87}\text{Sr}/^{86}\text{Sr}$ than younger rocks because ^{87}Rb had more time to decay in the older reservoir. At equal age, rock with higher Rb/Sr have higher $^{87}\text{Sr}/^{86}\text{Sr}$ than rock with low Rb/Sr because more ^{87}Rb is available to decay into ^{87}Sr . Combined effects of age and lithology explain the current first-order patterns of $^{87}\text{Sr}/^{86}\text{Sr}$ on the Earth surface, with high $^{87}\text{Sr}/^{86}\text{Sr}$ in regions

dominated with old felsic rocks (e.g., cratonic shields) and low $^{87}\text{Sr}/^{86}\text{Sr}$ in newly formed mafic terranes (e.g., Alaska volcanic terranes).

Application of $^{87}\text{Sr}/^{86}\text{Sr}$ in low temperature geochemistry

For decades, scientists have taken advantage of the well-documented $^{87}\text{Sr}/^{86}\text{Sr}$ variations in seawater to constrain the age of marine sediments (McArthur et al., 2001). The method relies on the assumption that $^{87}\text{Sr}/^{86}\text{Sr}$ of seawater depends primarily on the $^{87}\text{Sr}/^{86}\text{Sr}$ of the crust being altered at a given time period. $^{87}\text{Sr}/^{86}\text{Sr}$ analyses of marine carbonates from different time periods have helped to reconstruct a fairly complete, high resolution record of $^{87}\text{Sr}/^{86}\text{Sr}$ variation in seawater throughout Earth's history (Halverson et al., 2007; Shields and Veizer, 2002; Veizer, 1989). The $^{87}\text{Sr}/^{86}\text{Sr}$ signature in seawater displays a progressive increase with time associated with the increased felsic nature of the recycled crust. This background increase is overprinted by multimillion year time scale variations coinciding with different tectonic events, climate modes and supercontinent cycle stages (Veizer et al., 1999). The result is that the $^{87}\text{Sr}/^{86}\text{Sr}$ value and the pattern of $^{87}\text{Sr}/^{86}\text{Sr}$ variations of a given time period are relatively diagnostic (little redundancy in $^{87}\text{Sr}/^{86}\text{Sr}$ values through time). Moreover, all carbonates deposited at a given time period have a similar $^{87}\text{Sr}/^{86}\text{Sr}$ signature (Veizer, 1989) because of the long residence time of Sr in seawater (Vollstaedt et al., 2014). Combined, those characteristics can be used for chronostratigraphy by correlating the $^{87}\text{Sr}/^{86}\text{Sr}$ of marine sediments of unknown age with the well-documented and time-constrained $^{87}\text{Sr}/^{86}\text{Sr}$ marine curve (McArthur et al., 2001).

Another common application of $^{87}\text{Sr}/^{86}\text{Sr}$ is based on interpreting $^{87}\text{Sr}/^{86}\text{Sr}$

variations in seawater as a tool to reconstruct the tectonic history of the Earth's surface (Veizer et al., 1999). Volumes of literature have been published to estimate the current Sr isotope budget and interpret $^{87}\text{Sr}/^{86}\text{Sr}$ shifts and trends in seawater throughout Earth history. The modern Sr isotope budget in the ocean depends primarily on changes in the magnitude and $^{87}\text{Sr}/^{86}\text{Sr}$ signature of a continental radiogenic flux of Sr from runoff and groundwater and a nonradiogenic ocean Sr fluxes from crust-seawater interactions (Veizer et al., 1999). The most recent estimates of those fluxes indicate that the radiogenic continental flux represents 59% of the total Sr flux – 43% of which originates from siliciclastic sediments (0.721) and 57% from carbonates (0.708) – whereas the nonradiogenic mafic flux represents 41% of the Sr flux – 27% of which are from oceanic crust seawater interactions (0.703) and 73% from volcanic arcs (0.7035) (Allègre et al., 2010). Based on those estimates, periods when $^{87}\text{Sr}/^{86}\text{Sr}$ in seawater are high are thought to represent time when continental weathering rates or $^{87}\text{Sr}/^{86}\text{Sr}$ signatures of the continental rocks were high. High continental weathering rates coincide with periods of orogenesis (Peters and Gaines, 2012; Raymo et al., 1988), periods of equatorial positioning of plate tectonics (Goddéris et al., 2014) or periods of climate shifts from greenhouse to icehouse (Zachos et al., 1999). High $^{87}\text{Sr}/^{86}\text{Sr}$ signatures of the continental surface occur during periods of intense crustal recycling during collisional orogenesis (Condie and Aster, 2013). Periods when $^{87}\text{Sr}/^{86}\text{Sr}$ in seawater is low are thought to reflect periods of formation of nonradiogenic continental crust (Condie and Aster, 2013), increase in seafloor spreading rates (Graham et al., 1982) or occurrence of massive continental floodbasalt and continental arcs (Allègre et al., 2010; Das and Krishnaswami, 2007).

In the last decades, applications of $^{87}\text{Sr}/^{86}\text{Sr}$ for provenance of organic and nonorganic materials have been rapidly extending, at least in part due to the development of high performance laser ablation multicollector inductively coupled plasma mass spectrometry, which allows rapid and high precision analysis and requires very small amounts of sample. Those technological advances have opened the door to new applications for Sr isotope geochemistry, including: 1) reconstructing the migration pathways of mammals (Koch et al., 1995), birds (Sellick et al., 2009), fresh water, anadromous fishes (Barnett-Johnson et al., 2008; Kennedy et al., 2005; Walther et al., 2011) and paleofauna (Britton et al., 2011; Hoppe et al., 1999; Price et al., 2002), 2) determining feeding habits of ancient humans (Copeland et al., 2011) and animals (Feranec et al., 2007; Radloff et al., 2010), 3) distinguishing region of origin of agricultural or natural products such as rice (Kawasaki et al., 2002), wine (Marchionni et al., 2013), water (Voerkelius et al., 2010), milk (Crittenden et al., 2007) or illegal drugs (West et al., 2009), 4) identifying nonlocal individuals in archeology and forensic cases (Bentley, 2006; Price et al., 2002; Schroeder et al., 2009), 5) determining the geographic source of dust aerosols (Grousset and Biscaye, 2005; Kurtz et al., 2001), 6) reconstructing silicate and carbonate weathering patterns in watersheds (Blum et al., 1998; Gaillardet et al., 1997; Horton et al., 1999; Huh and Edmond, 1999; Huh et al., 1998a; Huh et al., 1998b; Millot et al., 2002; Millot et al., 2003; Pretti and Stewart, 2002; Probst et al., 2000; Rad et al., 2007), 7) identifying seasonal variations in sources of elements to river (Douglas et al., 2013; Nakano and Tanaka, 1997; Voss et al., 2014) and, 8) distinguishing element sources to soils and ecosystems (Bern et al., 2005; Chadwick et al., 2009; Pett-Ridge et al., 2009). In most of the current applications of Sr isotope

geochemistry for determining provenance, the spatial $^{87}\text{Sr}/^{86}\text{Sr}$ variations of the Sr sources are poorly constrained, particularly when the potential Sr sources cover large spatial scales (e.g., water or food sources for animals with large foraging areas). The application and interpretation of Sr isotope geochemistry in provenance studies at regional spatial scales requires the development of models predicting the $^{87}\text{Sr}/^{86}\text{Sr}$ signature of Sr sources.

Modeling $^{87}\text{Sr}/^{86}\text{Sr}$ variations

Several approaches have been tested in recent years to develop regional scale predictive $^{87}\text{Sr}/^{86}\text{Sr}$ maps of potential Sr sources including bedrock (Beard and Johnson, 2000), river water (Hegg et al., 2013) or bioavailable Sr (Frei and Frei, 2011; Price et al., 2002). The most common approach used in ecology and archeology is to use interpolation to generate a map of $^{87}\text{Sr}/^{86}\text{Sr}$ based on analyses of a reference substrate that record or approximate the $^{87}\text{Sr}/^{86}\text{Sr}$ of the Sr sources. For instance, in archeology, interpolated maps representing the $^{87}\text{Sr}/^{86}\text{Sr}$ variations of the “bioavailable Sr reservoir” have been derived from $^{87}\text{Sr}/^{86}\text{Sr}$ analyses of local surface water (Frei and Frei, 2011), local flora (Price et al., 2002) or local fauna (Bentley and Knipper, 2005; Hodell et al., 2004; Laffoon et al., 2012). While this method can give precise $^{87}\text{Sr}/^{86}\text{Sr}$ prediction at local scale, it is hampered by the challenge of selecting appropriate reference substrates, which is nontrivial as different sample materials may integrate different spatial and temporal scales of $^{87}\text{Sr}/^{86}\text{Sr}$ variation. Ultimately, applying this method at large spatial scale is also data intensive and costly, and in most cases traditional interpolation algorithms are unable to explicitly consider the discrete patterning of $^{87}\text{Sr}/^{86}\text{Sr}$ variations.

Another approach applied to derive predictive $^{87}\text{Sr}/^{86}\text{Sr}$ models consists of training a multiple linear regression model (MLRM) using lithology and age as predictor. This method has the advantage of partly accounting for processes governing the spatial structure of $^{87}\text{Sr}/^{86}\text{Sr}$ variations (Hegg et al., 2013). However, the dependence of $^{87}\text{Sr}/^{86}\text{Sr}$ on a large number of nonindependent predictors (age and multiple lithological classes) limits the performance of MLRM and requires a large number of $^{87}\text{Sr}/^{86}\text{Sr}$ analyses to make the model statistically robust. The MLRM approach appears to function relatively well in areas where lithological and geological complexity is low, limiting the number of potential predictors. However, the method becomes increasingly uncertain for areas with more complex geology where both age and lithology control $^{87}\text{Sr}/^{86}\text{Sr}$ variations.

A more promising and complementary approach to developing a unified framework to predict $^{87}\text{Sr}/^{86}\text{Sr}$ at large spatial scales is to develop process-based spatial models. This approach was initiated by Beard and Johnson (2000) who developed a model predicting $^{87}\text{Sr}/^{86}\text{Sr}$ in bedrock over the conterminous USA. Their method is based on the assumption that bedrock age is the primary control of $^{87}\text{Sr}/^{86}\text{Sr}$ variations, because rock age determines the fraction of ^{87}Rb that has decayed into ^{87}Sr . The predictive power of this model was relatively low, explaining roughly 30% of the total variance for both bedrock and water (Chesson et al., 2012; Hobson et al., 2010). Despite the poor predictive power of this initial model, Beard and Johnson's (2000) idea of using geological maps to predict $^{87}\text{Sr}/^{86}\text{Sr}$ was the inspiration for our work and laid the foundation for the development of new, more accurate process-based $^{87}\text{Sr}/^{86}\text{Sr}$ models.

Objectives and outline

In this dissertation, we present a series of modeling activities aimed at establishing a basis for process-based predictive GIS modeling of Sr isotopes distribution at continental to global scale. The approach leverages publically available geospatial data on rock geochemistry, surficial and bedrock geology, climate, hydrology, and aerosols to model the input and propagation of Sr from multiple geological sources through hydrosystems and ecosystems. In the second chapter, we formulate and calibrate a bedrock model which predicts $^{87}\text{Sr}/^{86}\text{Sr}$ in bedrock as a function of rock age and lithology. This initial bedrock model is coupled to a basic chemical weathering model to predict $^{87}\text{Sr}/^{86}\text{Sr}$ in soil and river waters. This initial chemical weathering model calculates the export of Sr from rock to river water as a function of the difference in weathering rates and Sr content of different rock types. The performance of the model is tested against rock, water and biological data over the conterminous USA and demonstrates encouraging performance. In the third chapter, we build upon our initial modeling effort to formulate a bioavailable Sr model which explicitly predicts the $^{87}\text{Sr}/^{86}\text{Sr}$ in biological material and accounts for the mixing of Sr from multiple sources in ecosystems. This model is used to predict the $^{87}\text{Sr}/^{86}\text{Sr}$ of bioavailable Sr for the circum-Caribbean region, and significantly improves the predictive power of our models when tested against biological datasets.

In the final chapter, we revisit the bedrock and water models by developing a unified flexible geostatistical framework to predict $^{87}\text{Sr}/^{86}\text{Sr}$ in Alaska rivers. In this final step, we improve the calibration of the bedrock model to predict local scale $^{87}\text{Sr}/^{86}\text{Sr}$ variability and represent prediction uncertainty. This new bedrock model is coupled to a

fully independent, Sr-specific chemical weathering model predicting the spatial variations in the rate of Sr release from rocks. The model is used to predict Sr and $^{87}\text{Sr}/^{86}\text{Sr}$ in rivers of Alaska and is tested against an independent dataset of $^{87}\text{Sr}/^{86}\text{Sr}$ analyses from streams and rivers of Alaska.

References

- Allègre, C.J. et al., 2010. The fundamental role of island arc weathering in the oceanic Sr isotope budget. *Earth and Planetary Science Letters*, 292(1–2): 51-56.
- Balasse, M., Ambrose, S.H., Smith, A.B., Price, T.D., 2002. The seasonal mobility model for prehistoric herders in the South-western Cape of South Africa assessed by isotopic analysis of sheep tooth enamel. *Journal of Archaeological Science*, 29(9): 917-932.
- Barnett-Johnson, R., Pearson, T.E., Ramos, F.C., 2008. Tracking natal origins of salmon using isotopes, otoliths, and landscape geology. *Limnology and Oceanography*, 53(4): 1633–1642.
- Beard, B.L., Johnson, C.M., 2000. Strontium isotope composition of skeletal material can determine the birth place and geographic mobility of humans and animals. *Journal of Forensic Sciences*, 45(5): 1049-1061.
- Bentley, R.A., 2006. Strontium isotopes from the earth to the archaeological skeleton: A review. *Journal of Archaeological Method and Theory*, 13(3): 135-187.
- Bentley, R.A., Knipper, C., 2005. Geographical patterns in biologically available strontium, carbon and oxygen isotope signatures in prehistoric SW Germany. *Archaeometry*, 47: 629-644.
- Bern, C.R., Townsend, A.R., Farmer, G.L., 2005. Unexpected dominance of parent-material strontium in a tropical forest on highly weathered soils. *Ecology*, 86(3): 626-632.
- Blum, J.D., Gazis, C.A., Jacobson, A.D., Page Chamberlain, C., 1998. Carbonate versus silicate weathering in the Raikhot watershed within the High Himalayan Crystalline Series. *Geology*, 26(5): 411-414.
- Bowen, G.J., 2010a. Statistical and Geostatistical Mapping of Precipitation Water Isotope Ratios. In: West, J.B., Bowen, G.J., Dawson, T.E., Tu, K.P. (Eds.), *Isoscapes*. Springer Netherlands, pp. 139-160.

- Bowen, G.J., 2010b. Isoscapes: Spatial pattern in isotopic biogeochemistry. *Annual Review of Earth and Planetary Sciences*, 38(1): 161-187.
- Bowen, G.J., Ehleringer, J.R., Chesson, L.A., Stange, E., Cerling, T.E., 2007. Stable isotope ratios of tap water in the contiguous United States. *Water Resources Research*, 43(3): W03419.
- Bowen, G.J., Kennedy, C.D., Liu, Z., Stalker, J., 2011. Water balance model for mean annual hydrogen and oxygen isotope distributions in surface waters of the contiguous United States. *Journal of Geophysical Research: Biogeosciences*, 116(G4): G04011.
- Bowen, G.J., Liu, Z., Vander Zanden, H.B., Zhao, L., Takahashi, G., 2014. Geographic assignment with stable isotopes in IsoMAP. *Methods in Ecology and Evolution*, 5(3): 201-206.
- Britton, K. et al., 2011. Strontium isotope evidence for migration in late Pleistocene rangifer: Implications for Neanderthal hunting strategies at the middle Palaeolithic site of Jonzac, France. *Journal of Human Evolution*, 61(2): 176-185.
- Capo, R.C., Stewart, B.W., Chadwick, O.A., 1998. Strontium isotopes as tracers of ecosystem processes: Theory and methods. *Geoderma*, 82(1-3): 197-225.
- Chadwick, O.A., Derry, L.A., Bern, C.R., Vitousek, P.M., 2009. Changing sources of strontium to soils and ecosystems across the Hawaiian Islands. *Chemical Geology*, 267(1-2): 64-76.
- Chesson, L.A. et al., 2012. Strontium isotopes in tap water from the coterminous USA. *Ecosphere* 3:art67. <http://dx.doi.org/10.1890/ES12-00122.1>
- Condie, K.C., Aster, R.C., 2013. Refinement of the supercontinent cycle with Hf, Nd and Sr isotopes. *Geoscience Frontiers*, 4(6): 667-680.
- Copeland, S.R. et al., 2011. Strontium isotope evidence for landscape use by early hominins. *Nature*, 474(7349): 76-78.
- Crittenden, R.G. et al., 2007. Determining the geographic origin of milk in Australasia using multi-element stable isotope ratio analysis. *International Dairy Journal*, 17(5): 421-428.
- Das, A., Krishnaswami, S., 2007. Elemental geochemistry of river sediments from the Deccan Traps, India: Implications to sources of elements and their mobility during basalt-water interaction. *Chemical Geology*, 242(1-2): 232-254.
- Douglas, T.A., Blum, J.D., Guo, L., Keller, K., Gleason, J.D., 2013. Hydrogeochemistry of seasonal flow regimes in the Chena River, a subarctic watershed draining

- discontinuous permafrost in interior Alaska (USA). *Chemical Geology*, 335(0): 48-62.
- Farmer, A., Cade, B.S., Torres-Dowdall, J., 2008. Fundamental limits to the accuracy of deuterium isotopes for identifying the spatial origin of migratory animals. *Oecologia*, 158(2): 183-192.
- Faure, G., 1977. *Principles of Isotope Geology*. Second edition, John Wiley and Sons, New York, 589 p.
- Feranec, R., Hadly, E., Paytan, A., 2007. Determining landscape use of Holocene mammals using strontium isotopes. *Oecologia*, 153(4): 943-950.
- Frei, K.M., Frei, R., 2011. The geographic distribution of strontium isotopes in Danish surface waters – A base for provenance studies in archaeology, hydrology and agriculture. *Applied Geochemistry*, 26(3): 326-340.
- Gaillardet, J., Dupre, B., Allegre, C.J., Négrel, P., 1997. Chemical and physical denudation in the Amazon River Basin. *Chemical Geology*, 142(3–4): 141-173.
- Goddéris, Y., Donnadiou, Y., Le Hir, G., Lefebvre, V., Nardin, E., 2014. The role of palaeogeography in the Phanerozoic history of atmospheric CO₂ and climate. *Earth-Science Reviews*, 128(0): 122-138.
- Graham, D.W., Bender, M.L., Williams, D.F., Keigwin Jr, L.D., 1982. Strontium-calcium ratios in Cenozoic planktonic foraminifera. *Geochimica et Cosmochimica Acta*, 46(7): 1281-1292.
- Grousset, F.E., Biscaye, P.E., 2005. Tracing dust sources and transport patterns using Sr, Nd and Pb isotopes. *Chemical Geology*, 222(3-4): 149-167.
- Halverson, G.P., Dudás, F.Ö., Maloof, A.C., Bowring, S.A., 2007. Evolution of the ⁸⁷Sr/⁸⁶Sr composition of Neoproterozoic seawater. *Palaeogeography, Palaeoclimatology, Palaeoecology*, 256(3–4): 103-129.
- Hegg, J.C., Kennedy, B.P., Fremier, A.K., 2013. Predicting strontium isotope variation and fish location with bedrock geology: Understanding the effects of geologic heterogeneity. *Chemical Geology*, 360–361(0): 89-98.
- Hobson, K., Barnett-Johnson, R., Cerling, T., 2010. Using Isoscapes to Track Animal Migration. In: West, J.B., Bowen, G.J., Dawson, T.E., Tu, K.P. (Eds.), *Isoscapes*. Springer Netherlands, pp. 273-298.
- Hodell, D.A., Quinn, R.L., Brenner, M., Kamenov, G., 2004. Spatial variation of strontium isotopes (⁸⁷Sr/⁸⁶Sr) in the Maya region: A tool for tracking ancient human migration. *Journal of Archaeological Science*, 31(5): 585-601.

- Hoppe, K.A., Koch, P.L., Carlson, R.W., Webb, S.D., 1999. Tracking mammoths and mastodons: Reconstruction of migratory behavior using strontium isotope ratios. *Geology*, 27(5): 439-442.
- Horton, T.W., Chamberlain, C.P., Fantle, M., Blum, J.D., 1999. Chemical weathering and lithologic controls of water chemistry in a high-elevation river system: Clark's Fork of the Yellowstone River, Wyoming and Montana. *Water Resources Research*, 35(5): 1643-1655.
- Huh, Y., Edmond, J.M., 1999. The fluvial geochemistry of the rivers of Eastern Siberia: III. Tributaries of the Lena and Anabar draining the basement terrain of the Siberian Craton and the Trans-Baikal Highlands. *Geochimica et Cosmochimica Acta*, 63(7-8): 967-987.
- Huh, Y., Panteleyev, G., Babich, D., Zaitsev, A., Edmond, J.M., 1998a. The fluvial geochemistry of the rivers of Eastern Siberia: II. Tributaries of the Lena, Omoloy, Yana, Indigirka, Kolyma, and Anadyr draining the collisional/accretionary zone of the Verkhoysk and Cherskiy ranges. *Geochimica et Cosmochimica Acta*, 62(12): 2053-2075.
- Huh, Y., Tsoi, M.Y., Zaitsev, A., Edmond, J.M., 1998b. The fluvial geochemistry of the rivers of Eastern Siberia: I. Tributaries of the Lena River draining the sedimentary platform of the Siberian Craton. *Geochimica et Cosmochimica Acta*, 62(10): 1657-1676.
- Kawasaki, A., Oda, H., Hirata, T., 2002. Determination of strontium isotope ratio of brown rice for estimating its provenance. *Soil Science and Plant Nutrition*, 48(5): 635-640.
- Kelly, S., Heaton, K., Hoogewerff, J., 2005. Tracing the geographical origin of food: The application of multi-element and multi-isotope analysis. *Trends in Food Science & Technology*, 16(12): 555-567.
- Kennedy, B.P., Chamberlain, C.P., Blum, J.D., Nislow, K.H., Folt, C.L., 2005. Comparing naturally occurring stable isotopes of nitrogen, carbon, and strontium as markers for the rearing locations of Atlantic salmon (*Salmo salar*). *Canadian Journal of Fisheries and Aquatic Sciences*, 62(1): 48-57.
- Koch, P.L., Halliday, A.N., Water, L.M., Stearley, R.F., Huston, T.J., Smith, G.R., 1992. Sr isotopic composition of hydroxyapatite from recent and fossil salmon: The record of lifetime migration and diagenesis. *Earth and Planetary Science Letters*, 108(4): 277-287.
- Koch, P.L., Heisinger, J., Moss, C., Carlson, R.W., Fogel, M.L., Behrensmeyer, A.K., 1995. Isotopic tracking of change in diet and habitat use in African elephants. *Science*, 267(5202): 1340-1343.

- Kurtz, A.C., Derry, L.A., Chadwick, O.A., 2001. Accretion of Asian dust to Hawaiian soils: Isotopic, elemental, and mineral mass balances. *Geochimica Et Cosmochimica Acta*, 65(12): 1971-1983.
- Laffoon, J.E., Davies, G.R., Hoogland, M.L.P., Hofman, C.L., 2012. Spatial variation of biologically available strontium isotopes ($^{87}\text{Sr}/^{86}\text{Sr}$) in an archipelagic setting: A case study from the Caribbean. *Journal of Archaeological Science*, 39(7): 2371-2384.
- LeGrande, A.N., Schmidt, G.A., 2006. Global gridded data set of the oxygen isotopic composition in seawater. *Geophysical Research Letters*, 33(12): L12604.
- Marchionni, S., Braschi, E., Tommasini, S., Bollati, A., Cifelli, F., Mulinacci, N., Mattei, M., Conticelli, S., 2013. High-precision $^{87}\text{Sr}/^{86}\text{Sr}$ analyses in wines and their use as a geological fingerprint for tracing geographic provenance. *Journal of Agricultural and Food Chemistry*, 61(28): 6822-6831.
- McArthur, J.M., Howarth, R.J., Bailey, T.R., 2001. Strontium isotope stratigraphy: LOWESS Version 3: Best fit to the marine Sr-isotope curve for 0–509 Ma and accompanying look-up table for deriving numerical age. *The Journal of Geology*, 109(2): 155-170.
- Millot, R., Gaillardet, J., Dupré, B., Allègre, C.J., 2002. The global control of silicate weathering rates and the coupling with physical erosion: New insights from rivers of the Canadian Shield. *Earth and Planetary Science Letters*, 196(1–2): 83-98.
- Millot, R., Gaillardet, J.é., Dupré, B., Allègre, C.J., 2003. Northern latitude chemical weathering rates: Clues from the Mackenzie River Basin, Canada. *Geochimica et Cosmochimica Acta*, 67(7): 1305-1329.
- Nakano, T., Tanaka, T.-i., 1997. Strontium isotope constraints on the seasonal variation of the provenance of base cations in rain water at Kawakami, Central Japan. *Atmospheric Environment*, 31(24): 4237-4245.
- Peters, S.E., Gaines, R.R., 2012. Formation of the 'Great Unconformity' as a trigger for the Cambrian explosion. *Nature*, 484(7394): 363-366.
- Pett-Ridge, J.C., Derry, L.A., Kurtz, A.C., 2009. Sr isotopes as a tracer of weathering processes and dust inputs in a tropical granitoid watershed, Luquillo Mountains, Puerto Rico. *Geochimica Et Cosmochimica Acta*, 73(1): 25-43.
- Pretti, V.A., Stewart, B.W., 2002. Solute sources and chemical weathering in the Owens Lake watershed, eastern California. *Water Resources Research*, 38(8):1-18.
- Price, T.D., Burton, J.H., Bentley, R.A., 2002. The characterization of biologically available strontium isotope ratios for the study of Prehistoric migration.

- archaeometry, 44(1): 117-135.
- Probst, A., El Gh'mari, A., Aubert, D., Fritz, B., McNutt, R., 2000. Strontium as a tracer of weathering processes in a silicate catchment polluted by acid atmospheric inputs, Strengbach, France. *Chemical Geology*, 170(1-4): 203-219.
- Rad, S.D., Allegre, C.J., Louvat, P., 2007. Hidden erosion on volcanic islands. *Earth and Planetary Science Letters*, 262(1-2): 109-124.
- Radloff, F.G.T., Mucina, L., Bond, W.J., Roux, P.J., 2010. Strontium isotope analyses of large herbivore habitat use in the Cape Fynbos region of South Africa. *Oecologia*, 164(2): 567-578.
- Raymo, M.E., Ruddiman, W.F., Froelich, P.N., 1988. Influence of late Cenozoic mountain building on ocean geochemical cycles. *Geology*, 16(7): 649-653.
- Saito, H., Goovaerts, P., 2000. Geostatistical interpolation of positively skewed and censored data in a dioxin-contaminated site. *Environmental Science & Technology*, 34(19): 4228-4235.
- Schroeder, H., O'Connell, T.C., Evans, J.A., Shuler, K.A., Hedges, R.E.M., 2009. Trans-Atlantic slavery: Isotopic evidence for forced migration to Barbados. *American Journal of Physical Anthropology*, 139(4): 547-557.
- Sellick, M.J., Kyser, T.K., Wunder, M.B., Chipley, D., Norris, D.R., 2009. Geographic variation of strontium and hydrogen isotopes in avian tissue: Implications for tracking migration and dispersal. *Plos One*, 4(3): e4735.
- Shields, G., Veizer, J., 2002. Precambrian marine carbonate isotope database: Version 1.1. *Geochemistry Geophysics Geosystems*, 3(6): 10.1029/2001GC000266.
- Veizer, J., 1989. Strontium isotopes in seawater through time. *Annual Review of Earth and Planetary Sciences*, 17(1): 141-167.
- Veizer, J. et al., 1999. Sr-87/Sr-86, delta C-13 and delta O-18 evolution of Phanerozoic seawater. *Chemical Geology*, 161(1-3): 59-88.
- Voerkelius, S. et al., 2010. Strontium isotopic signatures of natural mineral waters, the reference to a simple geological map and its potential for authentication of food. *Food Chemistry*, 118(4): 933-940.
- Vollstaedt, H. et al., 2014. The Phanerozoic $\delta^{88}/^{86}\text{Sr}$ record of seawater: New constraints on past changes in oceanic carbonate fluxes. *Geochimica et Cosmochimica Acta*, 128(0): 249-265.
- Voss, B.M. et al., 2014. Tracing river chemistry in space and time: Dissolved inorganic

- constituents of the Fraser River, Canada. *Geochimica et Cosmochimica Acta*, 124(0): 283-308.
- Walther, B.D., Dempster, T., Letnic, M., McCulloch, M.T., 2011. Movements of diadromous fish in large unregulated tropical rivers inferred from geochemical tracers. *PLoS One*, 6(4): e18351.
- West, J.B., Ehleringer, J.R., Cerling, T.E., 2007. Geography and vintage predicted by a novel GIS model of wine $\delta^{18}\text{O}$. *Journal of Agricultural and Food Chemistry*, 55(17): 7075-7083.
- West, J.B., Hurley, J.M., Dudas, F.O., Ehleringer, J.R., 2009. The stable isotope ratios of marijuana. II. Strontium isotopes relate to geographic origin. *Journal of Forensic Sciences*, 54(6): 1261-1269.
- Wetherill, G.W., Mark, R., Lee-Hu, C., 1973. Chondrites: Initial strontium-87/strontium-86 ratios and the early history of the solar system. *Science*, 182(4109): 281-283.
- Wunder, M., 2010. Using Isoscapes to Model Probability Surfaces for Determining Geographic Origins. In: West, J.B., Bowen, G.J., Dawson, T.E., Tu, K.P. (Eds.), *Isoscapes*. Springer Netherlands, pp. 251-270.
- Zachos, J.C., Opdyke, B.N., Quinn, T.M., Jones, C.E., Halliday, A.N., 1999. Early cenozoic glaciation, antarctic weathering, and seawater $^{87}\text{Sr}/^{86}\text{Sr}$: Is there a link? *Chemical Geology*, 161(1-3): 165-180.

CHAPTER II

MAPPING $^{87}\text{Sr}/^{86}\text{Sr}$ VARIATIONS IN BEDROCK AND WATER FOR LARGE SCALE PROVENANCE STUDIES

Reprinted from *Chemical Geology*, Vol. 304-305, C.P., Bataille, G.J., Bowen, Mapping
 $^{87}\text{Sr}/^{86}\text{Sr}$ variations in bedrock and water for large scale provenance studies, pp. 39-52.

Copyright 2012, with permission from Elsevier.



Research papers

Mapping $^{87}\text{Sr}/^{86}\text{Sr}$ variations in bedrock and water for large scale provenance studiesClément P. Bataille^{*}, Gabriel J. Bowen

Department of Earth and Atmospheric Sciences, Purdue University, West Lafayette, Indiana 47907, USA

ARTICLE INFO

Article history:

Received 1 June 2011

Received in revised form 23 January 2012

Accepted 24 January 2012

Available online 31 January 2012

Editor: J.D. Blum

Keywords:

Strontium rubidium method

Isoscape

GIS

Strontium isotope ratio

Provenance

ABSTRACT

Although variation in $^{87}\text{Sr}/^{86}\text{Sr}$ has been widely pursued as a tracer of provenance in environmental studies, forensics, archeology and food traceability, accurate methods for mapping variations in environmental $^{87}\text{Sr}/^{86}\text{Sr}$ at regional scale are not available. In this paper, we build upon earlier efforts to model $^{87}\text{Sr}/^{86}\text{Sr}$ in bedrock by developing GIS-based models for Sr isotopes in rock and water that include the combined effects of lithology and time. Using published data, we fit lithology-specific model parameters for generalized equations describing the concentration of radiogenic Sr in silicate and carbonate rocks. The new model explained more than 50% of the observed variance in measured Sr isotope values from independent global databases of igneous, metaigneous, and carbonate rocks, but performed more poorly (explaining 33% of the variance) for sedimentary and metasedimentary rocks. In comparison, a previously applied model formulation that did not include lithology-specific parameters explained only 20% and 8% of the observed variance for igneous and sedimentary rocks, respectively, and exhibited an inverse relationship with measured carbonate rock values. Building upon the bedrock model, we also developed and applied equations to predict the contribution of different rock types to $^{87}\text{Sr}/^{86}\text{Sr}$ variations in water as a function of their weathering rates and strontium content. The resulting water model was compared to data from 68 catchments and shown to give more accurate predictions of stream water $^{87}\text{Sr}/^{86}\text{Sr}$ ($R^2=0.70$) than models that did not include lithological weathering parameters. We applied these models to produce maps ("isoscapes") predicting $^{87}\text{Sr}/^{86}\text{Sr}$ in bedrock and water across the contiguous USA, and compared the mapped Sr isotope distributions to data on Sr isotope ratios of US marijuana crops. Although the maps produced here are demonstrably imperfect and leave significant scope for further refinement, they provide an enhanced framework for lithology-based Sr isotope modeling and offer a baseline for provenance studies by constraining the $^{87}\text{Sr}/^{86}\text{Sr}$ in strontium sources at regional scales.

© 2012 Elsevier B.V. All rights reserved.

1. Introduction

Strontium isotope ratio measurements ($^{87}\text{Sr}/^{86}\text{Sr}$) have been applied in a wide variety of geoscience studies including chronostatigraphy of marine sediments (Veizer et al., 1999), petrology of igneous rocks (DePaolo, 1981), cation provenance and mobility (Chaudhuri and Clauer, 1993; Miller et al., 1993; Grousset and Biscaye, 2005; Chadwick et al., 2009), and quantitative models of chemical weathering (Clow et al., 1997; Horton et al., 1999). More recently the use of $^{87}\text{Sr}/^{86}\text{Sr}$ has been extended to a wide range of new applications in hydrology (Hogan et al., 2000), forensics (Beard and Johnson, 2000; West et al., 2009), archeology (Hodell et al., 2004; Bentley et al., 2008), ecology (Koch et al., 1995; Chamberlain et al., 1997; Hoppe et al., 1999; Barnett-Johnson et al., 2008) and food traceability (Kelly et al., 2005; Crittenden et al., 2007; Voerkelius et al., 2010). These applications are based on the principle that $^{87}\text{Sr}/^{86}\text{Sr}$ of natural materials reflects the sources of strontium (Sr) available during their

formation (Dasch, 1969). For instance, in studies of animal provenance, the $^{87}\text{Sr}/^{86}\text{Sr}$ of the Sr assimilated in animal tissues reflects the different sources of ingested Sr obtained from water and/or food (Graustein, 1989). As a consequence, variations in $^{87}\text{Sr}/^{86}\text{Sr}$ of these tissues can be used to trace migration or changes in diet habits of a given organism (Capo et al., 1998). Interpreting the $^{87}\text{Sr}/^{86}\text{Sr}$ signature for provenance studies requires constraining the $^{87}\text{Sr}/^{86}\text{Sr}$ variations of potential environmental sources of Sr. In this work, we attempt to model the spatial variations of $^{87}\text{Sr}/^{86}\text{Sr}$ in bedrock and water, two important sources of Sr to biological systems.

The use of $^{87}\text{Sr}/^{86}\text{Sr}$ as a tracer is of particular interest because unlike for isotopes of the light elements, biological and instrumental mass-dependent fractionations are automatically corrected during measurements and thus, the $^{87}\text{Sr}/^{86}\text{Sr}$ directly reflects the Sr of the source. In addition their wide amplitude of variation on both large and small scales, low temporal variability, and relative high abundance for a trace element make Sr isotopes a strong candidate for tracing inorganic and organic materials, either independently or in conjunction with isotopic data from lighter elements (Graustein and Armstrong, 1983; Kawasaki et al., 2002; Bowen et al., 2005; Bowen, 2010).

^{*} Corresponding author. Tel.: +1 765 404 4772; fax: +1 765 496 1210.
E-mail address: cbataill@purdue.edu (C.P. Bataille).

Several different approaches have been taken to map Sr isotopic variations at large scale. The fundamental theory underlying Sr isotope variation in geological material was summarized by Faure (1977), who proposed two equations describing the evolution of $^{87}\text{Sr}/^{86}\text{Sr}$ in mantle and crustal rocks that remain the basis for modeling $^{87}\text{Sr}/^{86}\text{Sr}$ in bedrock. Although several efforts were made to map $^{87}\text{Sr}/^{86}\text{Sr}$ available to ecosystems over local to regional scales based on field measurements in water, soils and organisms (Price et al., 1994; Ezzo et al., 1997; Hodell et al., 2004; Bentley and Knipper, 2005), Beard and Johnson (2000) made the first attempt to model $^{87}\text{Sr}/^{86}\text{Sr}$ variations in bedrock over large spatial scales. In their work, Beard and Johnson simplified Faure's theory by considering rock age to be the only determinant of $^{87}\text{Sr}/^{86}\text{Sr}$ variations and mapped the $^{87}\text{Sr}/^{86}\text{Sr}$ in the USA based on rock unit ages reported in a digital geological map. Their study suggested strongly patterned $^{87}\text{Sr}/^{86}\text{Sr}$ variations at continental scales but did not include systematic verification from field measurements. Nor did the authors advocate the use of their 'first-pass' model for quantitative prediction of Sr isotope ratios. Because bedrock weathering is the ultimate source of Sr to biological systems, however, these authors proposed that with improved understanding the modeled patterns could be used to interpret the geographic origin of biological materials.

Although bedrock Sr is the ultimate source of Sr to Earth surface systems, its isotopic composition can differ substantially from that of soils, surface water and organisms due to factors such as variation in weathering rates for different minerals or inputs from other sources such as atmospheric aerosols (Capo et al., 1998; Stewart et al., 1998; Bentley, 2006; Chadwick et al., 2009). For constraining the isotopic variations in source of Sr for provenance studies it is most appropriate to model the "biologically available Sr" as an approximation of the Sr actually assimilated by organisms (Sillen et al., 1998; Price et al., 2002; Hodell et al., 2004; Frei and Frei, 2011). In this regard, a theoretical steady state and time dependent model predicting $^{87}\text{Sr}/^{86}\text{Sr}$ evolution in "biologically available Sr" has been developed (Stewart et al., 1998). This model details the potential factors and sources causing transfers of Sr from soil to water and from water to ecosystems, but its applicability remains limited at regional scale because of the large number of variables to be constrained. Furthermore, this model relies on empirical measurements to obtain the $^{87}\text{Sr}/^{86}\text{Sr}$ variations in bedrock (Stewart et al., 1998).

An alternative approach to mapping spatial Sr isotope variation has been proposed by the TRACE project, which developed an empirical model for predicting $^{87}\text{Sr}/^{86}\text{Sr}$ in groundwater based on the measurement of 650 different European natural mineral waters (Voerkelius et al., 2010). Using this dataset and a geological map of Europe, a mean $^{87}\text{Sr}/^{86}\text{Sr}$ was calculated for each geological unit underlying sampled waters, and these values were extrapolated to similar rock units to develop a comprehensive prediction map for the continent. Although this model was shown to reproduce the large scale patterns of $^{87}\text{Sr}/^{86}\text{Sr}$ variations in biological materials, it requires iterative subjective analysis of regional geological and Sr isotope data and as a result is not immediately generalizable to other regions. Furthermore, the prediction accuracy of this approach is highly dependent on the density of sampling, and improving the resolution or extending the spatial coverage will require expensive field campaigns.

These previous efforts illustrate the difficulties of mapping $^{87}\text{Sr}/^{86}\text{Sr}$ variation at different scales in different sources. In this paper, we focus on developing scalable spatial $^{87}\text{Sr}/^{86}\text{Sr}$ predictions for bedrock and water. We build upon the effort of Beard and Johnson to map $^{87}\text{Sr}/^{86}\text{Sr}$ in bedrock and we developed a simplified model of Sr cycling (Stewart et al., 1998) to extend $^{87}\text{Sr}/^{86}\text{Sr}$ prediction to water and ecosystems. We validate the models by using existing $^{87}\text{Sr}/^{86}\text{Sr}$ measurements. The resulting models provide baseline predictions for rock and water $^{87}\text{Sr}/^{86}\text{Sr}$ across the contiguous USA, and can be used over a range of spatial resolutions depending on the application

of interest. Although these models are demonstrably imperfect and incomplete and their predictive power limited with respect to that desired in many potential applications, this work represents an important step towards developing systematic spatial predictions for Sr isotopes with wide geochemical applications.

2. Bedrock models

Model derivation, calibration, and validation are described in the following sections. Additional details and documentation are available in the accompanying Supplementary material.

2.1. Silicate model theory

^{87}Sr production in rocks results from the radioactive decay of ^{87}Rb , which decays to ^{87}Sr with a half-life of 49 billion years. In a closed system, the ratio of radiogenic ^{87}Sr to the stable isotope ^{86}Sr in rocks slowly increases with time (t) as a function of the rock's Rb/Sr ratio:

$$\frac{^{87}\text{Sr}}{^{86}\text{Sr}} = \left(\frac{^{87}\text{Sr}}{^{86}\text{Sr}} \right)_i + \frac{\text{Rb}}{\text{Sr}} (e^{\lambda t} - 1), \quad (1)$$

where λ is the decay constant of the parent isotope ($1.42 \times 10^{-11} \text{ yr}^{-1}$) and $(^{87}\text{Sr}/^{86}\text{Sr})_i$ is the initial $^{87}\text{Sr}/^{86}\text{Sr}$ (Faure, 1977). Rb/Sr varies between different layers and different rocks because geochemical processes fractionate Rb and Sr due to the specific affinity of each element for different minerals (Carlson, 2003). Rb substitutes better for potassium (K) and Sr for calcium (Ca) in minerals, and Rb/Sr tends to be high in felsic and K-bearing sedimentary rocks and low in mafic and carbonate rocks (Rudnick, 2003). The dissimilar affinities of Rb and Sr cause Rb/Sr to vary at large scales between the mantle and the crust and at small scales between different rocks and minerals (Rudnick, 2003).

Our model attempts to trace the evolution of $^{87}\text{Sr}/^{86}\text{Sr}$ values in silicate rocks from the time of Earth's formation to present (Fig. 1). We consider that the geological history of each rock started 4.5 billion years ago in a chemically homogeneous Earth. At that time, the Rb and Sr present in the earth were well-mixed and the $^{87}\text{Sr}/^{86}\text{Sr}$ is estimated to have been 0.699 based on measurements of chondrites (Wasserbu et al., 1969). Prior to crustal differentiation, the $^{87}\text{Sr}/^{86}\text{Sr}$ evolved slowly but homogeneously in the bulk earth. Following differentiation, different crustal layers inherited a higher Rb/Sr than the mantle due to the higher affinity of Rb for crustal minerals. Consequently, as the crust evolved, its $^{87}\text{Sr}/^{86}\text{Sr}$ deviated from the residual mantle value (Faure, 1977). As new rocks were formed from crustal

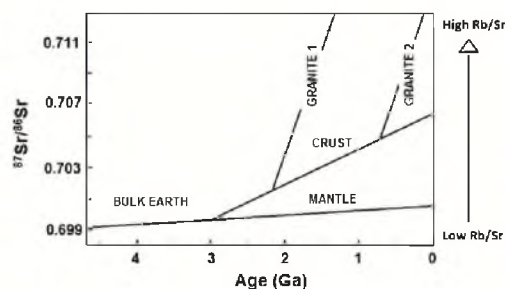


Fig. 1. Three-stage model for the evolution of $^{87}\text{Sr}/^{86}\text{Sr}$ in Earth materials through geological time. ^{87}Sr accumulates in all pools due to ^{87}Rb decay, with the rate depending of the Rb/Sr of each lithology. Granite1 and Granite2 are examples of rock formation occurring at different time during earth history. Modified from Encyclopedia of Geochemistry (2000) and Capo et al. (1998).

or mantle precursors, they inherited the $(^{87}\text{Sr}/^{86}\text{Sr})_i$ of their parent, but in most cases had different Rb/Sr, causing their $^{87}\text{Sr}/^{86}\text{Sr}$ to evolve along a different Rb/Sr slope than the parent material. Rocks with higher (lower) Rb/Sr than their parent evolved along a steeper (flatter) slope.

Because Rb and Sr are fractionated differently in geological processes, the Rb/Sr of a rock can be modified during tectonic, metamorphic or sedimentary transformations, thus modifying the $(^{87}\text{Sr}/^{86}\text{Sr})_i$ or the slope of evolution of $^{87}\text{Sr}/^{86}\text{Sr}$. For example, $(^{87}\text{Sr}/^{86}\text{Sr})_i$ and Rb/Sr values for the Idaho batholiths have been shown to vary largely along a 700 m transect depending on what host rock the batholith intruded (King et al., 2007). Since most geological materials in the crust have been recycled multiple times throughout earth history, and this history of transformations is usually incompletely documented in geological map data, the comprehensive history of $^{87}\text{Sr}/^{86}\text{Sr}$ evolution is difficult to reconstruct.

In our model, we make the simplifying assumption that the modern $^{87}\text{Sr}/^{86}\text{Sr}$ of silicate rocks can be approximated based on a three stage history, where all rocks of a given lithology are assumed to have been derived from a common parent material. In each new stage, it is assumed that the new rock produced inherits its parent material's mean $^{87}\text{Sr}/^{86}\text{Sr}$, but is differentiated chemically (Rb/Sr) from the parent material. First, ^{87}Sr was produced in the chemically undifferentiated Earth until an $^{87}\text{Sr}/^{86}\text{Sr}$ of 0.701 was reached at 3 Ga. At 3 Ga (an approximation of the age of crustal differentiation, t_1) chemical differentiation occurred, and from that time $^{87}\text{Sr}/^{86}\text{Sr}$ evolved independently in the mantle and multiple crustal rock reservoirs. Extant rock units were formed from one of these rock reservoirs at times corresponding to their ages (t_2) as documented in geological map data.

This theoretical framework gives:

$$\left(\frac{^{87}\text{Sr}}{^{86}\text{Sr}}\right)_{\text{rock}} = 0.701 + \left(\frac{\text{Rb}}{\text{Sr}}\right)_{\text{parent}} \left(e^{\lambda(t_1-t_2)} - 1\right) + \left(\frac{\text{Rb}}{\text{Sr}}\right)_{\text{rock}} \left(e^{\lambda t_2} - 1\right), \quad (2)$$

where $(\text{Rb}/\text{Sr})_{\text{parent}}$ is the Rb/Sr of the parent material, and $(\text{Rb}/\text{Sr})_{\text{rock}}$ is the Rb/Sr of the modern rock.

2.2. Silicate model calibration

Calculating the $^{87}\text{Sr}/^{86}\text{Sr}$ of a rock unit using Eq. (2) requires estimates of the parameters $(\text{Rb}/\text{Sr})_{\text{parent}}$ and $(\text{Rb}/\text{Sr})_{\text{rock}}$ as well as the approximate age the rock. Information on rock age is a common feature of digital geological maps, but estimating the parameters $(\text{Rb}/\text{Sr})_{\text{parent}}$ and $(\text{Rb}/\text{Sr})_{\text{rock}}$ for each lithology is not as straight forward. We proceeded in two steps by calibrating the silicate model independently for each parameter.

In the first calibration step, we assigned values for $(\text{Rb}/\text{Sr})_{\text{parent}}$, which determines the slope of $^{87}\text{Sr}/^{86}\text{Sr}$ evolution during stage 2. This parameter depends on the type of parent material (Fig. 1) which includes: 1) weathered bedrock for sedimentary material, 2) magma for igneous rock, 3) the parent lithology for metamorphic rocks. In the absence of information concerning the parent rock, we approximated the $(\text{Rb}/\text{Sr})_{\text{parent}}$ of sedimentary and metasedimentary rocks by assuming that they originate from a uniform source with a constant value of 0.24 corresponding to the average Rb/Sr of the upper crust (Goldstein and Jacobsen, 1988). To approximate the $(\text{Rb}/\text{Sr})_{\text{parent}}$ of igneous and metaigneous rocks, we separated these lithologies in 5 categories (ultramafic, mafic, intermediate, felsic intermediate and felsic) using the International Union of Geological Sciences (IUGS) classification (Le Bas and Streckeis, 1991). This effectively separates igneous rocks between Rb-poor mantle rocks and Rb-rich crustal rocks. We used data from the Western North American Volcanic and Intrusive Rock Database (www.navdat.org), including measurements for $(^{87}\text{Sr}/^{86}\text{Sr})_{\text{rock}}$, age (t_2) and $(\text{Rb}/\text{Sr})_{\text{rock}}$,

to back-calculate the $(\text{Rb}/\text{Sr})_{\text{parent}}$ for each of 5765 samples using Eq. (2). Finally, we classified these samples according to our 5 categories and calculated the average $(\text{Rb}/\text{Sr})_{\text{parent}}$ for samples in each category (see Supplementary Table 1).

In the second calibration step, we assigned values to the parameter $(\text{Rb}/\text{Sr})_{\text{rock}}$ by estimating the average Rb/Sr for 180 silicate rock unit types appearing in the United States Geological Survey state-level geological map geodatabases (Geological Survey (U.S.), State Geologic Map Compilation, 2005). For each of these rock unit types, we calculated the average (Rb/Sr) from identical or analogous lithologies in the USGS geochemical database (Geological Survey (U.S.) The National Geochemical Survey, 2004). We used this database because it included a large number of Rb and Sr measurements (252,661 measurements) covering 167 of the 180 lithologies selected. The 13 remaining lithologies were assigned $(\text{Rb}/\text{Sr})_{\text{rock}}$ by comparison with other analogous rocks (see Supplementary Table 1).

2.3. Carbonate model calibration

We modeled carbonate rocks separately because their $(^{87}\text{Sr}/^{86}\text{Sr})_i$ is not dependent on decay, but is a function of the variations of $^{87}\text{Sr}/^{86}\text{Sr}$ in seawater:

$$\left(\frac{^{87}\text{Sr}}{^{86}\text{Sr}}\right)_{\text{rock}} = \left(\frac{^{87}\text{Sr}}{^{86}\text{Sr}}\right)_{\text{seawater}} + \left(\frac{\text{Rb}}{\text{Sr}}\right)_{\text{rock}} \left(e^{\lambda t_2} - 1\right). \quad (3)$$

We apply the carbonate model to 10 lithologies from the USGS state-level geological map geodatabase (Supplementary material Table 1). Values of $(^{87}\text{Sr}/^{86}\text{Sr})_{\text{seawater}}$ were estimated for each rock age (Supplementary Table 2) using $^{87}\text{Sr}/^{86}\text{Sr}_{\text{seawater}}$ curves from the Precambrian Marine Carbonate Isotope Database (PMCI) (Shields and Veizer, 2002; see Supplementary Table 3). The estimation of $(\text{Rb}/\text{Sr})_{\text{rock}}$ values for each carbonate lithology was conducted as described for silicates in Section 2.2 (see Supplementary Table 1).

2.4. Model validation

We conducted separate validation exercises for igneous and sedimentary rocks because of the difference in calibration methods for $(\text{Rb}/\text{Sr})_{\text{parent}}$ described in Section 2.2. We expect a lower accuracy of the silicate model for sedimentary rock due to the absence of information concerning the parent rock for this type of rock. We used 9130 igneous rock and 207 sedimentary rock data from the global GEOROC database (Lehnert et al., 2000). The parameterized silicate model was applied to independently predict the $^{87}\text{Sr}/^{86}\text{Sr}$ of samples represented in these databases using the parameter values from Supplementary Table 1 associated with the database-specified lithology, and the predicted and observed values were compared. Data from 121 samples (1.3% of the samples) were removed from the igneous rock validation dataset. Among these samples, 78 (0.85% of all samples) were old felsic rocks (granites or rhyolites) displaying exceptionally high $^{87}\text{Sr}/^{86}\text{Sr}$ ranging from 0.850 to 4. These samples are also characterized by unusually high Rb/Sr ranging from 744 to 30. We recognize as a limitation of the current version of our model that it cannot accurately account for such highly radiogenic samples. The remaining 43 samples (0.47% of all samples) corresponded to rocks displaying $^{87}\text{Sr}/^{86}\text{Sr}$ values that are highly atypical for their lithological classification: e.g., 6 basalts were removed because their $^{87}\text{Sr}/^{86}\text{Sr}$ was higher than 0.730. In these cases we suspect that the database classifications provided an inaccurate or incomplete description of the sample lithology.

We validated the carbonate model by comparing model predictions with 246 published data from the PMCI (Shields and Veizer, 2002) and the GEOROC database (Lehnert et al., 2000). Although this comparison does not represent a completely independent validation of the model since some of the validation data were used in

reconstructing the paleo-seawater Sr isotope curves, it allows us to provide a first order assessment of model performance.

Although the validation data used here provide a broad representation of lithologies and ages they are not comprehensive, and thus limit our ability to validate the model, in that: 1) analyses gathered in these databases are biased toward rocks from active tectonic and volcanic areas, 2) $^{87}\text{Sr}/^{86}\text{Sr}$ values for continental sedimentary samples are under-represented in comparison with igneous rocks, and 3) Mesozoic and Cenozoic rocks represent more than 80% of the samples in the database. Additional inaccuracies in our parameterization and validation could result from a lack of control on the degree of alteration of database samples, which could lead to: 1) overestimation of Rb/Sr values because Sr is preferentially removed during weathering (Dasch, 1969), or 2) underestimation of $^{87}\text{Sr}/^{86}\text{Sr}$ values because rock preferentially lose Sr from their low $^{87}\text{Sr}/^{86}\text{Sr}$ mineral phases during weathering (e.g. Bullen et al., 1996).

2.5. Mapping bedrock $^{87}\text{Sr}/^{86}\text{Sr}$

Using the above equations, we calculated Sr isotope ratios for 319,824 mapped geological units represented in the United States Geological Survey state-level geological map geodatabases (Geological Survey (U.S.). State Geologic Map Compilation, 2005). Although these maps present some challenges (see Supplementary methods and <http://pubs.usgs.gov/of/2005/1325/documents/CONUSdocumentation.pdf>), they are unique in providing internally consistent, high resolution age and lithological information for the contiguous USA.

The 48 state lithological maps of the conterminous USA were downloaded in shape file format. Using ArcGIS, we merged the individual maps into a single shape file to obtain a geodatabase with three attributes relevant to our work:

- Unit_age: the text descriptor of the maximum age of the unit, and
- Rocktype1, and Rocktype2: the major and minor lithology descriptors.

We used these fields to join the map unit table with a set of tables containing the parameter values used in Eqs. (2) and (3):

- The table "Age" (Supplementary Table 2) listed each unique geologic time descriptor found in the map units table and related the attribute MAXAGE with a numeric age estimated from the USGS geological time scale (Geological Survey (U.S.). Geologic Names Committee, 2007).
- The tables "Lithology1" and "Lithology2" listed each lithologic descriptor present in the geodatabase and assigned values for the parameters $(\text{Rb}/\text{Sr})_{\text{parent}}$ and $(\text{Rb}/\text{Sr})_{\text{lithology}}$ (Supplementary Table 1).
- The table "Carbonates" (Supplementary Table 3) associated carbonate rock age with the $^{87}\text{Sr}/^{86}\text{Sr}$ of seawater.

Using the values from these associated tables, we calculated $^{87}\text{Sr}/^{86}\text{Sr}$ for each map polygon (geological map unit). In cases where both major and minor lithologies were documented for a map unit, we calculated separate Sr isotope ratio estimates for each lithology.

3. Water models

3.1. Theory

The $^{87}\text{Sr}/^{86}\text{Sr}$ of soluble Sr in stream water is largely determined by the delivery of Sr to runoff by chemical weathering of the underlying bedrock (Stewart et al., 1998), though in some cases the soluble Sr in water can originate from other inputs such as groundwater (Négre and Petelet-Giraud, 2005) atmospheric deposition of sea salt and mineral dust (Chadwick et al., 2009), hydrothermal processes (Pretti and Stewart, 2002), or soils and surficial deposits (Stueber

et al., 1975). Chemical weathering of bedrock is regulated by a complex combination of factors including lithological and mineralogical composition (Meybeck, 1987; Horton et al., 1999; Brantley et al., 2007), climate (particularly temperature and runoff; White and Blum, 1995), biology (Eckhardt, 1979; Brady and Carroll, 1994; Moulton et al., 2000) and erosion rates (Raymo et al., 1988; West et al., 2005). While these factors may be important for local studies, lithology and runoff have been identified as the two main controls of chemical weathering rates at regional scale (Beusen et al., 2009; Hartmann et al., 2009a; Jansen et al., 2010; Hartmann and Moosdorf, 2011). In order to simplify our large scale model, we limited our analysis to a pair of first order lithologically-based factors influencing the flux of Sr to water: 1) differential weathering rates of rocks and minerals, which we represent as a dimensionless weathering rate factor W (Supplementary Table 4), and 2) differences in Sr content (C) between lithologies. The chemical weathering of carbonates versus silicates illustrates the importance of these factors: carbonates have a higher Sr content and weather faster than silicates, therefore even trace quantities of calcite can be a dominant source of soluble Sr and control the $^{87}\text{Sr}/^{86}\text{Sr}$ of environmental waters (Clow et al., 1997; Anderson et al., 2000).

3.2. Weathering model calibration

In our model, the transfer of Sr from a rock to water is given by:

$$F = W_{\text{norm}} C, \quad (4)$$

where F is the flux of Sr from rock to water, C is the average Sr content (Supplementary Table 4) of each rock type calculated as described for $\text{Rb}/\text{Sr}_{\text{rock}}$ in Section 2.2 and W_{norm} is the weathering rate normalized to granite (Supplementary Table 4). We adopted two different approaches to estimating W_{norm} , depending on rock type. To estimate W_{norm} for igneous and sedimentary rocks, we calculated bulk rock dissolution rates for each rock type as:

$$K_{\text{rock}} = \sum_i a_i K_i, \quad (5)$$

where i is a given mineral, a_i is abundance of i in the given rock type and K the weathering rate value for that mineral based on laboratory measurements. We estimated a_i from the IUGS classification (Le Bas and Streckeisen, 1991; Supplementary Table 4). Mineral-specific values of K were taken from averaged values of mineral weathering rates found in laboratory experiments at $\text{pH}=5.5$ and $T=20^\circ\text{C}$ (Supplementary Table 5; Franke, 2009). However, because field studies suggest that at equal mineralogical composition, relative weathering rates of igneous and volcanic rocks differs (Drever and Clow, 1995), we scaled our W estimate as:

$$W_{\text{norm}} = \frac{K_{\text{rock}} R}{K_{\text{granite}}}, \quad (6)$$

where R is a correction factor related to differential reactive surface between rock type. Values of R were assigned by grouping rock types into three broad categories chosen to account for differences in permeability, and thus reactivity with aqueous solutions (Lewis, 1989), and comparing our calculated values of W_{norm} for each category with dissolution rate measurements in small monolithic catchments in France (Meybeck, 1987; Meybeck, 1987). The assigned values ($R=3$ for volcanic rocks, $R=2$ for metavolcanic and $R=1$ for crystalline igneous rocks) offer a rough approximation of relative field weathering rates useful for our initial large scale effort, and can be refined in future work.

Because the mineralogy of metamorphic and sedimentary rocks is difficult to estimate, we estimated W_{norm} of silicate sedimentary, pyroclastic and metamorphic rocks using a different approach. Based

on denudation rate measurements from small monolithic catchments (Meybeck, 1987; Meybeck, 1987), we distinguished between metamorphic and silicate sedimentary rocks, with low weathering rates similar to those of granite (assigned $W_{norm}=1$) and faster-weathering argillaceous sedimentary rocks ($W_{norm}=2$). Because no monolithic catchment dissolution rates measurements were available for pyroclastic rocks, we estimated W_{norm} from long term dissolution measurements of tuff tablets relative to those of granodiorite tablets exposed to the same conditions (Matsukura et al., 2007). Compared to regional scale estimates of chemical weathering based on dissolved silicate content (Bluth and Kump, 1994; Beusen et al., 2009; Hartmann et al., 2009; Jansen et al., 2010), our values show similar relative weathering rates across five major lithological groups: 1) carbonates and evaporites ($50 > W_{norm} > 25$), 2) tuff, pyroclastic flow and mafic volcanic rocks ($25 > W_{norm} > 5$), 3) other volcanic rocks and basic and intermediate igneous rocks ($5 > W_{norm} > 3$), 4) argillaceous sediments ($W_{norm}=2$) and 5) other metamorphic, sedimentary and felsic intrusive rock ($W_{norm}=1$). Although in good agreement with existing literature, our weathering formulation is limited in that it 1) does not account for runoff, climate, land cover or slope variations, and 2) is based on bulk dissolution rates and while accounting for differences in Sr content between rock type it does consider Sr-specific dissolution kinetics.

3.3. Mapping local and catchment water $^{87}\text{Sr}/^{86}\text{Sr}$

We combined the weathering and bedrock models to map $^{87}\text{Sr}/^{86}\text{Sr}$ variations in local and catchment-integrated waters. The local water model estimates the $^{87}\text{Sr}/^{86}\text{Sr}$ value of Sr leached from bedrock to water at each point on the map, whereas the catchment water model estimates the $^{87}\text{Sr}/^{86}\text{Sr}$ of surface waters flowing through each map location, including all contributions from up-catchment locations.

In the local water model, for each map unit polygon where major and minor lithologies were given we calculated the relative Sr weathering flux from major and minor lithologies:

$$(WC)_{tot} = 0.75 * (WC)_{major} + 0.25 * (WC)_{minor} \quad (7)$$

and the average Sr isotope ratio of local water, weighted by the fluxes from major and minor lithologies:

$$\left(\frac{^{87}\text{Sr}}{^{86}\text{Sr}}\right)_{local} = \left(\frac{0.75 * (WC)_{major}}{(WC)_{tot}}\right) * \left(\frac{^{87}\text{Sr}}{^{86}\text{Sr}}\right)_{major} + \left(\frac{0.25 * (WC)_{minor}}{(WC)_{tot}}\right) * \left(\frac{^{87}\text{Sr}}{^{86}\text{Sr}}\right)_{minor} \quad (8)$$

In these equations, the relative weights assigned to major and minor lithologies (0.75 and 0.25, respectively) represent a coarse generalization consistent with the only available constraint, that rocktype1 and rocktype2 are the most and second most abundant of the rock types present in each mapped unit (e.g. <http://pubs.usgs.gov/of/2005/1325/documents/CONUSdocumentation.pdf>).

Sr flux and local $^{87}\text{Sr}/^{86}\text{Sr}$ values were exported to raster data layers at 1 km spatial resolution for further analysis and mapping of catchment water $^{87}\text{Sr}/^{86}\text{Sr}$. The catchment water map was created using the Flow Accumulation tool (Spatial Analyst toolbox) in ArcGIS and 1 km gridded flow direction values from the Hydro 1 K digital elevation model (DEM; <http://edc.usgs.gov/products/elevation/gtopo30/hydro/namerica.html>). Modeled local water Sr isotope flux [$(^{87}\text{Sr}/^{86}\text{Sr})_{local} * (WC)_{tot}$] and Sr flux [(WC)_{tot}] values were accumulated downstream through the DEM river networks and divided to obtain estimated water $^{87}\text{Sr}/^{86}\text{Sr}$ values that represented an average of the up-stream Sr sources to each map pixel, weighted by the contribution of weathered Sr from each rock type in the catchment. We note that, although this model accounts

for lithology-driven variation in weathered Sr fluxes, it does not explicitly calculate the water balance of the catchment and so does not account for differences in Sr flux driven by differences in runoff from individual grid cells.

3.4. Model validation

To validate the catchment water model, we compared $^{87}\text{Sr}/^{86}\text{Sr}$ predictions with water $^{87}\text{Sr}/^{86}\text{Sr}$ measured at 68 watersheds in 4 regions of the contiguous USA (Fig. 2). Before calculating $^{87}\text{Sr}/^{86}\text{Sr}$ in water, we obtained maps of the sub-watersheds for the Susquehanna River (<http://www.srbc.net/atlas/index.asp>) and the Owen Lake Basin (<http://map24.epa.gov/EMR/>). No pre-processed maps of the sub-watersheds existed for the Scioto River and Clark Fork of the Yellowstone River basins. Consequently, we delineated each catchment (Fig. 2) by processing the national elevation dataset (Gesch, 2002) with the Hydrology toolbox in ArcGIS (Spatial Analyst toolbox). We successively clipped the digital elevation model (DEM) for the area considered (Geoprocessing tool/Clip Raster), reconditioned the DEM (Fill Sinks tool), calculated the flow direction (Flow Direction tool) and flow accumulation (Flow Accumulation tool) rasters, defined streams by reclassifying the flow accumulation raster (Stream Definition tool; thresholds typically between 0.1 and 1% of the maximum flow accumulation), segmented the streams (Stream Segmentation tool) and finally delineated the watersheds and sub-watersheds (Watershed tool). We further validated this delineation process by comparing the shape of the catchments with the different maps furnished in published studies (Stueber et al., 1975; Fisher and Stueber, 1976; Horton et al., 1999; Pretti and Stewart, 2002).

In order to test the sensitivity of the catchment water model to different modeling assumptions, we used the Spatial Statistics tool (ArcGIS Spatial Analyst toolbox) to calculate three different estimates of the average $^{87}\text{Sr}/^{86}\text{Sr}$ for each catchment:

- Two estimates without weighting for differences in Sr flux among grid cells within the watershed. The first, which we call the “age-only catchment water model”, is an unweighted average of $^{87}\text{Sr}/^{86}\text{Sr}$ values, calculated using the Beard and Johnson model (Beard and Johnson, 2000), across all grid cells in the catchment. The second, the “unweighted catchment water model” is an unweighted average of modeled “local water” $^{87}\text{Sr}/^{86}\text{Sr}$ values (Eq. 8) across all catchment grid cells.
- A third estimate accounted for differential Sr contributions from different map units within the catchment. This formulation, the “flux-weighted catchment water model”, was equivalent to that used to map catchment water Sr isotope values as described above: the sum of the Sr isotope flux for all watershed grid cells was divided by the sum of the total Sr flux.

To further test the relevance of our models for provenance applications, we compared the $^{87}\text{Sr}/^{86}\text{Sr}$ predictions using these three formulations with the $^{87}\text{Sr}/^{86}\text{Sr}$ measured in marijuana from 79 USA counties (West et al., 2009). In this case, the samples were identified by their county of origin, and we averaged grid cell values within the county boundaries, as represented in the National Atlas of the United States (www.nationalatlas.gov/), rather than within catchments (Fig. 2).

4. Results and discussion

4.1. Bedrock model

The silicate model explained 59% of the observed variance in an independent global dataset for 9009 igneous and metamorphic rocks and 33% of the variance for 207 sedimentary rocks (Fig. 3A and B). This new silicate model significantly improved the correlation with measurements in comparison with estimates from the age-only

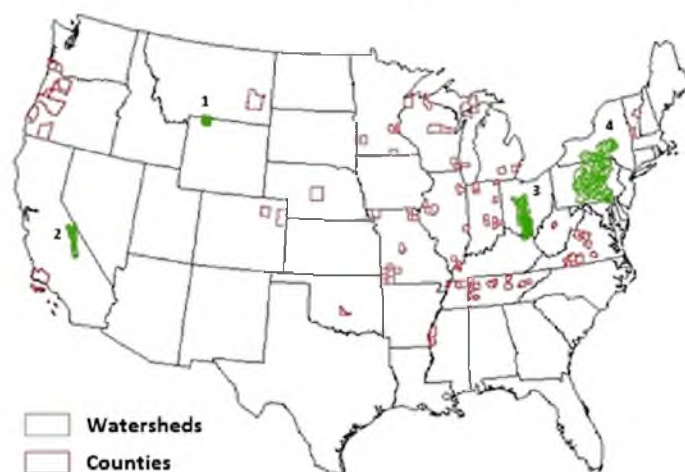


Fig. 2. Location of the samples used for the water model verification: Green: $^{87}\text{Sr}/^{86}\text{Sr}$ measurement in stream water from 1: Clarks Fork of the Yellowstone Basin (Horton et al., 1999); 2: Owens River Lake Basin (Pretti and Stewart, 2002); 3: Scioto River watershed (Stueber et al., 1975); 4: Susquehanna River Basin (Fisher and Stueber, 1976); Red: $^{87}\text{Sr}/^{86}\text{Sr}$ measurements of marijuana from 79 counties across the USA (West et al., 2009).

bedrock model. Moreover, for these datasets, the new model predictions cluster much closer to the 1:1 relationship than those of the age-only model. For the igneous and sedimentary datasets, respectively, the mean absolute error (MAE) of predictions are -0.00136 and -0.00968 for the silicate model and -0.00224 and -0.01936 for the age-only model. Whereas the age-only model globally underestimates the measured average $^{87}\text{Sr}/^{86}\text{Sr}$ (0.7059 and 0.7064 for the igneous and sedimentary data, respectively) and its variance (7.95×10^{-6} and 3.07×10^{-6} respectively) in both datasets, the new silicate model predicts values for the average (0.7072 and 0.716 respectively) and variance (0.000134 and 6.46×10^{-5}) of the validation datasets that are much closer to the observed values (average = 0.7082 and 0.7257, variance = 0.000348 and 0.000476). The root mean squared error for model predictions of igneous and sedimentary data in the validation datasets are 0.012 and 0.021 for the silicate model and 0.018 and 0.029 for the age-only model. In the absence of information about the parent rock, the first calibration step of the silicate model (Section 2.2) remains relatively inaccurate for sedimentary rocks, explaining the better performance of the model for igneous rocks than for sedimentary rocks. Overall, the new model has a tendency to underestimate $^{87}\text{Sr}/^{86}\text{Sr}$ values. This pattern likely results from the skewed distribution of samples in the

calibration datasets (see Section 2.4). While this distribution is not representative of element distribution in nature (Reimann and Filzmoser, 2000) it leads during the calibration process to give best-fit parameter values that tend to underestimate $^{87}\text{Sr}/^{86}\text{Sr}$ values for rare, undersampled, highly radiogenic rocks.

The carbonates model, when validated against a dataset of 246 carbonate rocks (Shields and Veizer, 2002), explains more than half of the observed variance (Fig. 4). In contrast, the age-only model predictions are inversely correlated with observed $^{87}\text{Sr}/^{86}\text{Sr}$ in carbonates because they do not account for the very low (≈ 0) Rb/Sr of these rocks. As a result the age-only bedrock model over-predicts the Sr isotope ratios of ancient carbonates that formed at time when seawater $^{87}\text{Sr}/^{86}\text{Sr}$ was low.

The bedrock model performs much better on the igneous validation dataset when its predictions are compared with the mean values of the different lithologies (Fig. 5). This result reflects the fact that the parameterized model does not account for small-scale chemical variability within and between rock units of the same lithology that can have a substantial effects on Sr isotope ratios (see example Section 2.1 from King et al., 2007). Although the parameterized approach applied here does not allow accurate prediction of such small-scale $^{87}\text{Sr}/^{86}\text{Sr}$ variations within a rock unit, Fig. 5 shows that

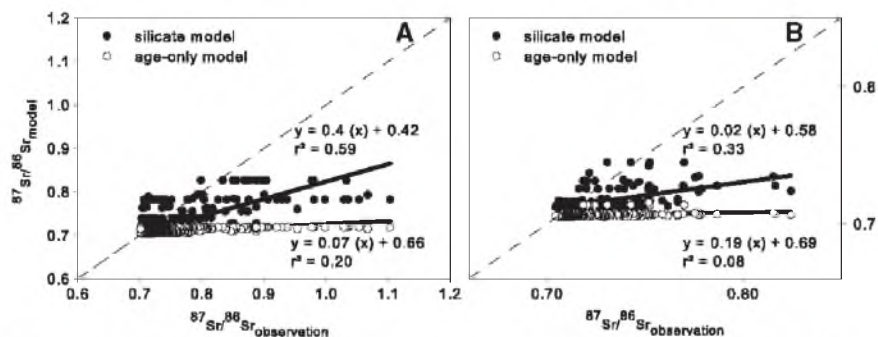


Fig. 3. Validation of silicate Sr isotope model. A. Linear correlation between 9009 worldwide $^{87}\text{Sr}/^{86}\text{Sr}$ igneous rock measurements and the $^{87}\text{Sr}/^{86}\text{Sr}$ predicted by the bedrock model and age-only model (Beard and Johnson, 2000). B. Linear correlation between 207 worldwide $^{87}\text{Sr}/^{86}\text{Sr}$ sedimentary rock measurements and the $^{87}\text{Sr}/^{86}\text{Sr}$ predicted by the bedrock model and age-only models. Dashed line in each panel shows the 1:1 relationship.

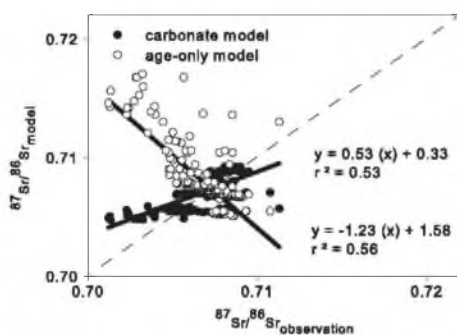


Fig. 4. Validation of carbonate Sr isotope model, showing linear correlations between 246 worldwide $^{87}\text{Sr}/^{86}\text{Sr}$ measurements for carbonate rocks and the $^{87}\text{Sr}/^{86}\text{Sr}$ predicted by the bedrock model and age-only models. Dashed line shows the 1:1 relationship.

it does allow accurate predictions of the differences among lithologies within an independent validation dataset. Further improving the spatial resolution of the model will require coupling with models or data

representing the evolution of magmatic fluids, metamorphic processes and sedimentary deposition at the scale of a rock unit.

Application of the bedrock model to predict Sr isotope ratios of major lithologies in rock units across the USA gives a range of predicted values from 0.704 to 0.816 (Fig. 6). The average $^{87}\text{Sr}/^{86}\text{Sr}$ for the USA is 0.7067 for the age-only model (Fig. 6B) and 0.7134 in the major bedrock model (Fig. 6A). Both models predict values below 0.716, the estimated average $^{87}\text{Sr}/^{86}\text{Sr}$ for the upper crust (Goldstein and Jacobsen, 1988). However, the major bedrock model more closely approaches this value and shows a much higher range of Sr isotope variations and higher maximum values for areas characterized by old rocks. Conversely, the age-only model more severely underestimates $^{87}\text{Sr}/^{86}\text{Sr}$ values and reduces the amplitude of variations relative to observations. Our results show that a large part of the inaccuracy found in the age-only model is driven by the omission of lithology-specific parameters.

In comparison with the age-only model, the major bedrock model shows more structure in $^{87}\text{Sr}/^{86}\text{Sr}$ variation over a range of spatial scales that are promising for provenance studies. On a continental scale (1000 km), we observe a general trend of decreasing $^{87}\text{Sr}/^{86}\text{Sr}$ from East to West. This trend is driven largely by the difference in rock age with older igneous rocks in the Appalachian and younger

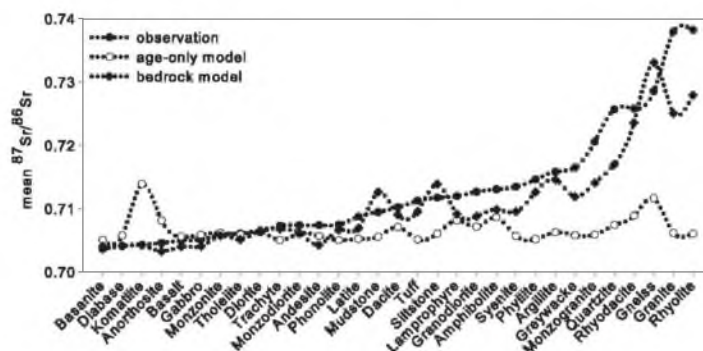


Fig. 5. Validation of silicate Sr isotope model by lithology. Average measured and predicted $^{87}\text{Sr}/^{86}\text{Sr}$ calculated for different lithologies represented in the global validation dataset. The dataset is the same as Fig. 3A but only lithologies with more than 10 available measurements have been selected.

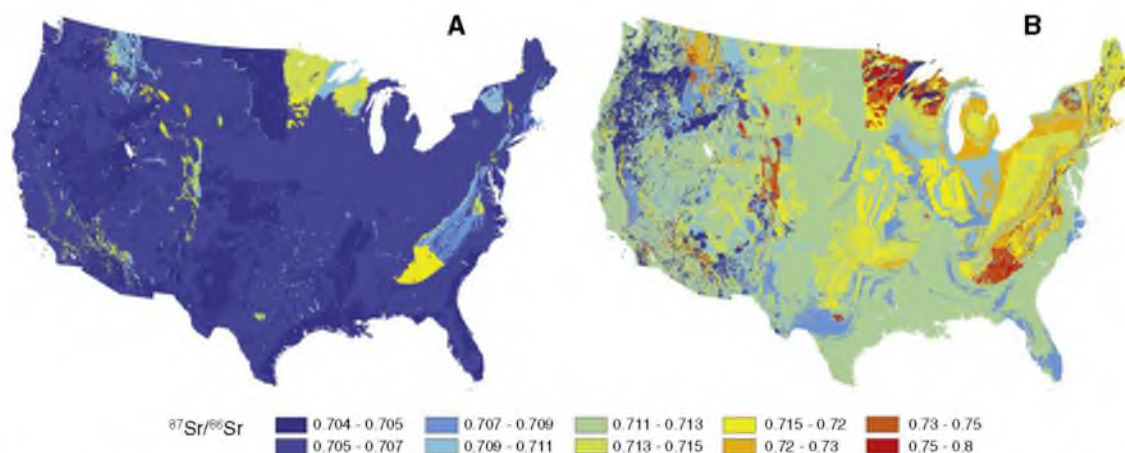


Fig. 6. Modeled bedrock Sr isotope ratios for the contiguous USA. A. Bedrock model $^{87}\text{Sr}/^{86}\text{Sr}$ variations in major bedrock lithologies for rock units throughout the USA, calculated using Eqs. (2) and (3); B. $^{87}\text{Sr}/^{86}\text{Sr}$ variations in the major bedrock using the age-only model (Beard and Johnson, 2000). $^{87}\text{Sr}/^{86}\text{Sr}$ discontinuities at state borders are related to inconsistencies in age or lithological classification between state geological maps and should be resolved through the development of a detailed, integrated, nation-wide map.

Table 1

Geology and measured and modeled $^{87}\text{Sr}/^{86}\text{Sr}$ values for bedrock in the catchment water model validation catchments. W: watershed; CF: Clark Fork of the Yellowstone; OL: Owen Lake; Sc: Scioto; Su: Susquehanna; N = North; S = South; E = East; W = West.

W	Geology	Sampled lithology	Measured $^{87}\text{Sr}/^{86}\text{Sr}$	Bedrock model $^{87}\text{Sr}/^{86}\text{Sr}$	Reference	
CF	N: granitic gneiss Beartooth Mountains	Granitic gneiss	None	0.748	(Horton et al., 1999)	
	S: Paleozoic marine sedimentary	Andesite		0.707		
OL	Eocene Andesite	Carbonates		0.7087	(Goff et al., 1991)	
	W: Sierra Nevada batholiths metavolcanic and igneous rocks	Sierra Nevada batholiths	0.706–0.725	0.706–0.722		
	E: White-Inyo mountains complex mixture of sedimentary, igneous and metamorphic rocks (Marchand, 1974)	Volcanic rocks	0.706–0.708	0.707		(Goff et al., 1991)
		Tuff	0.709–0.713	0.711		(Davies and Halliday, 1998)
Sc	Mixture of Paleozoic shales and carbonates covered by glacial till	Mesozoic granite	0.706–0.708	0.707	(Kistler and Peterman, 1973)	
		Devonian	0.7086	0.708–0.710		(Steele et al., 1972)
		Carbonates	0.732–0.745	0.719		
		Paleozoic shales	0.710			
		Shale leachate	0.708			
Su	N: Mixture of silicates and carbonates from the Paleozoic	Shales	0.741–0.755	0.719	(Whitney and Hurley, 1964)	
		Devonian limestone	0.7075	0.708–0.710		
	S: Precambrian to Mesozoic igneous, volcanic and metamorphic rocks	Igneous rocks	0.707–0.799	0.707–0.752	(Wetherill et al., 1968)	

volcanic rocks in the West. On a regional scale (100 km), we observe large $^{87}\text{Sr}/^{86}\text{Sr}$ variations in sedimentary basins due to the difference between silicates and carbonates. High resolution $^{87}\text{Sr}/^{86}\text{Sr}$ variation is most apparent in mountainous areas due to the complex juxtaposition of lithologies in these regions. Even at the scale of a county (10 km), the bedrock models (major and minor) suggest the potential for high resolution $^{87}\text{Sr}/^{86}\text{Sr}$ variations depending on the lithological complexity.

4.2. Catchment water models

4.2.1. Water model validation

The four watersheds selected for model validation represent a wide range of geological, climatic and physiographic conditions (Fig. 2, Table 1). We compiled $^{87}\text{Sr}/^{86}\text{Sr}$ measurements from 68 streams in these watersheds: 1) 13 samples from the watershed of the Clarks Fork of the Yellowstone River (WY): a mountainous catchment with a predominant geology of granite, andesite and carbonates (Horton et al., 1999), 2) 19 samples from the Owens Lake watershed (CA): a mountainous watershed dominated by a complex mixture of igneous and metamorphic rocks associated with dolomite (Pretti and Stewart, 2002), 3) 19 samples from the Scioto River basin (OH): a sedimentary basin dominated by shales, sandstones and marine carbonates (Stueber et al., 1975), and 4) 18 measurements from the Susquehanna River basin (PA): a catchment containing varied sedimentary, metamorphic and igneous rocks (Fisher and Stueber, 1976). For each watershed the measured values reported in the literature were compared with three model estimates of the catchment-integrated average water Sr isotope ratio, as described in Section 3.4.

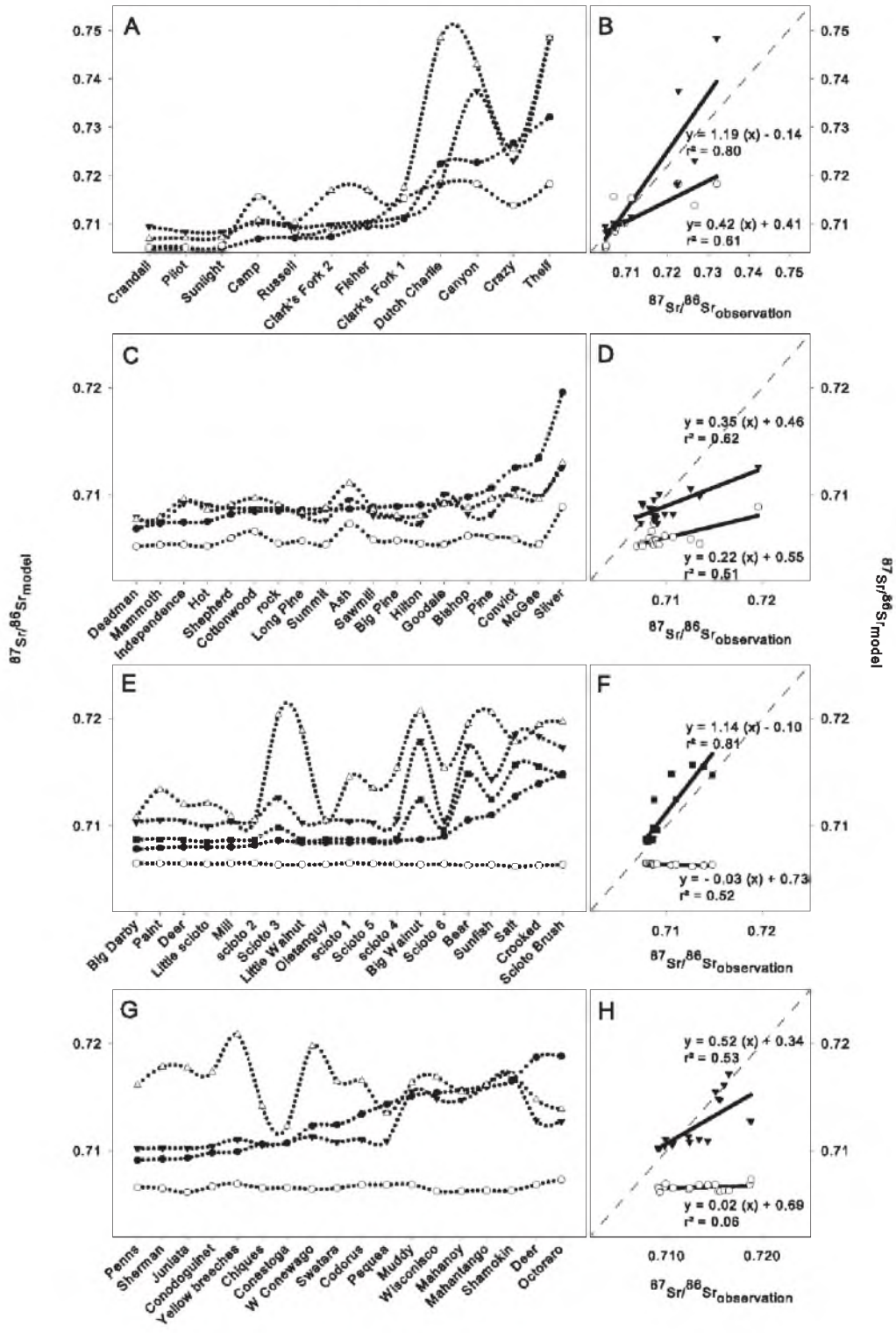
For each of these watersheds, because the bedrock models are the base maps of the catchment water model, we first tested the accuracy of the bedrock models by comparing the predictions with $^{87}\text{Sr}/^{86}\text{Sr}$ measurements of rock units within the selected watershed. Table 1 shows that for each of these watersheds, the bedrock model accurately predicts the $^{87}\text{Sr}/^{86}\text{Sr}$ of most lithologies, with the exception of the lower-than-predicted $^{87}\text{Sr}/^{86}\text{Sr}$ measured for shales from OH and PA and some igneous rocks from the Wissahickon formation (Owens Lake).

For the Clarks Fork of the Yellowstone Basin (Fig. 7A) each of the model formulations reproduces the basic pattern of $^{87}\text{Sr}/^{86}\text{Sr}$ differences across the sub-watersheds. However, the correlation (Fig. 7B) is closer to the 1:1 relationship for the flux-weighted catchment water model than for the unweighted and age-only catchment water models. In this basin, where Cenozoic sedimentary and volcanic rock coexists with Precambrian felsic rocks (Table 1), most of the $^{87}\text{Sr}/^{86}\text{Sr}$ variations in water are driven by the large differences in age of the different geological formations. In this geological setting, even if the age-only bedrock model does not account for differences in lithology it can be used to predict the first order patterns of variation in stream water $^{87}\text{Sr}/^{86}\text{Sr}$ values with reasonable accuracy. Prediction accuracy was further enhanced by incorporating lithological factors (Fig. 7B).

For the Owens Lake River Basin, in spite of the geological complexity of this watershed (Table 1), the $^{87}\text{Sr}/^{86}\text{Sr}$ of most streams was relatively constant at ~0.710 (Fig. 7C). In most of the streams, the flux-weighted catchment water model gives a more accurate prediction and stronger correlation (Fig. 7D) than the age-only and unweighted catchment water models. Silver Creek, located in the White-Inyo Mountains, is not correctly predicted by any of the water models. This stream runs through Cambrian marine sediments, gneisses and schists (Pretti and Stewart, 2002). In the catchment water models, the $^{87}\text{Sr}/^{86}\text{Sr}$ value is buffered to low values by the presence of dolomite with a predicted $^{87}\text{Sr}/^{86}\text{Sr}$ value of 0.709 (using our bedrock carbonate calculation). However, Pretti and Stewart (2002) argued that these dolomites probably exchanged Rb with shales during metamorphism and have significantly higher $^{87}\text{Sr}/^{86}\text{Sr}$ than otherwise expected, explaining the high $^{87}\text{Sr}/^{86}\text{Sr}$ in stream water of these catchments and the divergence with the modeled values.

McGee and Convict creeks, located in the Northern part of the Basin, lack metamorphosed dolomites in outcrop, but are also poorly predicted by the flux-weighted and unweighted catchment water models. These sub-watersheds present a complex hydro-geological setting, including Paleozoic or Precambrian metasedimentary rocks which are poorly represented by the lithological maps (Stevens and Greene, 1999). $^{87}\text{Sr}/^{86}\text{Sr}$ signature is also slightly overestimated by our models in streams within the Long Valley caldera such as

Fig. 7. Catchment water model validation results. Modeled and measured $^{87}\text{Sr}/^{86}\text{Sr}$ in (A and B) 12 streams of the Clarks Fork of the Yellowstone River Basin in Wyoming (Horton et al., 1999); (C and D) 19 streams of the Owen Lake in California (Pretti and Stewart, 2002); (E and F) 19 samples from the Scioto River Basin in Ohio (Stueber et al., 1975); (G and H) 18 streams of the Susquehanna River Basin in Pennsylvania (Fisher and Stueber, 1976). Black circle: observations; Open circle: age-only water model; Open triangle: unweighted catchment water model; Reversed black triangle: flux weighted catchment water model; Black square: celestite-corrected flux-weighted catchment water model for the Scioto River Basin. Dashed lines in the right hand panels show the 1:1 relationship.



Independence and Hot creeks. This area is characterized by low $^{87}\text{Sr}/^{86}\text{Sr}$ rocks and hydrothermal springs which contribute greatly to the water chemistry (Pretti and Stewart, 2002). Measured $^{87}\text{Sr}/^{86}\text{Sr}$ values for hot springs of the area ranged from 0.7078 to 0.7081 (Goff et al., 1991) which may explain the discrepancy with our modeled $^{87}\text{Sr}/^{86}\text{Sr}$. Pretti and Stewart (2002) also showed that these hot springs exert a strong influence at large scale, on the downstream $^{87}\text{Sr}/^{86}\text{Sr}$ value of the Owens River because of their high dissolved Sr load, an influence that would not be accounted for in our model. Other potential factors explaining the inaccuracy of the models include inputs of Sr from mineral dust (Clow et al., 1997), the poor representation of the geological complexity of these watersheds by 2D maps, or the inaccuracy of our weathering equations when several lithological weathering rates have to be approximated concomitantly.

For the Scioto River Basin, the unweighted catchment water model drastically overestimates the $^{87}\text{Sr}/^{86}\text{Sr}$ value in stream water in several catchments, whereas the age-only model underestimates the observed values (Fig. 7E). The flux-weighted catchment water model reduces the magnitude of overestimates relative to the unweighted catchment water model for almost all the watersheds, a difference that can be attributed to the higher Sr flux from carbonate units in the watersheds in comparison with silicates (Table 1). Several sub-watersheds in the Southern part of the Basin that are dominated by shales, such as Bear, Salt, Crooked and Scioto Brush Creeks, display low $^{87}\text{Sr}/^{86}\text{Sr}$ measurements relative to the high $^{87}\text{Sr}/^{86}\text{Sr}$ of their bedrock. This anomaly is due to the presence of minor amount of calcite in these shales (Table 1), which weathers preferentially and buffers the $^{87}\text{Sr}/^{86}\text{Sr}$ of the weathering flux. The Sr isotope ratio in two other sub-watersheds (Big Walnut and Scioto 3) with bedrock geology exclusively composed of silicates (Table 1) is overestimated by the flux-weighted catchment water model. However, these sub-watersheds are proximal to outcropping carbonate formations, and drillings from these catchments show that thick layers of carbonates are present at depth (Stueber et al., 1975). Groundwater discharged from these beds probably buffers the $^{87}\text{Sr}/^{86}\text{Sr}$ and explains the discrepancy between model and measurements (Fig. 7E).

Apart from these specific examples, the catchment water model shows a general tendency to overestimate the $^{87}\text{Sr}/^{86}\text{Sr}$ of watersheds of this Basin. Stueber et al. (1975) showed that glacial overburden within the Scioto River Basin, which contains a large amount of soluble celestite (SrSO_4) and pulverized Paleozoic carbonates with $^{87}\text{Sr}/^{86}\text{Sr}$ equal to 0.708 (Table 1), buffers the $^{87}\text{Sr}/^{86}\text{Sr}$ in these streams (Stueber et al., 1975). To attempt to account for this factor, we developed a correction for the contribution of till and carbonates to water. We based this correction on the work of Steele et al. (1972) who used the Sr concentration in water to estimate the contribution of each source of Sr. We used a surficial geology map (Clawges et al., 1999) to identify the distribution of glacial till in the Basin. In each sub-watershed covered by thick and thin glacial deposits, respectively, we considered that celestite contributed 75% (average contribution for watersheds covered by thick glacial till in Steele et al., 1972) and 50% (average contribution for watersheds covered by thin glacial till in Steele et al., 1972) of the Sr in water. The celestite-corrected water model substantially improved the accuracy of predictions within this Basin, explaining 81% of the variance with a model/data slope close to 1 (Fig. 7E and F). This result suggests that future work should include improved model formulations representing surficial deposits, particularly in area where thick glacial and eolian deposits are present. One impediment to this work is the relatively limited availability of systematic information on the age, origin and composition of these surficial deposits.

For the Susquehanna River Basin, the flux-weighted catchment water model dramatically improves the model predictions relative to the age-only and unweighted catchment water models (Fig. 7G and H). In most of the watersheds, the unweighted catchment

water model overestimates the $^{87}\text{Sr}/^{86}\text{Sr}$ whereas the flux-weighted catchment water model matches the observations closely because of the importance given to preferential dissolution of carbonates. The improved performance of the flux-weighted catchment water model is seen here despite the divergence between bedrock model predictions and measurements for shales (Table 1). Similar to the Scioto Basin, shale leachates here have a significantly lower $^{87}\text{Sr}/^{86}\text{Sr}$ than the whole rock due to the selected dissolution of minor amount of calcite (Table 1). The discrepancy between the flux-weighted catchment water model and observed $^{87}\text{Sr}/^{86}\text{Sr}$ values for Deer and Octoraro creeks can be explained by the inability of the bedrock model to accurately predict the $^{87}\text{Sr}/^{86}\text{Sr}$ of rocks from the Wissahickon Formation (Table 1).

4.2.2. A global view of the catchment water model

The flux-weighted catchment water model explains 70% of the variance of the Sr isotopes in water for the 68 watersheds tested with a linear correlation close to the 1:1 relationship (Fig. 8). Prediction accuracy for this model, estimated based on the validation data, is significantly improved relative to the other models, with MAE = 0.00051 and RMSE = 0.0034. In comparison, the age-only catchment water model explains 38% of the observed variance with MAE = -0.0039 and RMSE = 0.0056. In our approach, we added a number of lithological effects that increased the accuracy of water $^{87}\text{Sr}/^{86}\text{Sr}$ predictions in most of the geological settings. The resulting local water (Fig. 9A) and flux-weighted catchment water (Fig. 9B) maps for the contiguous USA show patterned $^{87}\text{Sr}/^{86}\text{Sr}$ variations similar to the bedrock models (Fig. 6A and B). Average $^{87}\text{Sr}/^{86}\text{Sr}$ values are highest in the new bedrock model and lowest in the flux-weighted catchment water model, where the preferential dissolution of low $^{87}\text{Sr}/^{86}\text{Sr}$ units (e.g. carbonates and mafic rocks) buffers the $^{87}\text{Sr}/^{86}\text{Sr}$ of the water catchment model in comparison with bedrock (Fig. 6D).

The maps predict large variations at a range of spatial resolutions, which are promising for provenance studies. Nevertheless, the $^{87}\text{Sr}/^{86}\text{Sr}$ prediction in water could be improved by considering the potential contribution of non-bedrock sources of Sr to water (Sillen et al., 1998; Stewart et al., 1998). In our validation process, we demonstrated the importance of accounting for the contribution of Sr-rich minerals (calcite, dolomite and celestite) because they often buffer the $^{87}\text{Sr}/^{86}\text{Sr}$ of whole rivers. Similarly, the effect of dust deposition in the Rockies (Clow et al., 1997), contributions from soil and surficial materials (Stewart et al., 1998) and the effect of local phenomenon such as hydrothermal contributions (Pretti and Stewart, 2002) and atmospheric deposition (Stewart et al., 1998) should be considered in future work.

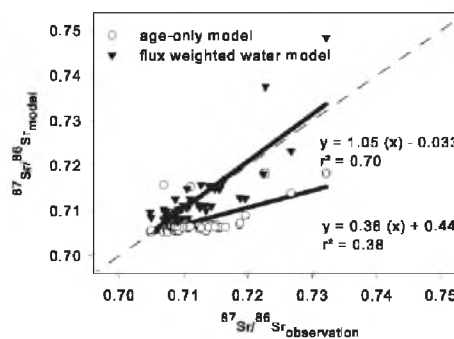


Fig. 8. Validation of the catchment water Sr isotope model across all study catchments, showing linear regressions between measured $^{87}\text{Sr}/^{86}\text{Sr}$ and flux-weighted catchment water and age-only water model predictions for 68 streams of the USA (celestite-corrected values are used for the Scioto River). Dashed line shows the 1:1 relationship.

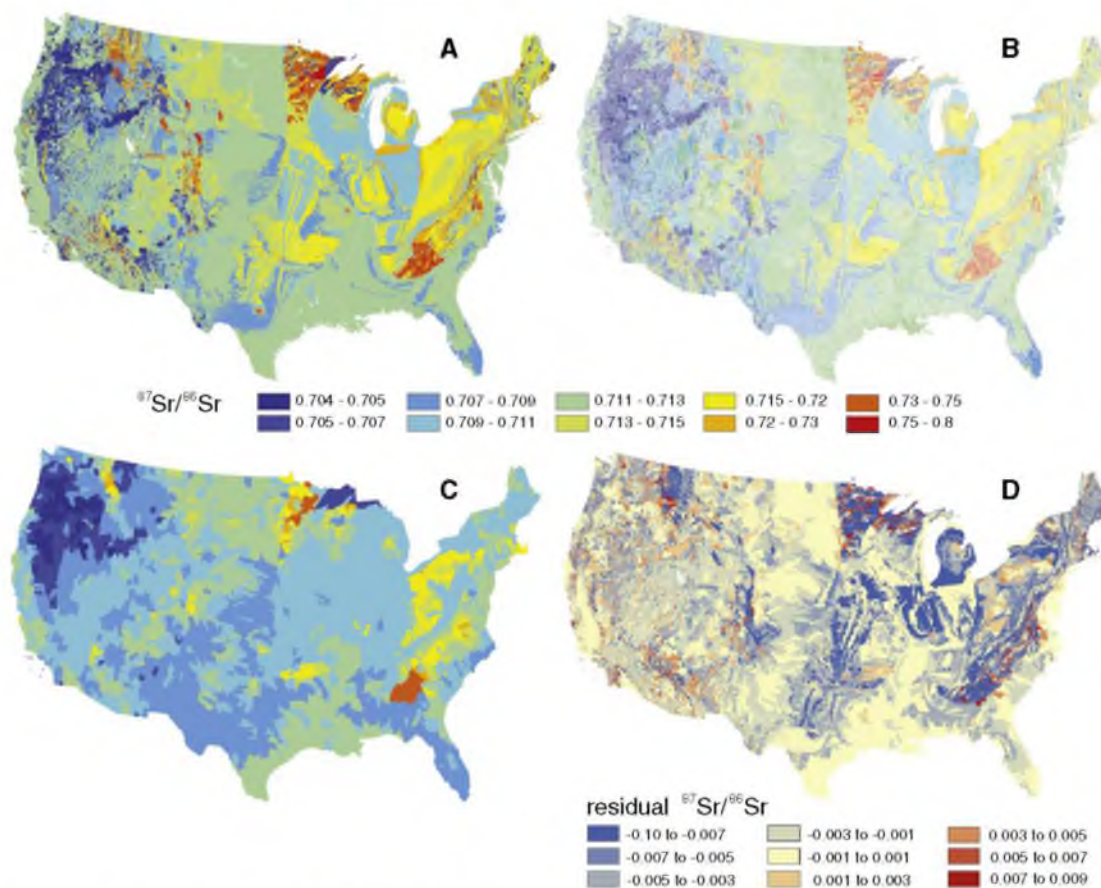


Fig. 9. Modeled Sr isotope ratios for (A) local water, (B) flux-weighted catchment water, (C) flux-weighted catchment water model values averaged within watersheds of the Watershed Boundary Dataset (<http://www.nrcs.usda.gov/wps/portal/nrcs/main/national/water/watersheds/dataset/>) and (D) residual between major bedrock (Fig. 6B) and average flux-weighted catchment water (Fig. 9C).

Applying predictive models to interpret the $^{87}\text{Sr}/^{86}\text{Sr}$ of biological materials is challenging because the contribution of different environmental sources of Sr to the organism are often unknown. In this study, we consider bedrock and water as two potential sources of Sr to plants, and compare our model predictions with data on the $^{87}\text{Sr}/^{86}\text{Sr}$ of marijuana measured for forensic purposes (West et al., 2009). Comparisons with this dataset were based on model values integrated across counties, as this was the most precise level of geographic information reported for the marijuana samples.

The flux-weighted catchment water model showed the strongest correlation and most accurate predictions in comparison with the measured marijuana sample $^{87}\text{Sr}/^{86}\text{Sr}$ values (Fig. 10). In contrast, the unweighted catchment water model showed the weakest correlation with the measured values. The strength of correlation for the age-only water model was intermediate, but this model drastically under-predicted the range of observed values (Fig. 10). $^{87}\text{Sr}/^{86}\text{Sr}$ predictions for several counties are buffered by the presence of carbonate bedrock, which explains the differences between the unweighted and flux-weighted catchment water models and supports the hypothesis of West et al. (2009) that carbonate bedrock effects were reflected in the marijuana Sr isotope dataset. Most of the marijuana $^{87}\text{Sr}/^{86}\text{Sr}$ values were approximated well by the flux-weighted catchment water model, however significant inaccuracies remain in complex

geological settings such as on the Minnesota shield or in the Appalachian Mountains. The correlations observed for the different models suggest that the $^{87}\text{Sr}/^{86}\text{Sr}$ value in plants is closer to a flux-weighted $^{87}\text{Sr}/^{86}\text{Sr}$ signal integrated over a large area (flux-weighted catchment water model) than to an unweighted average of the soluble $^{87}\text{Sr}/^{86}\text{Sr}$ of the rock units of the county (unweighted catchment water model). Although these results offer no direct information on the ultimate sources of Sr to marijuana plants, they suggest that spatial model formulations that more accurately represent bedrock Sr isotope ratios and account for weathering effects on Sr release to water may more accurately represent the isotope ratios of Sr taken up by these plants. Integrating the $^{87}\text{Sr}/^{86}\text{Sr}$ values over a county area likely reduces the accuracy of these comparisons given that these political boundaries usually do not have any significance in terms of hydrology, and this methodological issue could also help explain the weak correlation of the unweighted catchment water model in comparison with the age-only catchment model.

5. Conclusion and perspectives

We have developed and calibrated parameterized models for the prediction of regional to continental scale spatial variation in bedrock and catchment water Sr isotope ratios. Unlike previous models, our

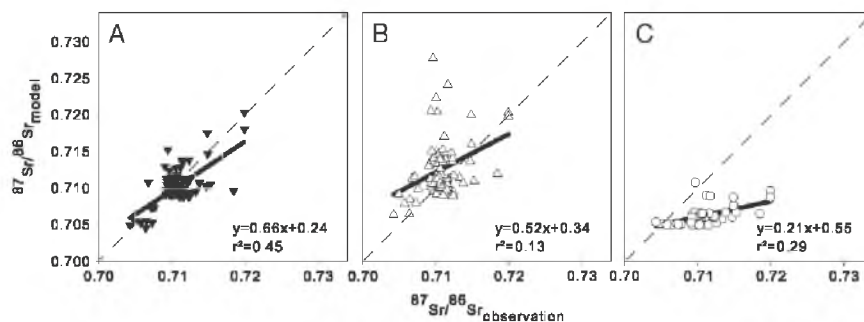


Fig. 10. Linear regression between $^{87}\text{Sr}/^{86}\text{Sr}$ in marijuana and the mean values of the modeled water in the county of sample origin. Water values are the average of all grid cells in the county, weighted as described for the (A) flux-weighted catchment water model, (B) unweighted catchment water model, and (C) age-only catchment water model. Symbols as in Fig. 7. Dashed line in each panel shows the 1:1 relationship.

formulation represents major lithology-specific effects and yet remains generalized to the extent that it could be applied in any region where basic digital geological map data (including lithology and age) are available. In spite of the limitations discussed throughout this paper, this new mapping method represents a significant advance in modeling major environmental Sr sources to ecosystems, and the strength of the correlations between the different models and the observations are encouraging. Moreover, although the predictive power of the model remains limited in many cases, our documentation of model performance through quantitative comparisons with observational data allows informed use of the model-derived data products.

A number of regions of the contiguous USA display promising $^{87}\text{Sr}/^{86}\text{Sr}$ variations at different scales which could be used to determine rock, water or biological material provenance. The Sr isoscapes could complement other existing isoscapes (Bowen et al., 2005) used for provenance studies because $^{87}\text{Sr}/^{86}\text{Sr}$ varies widely at regional and continental scales. The development of more detailed and harmonized seamless geological maps for the conterminous USA (Jansen et al., 2010) and other regions, as well as refined high resolution lithological studies and geochemical sampling, could rapidly improve the resolution and accuracy of these isoscapes.

In this respect, we suggest the following as critical next steps to improving the predictability of environmental Sr isotope ratios at large scales:

- 1) Develop more flexible parameterizations and parameter distributions that increase the ability of the model to represent highly radiogenic rock units.
- 2) Improve weathering rate calculations by including functions describing rate dependence on factors such as runoff, climate, pedology, vegetation and topography. Recent work from Jansen et al. (2010) offers a good starting point.
- 3) Develop submodels representing the contribution of atmospheric sources of Sr, particularly dust and sea salt, to soil and bioavailable Sr.
- 4) Identify systematic approaches to representing the contribution of Sr weathered from surficial deposits to water.
- 5) Ultimately, model and scale the contribution of these sources of Sr, including bedrock weathering, atmospheric sources and surficial Sr sources, to bioavailable and biological pools of interest, including soil, soil water, surface and groundwater and organismal Sr. The work of Stewart et al. (1998) provides a platform on which such an effort could be developed.
- 6) In all cases, these efforts will be advanced through the continued accumulation and compilation of Sr isotope measurements and elemental concentration data from a range of materials. Our results suggest that the most critical data gaps vary depending on

location, but include measurements of surficial deposits that are not adequately characterized on most geological maps and continued analysis of Sr isotope ratios of stream systems, which integrate the geochemistry of their watersheds and can reveal important inaccuracies in the model.

Acknowledgements

This research was supported by NSF Award DBI-0743543. We thank Casey Kennedy and Hilary Bataille for reviewing and commenting on this manuscript, and three anonymous reviewers for their comments which greatly improved this manuscript.

Appendix A. Supplementary data

Supplementary data to this article can be found online at doi:10.1016/j.chemgeo.2012.01.028.

References

- Anderson, S.P., Drever, J.L., Frost, C.D., Holden, P., 2000. Chemical weathering in the foreland of a retreating glacier. *Geochimica et Cosmochimica Acta* 64 (7), 1173–1189.
- Barnett-Johnson, K., Pearson, T.E., Ramos, F.C., Grimes, C.B., MacFarlane, R.B., 2008. Tracking natal origins of salmon using isotopes, otoliths, and landscape geology. *Limnology and Oceanography* 53 (4), 1633–1642.
- Beard, B.L., Johnson, C.M., 2000. Strontium isotope composition of skeletal material can determine the birth place and geographic mobility of humans and animals. *Journal of Forensic Sciences* 45 (5), 1049–1061.
- Bentley, R.A., 2006. Strontium isotopes from the earth to the archaeological skeleton: a review. *Journal of Archaeological Method and Theory* 13 (3), 135–187. doi:10.1007/s10816-006-9009-x.
- Bentley, R.A., Knipper, C., 2005. Geographical patterns in biologically available strontium, carbon and oxygen isotope signatures in prehistoric SW Germany. *Archaeometry* 47, 629–644.
- Bentley, R.A., Wahl, J., Price, T.D., Atkinson, T.C., 2008. Isotopic signatures and hereditary traits: snapshot of a Neolithic community in Germany. *Antiquity* 82 (316), 290–304.
- Beusen, A.H.W., Bouwman, A.F., Durr, H.H., Dekkers, A.L.M., Hartmann, J., 2009. Global patterns of dissolved silica export to the coastal zone: results from a spatially explicit global model. *Global Biogeochemical Cycles* 23.
- Bluth, G.J.S., Kump, L.R., 1994. Lithologic and climatic controls of river chemistry. *Geochimica et Cosmochimica Acta* 58 (10), 2341–2359.
- Bowen, G.J., 2010. Isoscapes: spatial pattern in isotopic biogeochemistry. *Annual Review of Earth and Planetary Sciences* 38, 161–187. doi:10.1146/annurev-earth-040809-152429.
- Bowen, G.J., Wassenaar, L.L., Hobson, K.A., 2005. Global application of stable hydrogen and oxygen isotopes to wildlife forensics. *Oecologia* 143 (3), 337–348. doi:10.1007/s00442-004-1813-y.
- Brady, P.V., Carroll, S.A., 1994. Direct effects of CO₂ and temperature on silicate weathering — possible implications for climate control. *Geochimica et Cosmochimica Acta* 58 (7), 1853–1856.
- Brandley, S.L., Goldhaber, M.B., Ragnarsdottir, K.V., 2007. Crossing disciplines and scales to understand the Critical Zone. *Elements* 3 (5), 307–314.

- Bullen, T.D., Krabbenhoft, D.P., Kendall, C., 1996. Kinetic and mineralogic controls on the evolution of groundwater chemistry and $87\text{Sr}/86\text{Sr}$ in a sandy silicate aquifer, northern Wisconsin, USA. *Geochimica et Cosmochimica Acta* 60 (10), 1807–1821.
- Capo, R.C., Stewart, B.W., Chadwick, O.A., 1998. Strontium isotopes as tracers of ecosystem processes: theory and methods. *Geoderma* 82 (1–3), 197–225.
- Carlson, R.W., 2003. Introduction to Volume 2. In: Heinrich, D.H., Karl, K.T. (Eds.), *Treatise on Geochemistry*. Pergamon, Oxford, pp. xv–xxiii.
- Chadwick, O.A., Derry, L.A., Bern, C., 2009. Changing sources of strontium to soils and ecosystems across the Hawaiian Islands. *Chemical Geology* 267, 64–76. doi:10.1016/j.chemgeo.2009.01.009.
- Chamberlain, C.P., et al., 1997. The use of isotope tracers for identifying populations of migratory birds. *Oecologia* 109 (1), 132–141.
- Chaudhuri, S., Clauer, N., 1993. Strontium isotopic compositions and potassium and rubidium contents of formation waters in sedimentary basins — clues to the origin of the solutes. *Geochimica et Cosmochimica Acta* 57 (2), 429–437.
- Clawges, R.M., Price, C.V., National Water-Quality Assessment Program (U.S.) and Geological Survey (U.S.), 1999. Digital data sets describing principal aquifers, surficial geology, and ground-water regions of the conterminous United States. U.S. Geological Survey open-file report 99-77. USGS, Rapid City, S.D.
- Clow, D.W., Mast, M.A., Bullen, T.D., Turk, J.T., 1997. Strontium 87 strontium 86 as a tracer of mineral weathering reactions and calcium sources in an alpine/subalpine watershed, Loch Vale, Colorado. *Water Resources Research* 33 (6), 1335–1351.
- Crittenden, R.G., et al., 2007. Determining the geographic origin of milk in Australasia using multi-element stable isotope ratio analysis. *International Dairy Journal* 17 (5), 421–428. doi:10.1016/j.idairyj.2006.05.012.
- Dasch, E.J., 1969. Strontium isotopes in weathering profiles, deep-sea sediments, and sedimentary rocks. *Geochimica et Cosmochimica Acta* 33 (12) 1521–8.
- Davies, G.R., Halliday, A.N., 1998. Development of the Long Valley rhyolitic magma system: strontium and neodymium isotope evidence from glasses and individual phenocrysts. *Geochimica et Cosmochimica Acta* 62 (21–22), 3561–3574.
- DePaolo, D.J., 1981. Trace element and isotopic effects of combined wallrock assimilation and fractional crystallization. *Earth and Planetary Science Letters* 53 (2), 189–202. doi:10.1016/0012-821X(81)90153-9.
- Drever, J.L., Clow, D.W., 1995. Weathering rates in catchments. In: Brantley, S., White, A. (Eds.), *Chemical weathering rates of silicate minerals*. Rev. in Mineral., vol. 31. Mineral. Soc. of Am., Washington, D. C., pp. 463–483.
- Eckhardt, F.E.W., 1979. Über die Einwirkung heterotropher Mikroorganismen auf die Zersetzung silikatischer Minerale. *Zeitschrift für Pflanzenernährung und Bodenkunde* 142 (3), 434–445.
- Ezzo, J.A., Johnson, C.M., Price, T.D., 1997. Analytical perspectives on prehistoric migration: a case study from east-central Arizona. *Journal of Archaeological Science* 24 (5), 447–466.
- Faure, G., 1977. Principles of isotope geology. Related Information: Smith and Wyllie intermediate geology series. Medium: X; Size: Pages: 475 pp.
- Fisher, R.S., Stueber, A.M., 1976. Strontium isotopes in selected streams within Susquehanna River Basin. *Water Resources Research* 12 (5), 1061–1068.
- Franke, W.A., 2009. The durability of rocks — developing a test of rock resistance to chemical weathering. *American Journal of Science* 309 (8), 711–730. doi:10.2475/08.2009.04.
- Frei, R., Frei, K.M., 2011. The geographic distribution of strontium isotopes in Danish surface waters — a base for provenance studies in archaeology, hydrology and agriculture. *Applied Geochemistry* 26, 326–340.
- Geological Survey (U.S.), 2004. The National Geochemical Survey, database and documentation, U.S. Geological Survey open-file report 2004-1001. U.S. Dept. of the Interior, U.S. Geological Survey, [Reston, Va.].
- Geological Survey (U.S.), 2005. State Geologic Map Compilation, U.S. Geological Survey open-file report (various), online at <http://tin.er.usgs.gov/geology/state/>.
- Geological Survey (U.S.), Geologic Names Committee, 2007. Divisions of geologic time — major chronostratigraphic and geochronologic units. Fact sheet 2007–3015. U.S. Geological Survey, [Reston, Va.].
- Gesch, D., 2002. The National Elevation Dataset. *Photogrammetric Engineering and Remote Sensing* 68 (1) 5–+.
- Goff, F., Wollenberg, H.A., Brooks, D.C., Kistler, R.W., 1991. A Sr-isotopic comparison between thermal waters, rocks, and hydrothermal calcites, Long Valley Caldera, California. *Journal of Volcanology and Geothermal Research* 48 (3–4), 265–281.
- Goldstein, S.J., Jacobsen, S.B., 1988. Nd and Sr isotopic systematics of river water suspended material — implications for crustal evolution. *Earth and Planetary Science Letters* 87 (3), 249–265.
- Graustein, W.C., 1989. $87\text{Sr}/86\text{Sr}$ ratios measure the sources and flow of strontium in terrestrial ecosystems. *Stable isotopes in ecological research*. *Ecological Studies* 68, 491–512.
- Graustein, W.C., Armstrong, R.L., 1983. The use of Sr-87 Sr-86 ratios to measure atmospheric transport into forested watersheds. *Science* 219 (4582), 289–292.
- Groussot, F.E., Biscaye, P.E., 2005. Continental aerosols, isotopic fingerprints of sources and atmospheric transport: a review. *Chemical Geology* 222, 149–167.
- Hartmann, J., Moosdorf, N., 2011. Chemical weathering rates of silicate-dominated lithological classes and associated liberation rates of phosphorus on the Japanese Archipelago — implications for global scale analysis. *Chemical Geology*. doi:10.1016/j.chemgeo.2010.12.004.
- Hartmann, J., Jansen, N., Dürr, H.H., Harashima, A., Okubo, K., Kempe, S., 2009. Predicting riverine dissolved silica fluxes into coastal zones from a hyperactive region and analysis of their first order controls. *International Journal of Earth Sciences*. doi:10.1007/s00531-008-0381-5.
- Hodell, D.A., Quinn, R.L., Brenner, M., Kamenov, G., 2004. Spatial variation of strontium isotopes ($87\text{Sr}/86\text{Sr}$) in the Maya region: a tool for tracking ancient human migration. *Journal of Archaeological Science* 31 (5), 585–601. doi:10.1016/j.jas.2003.10.009.
- Hogan, J.F., Blum, J.D., Siegel, D.J., Glaser, P.H., 2000. Sr-87/Sr-86 as a tracer of ground-water discharge and precipitation recharge in the Glacial Lake Agassiz Peatlands, northern Minnesota. *Water Resources Research* 36 (12), 3701–3710.
- Hoppe, K.A., Koch, P.L., Carlson, R.W., Webb, S.D., 1999. Tracking mammoths and mastodons: reconstruction of migratory behavior using strontium isotope ratios. *Geology* 27 (5), 439–442.
- Horton, T.W., Chamberlain, C.P., Fantle, M., Blum, J.D., 1999. Chemical weathering and lithologic controls of water chemistry in a high-elevation river system: Clark's Fork of the Yellowstone River, Wyoming and Montana. *Water Resources Research* 35 (5), 1643–1655.
- Jansen, N., Hartmann, J., Lauerwald, R., Dürr, H.H., Kempe, S., Loos, S., Middelkoop, H., 2010. Dissolved silica mobilization in the conterminous USA. *Chemical Geology* 270 (1–4), 90–109. doi:10.1016/j.chemgeo.2009.11.008.
- Kawasaki, A., Oda, H., Hirata, T., 2002. Determination of strontium isotope ratio of brown rice for estimating its provenance. *Soil Science and Plant Nutrition* 48 (5), 635–640.
- Kelly, S., Heaton, K., Hoogewerf, J., 2005. Tracing the geographical origin of food: the application of multi-element and multi-isotope analysis. *Trends in Food Science & Technology* 16 (12), 555–567. doi:10.1016/j.tifs.2005.08.008.
- King, E.M., Beard, B.L., Valley, J.W., 2007. Strontium and oxygen isotope evidence for strike/slip movement of accreted terranes in the Idaho Batholith. *Lithos* 96, 387–401.
- Kistler, R.W., Peterman, Z.E., 1973. Variations in Sr, Rb, K, Na, and initial Sr-87–Sr-86 in Mesozoic granitic rocks and intruded wall rocks in Central California. *Geological Society of America Bulletin* 84 (11), 3489–3511.
- Koch, P.L., et al., 1995. Isotopic tracking of change in diet and habitat use in African elephants. *Science* 267 (5202), 1340–1343.
- Le Bas, M.J., Streckeisen, A.L., 1991. The IUGS systematics of igneous rocks. *Journal of the Geological Society* 148 (5), 825–833. doi:10.1144/gsjgs.148.5.0825.
- Lehnert, K., Su, Y., Langmuir, C.H., Sarbas, B., Nohl, U., 2000. A global geochemical database structure for rocks. *Geochemistry, Geophysics, Geosystems* 1 (5), 1–14. doi:10.1029/1999gc000026.
- Lewis, M.A., 1989. Water. In: McCall, J., Marker, B. (Eds.), *Earth Science Mapping for planning, development and conservation*. Graham and Trotman.
- Marchand, D.E., 1974. Chemical weathering, soil development, and geochemical fractionation in a part of the White Mountains, Mono and Inyo Counties, California. *Geological Survey Professional Paper 352-J*. Erosion and Sedimentation in a Semi-arid Environment. U.S. Govt. Print. Off. Washington, pp. 379–424. v.p.
- Matsukura, Y., Hattajji, T., Oguchi, C.T., Hirose, T., 2007. Ten year measurements of weathering rates of rock tablets on a forested hillslope in a humid temperate region, Japan. *Zeitschrift für Geomorphologie* 51 (1), 27–40. doi:10.1127/0372-8854/2007/0051s-0027.
- Meybeck, M., 1987. Global chemical weathering of surficial rocks estimated from river dissolved loads. *American Journal of Science* 287 (5), 401–428.
- Miller, E.K., Blum, J.D., Friedland, A.J., 1993. Determination of soil exchangeable-cation loss and weathering rates using Sr isotopes. *Nature* 362 (6419), 438–441.
- Moulton, K.L., West, J., Berner, R.A., 2000. Solute flux and mineral mass balance approaches to the quantification of plant effects on silicate weathering. *American Journal of Science* 300 (7), 539–570.
- Négrel, Ph., Petelet-Girard, E., 2005. Strontium isotopes as tracers of groundwater-induced floods: the Somme case study (France). *Journal of Hydrology* 305, 99–119.
- Pretti, V.A., Stewart, B.W., 2002. Solute sources and chemical weathering in the Owens Lake watershed, eastern California. *Water Resources Research* 38 (8) doi:Artn 1127.
- Price, T.D., Johnson, C.M., Ezzo, J.A., Ericson, J., Burton, J.H., 1994. Residential-mobility in the prehistoric Southwest United States — a preliminary study using strontium isotope analysis. *Journal of Archaeological Science* 21 (3), 315–330.
- Price, T.D., Burton, J.H., Bentley, R.A., 2002. The characterization of biologically available strontium isotope ratios for the study of prehistoric migration. *Archaeometry* 44, 117–136.
- Raymo, M.E., Ruddiman, W.F., Froelich, P.N., 1988. Influence of late Cenozoic mountain building on ocean geochemical cycles. *Geology* 16 (7), 649–653.
- Reimann, C., Filzmoser, P., 2000. Normal and lognormal data distribution in geochemistry: death of a myth. Consequences for the statistical treatment of geochemical and environmental data. *Environmental Geology* 39, 1001–1014.
- Rudnick, R.L., 2003. Introduction to Volume 3. In: Heinrich, D.H., Karl, K.T. (Eds.), *Treatise on Geochemistry*. Pergamon, Oxford, pp. xv–xix.
- Shields, G., Veizer, J., 2002. Precambrian marine carbonate isotope database: Version 1.1. *Geochemistry, Geophysics, Geosystems* 3 doi:Artn 1031.
- Sillen, A., Hall, G., Richardson, S., Armstrong, R., 1998. $87\text{Sr}/86\text{Sr}$ ratios in modern and fossil food-webs of the Sterkfontein Valley: implications for early hominid habitat preference. *Geochimica et Cosmochimica Acta* 62 (14), 2463–2473. doi:10.1016/S0016-7037(98)00182-3.
- Steele, J.D., Stueber, A.M., Curtis, J.B., Pushkar, P., 1972. Strontium isotopic study of Scioto River Basin, Ohio. *Transactions — American Geophysical Union* 53 (4) 379–8.
- Stevens, C.H., Greene, D.C., 1999. Stratigraphy, depositional history, and tectonic evolution of Paleozoic continental-margin rocks in roof pendants of the eastern Sierra Nevada, California. *Geological Society of America Bulletin* 111, 919–933.
- Stewart, B.W., Capo, R.C., Chadwick, O.A., 1998. Quantitative strontium isotope models for weathering, pedogenesis and biogeochemical cycling. *Geoderma* 82 (1–3), 173–195.
- Stueber, A.M., Baldwin, A.D., Curtis, J.B., Pushkar, P., Steele, J.D., 1975. Geochemistry of strontium in Scioto River Drainage Basin, Ohio. *Geological Society of America Bulletin* 86 (7), 892–896.
- Veizer, J., et al., 1999. Sr-87/Sr-86, delta C-13 and delta O-18 evolution of Phanerozoic seawater. *Chemical Geology* 161 (1–3), 59–88.
- Voerkelius, S., et al., 2010. Strontium isotopic signatures of natural mineral waters, the reference to a simple geological map and its potential for authentication of food. *Food Chemistry* 118 (4), 933–940. doi:10.1016/j.foodchem.2009.04.125.

- Wasserba, G.J., Papanast, D.A., Sanz, H.G., 1969. Initial strontium for a chondrite and determination of a metamorphism or formation interval. *Earth and Planetary Science Letters* 7 (1) 33–8.
- West, A.J., Galy, A., Bickle, M., 2005. Tectonic and climatic controls on silicate weathering. *Earth and Planetary Science Letters* 235 (1–2), 211–228.
- West, J.B., Hurley, J.M., Dudas, F.O., Ehleringer, J.R., 2009. The stable isotope ratios of Marijuana. II. Strontium isotopes relate to geographic origin. *Journal of Forensic Sciences* 54 (6), 1261–1269. doi:10.1111/j.1556-4029.2009.01171.x.
- Wetherill, G.W., Davis, G.L., Leehu, C., 1968. Rb–Sr measurements on whole rocks and separated minerals from Baltimore Gneiss Maryland. *Geological Society of America Bulletin* 79 (6) 757–8.
- White, A.F., Blum, A.E., 1995. Effects of climate on chemical-weathering in watersheds. *Geochimica et Cosmochimica Acta* 59 (9), 1729–1747.
- Whitney, P.R., Hurley, P.M., 1964. The problem of inherited radiogenic strontium in sedimentary age determinations. *Geochimica et Cosmochimica Acta* 28, 425–436 (Apr).

Supplementary methods and tables

1. Geological map data:

- 1.1. We downloaded 48 state lithologic maps from the United States Geological Survey state-level geological map geodatabases (U.S. Geological Survey, 2005, State Geologic Map Compilation, USGS Open-File Report (various), online at <http://tin.er.usgs.gov/geology/state/>)
- 1.2. Using ArcGIS, we merged (Data Management toolbox) the individual maps into a single shape file to obtain a geodatabase with three attributes relevant to our work:
 - 1.2.1. Unit_age: Text or text and numeric field stating age of the unit (e.g., “Permian to Cretaceous”, “Tertiary 14-16Ma”))
 - 1.2.2. Rocktype1 and Rocktype2: Text fields stating the most abundant and second most abundant lithology of the mapped unit, coded using the Data Dictionary for Geologic Map Unit Classification, version 6.1 (<http://ngmdb.usgs.gov/www-nadm/dmdt/pdf/lithclass61.pdf>). The entries in these fields do not provide information on the quantitative abundance of the major and minor lithologies beyond the relative estimates provided by the field definitions (most abundant and second most abundant rock types present in the unit).
- 1.3. We exported the merged geodatabase attribute table into Excel.

Rationale: These maps were chosen as a basis for our work because they are unique in providing internally consistent, high-resolution age and lithological information for the contiguous USA. However, the digital maps are neither uniform nor seamless (see <http://pubs.usgs.gov/of/2005/1325/documents/CONUSdocumentation.pdf>), which presents challenges for our work. Most notably 1) a large number of unique lithological and age descriptors are used and must be interpreted prior to modeling, and 2) significant discontinuities in map units occur at some state boundaries, leading to artificial discontinuities in the Sr isotope map values. The discontinuities result from differences in resolution, combination and mapping philosophy among state maps. Both challenges will likely be rectified when an integrated, data-rich digital geological map is made available for the USA (Jansen et al., 2010).

2. Calibrating values of t_2 (equation 2):

- 2.1. In Excel, we sorted the attribute table of the geodatabase by unit_age
- 2.2. We extracted each unique geologic time descriptor in an Excel sheet (Table

“Age”). For different state maps the age descriptor is given in different format, either as a string stating a time period of the USGS geological time scale (e.g., “Cambrian to Ordovician”) or as numeric values (Table 2S.2).

- 2.3. In “Age”, we assigned a numeric age to each geologic time descriptor using the USGS division of geologic time (U.S. Geological Survey Geologic Names Committee, 2007).
- 2.4. We joined the “Age” table to the merged geodatabase in ArcGIS using the age descriptor as joining field

Rationale: In order to accommodate the wide range of formats and specificities of the age data, we chose to systematically approximate the age of rock units as the maximum age of the specified eon, era, period or epoch. To be consistent in our methodology and because the mean was not always calculable, we opted for using the maximum. This choice may cause our model to overestimate the $^{87}\text{Sr}/^{86}\text{Sr}$ values for units with age descriptors representing a large age range (e.g., Archean). However, because the sensitivity of $^{87}\text{Sr}/^{86}\text{Sr}$ to age is relatively weak (on average $^{87}\text{Sr}/^{86}\text{Sr}$ changes by 0.001 for 10Ma for felsic rocks and for 100Ma for mafic rocks) this did not affect significantly the modeled $^{87}\text{Sr}/^{86}\text{Sr}$.

3. Calibrating the silicate model:

3.1. Calibrating $(\text{Rb}/\text{Sr})_{\text{parent}}$ (equation 2) for each rock unit:

- 3.1.1. In Excel, we sorted the attribute table of the geodatabase by rocktype1
- 3.1.2. We extracted each unique rocktype1 lithologic descriptor in an excel sheet (Table “lithology1”)
- 3.1.3. We repeated steps 3.1.1-2. for rocktype2 and added the different unique lithologic descriptors to “lithology2”
- 3.1.4. For each lithologic descriptor, we classified the parent material type:
 - 3.1.4.1. For sedimentary and metasedimentary rocks, we approximated the $(\text{Rb}/\text{Sr})_{\text{parent}}$ by assuming a uniform parent rock with a constant Rb/Sr value of 0.24 corresponding to the average Rb/Sr of the upper crust (Goldstein and Jacobsen, 1988)
 - 3.1.4.2. For igneous, volcanic and metaigneous rocks, we approximated the $(\text{Rb}/\text{Sr})_{\text{parent}}$ by separating these lithologies in 5 categories representing different parent rocks (ultramafic, mafic, mafic intermediate, felsic intermediate and felsic). We based our categorization on the IUGS classification (Le Bas and Streckisen, 1991). The classification of each

rock type can be inferred from the $(Rb/Sr)_{parent}$ values shown in Table 2S.1.

Rationale: We used this categorization method to separate the modeling of $(^{87}Rb/^{86}Sr)_{parent}$ of igneous and volcanic rocks along a gradient from Rb-poor mantle rocks to Rb-rich crustal parent rocks, providing a first-order representation of chemical variation in silicate magma related to: 1) source composition (crust or mantle) and 2) depth of melting.

3.1.5. We obtained 5765 data from the Western North American Volcanic and Intrusive Rock Database (www.navdat.org) using the query:

3.1.5.1. Chemical constraint: Rb and Sr content and $^{87}Sr/^{86}Sr$ measurements,

3.1.5.2. Age constraint: Age ranges from 0 to 5000Ma (“loose search” mode, see www.navdat.org), and

3.1.5.3. Rock type constraint: all types.

3.1.6. For each sample:

3.1.6.1. We back-calculated $(Rb/Sr)_{parent}$ using equation 2 and the given age, Rb and Sr content, and $^{87}Sr/^{86}Sr$,

3.1.6.2. We assigned the sample to one of the parent rock categories defined in 3.1.4. based on their rock type, and

3.1.6.3. We sorted the table and calculated the numeric mean Rb/Sr for each parent rock category.

3.1.7. In “lithology1” and “lithology2”, we assigned an estimated parent rock Rb/Sr value to each lithologic descriptor based on the results of 3.1.6. (Table 2S.1).

This step (3.1.) creates the most uncertainty in this model because we separated the rock units in only seven parent rock categories. The $(^{87}Rb/^{86}Sr)_{parent}$ can vary largely from one formation to the next depending on the geological history of the region. As the number of $(^{87}Sr/^{86}Sr)_i$ data increase, in the future it will be preferable to use direct $(^{87}Sr/^{86}Sr)_i$ measurements or a more detailed lithological classification scheme to characterize $(^{87}Rb/^{86}Sr)_{parent}$.

3.2. Calibrating $(Rb/Sr)_{lithology}$ (equation 2):

3.2.1. We obtained 252,661 data, representing 167 of the 180 lithological

descriptors in “lithology1” and “lithology2”, from the Earthchem portal (<http://www.earthchemportal.org/>) using the query:

- 3.2.1.1. Database constraint: USGS results,
- 3.2.1.2. Chemical constraint: Rb and Sr content measurements, and
- 3.2.1.3. Sample type constraint: all sample type (mode “rock name given by collector or author”).
- 3.2.2. We calculated the mean Rb/Sr for each sample in this dataset.
- 3.2.3. We sorted the data by sample type and calculated the numeric mean Rb/Sr for each sample type.
- 3.2.4. In “lithology1” and “lithology2”, we assigned Rb/Sr values to each of the 167 lithologic descriptor based on the calculated averages (Table 2S.1).
- 3.2.5. For the 13 remaining lithologic descriptors with no associated samples, we assigned $(Rb/Sr)_{rock}$ by comparison with other analogous rocks (Table 2S.1).

Rationale: We considered both the numeric and geometric means as measures of the central tendency for model parameters. Because most of the rock types showed right-skewed distributions of their Rb/Sr values, the numeric means gave slightly higher estimates of Rb/Sr than the geometric means, and thus slightly improve the tendency of the model to underestimate the Sr isotope ratios of very radiogenic rocks. However, more work is needed to understand the potential impact of sample alteration and sampling bias on the calculated mean values (see “Bedrock models” section of Chapter II).

4. Calibrating equations for the carbonate model:

- 4.1. In Excel, we sorted the attribute table of the geodatabase by rocktype1 and rocktype2.
- 4.2. In an excel sheet (Table “carbonates”), we extracted the 10 unique lithologic descriptors related to carbonates: “carbonates”, “limestone”, “marble”, “calc-silicate rock”, “calc-silicate schist”, “dolostone”, “intrusive carbonatite”, “phosphorite”, “evaporite”, and “lake or marine deposit (nonglacial)”.
- 4.3. In “carbonates”, we used the numerical age of the geological unit to estimate the corresponding $(^{87}Sr/^{86}Sr)_{seawater}$ value from the curve of Shields and Veizer (2002) (Table 2S.3).

5. Mapping $^{87}Sr/^{86}Sr$:

- 5.1. We joined Tables 2S.1 and 2S.2 to the geodatabase by using lithologic descriptor rocktype1 as a joining field.
- 5.2. For each geological unit in the geodatabase, we calculated $(^{87}\text{Sr}/^{86}\text{Sr})_{\text{rock}}$ using equation 2 and our estimates of t_2 , $(\text{Rb}/\text{Sr})_{\text{parent}}$ and $(\text{Rb}/\text{Sr})_{\text{lithology}}$.
- 5.3. We repeated steps 5.1-2 for lithologic descriptor rocktype2.
- 5.4. We joined Table 2S.3 to the geodatabase using unit_age as a joining field.
- 5.5. In Excel, we sorted the geodatabase to identify all carbonate lithologic descriptors and used equation 3 to calculate the $^{87}\text{Sr}/^{86}\text{Sr}$ using our estimated values of $(\text{Rb}/\text{Sr})_{\text{seawater}}$ and $(\text{Rb}/\text{Sr})_{\text{lithology}}$.
- 5.6. Steps 5.1-5 gave two new fields in the geodatabase, “Sr_ratio1” and “Sr_ratio2”, that contained the modeled $^{87}\text{Sr}/^{86}\text{Sr}$ values for the major and minor lithologies present in each map unit.
6. Validating the silicate model:
 - 6.1. We downloaded 9130 data through the Earthchem portal using the query:
 - 6.1.1. Database constraint: Geroc-Start results,
 - 6.1.2. Chemical constraint: $^{87}\text{Sr}/^{86}\text{Sr}$,
 - 6.1.3. Age constraint: Age ranges from 0 to 5000Ma, and
 - 6.1.4. Sample type constraint: all sample type (mode “rock name given by collector or author”).
 - 6.2. We used sample type to assign value to the parameters $(\text{Rb}/\text{Sr})_{\text{parent}}$ and $(\text{Rb}/\text{Sr})_{\text{lithology}}$ using the values in Table 2S.1.
 - 6.3. We calculated $(^{87}\text{Sr}/^{86}\text{Sr})_{\text{model}}$ for each sample with equation 2 using the given age (t_2) and the assigned $(\text{Rb}/\text{Sr})_{\text{parent}}$ and $(\text{Rb}/\text{Sr})_{\text{lithology}}$.
 - 6.4. We compared $(^{87}\text{Sr}/^{86}\text{Sr})_{\text{model}}$ with $(^{87}\text{Sr}/^{86}\text{Sr})_{\text{observations}}$.
7. Validating the carbonate model:
 - 7.1. We downloaded 246 carbonate rock data through the Precambrian Marine Carbonate Isotopes database (Shields and Veizer, 2002).
 - 7.2. We used the age and rock type to assign values to the parameters $(\text{Rb}/\text{Sr})_{\text{seawater}}$

and $(Rb/Sr)_{lithology}$ using values from Tables 2S.1 and 2S.3.

7.3. We calculated $(^{87}Sr/^{86}Sr)_{model}$ for each sample with equation 3 using the given age (t_2) and the assigned $(Rb/Sr)_{seawater}$ and $(Rb/Sr)_{lithology}$

7.4. We compared $(^{87}Sr/^{86}Sr)_{model}$ with $(^{87}Sr/^{86}Sr)_{observation}$

Rationale: Discussion concerning database biases and method of verification are already given in the “Bedrock models” section of Chapter II

8. Calibrating the weathering model:

8.1. Calibrating *Sr content*:

8.1.1. In Excel, we sorted the attribute table of the geodatabase by rocktype 1.

8.1.2. We extracted each unique lithologic descriptor in an Excel sheet (table “Sr content”).

8.1.3. Using the data obtained in 3.2., we calculated the average *Sr content* for each sample and then the average for each lithologic descriptor.

8.1.4. In “Sr content”, we used the calculated averages to assign *Sr content* to each lithologic descriptor present in the geodatabase.

8.1.5. We repeated steps 8.1.1-4. for rocktype2.

8.1.6. Results of these steps are gathered in Table 2S.4.

8.1.7. We joined “Sr content” to the geodatabase using lithologic descriptor as a joining field.

8.2. Calibrating weathering rates:

8.2.1. In Excel, we sorted the attribute table of the geodatabase by rocktype1.

8.2.2. We extracted each unique lithologic descriptor in an Excel sheet (“weathering”).

8.2.3. For igneous rocks:

8.2.3.1. We estimated the abundance of common minerals, including quartz, biotite, alkali feldspars, plagioclases, feldspathoids, hornblende, olivine, pyroxenes, dolomite and calcite, from the IUGS classification (Le Bas and Streckeisen, 1991; Table 2S.4).

8.2.3.2. For each of these minerals, we obtained the specific mineral

weathering rates measured in laboratory by Franke (2009) at pH=5.5 and T=20°C (Table 2S.5).

- 8.2.3.3. We calculated the laboratory-based bulk rock dissolution rates using equation 5 and results from step 8.2.3-4.
- 8.2.3.4. We assigned a corrective factor R grouping igneous rocks into three broad categories chosen to account for differences in permeability, and thus reactivity with aqueous solutions, and comparing our calculated values of W_{norm} for each category with dissolution rate measurements in small monolithic catchments in France (Meybeck, 1986, Meybeck, 1987, Amiotte Suchet and Probst, 1993). The assigned values ($R = 3$ for volcanic rocks, $R = 2$ for metavolcanic and $R = 1$ for crystalline igneous rocks) offer a rough approximation of relative field weathering rates useful for our initial large-scale effort, and can be refined in future work.
- 8.2.4. For sedimentary and metamorphic rocks because mineralogy is difficult to estimate, we distinguished between metamorphic and nonargillaceous silicate sedimentary rocks, with low weathering rates similar to those of granite (assigned $W_{norm} = 1$) and faster-weathering argillaceous sedimentary rocks ($W_{norm} = 2$) based on denudation rate measurements from small monolithic catchments (Meybeck, 1986, Meybeck, 1987, Amiotte Suchet and Probst, 1993).
- 8.2.5. For pyroclastic rocks because no monolithic catchment dissolution rates measurements were available, we estimated W_{norm} from long term dissolution measurements of tuff tablets relative to those of granodiorite tablets exposed to the same conditions (Matsukura et al., 2007).
- 8.2.6. Resulting relative weathering rates are given in Table 2S.4.
- 8.2.7. We joined Table 2S.4 to the geodatabase using lithologic descriptor as a joining field.

Rationale: discussion concerning weathering model limitations and assumptions are available in Material and Methods of Chapter II

9. Mapping $^{87}\text{Sr}/^{86}\text{Sr}$ for the local water model (using ArcGIS):

- 9.1. For each geological unit, we applied equation 5 to calculate the Sr isotope ratio of Sr weathering to water from that unit, $(^{87}\text{Sr}/^{86}\text{Sr})_{local}$, using previously calculated values of Sr_ratio1 and Sr_ratio2, *Sr content* and W .

9.2. We imported the attribute table with the newly calculated field into ArcGIS.

10. Mapping $^{87}\text{Sr}/^{86}\text{Sr}$ for the catchment water model (using ArcGIS):

10.1. In new fields of the attribute table of the geodatabase:

10.1.1. We calculated $W * Sr\ content$, and

10.1.2. We calculated $W * Sr\ content * (^{87}\text{Sr}/^{86}\text{Sr})_{local}$.

10.2. In ArcGIS, we converted (Conversion toolbox) the field “ $W * Sr\ content$ ” and “ $W * Sr\ content * (^{87}\text{Sr}/^{86}\text{Sr})_{local}$ ” into raster layers.

10.3. We processed the digital elevation model (DEM; <http://edc.usgs.gov/products/elevation/gtopo30/hydro/namerica.html>) by:

10.3.1. Filling the DEM (Spatial Analyst toolbox)

10.3.2. Calculating the Flow direction raster (Spatial Analyst toolbox)

10.4. We used the flow accumulation tool (Spatial Analyst toolbox) with the flow direction raster as input and $W * Sr\ content$ as “Input weight raster” to obtain the Sr flux raster.

10.5. We used the flow accumulation tool (Spatial Analyst toolbox) with flow direction raster as input and $W * Sr\ content * (^{87}\text{Sr}/^{86}\text{Sr})_{local}$ as “Input weight raster” to obtain the modeled local water Sr isotope flux raster.

10.6. We calculated the catchment water $(^{87}\text{Sr}/^{86}\text{Sr})_{catchment}$ at each grid cell by dividing the modeled water Sr isotope flux raster by the Sr flux raster using the raster calculator (Spatial Analyst toolbox).

Table 2S.1 Values of $(Rb/Sr)_{parent}$ and $(Rb/Sr)_{lithology}$ used in equations 2 and 3 for each unique lithologic descriptor (rocktype1 and rocktype2) present in the USGS geodatabases (U.S. Geological Survey, 2005, State Geologic Map Compilation, online at <http://tin.er.usgs.gov/geology/state/>). Entries represent a comprehensive list of all lithological descriptors: entries that appear redundant appear in slightly different forms within the database.

ROCKTYPE	$(Rb/Sr)_{parent}$	$(Rb/Sr)_{lithology}$
alkali rhyolite	0.18	1.07
alkali syenite	0.13	1.04
alkalic intrusive rock	0.13	0.8
alkalic volcanic rock	0.13	0.8
alkali-granite (alaskite)	0.18	3.2
alkaline basalt	0.07	0.06
alluvial fan	0.24	0.5
alluvial terrace	0.24	0.5
Alluvium	0.24	0.5
amphibole schist	0.13	0.15
Amphibolites	0.13	0.18
Andesite	0.07	0.16
Anorthosite	0.05	0.04
Aplite	0.18	1.81
Arenite	0.24	0.93
Argillite	0.24	0.88
Arkose	0.24	0.68
ash-flow tuff	0.18	2.51
augen gneiss	0.18	0.75
Basalt	0.07	0.07
beach sand	0.24	0.5
Bentonite	0.24	0.75
bimodal suite	0.07	0.5
biogenic sediment	0.24	0.5
biotite gneiss	0.18	1.1
black shale	0.24	2.23
Blueschist	0.07	0.2
Breccias	0.18	0.7
Calcarenite		0.03
calc-silicate rock		0.2
calc-silicate schist		0.2
Carbonate		0.03
Cataclasite	0.09	0.37
Charnockite	0.07	0.08

Table 2S.1 continued

Chemical	0.24	0.7
Chert	0.24	0.46
Clastic	0.18	0.5
clay or mud	24	0.74
Claystone	0.24	0.89
Coal	0.24	0.5
coarse-grained mixed clastic	0.18	0.5
Colluviums	0.24	0.5
Conglomerate	0.24	0.76
Dacite	0.13	0.41
Delta	0.24	0.5
Diabase	0.05	0.11
Diorite	0.09	0.32
dolostone (dolomite)		0.37
dune sand	0.24	0.4
Dunite	0.05	0.13
Eolian	0.24	0.4
Evaporate		0.03
felsic gneiss	0.18	0.86
felsic metavolcanic rock	0.18	1
felsic volcanic rock	0.18	1
fine-grained mixed clastic	0.18	0.5
flaser gneiss	0.18	0.75
flood plain	0.24	0.5
Gabbro	0.07	0.08
Gabbroid	0.07	0.08
glacial drift	0.24	0.5
Glaciolacustrine	0.24	0.5
Gneiss	0.18	0.79
Granite	0.18	1.5
granitic gneiss	0.18	1.2
Granitoid	0.18	1.5
Granodiorite	0.13	0.48
Granofels	0.09	0.32
Granulite	0.05	0.08
Gravel	0.24	0.49
Greywacke	0.24	0.45
Greenschist	0.07	0.18
Greenstone	0.07	0.14
Hornblendite	0.07	0.1

Table 2S.1 continued

Hornfels	0.13	0.54
Ice		
Ignimbrite	0.24	3.1
Indeterminate	0.09	0.5
intermediate metavolcanic rock	0.09	0.35
intermediate volcanic rock	0.09	0.35
intrusive carbonatite		0.03
iron formation	0.24	0.5
Lahar	0.13	0.5
lake or marine deposit (non-glacial)		0.2
Lamprophyre	0.07	0.46
Landslide	0.24	0.5
Latite	0.13	0.47
lava flow	0.07	0.1
Limestone		0.2
Loess		0.37
mafic gneiss	0.07	0.35
mafic metavolcanic rock	0.07	0.35
mafic volcanic rock	0.07	0.35
Marble		0.12
mass wasting	0.24	0.5
medium-grained mixed clastic	0.18	0.5
Mélange	0.24	0.7
meta-argillite	0.24	0.81
meta-basalt	0.07	0.13
meta-conglomerate	0.24	0.62
metamorphic rock	0.09	0.44
meta-rhyolite	0.18	2.3
metasedimentary rock	0.24	0.91
metavolcanic rock	0.09	0.4
mica schist	0.18	1.1
Migmatite	0.07	0.49
mixed clastic/carbonate		0.2
mixed clastic/volcanic	0.13	0.5
Monzodiorite	0.09	0.3
Monzogranite	0.18	1.71
Monzonite	0.09	0.28
Moraine	0.24	0.5
mud flat	0.24	0.72
Mudstone	0.24	0.8

Table 2S.1 continued

Mylonite	0.09	0.35
nepheline syenite	0.13	0.67
Norite	0.05	0.04
Novaculite	0.24	0.46
oil shale	0.24	0.34
Orthogneiss	0.13	1.34
Orthoquartzite	0.13	0.59
Outwash	0.24	0.5
Paragneiss	0.24	1.1
Peat	0.24	0.5
Pegmatite	0.24	1.42
pelitic schist	0.24	1.18
peraluminous granite	0.18	1.23
Peridotite	0.05	0.11
Phonolite	0.13	0.7
Phosphorite		0.2
Phyllite	0.24	2.1
Phyllonite	0.24	2.1
Playa	0.24	0.5
plutonic rock (phaneritic)	0.18	0.7
Porphyry	0.09	0.4
Pumice	0.13	0.7
Pyroclastic	0.18	1.11
Pyroxenite	0.09	0.28
quartz diorite	0.09	0.32
quartz latite	0.09	0.47
quartz monzodiorite	0.09	0.35
quartz monzonite	0.09	0.29
quartz syenite	0.13	1.2
quartz-feldspar schist	0.18	0.94
Quartzite	0.13	0.81
Residuum	0.24	0.5
Rhyodacite	0.13	0.74
Rhyolite	0.18	2.3
Sand	0.24	0.59
Sandstone	0.24	0.69
Schist	0.18	0.96
sedimentary breccias	0.24	0.81
sedimentary rock	0.24	0.5
Serpentinite	0.05	0.18

Table 2S.1 continued

Shale	0.24	2.1
Silt	0.24	0.83
Siltstone	0.24	0.91
skarn (tactite)	0.09	0.36
Slate	0.18	1.2
stratified glacial sediment	0.24	0.5
Syenite	0.13	0.77
Talus	0.24	0.5
tectonic breccias	0.18	0.81
Tectonite	0.18	0.81
tephrite (basanite)	0.09	0.25
Terrace	0.24	0.5
Tholeiite	0.07	0.07
Till	0.24	0.5
Tonalite	0.09	0.25
Trachy andesite	0.09	0.29
Trachy basalt	0.09	0.13
Trachyte	0.13	1.04
Troctolite	0.05	0.06
Trondhjemite	0.09	0.19
Tuff	0.18	2.01
ultramafic intrusive rock	0.05	0.08
ultramafic rock	0.05	0.08
unconsolidated deposit	0.24	0.5
volcanic ash	0.18	0.91
volcanic breccia (agglomerate)	0.09	0.38
volcanic rock	0.09	0.45
volcanic rock (aphanitic)	0.09	0.45
Wacke	0.18	0.43
Water		
welded tuff	0.18	2.01

Table 2S.2 Assigned numerical age for each unique age descriptor present in the composite geodatabase. Entries represent a comprehensive list of all lithological descriptors

UNIT_AGE	TIME (Ma)
Holocene	0.1
Quaternary; Holocene	0.1
Quaternary-Holocene Series	0.1
Late Pleistoce to Holocene	1
Late Pleistocene	1
Late Pleistocene to Holocene	1
Quaternary (0-1 Ma)	1
Middle (?) Pleistocene	1.8
Middle (?) Pleistocene to Recent	1.8
Middle Pleistocene	1.8
Middle Pleistocene; Irvingtonian	1.8
Middle Pleistocene; Irvingtonian	1.8
Middle to Late Pleistocene	1.8
Quaternary; Late Pleistocene	1.8
Quaternary; Middle Pleistocene	1.8
Calabrian	2.1
Quaternary (1.5-2.5 Ma)	2.5
Early (?) Pleistocene	2.6
Early Pleistocene	2.6
Holocene to Pleistocene	2.6
Late Pleistocene to Early Pleistocene	2.6
Mostly Pleistocene	2.6
Pleistocene	2.6
Pleistocene and Holocene	2.6
Pleistocene to Holocene	2.6
Pleistocene/Holocene	2.6
Pleistocene; Early Wisconsinan	2.6
Pleistocene; Wisconsinan	2.6
Pleistocene-Holocene	2.6
Pleistocene-Illinoian ?	2.6
Pleistocene-Illinoian ? And Pre-Illinoian	2.6
Pleistocene-Illinoian ? and Pre-Illinoian	2.6
Pleistocene-Pre-Illinoian	2.6
Pleistocene-Upper Wisconsin	2.6
Quaternary	2.6
Quaternary; Pleistocene and Holocene?	2.6
Early Pleistocene and Late Pliocene	3

Table 2S.2 continued

Early Pleistocene and Late Pliocene	3
Late Pliocene to Early Pleistocene	3
Late-Pliocene	3
Tertiary (2.5-3.5 Ma)	3.5
Middle Pliocene to Holocene	3.6
Quaternary (0-4 Ma)	4
Tertiary (3-4 Ma)	4
Holocene to Pliocene	5.3
Pleistocene and Pliocene	5.3
Pleistocene to Pliocene	5.3
Pliocene to Early Pleistocene	5.3
Pliocene to Holocene	5.3
Pliocene to Pleistocene	5.3
Pliocene to Quaternary	5.3
Pliocene/Pleistocene	5.3
Pliocene-Pleistocene	5.3
Quaternary to Pliocene	5.3
upper Pliocene	5.3
Early-Pliocene	5.332
Pleistocene-Pliocene	5.332
Pliocene	5.332
Tertiary (3-7 Ma)	7
Tertiary (7.5-9.5 Ma)	9.5
Tortonian	10.2
Late Miocene	11.6
Late Miocene to Early Pliocene	11.6
Late Miocene to Pleistocene	11.6
Late Miocene to Pliocene	11.6
Late-Miocene	11.6
Upper Miocene	11.6
Tertiary (8-12 Ma)	12
Tertiary (9.5-13 Ma)	13
Serravallian	13.65
Tertiary (12-15 Ma)	15
Langhian	16
Late Miocene to Middle Miocene	16
Middle Miocene	16
Middle Miocene to Late Miocene	16
Middle Miocene to Late Miocene	16
Middle Miocene to Late Pliocene	16

Table 2S.2 continued

Middle Miocene to Pliocene	16
Middle Miocene, Serravallian	16
middle Miocene, Serravallian	16
Middle Miocene, Serravallian	16
Middle to Late Miocene	16
middle to late Miocene	16
Middle-Miocene	16
Tertiary (14-16 Ma)	16
Tertiary (14-18 Ma)	18
Tertiary (16-18 Ma)	18
Tertiary (12-19 Ma)	19
Burdigalian	20,43
Tertiary (4-22 Ma)	22
Early Miocene	23
early Miocene	23
Early Miocene to Early Pliocene	23
Early Miocene to Middle Miocene	23
Early Pleistocene to Miocene	23
Early to Middle Miocene	23
Early-Miocene	23
Lower Miocene	23
lower Miocene, Aquitanian	23
lower Miocene, Burdigalian	23
middle and lower Miocene, Langhian and Burdigalian	23
Miocene	23
Miocene	23
Miocene to Early Pliocene	23
Miocene to Holocene	23
Miocene to Pleistocene	23
Miocene to Pliocene	23
Miocene to Quaternary	23
Miocene(?) or Pliocene(?)	23
Miocene/Pliocene	23
Miocene-Pleistocene	23
Miocene-Pliocene	23
Neogene	23
Pliocene to Miocene	23
Pliocene-Miocene	23
Tertiary (19-23 Ma)	23
Tertiary-Neogene	23

Table 2S.2 continued

Aquitanian	23.03
Tertiary (22-24 Ma)	24
Tertiary (2-24 Ma)	24
Tertiary (2-24Ma)	24
Tertiary (22-25 Ma)	25
Tertiary (8-25 Ma)	25
Tertiary (8-25 Ma; most near 15)	25
Tertiary (8-28 Ma)	28
Chattian	28.4
Late Oligocene to Early Miocene	28.4
Late Oligocene to Middle Miocene	28.4
Late-Oligocene	28.4
Upper Oligocene-Upper Miocene	28.4
Early Oligocene	33.9
Early Oligocene to Early Miocene	33.9
Early -Oligocene	33.9
Middle to Late Tertiary	33.9
Miocene to Oligocene	33.9
Oligocene	33.9
Oligocene	33.9
Oligocene and Cambrian to Late Proterozoic, mixed	33.9
Oligocene and Early Miocene	33.9
Oligocene to Early Miocene	33.9
Oligocene to Middle Miocene	33.9
Oligocene to Miocene	33.9
Oligocene to Pleistocene	33.9
Oligocene to Pliocene	33.9
Oligocene(?) to Pleistocene(?)	33.9
Oligocene(?) to Pliocene	33.9
Oligocene(?) to Pliocene(?)	33.9
Oligocene/Miocene	33.9
Oligocene-Miocene	33.9
Rupelian	33.9
Late-Eocene	37.2
Priabonian	37.2
Late Eocene	40.4
Late Eocene to Early Miocene	40.4
Late Eocene to Early Oligocene	40.4
Late Eocene to Late Miocene	40.4
Late Eocene to Late Oligocene	40.4

Table 2S.2 continued

Late Eocene to Middle Eocene	40.4
Late Eocene to Middle Miocene	40.4
Late Eocene to Miocene	40.4
Late Eocene to Oligocene	40.4
Late-Middle Eocene	48.6
Middle Eocene	48.6
middle Eocene to Early Miocene	48.6
middle Eocene to early Miocene	48.6
Middle Eocene to Early Oligocene	48.6
Middle Eocene to Early Pliocene	48.6
Middle Eocene to Late Eocene	48.6
middle to late Eocene	48.6
Middle-Eocene	48.6
upper and middle Eocene, Priabonian through Lutetian	48.6
Lutetian	52
Early Eocene	55.8
Early to Middle Eocene	55.8
Early -Eocene	55.8
Eocene	55.8
Eocene (Olympic Pen) and Cretaceous(?) (Yakima Co)	55.8
Eocene to Early Oligocene	55.8
Eocene to Miocene	55.8
Eocene to Oligocene	55.8
Eocene to Pliocene	55.8
Eocene-Oligocene	55.8
Likely Eocene	55.8
lower Eocene, Ypresian	55.8
lower Eocene, Ypresian	55.8
Lower Eocene-Middle Eocene	55.8
Miocene to Eocene	55.8
Mostly Eocene but ranges from Miocene to Paleocene	55.8
Mostly Oligocene-Eocene	55.8
Oligocene and Eocene	55.8
Oligocene to Eocene	55.8
Probably Eocene	55.8
Tertiary but mostly Eocene	55.8
Ypresian	55.8
Late Paleocene to Early Eocene	58.7
Late Paleocene to Early Oligocene	58.7
Late-Paleocene	58.7

Table 2S.2 continued

Selandian	61.7
upper Paleocene, Selandian	61.7
Danian	65.5
Early -Paleocene	65.5
Eocene to Paleocene	65.5
lower Paleocene, Danian	65.5
Paleocene	65.5
Paleocene and Eocene	65.5
Paleocene to Early Eocene	65.5
Paleocene to Early Oligocene	65.5
Paleocene to Eocene	65.5
Paleocene to late Eocene	65.5
Paleocene to Late Miocene	65.5
Paleocene to Middle Eocene	65.5
Paleocene to middle Eocene	65.5
Paleocene to Oligocene	65.5
Paleocene to Pliocene	65.5
Paleocene(?) to Oligocene	65.5
Paleocene-Eocene	65.5
Paleogene, possibly Oligocene	65.5
Quaternary and Tertiary	65.5
Quaternary-Tertiary	65.5
Tertiary	65.5
Tertiary to Quaternary	65.5
Tertiary -Late-Pliocene to Paleocene	65.5
Tertiary -Paleogene	65.5
Tertiary -Quaternary	65.5
Maastrichtian	70.6
Upper Cretaceous, Maastrichtian	70.6
Upper Cretaceous, upper and middle Maastrichtian	70.6
Upper Cretaceous, upper Maastrichtian	70.6
Campanian	83.5
Upper Cretaceous, lower Campanian	83.5
Upper Cretaceous, upper Campanian	83.5
Santonian	85.8
Upper Cretaceous, lower Campanian and upper Santonian	85.8
Upper Cretaceous, middle and lower Santonian	85.8
Coniacian	89.3
Turonian	93.5
Cenomanian	99.6

Table 2S.2 continued

Early Tertiary-Late Cretaceous	99.6
Eocene to Late Cretaceous	99.6
Late Cretaceous	99.6
Late Cretaceous and Paleocene	99.6
Late Cretaceous and possibly Eocene	99.6
Late Cretaceous Paleocene	99.6
Late Cretaceous to Early Eocene	99.6
Late Cretaceous to Early Miocene	99.6
Late Cretaceous to Early Tertiary	99.6
Late Cretaceous to Eocene	99.6
Late Cretaceous to Oligocene	99.6
Late Cretaceous to Paleocene	99.6
Late Cretaceous to Pliocene	99.6
Late Cretaceous(?) to Eocene(?)	99.6
Late Cretaceous(?) to Miocene(?)	99.6
Late Cretaceous; Gulfian Series	99.6
Late Cretaceous-Gulfian	99.6
late Early to early Late Cretaceous	99.6
Late-Cretaceous	99.6
Paleocene to Upper Cretaceous	99.6
Paleocene-Late Cretaceous	99.6
Tertiary-Late Cretaceous	99.6
Upper Cretaceous	99.6
Upper Cretaceous, lower Cenomanian	99.6
Upper Cretaceous, upper and middle Campanian	99.6
Upper Cretaceous, upper Cenomanian	99.6
Upper Cretaceous-Paleocene	99.6
Albian	112
Early Cretaceous; Aptian; Albian Series	112
Early Cretaceous; Comanchean; Albian Series	112
Aptian	125
Berriasian	145.5
Cretaceous	145.5
Cretaceous (?)	145.5
Cretaceous or Eocene	145.5
Cretaceous to Eocene	145.5
Cretaceous(?)	145.5
Cretaceous(?) to Miocene	145.5
Cretaceous(?) to Oligocene(?)	145.5
Cretaceous?	145.5

Table 2S.2 continued

Cretaceous-Tertiary	145.5
Early and Late Cretaceous	145.5
Early and Late Cretaceous; Comanchean Series	145.5
Early Cretaceous	145.5
Early Cretaceous - Late Cretaceous	145.5
Early Cretaceous metamorphism (Jurassic protolith)	145.5
Early Cretaceous; Comanchean Series	145.5
Early Cretaceous; Comanchean Series	145.5
Early Cretaceous; Washita Series	145.5
Early Cretaceous-Late Cretaceous	145.5
Early Cretaceous-Late Jurassic	145.5
Early Late Cretaceous and Late Early Cretaceous	145.5
Early to Late Cretaceous	145.5
Early -Cretaceous	145.5
Eocene to Cretaceous	145.5
Late Cretaceous to Early Cretaceous	145.5
Late Early to Late Cretaceous	145.5
late Early to Late Cretaceous	145.5
Lower Cretaceous	145.5
Lower Cretaceous-Upper Cretaceous	145.5
Lower Tertiary -Cretaceous	145.5
Middle-Lower Cretaceous	145.5
Mostly Cretaceous	145.5
Tertiary and Cretaceous	145.5
Tertiary -Cretaceous	145.5
Tithonian	150.8
Kimmeridgian	155.7
Early Cretaceous to Late Jurassic	161
Late Jurassic	161
Late Jurassic and Early Cretaceous	161
Late Jurassic to Cretaceous	161
Late Jurassic to Early Cretaceous	161
Late Jurassic to Late Cretaceous	161
Late Jurassic to Middle Jurassic	161
Late Jurassic-Early Cretaceous	161
Late-Jurassic	161
Upper Jurassic-Lower Cretaceous	161
Upper Jurassic-Lower Cretaceous	161
Oxfordian	161.2
Callovian	164.7

Table 2S.2 continued

Bathonian	167.7
Early Cret to Middle Jur and minor Eocene	176
Early Cret to Middle Jur and minor Eocene	176
Late Jurassic to Middle Jurassic	176
Middle - Late? Jurassic	176
Middle Jurassic	176
Middle Jurassic to Early Cretaceous	176
Middle Jurassic to Late Cretaceous	176
Middle Jurassic to late Early Cretaceous	176
Middle Jurassic(?) to Late Cretaceous	176
Middle Jurassic?	176
Middle Jurassic-Lower Cretaceous	176
Middle Jurassic-Upper Jurassic	176
Middle to Late Jurassic	176
Middle? Jurassic	176
Middle-Jurassic	176
Pliensbachian	189.6
Sinemurian	196.5
Early-Jurassic	199.6
Hettangian	199.6
Jurassic	199.6
Jurassic - Lower Cretaceous	199.6
Jurassic (?)	199.6
Jurassic - Cretaceous	199.6
Jurassic in center but Oligocene to Eocene in north	199.6
Jurassic to Cretaceous	199.6
Jurassic to early Cretaceous	199.6
Jurassic to Miocene	199.6
Jurassic(?)	199.6
Jurassic(?)	199.6
Jurassic(?) and Triassic(?) to Lower Cretaceous	199.6
Jurassic(?) to Cretaceous(?)	199.6
Jurassic?	199.6
Jurassic-Cretaceous	199.6
Jurassic-Tertiary	199.6
Jur-Cret in San Juan Islands but Eocene in King County?	199.6
Jur-Cret in San Juan Islands but Eocene in King County?	199.6
Cretaceous-Jurassic	201.6
Early - Middle Jurassic	201.6
Early Cretaceous; Jurassic	201.6

Table 2S.2 continued

Early Jurassic	201.6
Early Jurassic – Triassic	201.6
Early Jurassic to Middle Jurassic	201.6
Early Jurassic-Triassic	201.6
Early to Middle Jurassic	201.6
Jurassic to early Cretaceous	201.6
Late Cretaceous-Jurassic	201.6
Lower Jurassic	201.6
Mostly Cretaceous-Jurassic	201.6
probably mainly Jurassic	201.6
Probably mostly Jurassic	201.6
Norian	216.5
Camian	228
Late Triassic	235
Late Triassic to Early Cretaceous	235
Late Triassic to Early Jurassic	235
Late Triassic? To Jurassic	235
Late Triassic? to Jurassic	235
Late-Triassic	235
Lower Jurassic and Upper Triassic	235
Upper Triassic	235
Upper Triassic; possibly Lower Jurassic at top	235
Upper Triassic; possibly Lower Jurassic at top plus Middle?	235
Middle to Late Triassic	245
Middle Triassic to Early Jurassic	245
Middle-Triassic	245
Cretaceous-Triassic	251
Early Middle (?) Triassic	251
Early to Middle Triassic	251
Early Triassic	251
Early Triassic to Middle Triassic	251
Early-Triassic	251
Jurassic to Triassic	251
Jurassic(?) and Triassic(?)	251
Jurassic(?) and Triassic(?) to Upper Jurassic	251
Jurassic-Triassic	251
Jurassic-Triassic	251
Late Cretaceous to Early Triassic	251
Lower Cretaceous-Triassic	251
Lower Triassic to Jurassic(?) and Triassic(?)	251

Table 2S.2 continued

Lower Triassic-Upper Jurassic	251
Lower Triassic-Upper Triassic	251
Mesozoic	251
Middle and Early Triassic	251
Triassic	251
Triassic and (or) Jurassic	251
Triassic and Jurassic	251
Triassic to Cretaceous	251
Triassic to Jurassic	251
Triassic to Late Jurassic	251
Triassic(?)	251
Triassic(?) and/or Jurassic(?)	251
Triassic?	251
Late Permian	260
Late Permian – Cimarronian	260
Late Permian- Custerian to Cimarronian	260
Late Permian- Custerian to Cimarronian	260
Late Permian- custerian to Cimarronian	260
Late Permian to Early Permian	260
Late Permian(?) to Early Jurassic	260
Late Permian(?) to Jurassic	260
Lopingian	260.4
Cisuralian	299
Cretaceous to Permian	299
Early Permian	299
Early Permian – Gearyan	299
early Permian Gearyan	299
Early Permian Gearyan	299
Early Permian to Early Triassic	299
Early to Late Permian	299
Lower Permian	299
Permian	299
Permian to Early Triassic	299
Permian to Jurassic	299
Permian to Jurassic (?)	299
Permian to Tertiary; most Mesozoic	299
Permian to Triassic	299
Permian(?) to Jurassic(?)	299
Permian; Guadalupe Series	299
Permian; Leonard and Guadalupe Series	299

Table 2S.2 continued

Permian; Leonard Series	299
Permian; Ochoa Series	299
Permian; Wolfcamp and Leonard Series	299
Permian; Wolfcamp Series	299
Permian; Wolfcamp to Leonard Series	299
Permian-Lower Triassic	299
Permian-Triassic	299
Permian-Upper Triassic	299
Probably Permian	299
Triassic to Permian	299
Triassic with some Permian	299
Triassic-Permian	299
Late Pennsylvanian	306
Late Pennsylvanian-Des Moinesian	306
Late Pennsylvanian-Missouri Series	306
Late Pennsylvanian-Missouria	306
Late Pennsylvanian-Missourian	306
Late Pennsylvanian-Missourian	306
Late Pennsylvanian-Missourian	306
Late Pennsylvanian-Missourian	306
Late Pennsylvanian-Virgilian	306
Late Pennsylvanian; Missouri Series	306
Late Pennsylvanian; Virgil Series	306
Late Pennsylvanian-Missouri Series	306
Late Pennsylvanian-Upper Series-Missourian Stage	306
Late Pennsylvanian-Upper Series-Virgilian Stage	306
Late Pennsylvanian-Virgil Series	306
Upper Pennsylvanian	306
Moscovian	311.7
Middle Pennsylvanian	312
Middle Pennsylvanian	312
Middle Pennsylvanian-Atokan	312
Middle Pennsylvanian-Des Moinesian	312
Middle Pennsylvanian-Desmoinesian	312
Middle Pennsylvanian-Missourian	312
Middle Pennsylvanian-Morrowan	312
Middle Pennsylvanian to Early Pennsylvanian	312
Middle Pennsylvanian; Atoka and Des Moines Series	312
Middle Pennsylvanian; Atoka Series	312
Middle Pennsylvanian-Atokan Stage	312
Middle Pennsylvanian-Des moines Series	312

Table 2S.2 continued

Middle Pennsylvanian-Des Moines Series	312
Middle Pennsylvanian-Middle Series-Desmonian Stage	312
Middle to Upper Pennsylvanian	312
Pennsylvanian; Middle and Late	312
Upper and Middle Pennsylvanian	312
Upper and Middle Pennsylvanian-Permian	312
Early Pennsylvanian	318
Early Pennsylvanian – Desmoinesian	318
Early Pennsylvanian – Morrowan	318
Early Pennsylvanian and Late Mississippian	318
Early Pennsylvanian-Desmoinesian	318
Early Pennsylvanian-Desmonesian	318
Early Pennsylvanian-Morrowan	318
Early Permian to Early Pennsylvanian	318
Early; Middle; and Late Pennsylvanian	318
Lower Pennsylvanian	318
Lower Pennsylvanian-Permian	318
Lower to Middle Pennsylvanian	318
Mesozoic-Pennsylvanian	318
Middle and Lower Pennsylvanian	318
Pennsylvanian-Desmoinesian	318
Pennsylvanian to Early Permian	318
Pennsylvanian to Late Permian	318
Pennsylvanian to Permian	318
Pennsylvanian to Permian?	318
Pennsylvanian to Triassic	318
Pennsylvanian; Des Moines Series	318
Pennsylvanian; Missouri Series	318
Pennsylvanian; Morrow Series	318
Pennsylvanian; Virgil Series	318
Permian and Pennsylvanian	318
Permian and Pennsylvanian	318
Permian and/or Pennsylvanian	318
Permian to Pennsylvanian	318
Permian/Pennsylvanian	318
Permian-Pennsylvanian	318
Triassic-Pennsylvanian	318
Bashkirian	318.1
Pennsylvanian	318.1
Late Mississippian	326

Table 2S.2 continued

Late Mississippian-Chesteran Series	326
Late Mississippian- Chesterian	326
Late Mississippian- Chesterian Series	326
Late Mississippian- Meramecian	326
Late Mississippian; Chesteran; and Devonian	326
Late Mississippian-Chesteran Series	326
Late Mississippian-Chesterian	326
Late Mississippian-Chesterian Series	326
Late Mississippian-Meramecian Series	326
Late-Mississippian	326
Upper Mississippian	326
Upper Mississippian-Lower Cretaceous	326
Upper Mississippian-Permian	326
Serpukhovian	326.4
Visean	345.3
Carboniferous	359
Carboniferous to Permian	359
Carboniferous-Pennsylvanian	359
Early Mississippian	359
Early Mississippian - Kinderhookian Series	359
Early Mississippian - Meramecian to Osagean	359
Early Mississippian - Osagean Series	359
Early Mississippian Kinderhookian Series	359
Early Mississippian- Meramecian to Osagean	359
Early Mississippian-Kinderhookian Series	359
Early Mississippian-Osagean Series	359
Early Mississippian-Oseagean Series	359
Jurassic to Mississippian	359
Late Cretaceous to Mississippian	359
Late Paleozoic	359
Late Paleozoic dep? With Cretaceous metamorphism?	359
Late Paleozoic dep? with Cretaceous metamorphism?	359
Lower Mississippian	359
Lower Mississippian-Upper Mississippian	359
Mississippian	359
Mississippian – Pennsylvanian	359
Mississippian- Osagian	359
Mississippian to Early Permian	359
Mississippian to Pennsylvanian	359
Mississippian to Permian	359

Table 2S.2 continued

Mississippian to Triassic	359
Pennsylvanian – Mississippian	359
Pennsylvanian and Mississippian	359
Pennsylvanian-Mississippian	359
Pennsylvanian-Mississippian	359
Triassic to Mississippian	359
Mississippian	359.2
Tournaisian	359.2
Famennian	374.5
Early Mississippian to Late Devonian	385
Early Mississippian to Late Devonian	385
Late Devonian	385
Late Devonian to Early Permian	385
Late Devonian to Early Triassic	385
Late Devonian to Mississippian	385
Late Devonian	385
Upper Devonian	385
Upper Devonian	385
Upper Devonian-Lower Mississippian	385
Upper Devonian-Upper Mississippian	385
Late-Devonian	385.3
Frasnian	385.6
Givetian	391.8
Eifelian	397.5
Middle - Upper Devonian	398
Middle Devonian	398
Middle Devonian	398
Middle to Late Devonian	398
Middle-Devonian	398
Emsian	407
Pragian	411.2
Carboniferous and/or Devonian	416
Devonian	416
Devonian – Mississippian	416
Devonian and Permian	416
Devonian and/or Mississippian	416
Devonian to Jurassic	416
Devonian to Jurassic	416
Devonian to Late Jurassic	416
Devonian to Mississippian	416

Table 2S.2 continued

Devonian to Pennsylvanian	416
Devonian to Permian	416
Devonian to Permian but Triassic in Asotin Co	416
Devonian to Permian but Triassic in Asotin Co	416
Devonian to Permian with minor Mesozoic	416
Devonian to Permian with some Jurassic	416
Devonian(?)	416
Devonian(?) and Permian	416
Devonian?	416
Devonian? Or Mississippian?	416
Devonian-Cambrian	416
Devonian-Mississippian	416
Devonian-Permian	416
Early - Late Devonian	416
Early Devonian	416
Early Devonian - Late Devonian	416
Early Devonian	416
Early Mississippian to Early Devonian	416
Early-Devonian	416
Late Mississippian; Chesteran; and Devonian	416
Late Mississippian ; Chesteran; and Devonian	416
Late to Early Devonian	416
Late; Middle; and early Mississippian and Devonian	416
Late; Middle; and Early Mississippian and Devonian	416
Lockovian	416
Lower (?) and Middle Devonian	416
Lower Devonian	416
Lower Devonian; Siegenian	416
Lower to Middle Devonian	416
Mississippian and Devonian	416
Mississippian to Devonian	416
Mississippian-Devonian	416
Uncertain, possibly Permian or Devonian	416
Upper or Middle Paleozoic	416
Pridoli	418.7
Ludlow	421.3
Late Silurian	423
Upper Silurian	423
Upper Silurian - (Pridolian and Ludlovian)	423
Upper Silurian?	423

Table 2S.2 continued

Lower Devonian and Upper Silurian	426
Late and Middle Silurian	428
Lower Devonian and Middle Silurian	428
Middle (?) and Upper Silurian	428
Middle Silurian	428
Middle Silurian-Upper Silurian	428
Upper to Middle Silurian (Ludlovian and Wenlockian)	428
Wenlock	428.2
Telychian	436
Aeronian	438
Llandovery	443.7
Devonian – Silurian	444
Devonian and Silurian	444
Devonian or Silurian or both	444
Devonian to Silurian	444
Devonian/Silurian	444
Devonian? - Silurian?	444
Early - Late Silurian	444
Early and Middle Silurian	444
Early and Middle(?) Triassic	444
early Late Silurian	444
Early Mississippian to Early Silurian	444
Early Silurian	444
Late Silurian to Early Silurian	444
Late Silurian- to Early Silurian	444
Lower (?) and Middle Silurian	444
Lower Devonian – Silurian	444
Lower Devonian and Silurian	444
Lower Silurian	444
Lower Silurian (Llandoveryan)	444
Lower Silurian (upper Llandoveryan)	444
Lower Silurian?	444
Lower? - Middle? Silurian	444
Lower?- Middle? Silurian	444
Middle and Lower Silurian	444
Silurian	444
Silurian	444
Silurian to Early Devonian	444
Silurian?	444
Silurian?-Devonian	444

Table 2S.2 continued

Silurian-Devonian	444
Early Devonian to Early Silurian	446
Katian	455.8
Sandbian	460.9
Early Silurian to Late Ordovician	461
Early Silurian? And Late Ordovician	461
Early Silurian? and Late Ordovician	461
Late Ordovician	461
Late Ordovician ?	461
Late Ordovician to Late Silurian	461
Late Ordovician to Middle Ordovician	461
Late Ordovician to Silurian	461
Late Ordovician; Mississippian; and Devonian	461
Late Ordovician-Cincinnatian series	461
Late-Ordovician	461
Lower Silurian and Upper Ordovician	461
Lower Silurian and Upper Ordovician?	461
Lower Silurian or Upper Ordovician	461
Upper Ordovician	461
Upper Ordovician - Lower Silurian	461
Upper Ordovician?	461
Late and Middle Ordovician	470
Middle - Upper Ordovician	472
Middle and Late Ordovician	472
Middle Ordovician	472
Middle Ordovician?	472
Middle Ordovician-Mohawkian Series	472
Middle Ordovician-Upper Devonian	472
Middle Ordovician-Upper Mississippian	472
Middle Ordovician-Upper Ordovician	472
Middle to Lower? Ordovician	472
Middle? Ordovician	472
Middle? Ordovician	472
Middle-Ordovician	472
Silurian to Middle Ordovician	472
Upper and Middle Ordovician	472
Upper? and Middle Ordovician	472
Tremadocian	487
Devonian – Ordovician	488
Devonian in part, probably Ordovician in part	488

Table 2S.2 continued

Devonian to Ordovician	488
Devonian/Ordovician	488
Devonian-Ordovician	488
Devonian-Ordovician	488
Early Ordovician	488
Early Ordovician - Ibexian Series	488
Early Ordovician-Beekmantown Series	488
Early Ordovician-Chazy Series	488
Early Ordovician-Ibexian Series	488
Late Mississippian to Early Ordovician	488
Lower and Middle Devonian	488
Lower Ordovician	488
Lower? Ordovician	488
Middle or Lower Ordovician	488
Middle or Lower Ordovician?	488
Middle Ordovician or older	488
Middle Ordovician to Early Ordovician	488
Middle Ordovician to Upper Cambrian?	488
Mississippi, Devonian, and Ordovician	488
Mississippi, Devonian, and Ordovician	488
Mississippian to Ordovician	488
Mississippian-Ordovician	488
Ordovician (?)	488
Ordovician to Devonian	488
Ordovician to Early Devonian	488
Ordovician to Jurassic	488
Ordovician to Silurian	488
Ordovician to Triassic	488
Ordovician(?) to Devonian(?)	488
Ordovician(?) to Permian(?)	488
Ordovician(?) to Triassic(?)	488
Ordovician?	488
Ordovician? - Silurian?	488
Ordovician-Devonian	488
Ordovician-Silurian	488
Paleozoic (Ordovician?)	488
Silurian – Ordovician	488
Silurian and Ordovician	488
Silurian or Ordovician	488
Silurian or Ordovician or both	488

Table 2S.2 continued

Silurian to Ordovician	488
Silurian/Ordovician	488
Early -Ordovician	488.3
Ordovician	488.3
Tremadocian	488.3
Early Ordovician to Late Cambrian	501
Early Paleozoic - Late Precambrian (?)	501
Furongian	501
Late Cambrian	501
Late Cambrian(?) to Early Permian	501
Late Cambrian(?) to Early Permian(?)	501
Late Cambrian? To Early Ordovician	501
Late Cambrian? to Early Ordovician	501
Late Cambrian-Croixian Series	501
lower Middle Ordovician to Upper Cambrian	501
Lower Ordovician and Upper Cambrian	501
Ordovician to Late Cambrian	501
Upper Cambrian	501
Upper Cambrian to Lower Ordovician	501
Upper Cambrian?	501
Upper Cambrian? - Lower Ordovician?	501
Late Cambrian to Middle Cambrian	521
Middle Cambrian to Early Ordovician	521
Middle Cambrian to Late Cambrian	521
Middle Cambrian to Ordovician	521
Middle Cambrian-Upper Cambrian	521
Middle Cambrian-Upper Ordovician	521
Middle-Cambrian	521
Ordovician to Middle Cambrian	521
Upper and Middle? Cambrian	521
Cambrian	542
Cambrian - Lower Ordovician	542
Cambrian - Middle Ordovician	542
Cambrian – Ordovician	542
Cambrian ?	542
Cambrian and Ordovician	542
Cambrian Ordovician	542
Cambrian to Devonian	542
Cambrian to Jurassic	542
Cambrian, Devonian, and Mississippi	542

Table 2S.2 continued

Cambrian, Devonian, and Mississippi	542
Cambrian?	542
Cambrian? - Orovician?	542
Cambrian?-Ordovician?	542
Cambrian-Ordovician	542
Cambrian-Permian	542
Cambrian-Precambrian boundary	542
Cambro-Ordovician	542
Cambro-Ordovician? to Carboniferous	542
Cambro-Ordovician? to Carboniferous?	542
Devonian – Cambrian	542
Early Cambrian	542
Early Cambrian - Lower Ordovician	542
Early Cambrian - Middle Ordovician	542
Early Cambrian to Middle Cambrian	542
Early Cambrian-Middle Ordovician	542
Early Paleozoic	542
Early Paleozoic (?)	542
Early Paleozoic and Late Mississippian	542
Early Paleozoic(?)	542
Early to Middle Cambrian	542
Early-Cambrian	542
Lower Cambrian	542
Lower Cambrian and perhaps partly older	542
Lower Cambrian and perhaps partly older	542
Lower Devonian or younger	542
Lower Ordovician and Cambrian	542
Lower Ordovician or Cambrian or both	542
Middle and Lower Cambrian	542
Middle Cambrian	542
Middle Cambrian to Devonian	542
Mississippian-Cambrian	542
Mississippian to Cambrian	542
Mississippian-Cambrian	542
Ordovician – Cambrian	542
Ordovician and Cambrian	542
Ordovician to Cambrian	542
Ordovician/Cambrian	542
Ordovician-Cambrian	542
Paleozoic	542

Table 2S.2 continued

Paleozoic	542
Paleozoic (?)	542
Paleozoic or Mesozoic	542
Paleozoic sedimentary rocks with Mesozoic intrusive rocks	542
Paleozoic to Jurassic(?)	542
Paleozoic to Mesozoic	542
Paleozoic to Triassic	542
Paleozoic(?) to Jurassic	542
Paleozoic(?) to Jurassic(?)	542
Paleozoic(?) to Late Jurassic	542
Paleozoic(?) to Mesozoic(?)	542
Paleozoic(?), Triassic(?), and Jurassic	542
Phanerozoic	542
Probably lower Paleozoic	542
Silurian to Cambrian	542
Ediacarian	629
Cryogenian	821
Cambrian and Late Proterozoic	1000
Cambrian and/or Neoproterozoic	1000
Cambrian or Neoproterozoic	1000
Cambrian to Late Proterozoic	1000
Cambrian to Neoproterozoic	1000
Cambrian/Late Proterozoic	1000
Cambrian/Precambrian	1000
Devonian - Precambrian Z	1000
Early Paleozoic – Neoproterozoic	1000
Early Paleozoic-Neoproterozoic	1000
Late Precambrian	1000
Late Precambrian – Cambrian	1000
Late Precambrian (?)	1000
Late Precambrian (?) - Early Paleozoic	1000
Late Proterozoic	1000
Late Proterozoic to Early Cambrian	1000
Late Proterozoic to Jurassic	1000
Late Proterozoic to Middle Devonian	1000
Late Proterozoic to Pennsylvanian	1000
Late Proterozoic(?) or older?	1000
Late Proterozoic(?) to Early Jurassic	1000
Late Proterozoic(?) to Mesozoic(?)	1000
Late Proterozoic(?) to Paleozoic(?)	1000

Table 2S.2 continued

Late Proterozoic? or older?	1000
Late Proterozoic? To Devonian?	1000
Late Proterozoic? to Devonian?	1000
Late-Proterozoic	1000
Lower Cambrian and (or) Late Proterozoic	1000
Lower Cambrian and Late Proterozoic	1000
Lower Cambrian and Proterozoic Z	1000
Lower Devonian, Silurian, or Proterozoic Z	1000
Lower Ordovician and Proterozoic Z	1000
Middle Paleozoic to Neoproterozoic	1000
Neoproterozoic	1000
Neoproterozoic	1000
Ordovician - Precambrian Z	1000
Ordovician and Proterozoic Z	1000
Ordovician or older	1000
Ordovician or Proterozoic Z	1000
Ordovician to Neoproterozoic	1000
Ordovician to Proterozoic Z	1000
Ordovician, Cambrian, or Proterozoic Z	1000
Ordovician? - Late Proterozoic?	1000
Paleozoic or Neoproterozoic	1000
Paleozoic to Neoproterozoic	1000
Paleozoic/Late Proterozoic	1000
Pennsylvanian? Or Late Proterozoic?	1000
Pennsylvanian? or Late Proterozoic?	1000
Precambrian Z	1000
Proterozoic Z	1000
Proterozoic Z or Cambrian or both	1000
Proterozoic Z or younger	1000
Proterozoic Z to earliest Paleozoic	1000
Proterozoic Z?	1000
Proterozoic Z? and Permian	1000
Proterozoic Z-Cambrian	1000
Proterozoic Z-Ordovician	1000
Proterozoic Z-Ordovician	1000
Proterozoic Z-Pennsylvanian	1000
Silurian - Precambrian Z	1000
Silurian?, Ordovician, or Proterozoic Z	1000
Tertiary to Late Proterozoic	1000
Tonian	1000

Table 2S.2 continued

Stenian	1200
preCambrian (Proterozoic); Grenville Series	1300
Ectasian	1400
preCambrian (Proterozoic); Llano Series	1400
Middle-Proterozoic	1443
Calymmian	1600
Cretaceous to Middle Proterozoic	1600
Early -Middle Proterozoic	1600
Early -Middle-Proterozoic	1600
Eocene and Middle Proterozoic, mixed	1600
Eocene to Middle Proterozoic	1600
Late and Middle Proterozoic, undivided	1600
Late Middle Proterozoic	1600
Late to middle Proterozoic	1600
late to middle Proterozoic	1600
Late to Middle Proterozoic	1600
Mesoproterozoic	1600
Middle Middle Proterozoic	1600
Middle Proterozoic	1600
Middle Proterozoic(?)	1600
Middle to Late Proterozoic	1600
Middle/Late Proterozoic	1600
Middle-Proterozoic	1600
Ordovician to Middle Proterozoic	1600
Precambrian - Middle Proterozoic	1600
Precambrian Y	1600
Proterozoic Y	1600
Proterozoic Y to Proterozoic Z	1600
Proterozoic Y-Pennsylvanian	1600
Statherian	1760.1
Orosirian	2050
Middle-Early -Proterozoic	2100
Rhyacian	2300
Cretaceous to Early Proterozoic	2500
Early Middle Proterozoic	2500
Early Middle Proterozoic to Early Proterozoic	2500
Early Proterozoic	2500
Early Proterozoic	2500
Early Proterozoic to Cretaceous	2500
Early Proterozoic to Late Cretaceous	2500

Table 2S.2 continued

Early Proterozoic to Mesozoic	2500
Early Proterozoic to Miocene	2500
Early Proterozoic to Tertiary	2500
Early Proterozoic	2500
Late to Early Proterozoic	2500
Late-Archean	2500
Lower Proterozoic	2500
Middle and Lower Proterozoic	2500
Middle Proterozoic to Early Proterozoic	2500
Middle Proterozoic to Early Proterozoic	2500
Paleoproterozoic	2500
preCambrian (Proterozoic)	2500
preCambrian-Proterozoic	2500
Proterozoic	2500
Proterozoic – Cambrian	2500
Proterozoic - Paleozoic ?	2500
Proterozoic W	2500
Proterozoic X	2500
Proterozoic Y; may contain some older rocks	2500
Proterozoic; Late Cretaceous; Tertiary	2500
Siderian	2500
Early Proterozoic to Late Archean	2800
Early Proterozoic to Late Archean ?	2800
Late Archean	2800
Late Archean – Tertiary	2800
Neoarchean	2800
Mesoarchean	2850
Archean to Early Proterozoic	3000
Precambrian	3000
preCambrian	3000
Precambrian to Paleozoic	3000
precambrian to Paleozoic	3000
Precambrian to Phanerozoic	3000
Precambrian to Silurian	3000
precambrian?	3000
Precambrian?-Cambrian?	3000
precambrian?-Cambrian?	3000
Precambrian-Paleozoic	3000
Tertiary – Archean	3000
Middle Archean-Late Archaen	3200

Table 2S.2 continued

Middle Archean-Late Archean	3200
Paleoarchean	3600
Archean	3850
Early Archean	3850
Middle to Early Archean	3850
?	
Age not given	
age uncertain	
Undetermined	
Unknown	
Unknown	
Silurian and perhaps Ordovician	488
Early Permian Gearyan	299
Lower Devonian and Middle Ordovician	472
Miocene-Oligocene	23
Mississippian Pennsylvanian	359
Proterozoic-Paleozoic	2500
Devonian? or Mississippian?	416

Table 2S.3 Estimated values of $(^{87}\text{Sr}/^{86}\text{Sr})_{\text{seawater}}$ throughout Earth history as used in equation 3.

TIME (Ma)	$(^{87}\text{Sr}/^{86}\text{Sr})_{\text{seawater}}$
0.1	0.709
1	0.709
1.8	0.7089
2.1	0.7089
2.5	0.7089
2.6	0.7089
3	0.7089
3.5	0.7088
3.6	0.7088
4	0.7088
5.3	0.7088
5.332	0.7088
7	0.7087
9.5	0.7086
10.2	0.7086
11.6	0.7085
12	0.7085
13	0.7084
13.65	0.7084
15	0.7083
16	0.7083
18	0.7082
19	0.7082
20.43	0.7081
22	0.708
23	0.708
23.03	0.708
24	0.7079
25	0.7079
28	0.7078
28.4	0.7077
33.9	0.7077
37.2	0.7077
40.4	0.7077
48.6	0.7077

Table 2S.3 continued

52	0.7077
55.8	0.7077
58.7	0.7077
61.7	0.7077
65.5	0.7077
70.6	0.7077
83.5	0.7075
85.8	0.7075
89.3	0.7075
93.5	0.7075
99.6	0.7074
112	0.7073
125	0.7072
145.5	0.707
150.8	0.707
155.7	0.7069
161	0.7069
161.2	0.7069
164.7	0.7068
167.7	0.7068
176	0.707
189.6	0.7071
196.5	0.7072
199.6	0.7072
201.6	0.7072
216.5	0.7074
228	0.7075
235	0.7076
245	0.7076
251	0.7077
260	0.7071
260.4	0.707
299	0.7082
306	0.7082
311.7	0.7082
312	0.7082
318	0.7082
318.1	0.7082

Table 2S.3 continued

326	0.708
326.4	0.708
345.3	0.7079
359	0.7079
359.2	0.7079
374.5	0.7079
385	0.7079
385.3	0.7079
385.6	0.7079
391.8	0.7082
397.5	0.7085
398	0.7085
407	0.7087
411.2	0.7085
416	0.7085
418.7	0.7084
421.3	0.7083
423	0.7082
426	0.7081
428	0.7081
428.2	0.7081
436	0.7081
438	0.7081
443.7	0.7081
444	0.7081
446	0.7081
455.8	0.708
460.9	0.708
461	0.708
470	0.7081
472	0.7082
487	0.7085
488	0.7085
488.3	0.7085
501	0.709
521	0.709
542	0.709
629	0.708

Table 2S.3 continued

821	0.7064
1000	0.705
1200	0.705
1300	0.705
1400	0.705
1443	0.705
1600	0.705
1760.1	0.705
2050	0.705
2100	0.705
2300	0.7047
2500	0.7045
2800	0.7042
2850	0.7042
3000	0.704
3200	0.7038
3600	0.7034
3850	0.7032

Table 2S.4 Values of *Sr content* and *W* used in equations 5 and 6 for each unique lithologic descriptor (rocktype1 and rocktype2) present in the composite geodatabase. Q=quartz, B=biotite, A=alkali feldspars, Pl=plagioclase, F=feldspatoids, H=hornblende, O=olivine, Px=pyroxene, D=dolomite, C=calcite.

Rocktype	Q	B	A	Pl	F	H	O	Px	D	C	Krock	R	W_{norm}	<i>Sr</i> ppm
alkali rhyolite	25	10	45	5	5	10					10.6	3	3	48
alkali syenite		10	50		20	10		10			15.1	3	4	248
alkalic intrusive rock	15	10	50	10	5	10					11.7	1	1	200
alkalic volcanic rock	15	10	50	10	5	10					11.7	3	3	200
alkali-granite (alaskite)	25	10	45	5	5	10					10.6	1	1	81
alkaline basalt			15	40		5		40			18.7	3	5	629
alluvial fan													1	200
alluvial terrace													1	200
Alluvium													1	200
amphibole schist	5			35		20		40			27.8	1	3	298
amphibolite	10	10	10	10	10	40		10			34.6	1	3	266
Andesite	10	5	15	60		10					19.5	3	5	387
anorthosite				80			10	10			39.7	1	4	291
Aplite	40	10	20	20		10					11.8	1	1	359
Arenite													1	148
Argillite													1	182
Arkose													1	140
ash-flow tuff													10	188
augen gneiss	35	10	30	15		10					11.1	1	1	169
Basalt	10	5	5	50	10		10	10			36.4	3	10	488
beach sand													1	200
Bentonite													2	250
bimodal suite	5	10	20	40		15		10			20.9	3	6	200
biogenic sediment													1	200
biotite gneiss													1	401
biotite schist													1	401
black shale													2	203
Blueschist	10	5	5	50	10		10	10			36.4	1	3	162
Breccias													1	286
Calcarenite									50	50	450	1	41	500
calc-silicate rock	50									50	300.2	1	27	612
calc-silicate schist	50									50	300.2	1	27	565

Table 2S.4 continued

Carbonate										10 0	600	1	55	712
Cataclasite													1	350
charnockite				50				50			18.5	1	2	315
Chemical													1	300
Chert													1	168
Clastic													1	200
clay or mud													2	205
Claystone													2	211
Coal													1	200
coarse-grained mixed clastic													1	200
Colluviums													1	200
conglomerate													1	201
Dacite	20	10	10	40		10		10			17.2	3	5	381
Delta													1	200
Diabase	10	5	5	60	10			10			16.4	3	4	290
Diorite	10	5	5	50	10			10	10		36.4	1	3	415
dolostone (dolomite)										10 0	300	1	27	530
dune sand													1	200
Dunite							90	10			199.7	1	18	111
Eolian													1	200
Evaporite										10 0	300	1	9	800
felsic gneiss	35	10	30	15		10					11.1	1	1	333
felsic metavolcanic rock	35	10	30	15		10					11.1	2	2	200
felsic volcanic rock	35	10	30	15		10					11.1	3	3	200
fine-grained mixed clastic													1	200
flaser gneiss	35	10	30	15		10					11.1	1	1	199
flood plain													1	200
Gabbro	10	5	5	50	10			10	10		36.4	1	3	437
Gabbroid	10	5	5	50	10			10	10		36.4	1	3	437
glacial drift													1	200
glaciolacustrine													1	200
Gneiss													1	312
Granite	35	10	30	15		10					11.1	1	1	199
granitic gneiss	35	10	30	15		10					11.1	1	1	280
granitoid	35	10	30	15		10					11.1	1	1	199
granodiorite	20	5	15	30	5	5	5	5	5		23.1	1	2	325

Table 2S.4 continued

melange													1	200
meta-argillite													2	164
meta-basalt	10	5	5	50	10		10	10			36.4	2	7	261
meta-conglomerate													1	201
metamorphic rock													1	322
meta-rhyolite	35	10	30	15		10					11.1	2	2	123
metasedimentary rock													1	200
metavolcanic rock													2	300
mica schist													1	149
migmatite													1	334
mixed clastic/carbonate	50									50	300.2	1	27	600
mixed clastic/volcanic													1	250
monzodiorite	20	10	10	40	10		5	5			22.8	1	2	619
monzogranite	40	10	20	20		10					11.8	1	1	185
monzonite	10	10	30	30	10	5		5			13.8	1	1	680
moraine													1	200
mud flat													2	306
mudstone													2	321
mylonite													1	368
nepheline syenite	10	10	40		20	10		10			14.9	3	4	713
norite	10	5	5	50	10		10	10			36.4	1	3	411
novaculite													1	94
oil shale													1	470
olistostrome													2	321
orthogneiss													1	317
orthoquartzite													1	122
outwash													1	200
paragneiss													1	252
peat													1	200
pegmatite	35	10	30	15		10					11.1	1	1	281
pelitic schist													1	152
peraluminous granite	35	10	30	15		10					11.1	1	1	181
peridotite							50	50			118.5	1	11	228
phonolite		10	40	10	10	10	10	10			36.4	3	10	772
phosphorite	50									50	300.2	1	27	730

Table 2S.4 continued

tholeiite				40			20	40			58.8	3	16	265
till													1	200
tonalite	5	10	20	40		10	5	10			28.4	3	8	387
trachyandesite	10	10	30	30		20					20.9	3	6	833
trachybasalt	10	5	15	50	5	10	5	10			31.4	3	9	939
trachyte	10	5	45	15		10	10	5			34.1	3	9	408
troctolite	10	5	5	60	10			10			16.4	1	1	246
trondhjemite	10	5	20	40		10	5	10			28.3	1	3	406
tuff													10	188
ultramafic intrusive rock							50	50			118.5	1	11	200
ultramafic rock							50	50			118.5	1	11	200
ultramafite (komatiite)							50	50			118.5	1	11	44
unconsolidated deposit													1	200
volcanic ash													10	160
volcanic breccia (agglomerate)													3	217
volcanic rock													3	315
volcanic rock (aphanitic)													3	315
wacke													1	336
Water														
welded tuff													10	188

Table 2S.5 Bulk dissolution rates of common minerals in laboratory as found by Franke (2009).

Mineral	K ($\text{mg}\cdot\text{m}^{-2}\cdot\text{d}^{-1}$) 20°C, pH=5.5
Quartz	0.3
Biotite	1.6
Alkali feldspar	2.5
Plagioclase	20
Hornblende	25
Feldspathoid	70
Olivine	220
Pyroxene	17
Dolomite	300
Calcite	600

CHAPTER III

MAPPING MULTIPLE SOURCE EFFECTS ON THE STRONTIUM ISOTOPIC SIGNATURES OF ECOSYSTEMS FROM THE CIRCUM-CARRIBBEAN REGION

Reprinted with permission from Ecosphere. Bataille, C.P., Laffoon, J., Bowen, G.J.,
2012. Mapping multiple source effects on the strontium isotopic signatures of ecosystems
from the circum-Caribbean region. Ecosphere, 3(12): art118.

Mapping multiple source effects on the strontium isotopic signatures of ecosystems from the circum-Caribbean region

CLEMENT P. BATAILLE,^{1,†} JASON LAFFOON,² AND GABRIEL J. BOWEN¹

¹Department of Earth, Atmospheric and Planetary sciences, Purdue University, West Lafayette, Indiana 47907 USA

²Faculty of Archaeology, Leiden University, Leiden 2311HG The Netherlands

Citation: Bataille, C. P., J. Laffoon, and G. J. Bowen. 2012. Mapping multiple source effects on the strontium isotopic signatures of ecosystems from the circum-Caribbean region. *Ecosphere* 3(12):118. <http://dx.doi.org/10.1890/ES12-00155.1>

Abstract. A method for mapping strontium isotope ratio ($^{87}\text{Sr}/^{86}\text{Sr}$) variations in bedrock and water has been recently developed for use in the interpretation of $^{87}\text{Sr}/^{86}\text{Sr}$ datasets for provenance studies. The mapping process adopted the simplifying assumption that strontium (Sr) comes exclusively from weathering of the underlying bedrock. The scope of this bedrock-only mapping method is thus limited to systems where the contributions of other sources of Sr are minimal. In this paper, we build on this $^{87}\text{Sr}/^{86}\text{Sr}$ mapping method by developing a mixing model of Sr fluxes from multiple sources to the bioavailable Sr pool. The new multiple source model includes: (1) quantitative calculations of Sr fluxes from bedrock weathering using an empirical rock weathering model; and (2) addition of sub-models calculating the contribution of Sr fluxes from atmospheric aerosols based on outputs from global climate model simulations. We compared the performance of the new multiple source model and the bedrock-only mapping method in predicting observed values from two datasets of bioavailable $^{87}\text{Sr}/^{86}\text{Sr}$ from the circum-Caribbean region (Antilles and Mesoamerica). Although the bedrock-only method performs relatively well in Mesoamerica ($n = 99$, MAE = 0.00011, RMSE = 0.00073), its prediction accuracy is lower for the Antillean dataset ($n = 287$, MAE = 0.0021, RMSE = 0.0027). In comparison, the new multiple source model, which accounts for the deposition of sea salt and mineral dust aerosols, performs comparably well in predicting the observed $^{87}\text{Sr}/^{86}\text{Sr}$ values in both datasets (MAE = 0.00040, RMSE = 0.00087 and MAE = 0.00014, RMSE = 0.0010). This study underscores the potential of using process-oriented spatial modeling to improve the predictive power of Sr isoscapes over large spatial scales and to refine sampling strategies and bioavailable Sr dataset interpretations for provenance studies.

Key words: bioavailable strontium; isoscape; Isoscapes Special Feature; provenance; strontium budget; strontium isotope ratio.

Received 29 May 2012; **revised** 4 October 2012; **accepted** 15 October 2012; **final version received** 14 November 2012; **published** 27 December 2012. Corresponding Editor: J. West.

Copyright: © 2012 Bataille et al. This is an open-access article distributed under the terms of the Creative Commons Attribution License, which permits restricted use, distribution, and reproduction in any medium, provided the original author and sources are credited.

† E-mail: cbataill@purdue.edu

INTRODUCTION

Strontium isotope ratios ($^{87}\text{Sr}/^{86}\text{Sr}$) have been increasingly and successfully employed as provenance tracers of a wide variety of environmental processes (Graustein and Armstrong 1983, Capo

et al. 1998, Kelly et al. 2005, Bentley 2006). The method relies on comparing the $^{87}\text{Sr}/^{86}\text{Sr}$ signature of a sample(s) of unknown origin to that of reference samples: generally local sample materials such as rock, soil, water, plant or animal. At larger spatial scales and/or for large datasets,

where development of comprehensive reference collections can be prohibitive, the identification of provenance using $^{87}\text{Sr}/^{86}\text{Sr}$ data requires comparative analyses with reference $^{87}\text{Sr}/^{86}\text{Sr}$ maps (Price et al. 2002, Hodell et al. 2004, Bentley 2006, Evans et al. 2009).

Previous efforts have been made to map $^{87}\text{Sr}/^{86}\text{Sr}$ variations at large scales (Beard and Johnson 2000, Bataille and Bowen 2012) for use in the interpretation of $^{87}\text{Sr}/^{86}\text{Sr}$ for provenance studies. Bataille and Bowen (2012) developed a model for environmental Sr isotope variation based on the assumption that bedrock weathering represents the primary source of environmentally available Sr. Their GIS-based model uses lithology-specific model parameters and generalized ^{87}Rb decay equations to account for the combined effects of lithology and time on $^{87}\text{Sr}/^{86}\text{Sr}$ variations in bedrock. Although the predictive power of this method is still less than optimal, comparison with validation datasets shows promise for predicting geographic $^{87}\text{Sr}/^{86}\text{Sr}$ variation in different sample materials. Bataille and Bowen's model formulation only considers $^{87}\text{Sr}/^{86}\text{Sr}$ variations in bedrock and water and does not explicitly address other Sr sources that may contribute to $^{87}\text{Sr}/^{86}\text{Sr}$ variations in biologically available (bioavailable) Sr. Mapping bioavailable $^{87}\text{Sr}/^{86}\text{Sr}$ variations is fundamentally important for constraining local $^{87}\text{Sr}/^{86}\text{Sr}$ signatures for ecological (Capo et al. 1998) and archeological (Bentley 2006) studies of provenance.

In many locations, the bioavailable Sr pool can reflect the complex integration of multiple sources (bedrock and atmospheric sources) and sinks of Sr that interact with the ecosystem over different time scales. At the base of the ecosystem, plants uptake and incorporate Sr from the exchangeable Sr pool in soil, defined as the pool of Sr bound to organic matter and/or soil minerals and exchanging with plants and/or soil water (Capo et al. 1998, Stewart et al. 1998). This exchangeable Sr pool is operationally defined as the Sr leached from dry soil with reagents such as buffered ammonium chloride in methanol (Capo et al. 1998).

Stewart et al. (1998) proposed mathematical formulations to model bioavailable $^{87}\text{Sr}/^{86}\text{Sr}$ for local ecosystems, but this model is currently not applicable at regional scales because it requires a

large number of site-specific parameters as input. Consequently, most attempts to map regional $^{87}\text{Sr}/^{86}\text{Sr}$ variation in ecosystems have involved interpolating average $^{87}\text{Sr}/^{86}\text{Sr}$ measurements from local biomass (Price et al. 2002). However, this method can be data-intensive and costly and in most cases does not explicitly consider the underlying spatial structure of factors which likely govern Sr isotope variation (e.g., bedrock distribution, climate, atmospheric deposition). This method is also hampered by the challenge of selecting appropriate samples, which is non-trivial as different sample materials may integrate different spatial and temporal scales of $^{87}\text{Sr}/^{86}\text{Sr}$ variation.

Empirical mapping studies could greatly benefit from the parallel development of process-oriented spatial models. These models can help refine the interpretation of bioavailable Sr datasets and produce cost-effective reference isoscapes for provenance studies. These maps can be tested on compiled datasets of Sr isotope measurements from a range of materials. In this paper, we further develop the model of Bataille and Bowen (2012) by adding components that account for contributions from bedrock and non-bedrock sources to a mixed bioavailable Sr pool. We couple Bataille and Bowen's model to an empirical, process-oriented chemical weathering model to calculate estimates of soluble Sr fluxes from bedrock weathering to the bioavailable zone in soils. This model accounts for chemical weathering rate dependence on runoff and lithology (Jansen et al. 2010). We also include sub-models representing the contribution of atmospheric sources (dust and sea salt aerosol) to the soluble Sr in soils. We use a simple box model to describe the mixing of these different sources within the soil, and test the new model against two datasets of bioavailable Sr isotopes from the circum-Caribbean region.

The circum-Caribbean region is an ideal area to validate models describing the interaction of multiple Sr sources to soil water because it receives: (1) spatially variable inputs of Sr from bedrock weathering due to its diverse geology; (2) large annual inputs of Sr from atmospheric aerosols through dry and wet deposition of Saharan mineral dust and sea salt from the surrounding ocean; and (3) more episodic inputs of Sr-rich tephra from volcanic eruptions. In

addition, large amounts of data have been gathered in this region, including studies assessing the comprehensive Sr budget of ecosystems by measuring $^{87}\text{Sr}/^{86}\text{Sr}$ in rainfall, soil, the exchangeable Sr pool, bedrock and plants (Bern et al. 2005, Pett-Ridge et al. 2009b, Pozwa et al. 2002) and work producing several hundred $^{87}\text{Sr}/^{86}\text{Sr}$ measurements of local plants and animals for archeological provenance studies (Price et al. 2000, Hodell et al. 2004, Wright 2005, Price et al. 2006, Price et al. 2007, White et al. 2007, Price 2008, Price et al. 2010, Wright et al. 2010, Thornton 2011, Laffoon et al. 2012). The combination of these bioavailable Sr isotope datasets with the natural gradient of atmospheric deposition and varied lithologies of the circum-Caribbean region offers an excellent opportunity to develop and validate our multi-source mapping approach.

MATERIAL AND METHODS

Model derivation, calibration, and validation are described in the following sections. Additional details and documentation are available in the accompanying Appendix.

Model formulation

Previous research has contributed to our understanding of the factors controlling the mixing of multiple Sr sources in soils and ecosystems (Kennedy et al. 1998, Chadwick et al. 1999, Nakano et al. 2001, Pozwa et al. 2002, Bern et al. 2005, Chadwick et al. 2009, Pett-Ridge et al. 2009a, Pett-Ridge et al. 2009b). The contribution of atmospherically derived Sr to the soluble Sr in soil depends mostly on the magnitude of the bedrock weathering flux. When the flux of soluble Sr from bedrock weathering is low, the atmospheric contribution can become the dominant source of soluble Sr to soils and ecosystems. Comprehensive modeling of the soluble Sr mass balance in soil requires detailed soil models accounting for (1) inputs of Sr varying with relative weathering rates and/or deposition rates of each source, (2) outputs of Sr varying with leaching rates and/or erosion associated with each source. Although the theoretical formulation of such models exist (Hilley and Porder 2008, Hilley et al. 2010, Porder and Hilley 2011), not enough data are available

to apply them at large scales.

Here, we develop a simple model that estimates the $^{87}\text{Sr}/^{86}\text{Sr}$ of bioavailable Sr in the circum-Caribbean region as a function of Sr inputs from a limited number of sources (Fig. 1). We assume that the bioavailable Sr pool is well represented by the mixing of soluble Sr from weathering of primary minerals ($F_{w \rightarrow \text{bio}}$), weathering of deposited Saharan mineral dust ($F_{d \rightarrow \text{bio}}$), and deposition of dissolved sea salt in rainfall ($F_{ss \rightarrow \text{bio}}$). We neglect: (1) bedrock sources other than the major surficial bedrock; (2) local and regional atmospheric sources of Sr, such as recycling of local minerals by erosion and/or deposition of burned or dead biomass (Nakano and Tanaka 1997) and volcanic ash (Muhs and Budahn 2009); and (3) other continental atmospheric sources, e.g., North American mineral dust (Muhs et al. 2007). This assumption is supported by the low deposition rates of these other atmospheric sources of Sr in comparison with sea salt and Saharan dust in the circum-Caribbean region (Muhs et al. 1990, Bern et al. 2005, Muhs et al. 2007) despite their importance

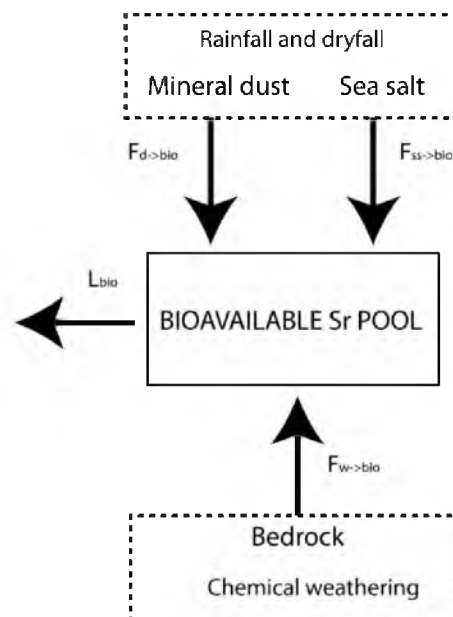


Fig. 1. Representation of the box model with fluxes of dissolved Sr mixing in the soluble bioavailable Sr pool. L_{bio} represents the losses of Sr from the bioavailable pool to other pools.

in other geographic settings (Graustein and Armstrong 1983, Naiman et al. 2000).

We model the bioavailable Sr pool as a well-mixed reservoir at steady state. Both assumptions are likely to be invalid for some systems, especially those affected by disturbance in which changes in Sr cycling and vertical or small-scale spatial gradients exist, but are necessary simplifications for this investigatory large-scale regional modeling. We test the sensitivity of our models to several different Sr sources using three model versions.

The first is a “bedrock model” (as used in Bataille and Bowen 2012), in which the isotopic composition of bioavailable Sr is equal to the isotopic composition of Sr released from local bedrock weathering. Eq. 1 from Bataille and Bowen (2012) encapsulates the theory for both silicate and carbonate rocks:

$$\left(\frac{^{87}\text{Sr}}{^{86}\text{Sr}}\right)_b = 0.701 + \left(\frac{^{87}\text{Rb}}{^{86}\text{Sr}}\right)_{\text{parent}} (e^{\lambda(t_1 - t_0)} - 1) + \left(\frac{^{87}\text{Rb}}{^{86}\text{Sr}}\right)_{\text{rock}} (e^{\lambda t_2} - 1) \quad (1)$$

where $(^{87}\text{Rb}/^{86}\text{Sr})_{\text{parent}}$ and $(^{87}\text{Rb}/^{86}\text{Sr})_{\text{rock}}$ refer to the $^{87}\text{Rb}/^{86}\text{Sr}$ of the parent material and the modern rock unit, respectively, t_1 is an approximate age of crustal differentiation (3000 Ma), and t_2 the age of the modern rock unit. $^{87}\text{Rb}/^{86}\text{Sr}$ can be expressed as:

$$\left(\frac{^{87}\text{Rb}}{^{86}\text{Sr}}\right) = \frac{\text{Rb}(\text{Ab}^{87}\text{Rb})(W\text{Sr})}{\text{Sr}(\text{Ab}^{86}\text{Sr})(W\text{Rb})} \approx 2.89 \frac{\text{Rb}}{\text{Sr}} \quad (2)$$

where W refers to the atomic weight of an element and Ab to the abundance (%) of an isotope.

In Eq. 1, the parent rock term is treated differently in the silicate and carbonate models. Silicates parent rock term is calibrated by assuming that the silicon content of the rock type is an indicator of magma source composition whereas carbonates parent rock term was calibrated using seawater $^{87}\text{Sr}/^{86}\text{Sr}$ variations throughout geological time (for details see Bataille and Bowen 2012).

The second is a “two source mixing model” describing the mixing of sea salt and bedrock

derived Sr:

$$\left(\frac{^{87}\text{Sr}}{^{86}\text{Sr}}\right)_{2s} = \frac{F_{\text{ss} \rightarrow \text{bio}} \left(\frac{^{87}\text{Sr}}{^{86}\text{Sr}}\right)_{\text{ss}} + F_{\text{w} \rightarrow \text{bio}} \left(\frac{^{87}\text{Sr}}{^{86}\text{Sr}}\right)_b}{F_{\text{ss} \rightarrow \text{bio}} + F_{\text{w} \rightarrow \text{bio}}} \quad (3)$$

where 2s indicates the two source mixing model, $F_{\text{ss} \rightarrow \text{bio}}$ and $F_{\text{w} \rightarrow \text{bio}}$ and $(^{87}\text{Sr}/^{86}\text{Sr})_{\text{ss}}$ and $(^{87}\text{Sr}/^{86}\text{Sr})_b$ are the magnitudes and Sr isotope ratios of the sea salt and bedrock weathering fluxes, respectively.

The third is a “three source mixing model” describing the mixing of sea salt, mineral dust, and bedrock weathering Sr:

$$\left(\frac{^{87}\text{Sr}}{^{86}\text{Sr}}\right)_{3s} = \frac{F_{\text{ss} \rightarrow \text{bio}} \left(\frac{^{87}\text{Sr}}{^{86}\text{Sr}}\right)_{\text{ss}} + F_{\text{d} \rightarrow \text{bio}} \left(\frac{^{87}\text{Sr}}{^{86}\text{Sr}}\right)_d + F_{\text{w} \rightarrow \text{bio}} \left(\frac{^{87}\text{Sr}}{^{86}\text{Sr}}\right)_b}{F_{\text{ss} \rightarrow \text{bio}} + F_{\text{d} \rightarrow \text{bio}} + F_{\text{w} \rightarrow \text{bio}}} \quad (4)$$

where 3s indicates the three source mixing model, $F_{\text{d} \rightarrow \text{bio}}$ and $(^{87}\text{Sr}/^{86}\text{Sr})_d$ are the magnitude and Sr isotope ratio, respectively, of the dust deposition flux.

Model parameterization

Bedrock weathering flux.—To calculate $F_{\text{w} \rightarrow \text{bio}}$, we applied the continental-scale, process-oriented, empirical weathering model developed by Jansen et al. (2010) on the Caribbean USGS geodatabase. The model calculates the rate of Si dissolution from different rock types as:

$$F_{\text{DSi}} = b_0 q^{b_n} \quad (5)$$

where F_{DSi} is the flux of dissolved SiO_2 to river water ($\text{t} \cdot \text{km}^{-2} \cdot \text{a}^{-1}$) from the bedrock lithology at a given map location having mean annual runoff q ($\text{L} \cdot \text{a}^{-1} \cdot \text{m}^{-2}$), lithology-specific parameters b_n and b_0 . The latter two parameters have been calibrated by Jansen et al. 2010 using measurements of dissolved silica loads in rivers from Hartmann et al. 2010. We were not able to compile enough measured F_{DSi} data to recalibrate this model for the circum-Caribbean region and instead opted to use an existing calibration. Two calibrations exist, one for the conterminous USA (Jansen et al. 2010) and one for Japan (Hartmann et al. 2010, Jansen et al. 2010). We use the Japan calibration because it reflects a range of environmental conditions (coastal and insular region), climate

(high temperature and precipitation), and geological settings (subduction area) that are reasonably good analogs for the circum-Caribbean region. We obtained b_0 and b_n values by matching each rock type in the Caribbean bedrock geology geodatabase with an equivalent lithological category given in Jansen et al. (2010) (see Appendix: Table A1). The Japan calibration does not offer values for mafic plutonic rocks and carbonates, and for both we used the calibrated values from the conterminous USA (Jansen et al. 2010).

In order to obtain a high-resolution gridded runoff dataset for our study area we calculated q as:

$$q = \text{MAP} - \text{MAAET} \quad (6)$$

where MAP is the mean annual precipitation ($\text{mm}\cdot\text{a}^{-1}$) obtained from the WorldClim website (Hijmans et al. 2005) and MAAET the mean annual actual evapotranspiration in $\text{mm}\cdot\text{a}^{-1}$ obtained from the Global High-Resolution Soil-Water balance from the CGIAR-CSI website (Trabucco and Zomer 2010). Previous applications of the weathering model have used modeled runoff grids from the Global Runoff Data Center (GRDC) (Fekete et al. 2002), but these data provide insufficient spatial resolution for the island regions we examine here. Our runoff estimates compare well with the GRDC grids for catchments where they overlap: by resampling our estimates to the 0.5° GRDC resolution we found that at 55% of the GRDC gridcells our runoff estimates are within 20% of the GRDC values and at only 10% do the two estimates differ by more than 40%.

Modeled F_{DSi} values were used to obtain Sr weathering fluxes for each lithology using a Sr/SiO₂-normalization technique similar to Hartmann and Moosdorf (2011a):

$$F(\text{Sr})_{\text{w}\rightarrow\text{bio}} \approx F_{\text{DSr}} = F_{\text{DSi}} \left(\frac{\text{Sr}}{\text{SiO}_2} \right). \quad (7)$$

Here F_{DSr} is the flux of soluble Sr from the bedrock lithology at a given map location to the river and (Sr/SiO_2) is the molar ratio of Sr to SiO₂. Sr/SiO₂ ratios are approximated as the median value for each rock type based on 121,253 analyses available through the Earthchem Portal (www.earthchem.org; query by “chemistry”: all Sr AND SiO₂, “database”: Georoc results).

Calculated medians and associated standard deviations for each rock category descriptor used in Bataille and Bowen (2012) are available in Appendix: Table A1.

Our application of this model to estimate contributions of Sr from bedrock to the bioavailable pool involves two fundamental assumptions. First, by adopting a model calibrated using data from rivers, we are effectively assuming that river SiO₂ loads depend solely on the flux of silicon (Si) from bedrock (F_{DSi}) and that Si from other sources is negligible. This assumption is justified for sea salt aerosol because sea salt contains only small amounts of Si. This assumption is not always justified for mineral dust can participate in the Si flux to river water (Chadwick et al. 1999). Second, Eq. 7 assumes that the bedrock weathering flux of Sr is approximately equal to the flux into the bioavailable pool. This may not be the case in many systems because plants cycle cations primarily from the upper soil and some Sr may be routed directly to stream systems via groundwater without interacting with the bioavailable zone (Nakano et al. 2001, Pozwa et al. 2002). To the degree that they are incorrect, both assumptions would lead to overestimation of $F_{\text{w}\rightarrow\text{bio}}$, and this possibility is considered in the interpretation of our results.

Bedrock Sr isotope flux.—We applied the bedrock Sr isotope mapping method developed by Bataille and Bowen (2012) to calculate $(^{87}\text{Sr}/^{86}\text{Sr})_{\text{b}}$ as a function of rock age and lithology (Fig. 2). The bedrock-only model from Bataille and Bowen (2012) represents an averaged $^{87}\text{Sr}/^{86}\text{Sr}$ prediction of the dominant bedrock limited by the resolution of geological maps. Consequently, the bedrock-only model does not account for $(^{87}\text{Sr}/^{86}\text{Sr})_{\text{b}}$ variations due to contribution of non dominant lithologies and/or $(^{87}\text{Sr}/^{86}\text{Sr})_{\text{b}}$ variations related to compositional variation within rock units (e.g., van Soest et al. 2002) or to difference in the length of bedrock exposure to weathering (Lasaga 1984, Lasaga and Blum 1985). This lack of resolution in the geological map is particularly significant for carbonates because their high Sr/SiO₂ ratio and their high weatherability (see Appendix: Table A1) causes them to be the dominant source of Sr in many catchments even when they are only present in traces (Anderson et al. 2000). The optimized model parameters are subject to uncertainties

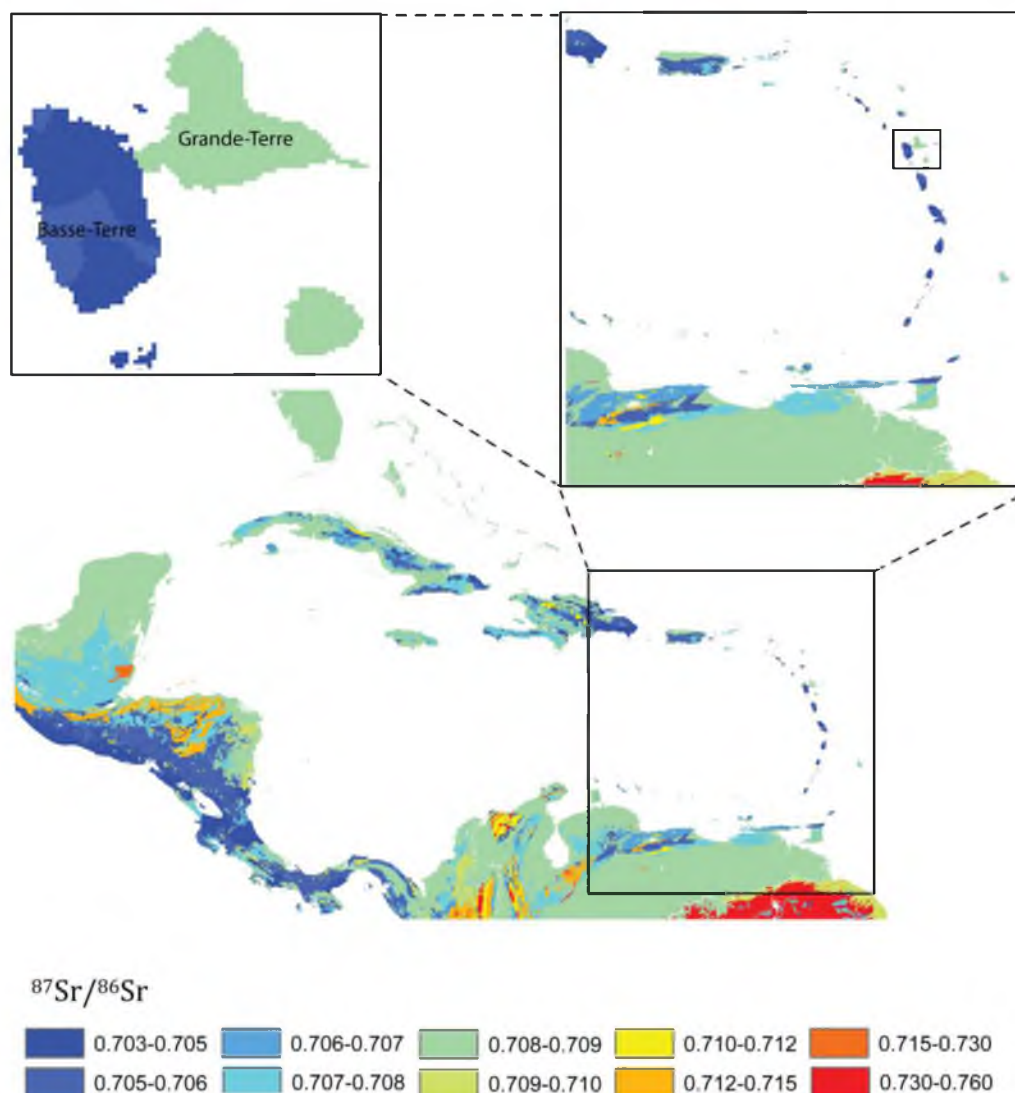


Fig. 2. Bedrock-only model $^{87}\text{Sr}/^{86}\text{Sr}$ variations calculated using equations from Bataille and Bowen (2012).

and biases related to the incompleteness of the databases used for calibration and the non-random distribution of samples therein, as discussed by Bataille and Bowen (2012).

We developed our bedrock Sr isotope map using a geodatabase describing the age and lithology of rock units throughout the Caribbean region (French et al. 2004). The lithological descriptors used in this database are different than those in the database previously used by Bataille and Bowen (2012) for the conterminous USA. For our new application we matched each

lithological descriptor in the Caribbean geodatabase with its closest analogous descriptor found in Bataille and Bowen (2012) (see Appendix: Table A1). Calculations for carbonate lithologies were conducted as described in Bataille and Bowen (2012).

Limitations arise from applying this $^{87}\text{Sr}/^{86}\text{Sr}$ mapping method to the Caribbean geodatabase because the lithological descriptors used are highly generalized. Intrusive igneous rocks are particularly poorly characterized. As a result, we selected all of the polygons having intrusive rock

types and reclassified each of these as granite, granodiorite, quartz diorite, or gabbro based on local geological maps of Puerto Rico (Reed et al. 2005), Hispanolia (Draper et al. 1995), Trinidad and Tobago (Saunders and Snoke 1998), and Cuba (Pushcharovski 1989). New lithological maps for this area will soon be available (Moosdorf et al. 2010) and will help resolve these issues (Moosdorf, *personal communication*).

Atmospheric sources.—To calculate $F_{d \rightarrow bio}$, we assumed that the Sr content of mineral dust, and its $^{87}\text{Sr}/^{86}\text{Sr}$, were constant over the study area. Mineral dust mineralogy and geochemistry is highly variable seasonally but long term average deposition is relatively homogeneous in the Caribbean (Prospero et al. 1970, Trapp et al. 2010). We assigned a concentration and $^{87}\text{Sr}/^{86}\text{Sr}$ of mineral dust equal to the average Sr content and $^{87}\text{Sr}/^{86}\text{Sr}$ of mineral dust collected over the Caribbean region: 195 ppm (Grousset et al. 1992, Rognon et al. 1996, Grousset and Biscaye 2005) and 0.71788, respectively (Grousset and Biscaye 2005, Formenti et al. 2011).

We obtained long-term average mineral dust deposition rates at $1^\circ \times 1^\circ$ spatial resolution from a synthesis (Mahowald et al. 2005) of results from three reanalysis models, each run for 10+ years (Luo et al. 2003, Ginoux et al. 2004, Tegen et al. 2004). The results have been shown to compare well with available satellite observations (Mahowald et al. 2005). However, aerosol modeling is a relatively recent field and large uncertainties remain in the models because the physics of aerosol deposition are not fully understood (Huneeus et al. 2011).

The low-resolution dust product does not represent variation in deposition rates driven by fine-scale variation in dust scavenging by precipitation, which may be an important control on dust deposition across our study region (Rea 1994). We downscaled the low resolution ($1^\circ \times 1^\circ$) dataset as:

$$F(\text{Sr})_{d \rightarrow bio} = (\text{Sr})_d(0.75D_d\text{PPF} + 0.25D_d) \quad (8)$$

where $(\text{Sr})_d$ is the abundance of Sr in mineral dust (in percent), D_d is the deposition rate of mineral dust from the reanalysis dataset in $\text{t}\cdot\text{km}^{-2}\cdot\text{a}^{-1}$, 0.75 is the proportion of wet deposition of mineral dust in the circum-Caribbean region (Jickells et al. 1998, Prospero et al. 2010), 0.25 the proportion of dry deposition of mineral

dust, and PPF is a “precipitation corrective factor” used to account for the enhancement of atmospheric deposition over land areas (relative to the open ocean) due to higher precipitation rates (Rea 1994). The PPF is defined as:

$$\text{PPF} = \frac{\text{MAP}_{hr}}{\text{MAP}_r} \quad (9)$$

where MAP_{hr} is the high resolution (30 arc-second) mean annual precipitation on land obtained from the WorldClim dataset (Hijmans et al. 2005) and MAP_r is the estimated mean annual precipitation amount for the same location calculated by bilinear interpolation of the low resolution ($2.5^\circ \times 2.5^\circ$) Global Precipitation Climatology Project Version 2.2 (GPCP).

This downscaling calculation acts primarily to enhance the fine-scale structure of the dust deposition field over island regions, where the coarse-resolution GPCP and dust model output do not represent high-frequency variation in precipitation rates and dust scavenging by precipitation. Local deposition rates are affected by a maximum of a factor of three due to this calculation. The calculation is not mass-conservative, but should provide a first-order approximation of the relative rates of dust deposition as a combination of large-scale circulation features represented in the reanalysis dataset and fine-scale scavenging processes related to regional variation in rainfall rates.

Our calculations estimate the rate of delivery of Sr from dust to the surface of soils, but this will only be equal to the flux of Sr to the bioavailable pool if Sr present in mineral dust is soluble enough to be released before mineral dust is removed by erosion (Kennedy et al. 1998). In the circum-Caribbean region, chemical weathering and release of Sr from Saharan mineral dust is likely rapid relative to rates of removal of dust by surface erosion because: (1) mineral dust deposits on acidic soils; (2) dust reaching the Caribbean is finely-grained ($\sim 2 \mu\text{m}$) and has a high exchange surface (Prospero et al. 1970); and (3) dust Sr is mostly contained in easily weatherable minerals such as calcite, dolomite, and plagioclase (Glaccum and Prospero 1980, Schütz and Seibert 1987, Kandler et al. 2007, Formenti et al. 2011). To the degree that dust is lost to erosion prior to dissolution of Sr, this will cause our model to overestimate the relative contribution of dust Sr

to the bioavailable pool. To estimate $F_{ss \rightarrow bio}$ and $(^{87}Sr/^{86}Sr)_{ss}$, we obtained the long term annual deposition of wet and dry sea salt aerosols from a Community Climate System Model 3 (CCSM3) simulation ($1.4^\circ \times 1.4^\circ$) in current climate conditions (Mahowald et al. 2006). This dataset shows good agreement with available satellite observations, and associated details and limitations are discussed in Mahowald et al. (2006). We assigned fixed values for Sr concentration and isotopic composition (0.04% and 0.7092) corresponding to the average abundance of Sr and $^{87}Sr/^{86}Sr$ in bulk sea salt. We downscaled the coarse resolution grid ($1.4^\circ \times 1.4^\circ$) to a 30 arc-second grid using a formulation equivalent to that used for dust deposition:

$$F(Sr)_{ss \rightarrow bio} = \%(Sr)_{ss}(\text{wetD}_{ss} \text{PPF} + \text{dryD}_{ss}) \quad (10)$$

where $(Sr)_{ss}$ is the abundance of Sr in sea salt (in percent) and wetD_{ss} and dryD_{ss} are the wet and dry deposition rates of sea salt in $t \cdot km^{-2} \cdot a^{-1}$ as given by CCSM3. Our calculation may overestimate the contribution of sea salt Sr to the bioavailable pool if a significant fraction of deposited Sr is rapidly leached to surface or groundwater, bypassing the bioavailable pool. Although controls on sea salt Sr retention in the bioavailable pool are uncertain, several authors have demonstrated that across a wide range of conditions a significant fraction of the soluble Sr from sea salt is incorporated in the soil exchangeable cation pool and retained in the bioavailable zone (Stewart et al. 1998, Nakano et al. 2001, Stewart et al. 2001, Pozwa et al. 2002), rather than being leached rapidly from soils.

Model evaluation

Bedrock-only model evaluation.—We evaluate the accuracy of the bedrock Sr isotope model using a dataset of $^{87}Sr/^{86}Sr$ ratios of igneous rocks from the Caribbean region ($n = 920$) from the Earthchem Portal (www.earthchem.org; Query by “chemistry”: $^{87}Sr/^{86}Sr$, “Location”: circum-Caribbean region, “Age” = Age exists:). The parameterized silicate model was applied to predict the $^{87}Sr/^{86}Sr$ of samples represented in this database, and the predicted and observed values were compared. Data from 11 samples (1.1% of the samples) were removed from the igneous rock validation dataset. These samples were very old felsic rocks (granites, rhyolites, gneisses) display-

ing exceptionally high $^{87}Sr/^{86}Sr$, for which we have previously shown the model to perform poorly (Bataille and Bowen 2012). The bedrock model reproduces the pattern of $^{87}Sr/^{86}Sr$ variations in bedrock ($\text{mod} = 0.45\text{obs} + 0.39$; $R^2 = 0.46$) and predicts the absolute $^{87}Sr/^{86}Sr$ values of the validation samples with MAE = 0.000249 and RMSE = 0.00113 (where MAE = mean absolute error and RMSE = root mean square error).

We also qualitatively evaluated the spatial patterns of bedrock-model predicted $^{87}Sr/^{86}Sr$ variation against patterns documented by observational studies in the region. At a regional scale, predicted bedrock $^{87}Sr/^{86}Sr$ variation is controlled by the signatures of three dominant lithologies, and corresponds well with observations from: (1) tertiary mafic to intermediate volcanic rocks which border the eastern (Antilles) and western (Central America volcanic front) limits of the Caribbean plate, displaying modeled $^{87}Sr/^{86}Sr$ from 0.7041 to 0.705 and measured values between 0.703 and 0.708 (van Soest et al. 2002, Vogel et al. 2006); (2) Cretaceous to modern carbonates present either as carbonate blocks such as the Chorotega block, an over-thickened oceanic crust block (e.g., Yucatan Peninsula) or as marine terraces, with modeled values ranging from 0.707 to 0.7092, similar to reported values (Hodell et al. 2004); and (3) felsic plutonic (modeled values from 0.730 to 0.767) or old metamorphic rocks (modeled values from 0.704 to 0.767) of the Guiana shield, for which the model estimates are also in the range of the observations (www.earthchem.org; Query by “chemistry”: $^{87}Sr/^{86}Sr$, “database”: Georoc results, “location”—northern South America).

At local scales, modeled $^{87}Sr/^{86}Sr$ variations are more difficult to validate because of the scarcity of observations. Modeled $^{87}Sr/^{86}Sr$ values do correlate well with existing regional geological features driven by: (1) differences in carbonate age, which drive slight $^{87}Sr/^{86}Sr$ variations in both Mesoamerica and the Antilles; and (2) small scale geological processes such as metamorphism around the Motagua shear or local plutonism in both the Antilles and Mesoamerica (French et al. 2004). However, as discussed in Bataille and Bowen (2012), the bedrock-only model gives ‘smoothed’ $^{87}Sr/^{86}Sr$ predictions and does not account for local geological processes causing $^{87}Sr/^{86}Sr$ to vary within lithological units having

Table 1. Chemical weathering model validation. Modeled and observed (Obs) F_{DSi} and F_{DSr} in the circum-Caribbean region in $\text{t}\cdot\text{km}^{-2}\cdot\text{a}^{-1}$.

Watershed area	Area (km^2)	Lithology	F_{DSi}		F_{DSr}	
			Obs mean	Model mean	Obs mean	Model mean
Icacos basin ^A	3.26	Granodiorite	48.4	42.3	0.59	0.14
Dominique Island ^B	751	Pyroclastic and mafic volcanic	24.9	39.1	nd	nd
Martinique ^C	1080	Pyroclastic and mafic volcanic	~100	62.4	0.075	0.046
Basse Terre Guadeloupe ^D	848	Pyroclastic and mafic volcanic	~80	59.2	0.082	0.044
Central Panama ^E						
Rio Charges	580	Mafic volcanic and granodiorite	~60	33.4	0.042	0.028
Rio Pequini	281	Recent volcanic	~85	48.1	0.107	0.089
Magdalena river ^F	257000	Complex	12.7	13.4	nd	nd

Notes: Sources are: A, White et al. (1998); B, Goldsmith et al. (2010); C, Rad et al. (2007); D, Harmon et al. (2009); E, Meybeck and Ragu (1997). Both F_{DSi} and F_{DSr} are corrected for sea salt contribution but not for mineral dust contribution. The abbreviation “nd” indicates no data available.

internal heterogeneity in age or composition. In the circum-Caribbean region, this limitation affects the accuracy of the prediction for mafic volcanic rocks, which display highly variable $^{87}\text{Sr}/^{86}\text{Sr}$ (0.703–0.708) depending on the time of interaction between the magma and more radiogenic wall rock (van Soest et al. 2002, Vogel et al. 2006).

Weathering model evaluation.—We evaluated the performance of the bedrock weathering model, applied using the calibration developed for Japan, by comparing its predictions with F_{DSi} measurements for our study region. The validation dataset (Table 1) for this area is likely biased towards high F_{DSi} areas because most of the observed F_{DSi} values reported in this region are associated with research on extremely high chemical weathering rates in volcanic highlands (Rad et al. 2007, Allegre et al. 2010). For comparison, in 516 catchments of the Japanese Archipelago, the calibrated weathering model explains more than 70% of the F_{DSi} variance (Hartmann 2009).

Several significant factors related to weathering rate are not accounted for in the model, such as topography, land cover, and temperature (Hartmann 2009). We expected the chemical weathering model to underestimate weathering rates and solute fluxes because of both high topographic relief and high mean annual temperatures in the circum-Caribbean region (White and Blum 1995). However, the presence of thick tropical soils may counteract this effect (Stallard and Edmond 1983). Other important sources of error for F_{DSi} estimates come from inaccuracies in the correspondence between lithological descrip-

tors of the Caribbean geodatabase and the classes of Jansen et al. (2010; see Appendix: Table A1).

Despite these theoretical limitations, the error in our F_{DSi} predictions across a range of catchment types spanning an order-of-magnitude range in observed F_{DSi} values does not exceed a factor of two at any site (Table 1). As expected, F_{DSi} for the young volcanic-dominated catchment (e.g., Guadeloupe, Martinique) is underestimated. Observed F_{DSi} values are more closely approximated by the model in catchments dominated by other lithologies. Few data are available to validate the weathering model, calibrated using values from Japan, on the circum-Caribbean region, but future work by Moodsdorf et al. (*personal communication*) to calibrate the model to tropical regions should improve the performance of our model. In the absence of other existing data available to recalibrate the weathering model, the F_{DSi} predictions cannot be assumed to be accurate to within better than a factor of two in the circum-Caribbean region.

Further uncertainties arise from using the Sr/SiO₂ normalization technique and a Si-specific weathering model because we do not take into account Sr-specific dissolution kinetics. However, Hartmann and Moosdorf (2011b) demonstrated good performance using a similar method to estimate the flux of phosphorus to rivers in Japan by re-scaling results from a silicate weathering model. When compared to the few observed F_{DSr} measured in this region (Table 2), our predicted F_{DSr} underestimates the observed F_{DSr} in all the catchments likely due to presence of trace quantities of non-siliciclastic minerals within

Table 2. Mixing model validation. Modeled and observed (Obs) contributions of the different sources of Sr to the bioavailable Sr.

Location	Atmospheric (%)		Bedrock (%)		$^{87}\text{Sr}/^{86}\text{Sr}$ bedrock		$^{87}\text{Sr}/^{86}\text{Sr}$ bioavailable	
	Model	Obs	Model	Obs	Model	Obs	Model	Obs
Analog catchment, Guyana ^A	Tot: 65; Ss:50; Dust:15	Tot:~75	35	25	0.731	0.72–76	0.718	0.716
Luquillos mountains, Puerto Rico ^B	Tot:25; Ss:20; Dust:5	Tot:~50; Ss:25; Dust:25	75	50	0.705	0.7041	0.7065	0.7095
Osa Peninsula, Costa Rica ^C								
SPU site	Tot:9; Ss:8; Dust:1	<10	91	>90	0.708	nd	0.7082	0.7062
RMU site	Tot:6; Ss: 5; Dust:1	<10	94	>90	0.7056	0.7039	0.7059	0.7041

Notes: The modeled contributions are calculated with the three source mixing model. The observed contributions are from: A, Pozwa et al. (2002; this catchment [5°20' N, 52°10' W] is not encompassed by the map and we used an analog catchment located in Guyana [7°3' N, 60°16' W] with similar geology [felsic metamorphic rocks], similar $^{87}\text{Sr}/^{86}\text{Sr}$ [modeled bedrock in the analog catchment is 0.731 and observed in the French Guyana ranges from 0.72 to 0.76], and climate [MAP around 2500 mm in the analog catchment and 3000 mm a^{-1} in the French Guyana catchment]); B, Pett-Ridge et al. (2009a); C, Bern et al. (2005). SPU and RMU are two sites with different lithologies. The abbreviation “nd” indicates no data available.

siliciclastic units as suggested by Hartmann and Moosdorf (2011b). The underestimation of F_{Dsr} propagates in our mixing model (Eqs. 3 and 4).

Mixing model evaluation.—To semi-quantitatively evaluate the performance of the three source mixing model in representing the relative contributions of Sr from different sources to the bioavailable Sr pool, we compared our model output with data from three studies which quantified the contribution of each source to soil water. For each of these studies, we reported the contribution from bedrock weathering, sea salt, and dust deposition and compared them to the results of our model.

Although numerous assumptions were made to develop the three source mixing model, this simple formulation reproduces the pattern of variation in the relative contribution of different sources of Sr to the bioavailable Sr pool (Table 2). In both catchments of the Osa Peninsula the model matches the observations well, with bedrock weathering being the dominant source of Sr to ecosystems. In the Guyana (analog) catchment, bedrock weathering is slow and atmospheric deposition becomes dominant. In the Luquillos Mountains, our model underestimates the contribution of mineral dust weathering to the bioavailable Sr pool. This underestimation is transmitted from the mineral dust deposition dataset which has been shown to underestimate dust deposition in this watershed (Pett-Ridge et al. 2009a). Overall, however, the analysis suggests that our Sr fluxes estimates for different sources can be confidently used to give an order of magnitude estimate of each Sr source’s contribution to bioavailable Sr. Moreover, in most circum-Caribbean ecosystems,

one source of Sr (either atmospheric or weathering), is largely dominant. In areas where Sr fluxes from the different sources are very different, such as the Guyana and Osa Peninsula sites (Table 1), the mixing model prediction uncertainty decreases whereas the uncertainty increases when the relative contribution of Sr from the different sources are at the same order of magnitude, such as in the Luquillos Mountains (Table 1).

Evaluation of bioavailable Sr isotope models.—We evaluated the performance of the different model formulations against published datasets reporting bioavailable Sr isotope measurements. Because different sample materials reflect different spatial scales of integration, we limited our comparison to $^{87}\text{Sr}/^{86}\text{Sr}$ measurements made on sample materials likely to reflect average Sr inputs from local (~1 km² or less) areas. We thus excluded from the analysis animals with large home ranges and river water, focusing our analysis mainly on data from plants and animals with small home ranges (Fig. 3).

Bedrock is a significant source of Sr to ecosystems in the circum-Caribbean region, as evidenced by the significant correlation between the bedrock-only modeled $^{87}\text{Sr}/^{86}\text{Sr}$ and observed values in both validation datasets. All three model versions perform similarly well in predicting the observed variation in $^{87}\text{Sr}/^{86}\text{Sr}$ values within the Mesoamerican dataset, explaining more than 80% of the observed variation. Models that include atmospheric deposition (the two and three source mixing models) show similar $^{87}\text{Sr}/^{86}\text{Sr}$ predictability (Fig. 4B, MAE = 0.00031, RMSE = 0.00079 and Fig. 4C, MAE = 0.00040, RMSE = 0.00087, respectively) in comparison

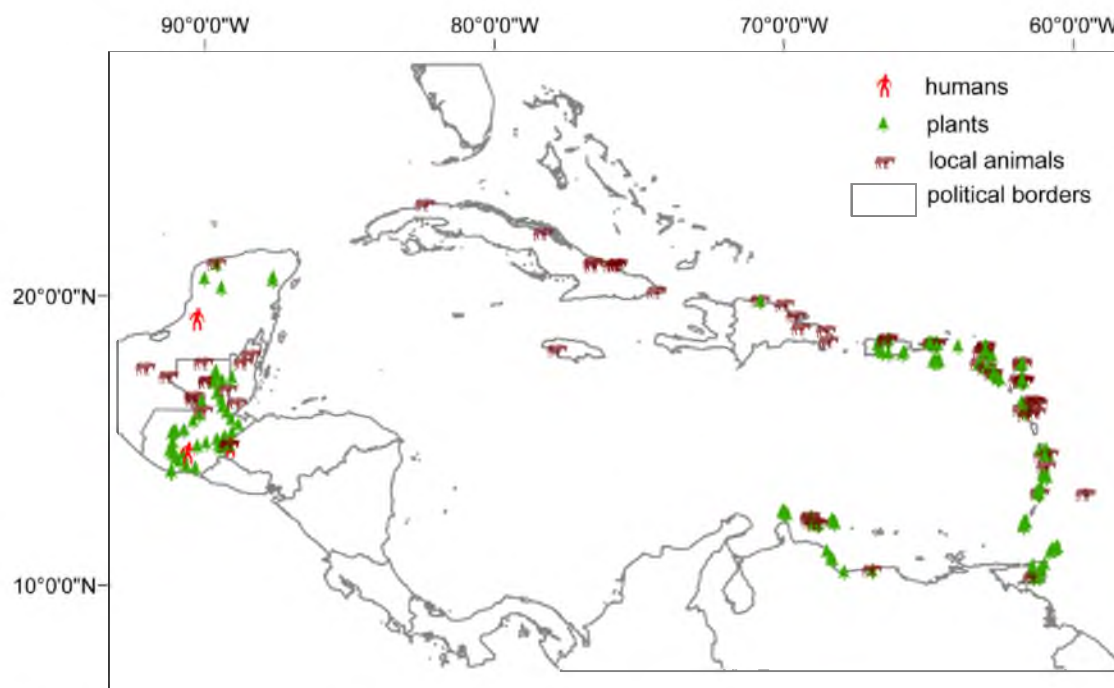


Fig. 3. Sample locations for data included in the validation datasets. The Mesoamerica dataset ($n = 99$) is a compilation of $^{87}\text{Sr}/^{86}\text{Sr}$ measurements of modern plants, and modern and archeological animal remains from several sources (Price et al. 2000, Buikstra et al. 2004, Hodell et al. 2004, Wright 2005, Price et al. 2006, Price et al. 2007, White et al. 2007, Price 2008, Price et al. 2010, Wright et al. 2010, Thornton 2011). The Antillean dataset ($n = 287$) is a compilation of $^{87}\text{Sr}/^{86}\text{Sr}$ measurements of modern plants, and modern and archeological animal remains from Laffoon et al. (2012).

with the bedrock-only model (Fig. 4A, MAE = 0.00011, RMSE = 0.00073). While the correlation between predicted $^{87}\text{Sr}/^{86}\text{Sr}$ and observed $^{87}\text{Sr}/^{86}\text{Sr}$ values is strong, it is dominated by a few individuals, and modeled $^{87}\text{Sr}/^{86}\text{Sr}$ does not represent well the high variability in observed $^{87}\text{Sr}/^{86}\text{Sr}$ (Fig. 4A–C). The modeled $^{87}\text{Sr}/^{86}\text{Sr}$ approximates well the regional $^{87}\text{Sr}/^{86}\text{Sr}$ signature driven by relatively non-changing factor such as geology and atmospheric deposition but the models do not account for more variable local factors such as Sr recycling influencing the local observed $^{87}\text{Sr}/^{86}\text{Sr}$ signature. The poor resolution of the geological map for Mesoamerica also adds some uncertainty. Samples collected in Mesoamerica are primarily underlain by two lithological types: young mafic volcanic rocks (with $^{87}\text{Sr}/^{86}\text{Sr}$ around 0.703–0.704) or marine carbonates (with $^{87}\text{Sr}/^{86}\text{Sr}$ around 0.707–0.709) which explain the bimodal distribution in the observed

$^{87}\text{Sr}/^{86}\text{Sr}$ values in Fig. 4 A–C. However, in the geological map the age of carbonates is often coarsely defined (e.g., “Tertiary”) which leads to uncertainty in all models (Fig. 4A–C) as $^{87}\text{Sr}/^{86}\text{Sr}$ of carbonates varied rapidly throughout geological time (Veizer et al. 1999). Similarly, the level of details of lithological description is not consistent: sometimes the map describes units as “volcanic rocks” which results in modeled $^{87}\text{Sr}/^{86}\text{Sr}$ around 0.705 and some other time it gives “mafic volcanic rocks” resulting in a modeled $^{87}\text{Sr}/^{86}\text{Sr}$ values around 0.703. In reality, most volcanic units of the volcanic front in Mesoamerica are mafic volcanics with $^{87}\text{Sr}/^{86}\text{Sr}$ around 0.703 with an observed bioavailable Sr signature ranging from 0.703 to 0.705. All models slightly overestimate the bioavailable $^{87}\text{Sr}/^{86}\text{Sr}$ signature for these rocks (Fig. 4A–C).

In contrast, more of the observed variation in the bioavailable Sr isotope dataset from the

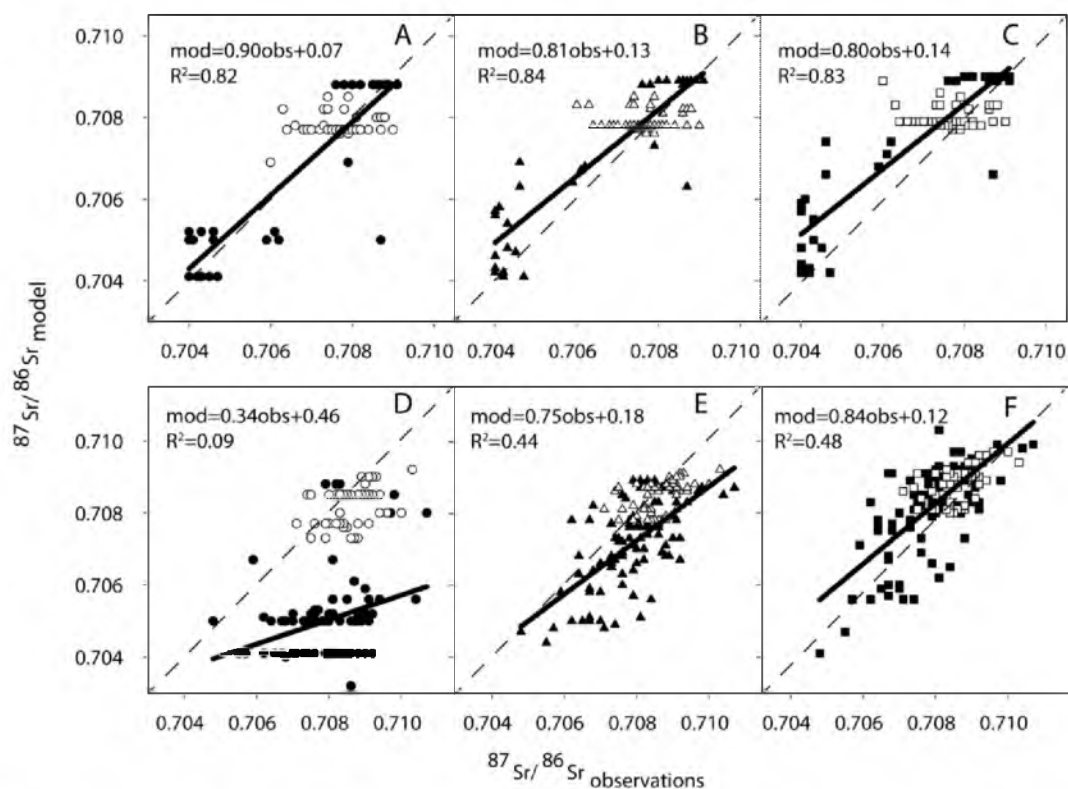


Fig. 4. Bioavailable Sr isotope model validation results. Modeled and measured $^{87}\text{Sr}/^{86}\text{Sr}$ for the Mesoamerican (A–C) and Antillean (D–F) validation datasets. Circles show results from the bedrock-only model (A, D), triangles show results from the two source mixing model (sea-salt, and bedrock weathering; B, E), and squares show results from the three source mixing model (sea-salt, dust, and bedrock weathering age-only water model; C, F). Filled symbols represents individuals sampled on silicates dominated areas and open symbols represent individuals sampled on carbonates dominated areas. Linear regression models are calculated on silicates only. Dashed lines show the 1:1 relationship.

Antilles is explained by the two models that include atmospheric deposition (the two source and three source mixing models, each explaining about 50% of the observed variation) than by the bedrock-only model ($R^2 = 0.09$). The models including atmospheric deposition also provide more accurate predictions of the observed values (Fig. 4E, two-source model MAE = 0.00063 and RMSE = 0.0013, and three source model Fig. 4F, MAE = 0.00014, RMSE = 0.0010) in comparison with the bedrock-only model (Fig. 4D, MAE = 0.0021, RMSE = 0.0027). The improvement of the MAE and RMSE for the three source mixing model in comparison with the two source mixing model demonstrates that consideration of both types of atmospheric sources are necessary to

accurately predict $^{87}\text{Sr}/^{86}\text{Sr}$ in the Antilles. In this region, sea salt deposition is often the dominant atmospheric source in terms of Sr flux, but dust deposition is an important contributor to the bioavailable $^{87}\text{Sr}/^{86}\text{Sr}$ signature because Saharan dust is highly radiogenic.

Spatial pattern of bioavailable $^{87}\text{Sr}/^{86}\text{Sr}$

Analysis of the relative magnitude of modeled fluxes in the fully integrated, three source model, shows that, although the fluxes vary substantially across the study domain, bedrock is usually the dominant contributor of Sr to circum-Caribbean ecosystems (Fig. 5A). On a continental scale (1000 km), we observe a general trend of decreasing contribution of atmospheric derived

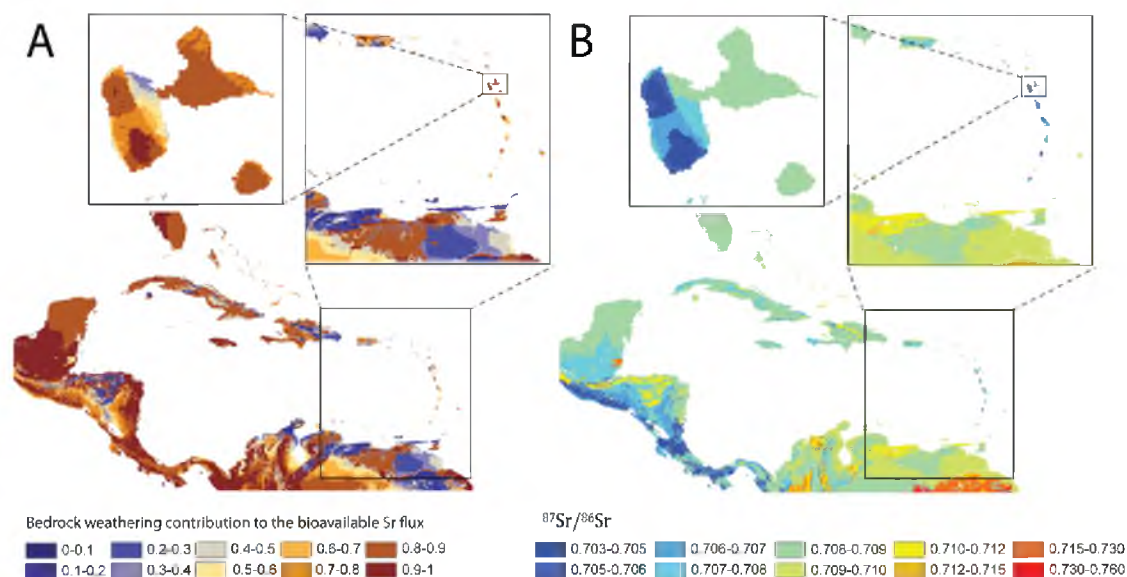


Fig. 5. (A) Contribution of bedrock weathering to the bioavailable Sr pool calculated as $F(\text{Sr})_{w \rightarrow \text{bio}} / (F(\text{Sr})_{w \rightarrow \text{bio}} + F(\text{Sr})_{\text{ss} \rightarrow \text{bio}} + F(\text{Sr})_{\text{d} \rightarrow \text{bio}})$. (B) Modeled Sr isotope ratios for the circum-Caribbean region from the three source mixing model.

Sr from east to west, which can be attributed to decreasing deposition rates of Saharan dust (Fig. 5A). On a more regional or local scale (i.e., 100 km–1 km), variation in the bedrock contribution is controlled by variation in weathering rates due to differences in both lithology and runoff. Even when atmospheric deposition rates are large, $^{87}\text{Sr}/^{86}\text{Sr}$ of ecosystems developing on highly weatherable Sr-rich carbonate substrates (e.g., the Maya block or marine deposits in the Antilles and Bahamas) resemble their carbonate parent (Fig. 5B). $^{87}\text{Sr}/^{86}\text{Sr}$ of ecosystems developing on highly weatherable but Sr-poor volcanic rocks (e.g., Antillean island arc and the Central American volcanic front) are predicted to be more variable at small spatial scales, with Sr isotope ratios and relative contributions of Sr to the bioavailable pool depending on the local interaction of lithology and climate (Fig. 5B). Only ecosystems developing on slowly weathering parent material (e.g., felsic Precambrian rocks of the Guyana shield and Chortis block) show a strong influence of atmospheric deposition (e.g., $F(\text{Sr})_{w \rightarrow \text{bio}} < 0.5$).

Both types of aerosols, sea salt and dust deposition, contribute significantly to the predicted bioavailable $^{87}\text{Sr}/^{86}\text{Sr}$ in parts of the study

region (Fig. 6A, B). Sea salt deposition is relatively ubiquitous and constant throughout the circum-Caribbean and contributes to the modeled $^{87}\text{Sr}/^{86}\text{Sr}$ by increasing $^{87}\text{Sr}/^{86}\text{Sr}$ in ecosystems developing on slowly weathering mafic (felsic) rocks in all regions (Fig. 6A). The contribution of mineral dust is more variable spatially, both over large scales (e.g., declining from the east to west across the region) and regionally (e.g., due to variation in precipitation scavenging rates). Because dust Sr in this region is relatively radiogenic, its relative influence on the modeled Sr isotope ratios is greatest in areas of high deposition rate that are also characterized by mafic bedrock, where the differences between bedrock and dust $^{87}\text{Sr}/^{86}\text{Sr}$ are largest (Fig. 6B).

To better illustrate the processes considered in the two and three source mixing models, we analyzed the modeled pattern of $^{87}\text{Sr}/^{86}\text{Sr}$ variation at finer scales on the Guadeloupe Islands (inset panels in Fig. 2; Fig. 5A, B, Fig. 6A, B). The islands of Guadeloupe are an interesting location to study bioavailable Sr because they present varied geological and climatic conditions. Guadeloupe consists of several different islands with bedrock geology dominated by either Tertiary marine carbonates with $^{87}\text{Sr}/^{86}\text{Sr}$ around

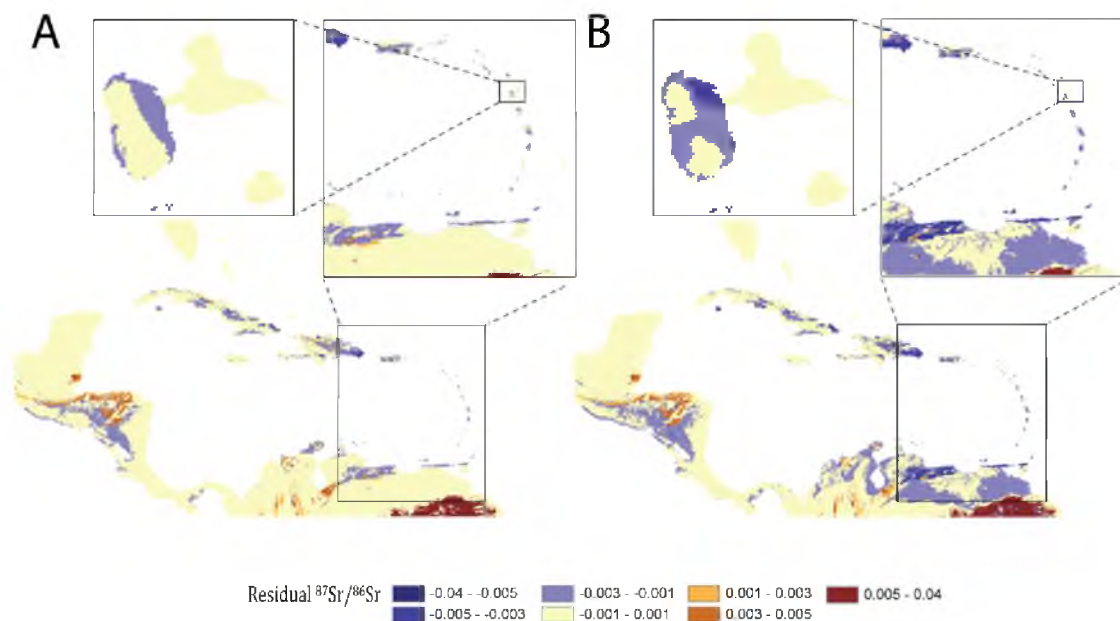


Fig. 6. (A) Difference between predicted $^{87}\text{Sr}/^{86}\text{Sr}$ from the bedrock-only model and $^{87}\text{Sr}/^{86}\text{Sr}$ from the two source mixing model including both sea salt and bedrock weathering. (B) Difference between predicted $^{87}\text{Sr}/^{86}\text{Sr}$ from the bedrock-only model and $^{87}\text{Sr}/^{86}\text{Sr}$ from the three source mixing model including sea salt, mineral dust, and bedrock weathering fluxes.

0.7085 or Tertiary intermediate and mafic volcanic rocks with $^{87}\text{Sr}/^{86}\text{Sr}$ ranging from 0.703 to 0.705 (www.earthchem.org). Geomorphology and erosion rates also differ between the islands, with the relatively flat Grande-Terre Island characterized by quasi constant MAP (2000 mm/yr) and the mountainous Basse-Terre Island characterized by highly variable temperature and precipitation.

For Grande-Terre, our three source model suggests that despite high aerosol deposition rates the bioavailable $^{87}\text{Sr}/^{86}\text{Sr}$ is equal to the $^{87}\text{Sr}/^{86}\text{Sr}$ of the carbonate bedrock. The modeled $^{87}\text{Sr}/^{86}\text{Sr}$ values are quite similar to those of sea salt aerosols due to the young age and similar Sr isotopic composition of the local carbonate bedrock, but analysis of the model results shows that bedrock weathering contributes at least 90% of the bioavailable Sr and thus dominates the absolute isotopic value of the bioavailable Sr pool and gives highly invariant values across the island. This result is consistent with observations from older carbonate terrains in the region, where bioavailable Sr isotope values tend to follow bedrock values rather than the sea salt

value (Hodell et al. 2004, Laffoon et al. 2012). Despite the relatively homogenous $^{87}\text{Sr}/^{86}\text{Sr}$ of the intermediate volcanic rocks on Basse-Terre, the modeled bioavailable $^{87}\text{Sr}/^{86}\text{Sr}$ is highly variable and can diverge significantly from bedrock. Bedrock weathering contributes between 50% and 90% of the bioavailable Sr depending mostly on bedrock weathering rates. At the top of La Soufriere (the main volcano on Basse-Terre, Guadeloupe), modeled weathering rates are high because of high runoff. Despite large deposition rates of atmospheric Sr, bedrock weathering contributes up to 90% of the bioavailable Sr in this area. In contrast, in the lower lands around the volcano, runoff and weathering rates are lower and atmospheric deposition is predicted to contribute significantly to the bioavailable pool. This is also visible on the island of Saba where, despite the presence of a highly weatherable volcanic substrate, the relatively low rainfall amount ($<2000 \text{ mm}\cdot\text{yr}^{-1}$) does not favor high chemical weathering rates and induces a dominance of atmospheric derived Sr to the bioavailable pool (Laffoon et al. 2012).

Most of the sampling sites (Fig. 2) are

characterized by roughly similar tropical humid climates, although some areas, for example the Leeward Antilles (Aruba, Bonaire, Curacao and the Venezuelan archipelago), are characterized by more semi-arid conditions. In the Leeward Antilles, our three source mixing model predicts a relatively invariant $^{87}\text{Sr}/^{86}\text{Sr}$ value around 0.708–0.709 due to a dominance of sea salt derived Sr in comparison with the other sources. Bedrock contribution to the modeled $^{87}\text{Sr}/^{86}\text{Sr}$ is low because low runoff limits chemical weathering of bedrock. In the Leeward Antilles, in spite of a variable lithology with bedrock $^{87}\text{Sr}/^{86}\text{Sr}$ ranging from 0.703–0.709 (www.earthchem.org), the modeled $^{87}\text{Sr}/^{86}\text{Sr}$ compare well to observations of bioavailable $^{87}\text{Sr}/^{86}\text{Sr}$ which remain relatively invariant and range from 0.7075–0.709 (Laffoon et al. 2012). The good correlation between model and observations for this region was surprising because in semi-arid conditions soils are usually thin (~1 m) due to water and wind erosion and average rooting depth is usually deep (McCulley et al. 2004) both of which should favor strong contribution from bedrock derived Sr. However, Capo and Chadwick (1999) demonstrated that in semi-arid to arid conditions most of the exchangeable Sr originates from atmospheric deposition (either sea salt or dust) because bedrock weathering rates are slow. Geochemical analysis of soils from the Leeward Antilles (Vries 2000) showed an accumulation of sea salt and carbonate mineral dust which tend to confirm the results of our model simulation.

DISCUSSION

Our model shows that across most of the circum-Caribbean ecosystems, bedrock weathering is the dominant source of Sr to ecosystems.

The contribution of atmospheric deposition is significant in many areas but is rarely dominant. This pattern is somewhat surprising because previous research on Sr cycling in a similar tropical climate in Hawaii showed dominant to exclusive atmospheric contribution to ecosystems when soils are older than 20 ka (Chadwick et al. 2009). While this pattern could be an artifact of the model, it has been observed in other studies in the circum-Caribbean region (e.g., Bern et al. 2005). Several mechanisms can be advanced to

explain the maintenance of bedrock as the main source of Sr to ecosystems in the circum Caribbean region such as: (1) immobilization and preferential recycling of nutrients in upper soils and biomass, which can concentrate bedrock derived Sr in the bioavailable zone (Jobbagy and Jackson 2001, Porder and Chadwick 2009); (2) deposition of locally eroded fresh primary minerals by rivers and landslides (Bern et al. 2005) and/or atmospheric deposition of bedrock-like Sr such as local dust, biomass, and volcanic ash (Muhs and Budahn 2009); (3) preferential loss of atmospheric Sr relative to bedrock Sr due to processes such as rapid leaching of soluble sea salt Sr and surficial erosion of mineral dust Sr (Porder and Hilley 2011); (4) ecological characteristics of plants that favor uptake of bedrock derived nutrients, such as deep rooting (Jobbagy and Jackson 2001, Pozwa et al. 2002, Pozwa et al. 2004); and (5) geomorphological and hydrological processes coupling stream and soil water (Nakano et al. 2001).

Our results suggest that bedrock dominance is a wide-spread pattern in the circum-Caribbean region. Among the mechanisms proposed, immobilization and preferential recycling of nutrients and deposition of locally eroded fresh primary minerals are more likely to affect circum-Caribbean ecosystems at large scales than are the other factors related to local soil type, plant species, and/or geomorphology. Recycling of bedrock-derived Sr by ecosystems could maintain bedrock dominance for long periods of time by renewing the stock of fresh primary mineral. However, Porder and Chadwick (2009) showed that at MAP greater than $1,400 \text{ mm}\cdot\text{a}^{-1}$ plant recycling of bedrock-derived Sr was limited. Type and rate of erosion favors the contribution of bedrock-derived Sr by lowering the bedrock depth to plants, decreasing the residence time of primary minerals, and favoring redeposition of freshly eroded primary minerals. Both mechanisms should be further investigated to understand Sr cycling in the circum-Caribbean region.

Our two- and three source mixing models show relatively good power to predict bioavailable Sr isotope patterns at large spatial scales throughout the circum-Caribbean region. However, these models are highly simplified representations of Sr cycling within these systems and

do not consider a number of processes that can contribute to bioavailable $^{87}\text{Sr}/^{86}\text{Sr}$. Our models estimate the mixing ratios of soluble Sr in soil as a simple function of climate and lithology specific chemical weathering rates and atmospheric deposition rates. Other variables such as erosion, pedology, geomorphology, hydrological flowpaths, or plant ecology, which have been shown in local studies of Sr systematics, are not explicitly considered in these models. Some of these variables are correlated with others incorporated in our models (e.g., runoff and/or lithology), helping to explain the relatively good performance of the models. Higher precipitation rates, for instance, increase runoff and bedrock weathering rates in our models, and often lead to a dominance of bedrock Sr. In reality, although increasing precipitation increases runoff it can also increase erosion. Both processes (runoff and erosion) increase the bedrock-derived Sr flux to the bioavailable zone. Significant potential remains for refining our models through explicit incorporation of some of these additional variables, which may help to predict the 30–50% of bioavailable Sr isotope variation remaining unexplained in our analysis. The results of this first analysis, however, suggest that relatively simple multi-source models can explain a large fraction of regional Sr isotope variation and provide relatively accurate predictions of bioavailable $^{87}\text{Sr}/^{86}\text{Sr}$ in the circum-Caribbean region.

Implications for Sr isotope provenance applications

Despite significant progress in the mapping of bioavailable $^{87}\text{Sr}/^{86}\text{Sr}$ in many regions, applications that rely exclusively on empirical data are still relatively few in number and generally limited in scale because of the substantial investments of time, energy, and resources required. Integrated approaches that combine empirical and theoretical modeling will be of great benefit to the further development of biosphere $^{87}\text{Sr}/^{86}\text{Sr}$ mapping and to provenance studies more generally, especially if they can provide reliable predictions of bioavailable $^{87}\text{Sr}/^{86}\text{Sr}$ under a broad array of geographic settings and environmental conditions. One potential contribution of these efforts is that models which explicitly consider multiple factors that influence the spatial variation of bioavailable $^{87}\text{Sr}/^{86}\text{Sr}$ can help to guide sample selection

strategies. The choice of both appropriate sample materials and methods for provenance studies cannot be independent of a clear understanding of the Sr cycle at the scale studied.

In areas where bedrock is easily weatherable and the dominant source of Sr, $^{87}\text{Sr}/^{86}\text{Sr}$ should remain fairly constant in the different pools of the Sr cycle (e.g., groundwater, soil water, plants and animals). In such cases, the development of bioavailable $^{87}\text{Sr}/^{86}\text{Sr}$ maps through focused sampling of any of these sample materials combined with the bedrock-only model (Bataille and Bowen 2012) should be sufficient to predict accurately the bioavailable $^{87}\text{Sr}/^{86}\text{Sr}$. In environments where multiple sources of Sr interact, different sample materials may cycle Sr differently and display highly variable $^{87}\text{Sr}/^{86}\text{Sr}$ ratios. In these areas, defining the different processes interacting in the Sr cycle of local soils is important to correctly interpret the magnitude, pattern and scale of variability of $^{87}\text{Sr}/^{86}\text{Sr}$ and how these relate to the spatial scale of integration represented by different sample materials. This is well illustrated by the contrasting spatial patterns of $^{87}\text{Sr}/^{86}\text{Sr}$ variation from Grande-Terre and Basse-Terre, Guadeloupe. Despite the fact that both islands are characterized by relatively uniform geologies, biosphere $^{87}\text{Sr}/^{86}\text{Sr}$ on Grande-Terre is similar over large spatial scales (essentially the entire island) while biosphere $^{87}\text{Sr}/^{86}\text{Sr}$ on Basse-Terre is heterogeneous and highly variable at small localized spatial scales. For Grande-Terre the marine limestone substrate is rich in easily weatherable, Sr-rich minerals and $^{87}\text{Sr}/^{86}\text{Sr}$ of the local biosphere is dominated by a single isotopically homogenous source of Sr. In contrast, the intermediate volcanic lithology of Basse-Terre is less weatherable and less rich in Sr and thus local variations in the conditions influencing the proportional contribution of bedrock/soil Sr to local bioavailable Sr budgets also strongly influence the spatial variation of $^{87}\text{Sr}/^{86}\text{Sr}$. Therefore, a higher sampling density is required to empirically map, or calibrate and validate models for, the relatively localized spatial variation of $^{87}\text{Sr}/^{86}\text{Sr}$ on Basse-Terre, whereas a reduced sampling density should suffice for Grande-Terre.

Comparison between bedrock, flux-weighted catchment water and bioavailable Sr isoscape predictions and observed $^{87}\text{Sr}/^{86}\text{Sr}$ in plants,

rocks and river waters (Bataille and Bowen 2012, Chesson et al. 2012) highlights the necessity of developing specific isoscapes for each substrate (e.g., rock, river water, biomass) because each substrate can cycle Sr from different sources. For instance, Chesson et al. (2012) showed large divergence between the local bedrock Sr and tap water $^{87}\text{Sr}/^{86}\text{Sr}$. This is not surprising because US tap waters generally originate from large rivers or subsurface aquifers which reflect $^{87}\text{Sr}/^{86}\text{Sr}$ from the weathering of large drainage basins and/or subsurface rock units. When substrates sample Sr from local sources or ecosystems, then mapping the bioavailable $^{87}\text{Sr}/^{86}\text{Sr}$ requires explicit considerations of local variables such as presented in this study or in Capo et al. (1998). In contrast, when the dominant source of Sr of the substrate is river water, modeling efforts will be better focused on regional variables such as weathering and catchment hydrology. When both local (bioavailable) and regional (river waters) Sr sources participate in governing the $^{87}\text{Sr}/^{86}\text{Sr}$ values of Sr assimilated by a sample substrate (e.g., humans), a quantification of the contribution from each source may be required.

Conclusions

We present new models and isoscapes for large-scale patterns of bioavailable $^{87}\text{Sr}/^{86}\text{Sr}$ in the circum-Caribbean region that include consideration of both bedrock and atmospheric Sr sources. In spite of the relative simplicity of the models and the limitations discussed throughout this paper, this new mapping method demonstrates good predictive power and can contribute to future provenance studies and inform further data collection. Our results suggest that throughout this region bioavailable $^{87}\text{Sr}/^{86}\text{Sr}$ is generally dominated by bedrock Sr, but that in some areas atmospheric deposition is significant and must be considered when interpreting $^{87}\text{Sr}/^{86}\text{Sr}$ datasets for provenance studies.

The following steps are the most critical to continue the development of Sr isoscapes for different substrates: (1) focus on improving, simplifying and validating modeling strategies for three relevant pools of Sr for provenance studies: bedrock, bioavailable Sr, and river water; (2) account for local processes influencing the Sr cycling, such as local Sr recycling through erosion and dust, pedology and surficial depos-

its; (3) expand modeling in each representative pool to broader geographic coverage using the new lithological world map (Moosdorf et al. 2010). Ultimately a Sr isoscape of the world could be applied to a variety of fields including large scale provenancing studies in ecology and archeology (e.g., Bentley 2006), dust modeling (e.g., Nakai et al. 1993) or refining Sr budget in seawater (e.g., Vance et al. 2009).

ACKNOWLEDGMENTS

This research was supported by NSF Award DBI-0743543. GCM outputs for sea salt and mineral dust were kindly provided by Natalie Mahowald. We thank Nils Moosdorf for advice in applying and interpreting the chemical weathering model to the circum-Caribbean region. The dataset of bioavailable $^{87}\text{Sr}/^{86}\text{Sr}$ from the Antilles was generated by JEL in collaboration with Gareth Davies of the Department of Petrology, VU, Free University Amsterdam and was financially supported by an NWO-funded research grant under the supervision of Corinne Hofman and Menno Hoogland of the Faculty of Archaeology, Leiden University, The Netherlands.

LITERATURE CITED

- Allegre, C. J., P. Louvat, J. Gaillardet, L. Meynadier, S. Rad, and F. Capmas. 2010. The fundamental role of island arc weathering in the oceanic Sr isotope budget. *Earth and Planetary Science Letters* 292:51–56.
- Anderson, S. P., J. I. Drever, C. D. Frost, and P. Holden. 2000. Chemical weathering in the foreland of a retreating glacier. *Geochimica Et Cosmochimica Acta* 64(7):1173–1189.
- Bataille, C. P. and G. J. Bowen. 2012. Mapping $^{87}\text{Sr}/^{86}\text{Sr}$ variations in bedrock and water for large scale provenance studies. *Chemical Geology* 304-305:39–52.
- Bentley, R. A. 2006. Strontium isotopes from the earth to the archaeological skeleton: A review. *Journal of Archaeological Method and Theory* 13(3):135–187.
- Beard, B. L. and C. M. Johnson. 2000. Strontium isotope composition of skeletal material can determine the birth place and geographic mobility of humans and animals. *Journal of Forensic Sciences* 45(5):1049–1061.
- Bern, C. R., A. R. Townsend, and G. L. Farmer. 2005. Unexpected dominance of parent-material strontium in a tropical forest on highly weathered soils. *Ecology* 86(3):626–632.
- Buikstra, J. E., T. D. Price, L. E. Wright, and J. H. Burton. 2004. Tombs from the Copan Necropolis: a

- life-history approach. Pages 191–213 in E. E. Bell, M. A. Canuto, and R. J. Sharer, editors. *Understanding early Classic Copan*. University of Pennsylvania Museum of Archaeology and Anthropology, Philadelphia, Pennsylvania, USA.
- Capo, R. C. and O. A. Chadwick. 1999. Sources of strontium and calcium in desert soil and calcrete. *Earth and Planetary Science Letters* 170(1–2):61–72.
- Capo, R. C., B. W. Stewart, and O. A. Chadwick. 1998. Strontium isotopes as tracers of ecosystem processes: theory and methods. *Geoderma* 82(1–3):197–225.
- Chadwick, O. A., L. A. Derry, C. R. Bern, and P. M. Vitousek. 2009. Changing sources of strontium to soils and ecosystems across the Hawaiian Islands. *Chemical Geology* 267(1–2):64–76.
- Chadwick, O. A., L. A. Derry, P. M. Vitousek, B. J. Huebert, and L. O. Hedin. 1999. Changing sources of nutrients during four million years of ecosystem development. *Nature* 397:491–497.
- Chesson, L. A., B. J. Tipple, G. N. Mackey, S. A. Hynek, D. P. Fernandez, and J. R. Ehleringer. 2012. Strontium isotopes in tap water from the coterminous USA. *Ecosphere* 3:art67.
- Draper, G. J., J. F. Lewis, and G. Gutiérrez. 1995. Geologic map of Hispaniola. <http://www.fiu.edu/orgs/caribgeol/hispaniola.html>
- Evans, J. A., J. Montgomery, and G. Wildman. 2009. Isotope domain mapping of ⁸⁷Sr/⁸⁶Sr biosphere variation on the Isle of Skye, Scotland. *Journal of the Geological Society* 166(4):617–631.
- Fekete, B. M., C. J. Vörösmarty, and W. Grabs. 2002. High-resolution fields of global runoff combining observed river discharge and simulated water balances. *Global Biogeochemical Cycles* 16(3):1042.
- Formenti, P., L. Schutz, Y. Balkanski, K. Desboeufs, M. Ebert, K. Kandler, A. Petzold, D. Scheuvens, S. Weinbruch, and D. Zhang. 2011. Recent progress in understanding physical and chemical properties of African and Asian mineral dust. *Atmospheric Chemistry and Physics* 11(16):8231–8256.
- French, C. D., and C. J. Schenk. and U.S. Geological Survey. 2004. Map showing geology, oil and gas fields, and geologic provinces of the Caribbean Region. Open-file report 97-470-K. U.S. Geological Survey, Central Energy Resources Team, Denver, Colorado, USA.
- Ginoux, P., J. M. Prospero, O. Torres, and M. Chin. 2004. Long-term simulation of global dust distribution with the GOCART model: correlation with North Atlantic Oscillation. *Environmental Modelling and Software* 19(2):113–128.
- Glaccum, R. A. and J. M. Prospero. 1980. Saharan aerosols over the tropical North Atlantic—Mineralogy. *Marine Geology* 37(3–4):295–321.
- Goldsmith, S. T., A. E. Carey, B. M. Johnson, S. A. Welch, W. B. Lyons, W. H. McDowell, and J. S. Pigott. 2010. Stream geochemistry, chemical weathering and CO₂ consumption potential of andesitic terrains, Dominica, Lesser Antilles. *Geochimica et Cosmochimica Acta* 74(1):85–103.
- Graustein, W. C. and R. L. Armstrong. 1983. The use of strontium-87/strontium-86 ratios to measure atmospheric transport into forested watersheds. *Science* 219:289–292.
- Grousset, F. E. and P. E. Biscaye. 2005. Tracing dust sources and transport patterns using Sr, Nd and Pb isotopes. *Chemical Geology* 222(3–4):149–167.
- Grousset, F. E., P. Rognon, G. Coudegaussen, and P. Pedemay. 1992. Origins of Peri-Saharan dust deposits traced by their Nd and Sr isotopic composition. *Palaeogeography Palaeoclimatology Palaeoecology* 93(3–4):203–212.
- Harmon, R. S., W. B. Lyons, D. T. Long, F. L. Ogden, H. Mitasova, C. B. Gardner, K. A. Welch, and R. A. Witherow. 2009. Geochemistry of four tropical montane watersheds, Central Panama. *Applied Geochemistry* 24(4):624–640.
- Hartmann, J. 2009. Bicarbonate-fluxes and CO₂-consumption by chemical weathering on the Japanese Archipelago: Application of a multi-lithological model framework. *Chemical Geology* 265(3–4):237–271.
- Hartmann, J., N. Jansen, H. H. Dürr, A. Harashima, K. Okubo, and S. Kempe. 2010. Predicting riverine dissolved silica fluxes to coastal zones from a hyperactive region and analysis of their first order controls. *International Journal of Earth Sciences* 99:207–230.
- Hartmann, J. and N. Moosdorf. 2011a. Coupling spatial geochemical and lithological information to distinguish silicate and non-silicate chemical weathering fluxes. *Applied Geochemistry* 26 Supplement (0):S281–S284.
- Hartmann, J., and N. Moosdorf. 2011b. Chemical weathering rates of silicate-dominated lithological classes and associated liberation rates of phosphorus on the Japanese Archipelago: Implications for global scale analysis. *Chemical Geology* 287:125–157.
- Hijmans, R. J., S. E. Cameron, J. L. Parra, P. G. Jones, and A. Jarvis. 2005. Very high resolution interpolated climate surfaces for global land areas. *International Journal of Climatology* 25(15):1965–1978.
- Hilley, G. E., C. P. Chamberlain, S. Moon, S. Porder, and S. D. Willett. 2010. Competition between erosion and reaction kinetics in controlling silicate-weathering rates. *Earth and Planetary Science Letters* 293(1–2):191–199.
- Hilley, G. E. and S. Porder. 2008. A framework for predicting global silicate weathering and CO₂ drawdown rates over geologic time-scales. *Proceedings of the National Academy of Sciences USA* 105(44):16855–16859.

- Hodell, D. A., R. L. Quinn, M. Brenner, and G. Kamenov. 2004. Spatial variation of strontium isotopes (Sr-87/Sr-86) in the Maya region: a tool for tracking ancient human migration. *Journal of Archaeological Science* 31(5):585–601.
- Huneus, N., et al. 2011. Global dust model intercomparison in AeroCom phase I. *Atmospheric Chemistry and Physics* 11(15):7781–7816.
- Jansen, N., J. Hartmann, R. Lauerwald, H. H. Dürr, S. Kempe, S. Loos, and H. Middelkoop. 2010. Dissolved silica mobilization in the conterminous USA. *Chemical Geology* 270(1-4):90–109.
- Jickells, T. D., S. Dorling, W. G. Deuser, T. M. Church, R. Arimoto, and J. M. Prospero. 1998. Air-borne dust fluxes to a deep water sediment trap in the Sargasso Sea. *Global Biogeochemical Cycles* 12(2):311–320.
- Jobbágy, E. G. and R. B. Jackson. 2001. The distribution of soil nutrients with depth: Global patterns and the imprint of plants. *Biogeochemistry* 53(1):51–77.
- Kandler, K., N. Benker, U. Bundke, E. Cuevas, M. Ebert, P. Knippertz, S. Rodríguez, L. Schütz, and S. Weinbruch. 2007. Chemical composition and complex refractive index of Saharan Mineral Dust at Izaña, Tenerife (Spain) derived by electron microscopy. *Atmospheric Environment* 41(37):8058–8074.
- Kelly, S., K. Heaton, and J. Hoogewerff. 2005. Tracing the geographical origin of food: The application of multi-element and multi-isotope analysis. *Trends in Food Science and Technology* 16(12):555–567.
- Kennedy, M. J., O. A. Chadwick, P. M. Vitousek, L. A. Derry, and D. M. Hendricks. 1998. Changing sources of base cations during ecosystem development, Hawaiian Islands. *Geology* 26(11):1015–1018.
- Laffoon, J. E., G. R. Davies, M. L. P. Hoogland, and C. L. Hofman. 2012. Spatial variation of biologically available strontium isotopes (⁸⁷Sr/⁸⁶Sr) in an archipelagic setting: A case study from the Caribbean. *Journal of Archaeological Science* 39(7):2371–2384.
- Lasaga, A. C. 1984. Chemical-kinetics of water-rock interactions. *Journal of Geophysical Research* 89(Nb6):4009–4025.
- Lasaga, A. C. and A. E. Blum. 1985. Growth dissolution rate laws of minerals based on experimental-data and Monte-Carlo simulations of surface processing. *Abstracts of Papers of the American Chemical Society* 190(Sep):59-GEC.
- Luo, C., N. M. Mahowald, and J. del Corral. 2003. Sensitivity study of meteorological parameters on mineral aerosol mobilization, transport, and distribution. *Journal of Geophysical Research: Atmospheres* 108(D15).
- Mahowald, N. M., A. R. Baker, G. Bergametti, N. Brooks, R. A. Duce, T. D. Jickells, N. Kubilay, J. M. Prospero, and I. Tegen. 2005. Atmospheric global dust cycle and iron inputs to the ocean. *Global Biogeochemical Cycles* 19(4).
- Mahowald, N. M., J. F. Lamarque, X. X. Tie, and E. Wolff. 2006. Sea-salt aerosol response to climate change: Last Glacial Maximum, preindustrial, and doubled carbon dioxide climates. *Journal of Geophysical Research: Atmospheres* 111(D5).
- McCulley, R. L., E. G. Jobbágy, W. T. Pockman, and R. B. Jackson. 2004. Nutrient uptake as a contributing explanation for deep rooting in arid and semi-arid ecosystems. *Oecologia* 141(4):620–628.
- Meybeck, M. and A. Ragu. 1997. Presenting the GEMS-GLORI, a compendium of world river discharge to the oceans. *Freshwater Contamination* (243):3–14.
- Moosdorf, N., J. Hartmann, and H. H. Dürr. 2010. Lithological composition of the North American continent and implications of lithological map resolution for dissolved silica flux modeling. *Geochemistry Geophysics Geosystems* 11(11):Q11003.
- Muhs, D. R. and J. R. Budahn. 2009. Geochemical evidence for African dust and volcanic ash inputs to terra rossa soils on carbonate reef terraces, northern Jamaica, West Indies. *Quaternary International* 196:13–35.
- Muhs, D. R., J. R. Budahn, J. M. Prospero, and S. N. Carey. 2007. Geochemical evidence for African dust inputs to soils of western Atlantic islands: Barbados, the Bahamas, and Florida. *Journal of Geophysical Research: Earth Surface* 112(F2).
- Muhs, D. R., C. A. Bush, K. C. Stewart, T. R. Rowland, and R. C. Crittenden. 1990. Geochemical evidence of Saharan dust parent material for soils developed on Quaternary limestones of Caribbean and western Atlantic islands. *Quaternary Research* 33(2):157–177.
- Naiman, Z., J. Quade, and P. J. Patchett. 2000. Isotopic evidence for eolian recycling of pedogenic carbonate and variations in carbonate dust sources throughout the southwest United States. *Geochimica et Cosmochimica Acta* 64(18):3099–3109.
- Nakai, S. L., A. N. Halliday, and D. K. Rea. 1993. Provenance of dust in the Pacific Ocean. *Earth and Planetary Science Letters* 119:143–157.
- Nakano, T. and T.-I. Tanaka. 1997. Strontium isotope constraints on the seasonal variation of the provenance of base cations in rain water at Kawakami, Central Japan. *Atmospheric Environment* 31(24):4237–4245.
- Nakano, T., Y. Yokoo, and M. Yamanaka. 2001. Strontium isotope constraint on the provenance of basic cations in soil water and stream water in the Kawakami volcanic watershed, central Japan. *Hydrological Processes* 15(10):1859–1875.
- Pett-Ridge, J. C., L. A. Derry, and J. K. Barrows. 2009a. Ca/Sr and ⁸⁷Sr/⁸⁶Sr ratios as tracers of Ca and Sr cycling in the Rio Icacos watershed, Luquillo Mountains, Puerto Rico. *Chemical Geology*

- 267(1-2):32-45.
- Pett-Ridge, J. C., L. A. Derry, and A. C. Kurtz. 2009b. Sr isotopes as a tracer of weathering processes and dust inputs in a tropical granitoid watershed, Luquillo Mountains, Puerto Rico. *Geochimica et Cosmochimica Acta* 73(1):25-43.
- Porder, S. and O. A. Chadwick. 2009. Climate and soil-age constraints on nutrient uplift and retention by plants. *Ecology* 90(3):623-636.
- Porder, S. and G. E. Hilley. 2011. Linking chronosequences with the rest of the world: predicting soil phosphorus content in denuding landscapes. *Biogeochemistry* 102(1-3):153-166.
- Pozwa, A., E. Dambrine, B. Ferry, B. Pollier, and M. Loubet. 2002. Do deep tree roots provide nutrients to the tropical rainforest? *Biochemistry* 60:97-118.
- Pozwa, A., B. Ferry, E. Dambrine, B. Pollier, T. Wickman, M. Loubet, and K. Bishop. 2004. Variations of bioavailable Sr concentration $^{87}\text{Sr}/^{86}\text{Sr}$ ratio in boreal forest ecosystems: Role of biocycling, mineral weathering and depth of root uptake. *Biochemistry* 67:1-20.
- Price, T. D. 2008. Isotopes and human migration: Case studies in biogeochemistry. Pages 243-272 in H. Schutkowski, editor. *Between biology and culture*. Cambridge University Press, Cambridge, UK.
- Price, T. D., J. H. Burton, and R. A. Bentley. 2002. The Characterization of biologically available strontium isotope ratios for the study of prehistoric migration. *Archaeometry* 44:117-136.
- Price, T. D., J. H. Burton, R. J. Sharer, J. E. Buikstra, L. E. Wright, L. P. Traxler, and K. A. Miller. 2010. Kings and commoners at Copan: Isotopic evidence for origins and movement in the Classic Maya period. *Journal of Anthropological Archaeology* 29(1):15-32.
- Price, T. D., J. H. Burton, L. E. Wright, C. D. White, and F. J. Longstaffe. 2007. Victims of sacrifice: isotopic evidence for place of origin. Pages 263-292 in *New perspectives on human sacrifice and ritual body treatments in ancient Maya society*. Springer, New York, New York, USA.
- Price, T. D., W. D. Middleton, and L. Manzanilla. 2000. Immigration and the ancient city of Teotihuacan in Mexico: a study using strontium isotope ratios in human bone and teeth. *Journal of Archaeological Science* 27:903-913.
- Price, T. D., V. Tiesler, and J. H. Burton. 2006. Early African diaspora in colonial Campeche, Mexico: strontium isotopic evidence. *American Journal of Physical Anthropology* 130(4):485-490.
- Prospero, J. M., E. Bonatti, C. Schubert, and T. N. Carlson. 1970. Dust in Caribbean atmosphere traced to an African dust storm. *Earth and Planetary Science Letters* 9(3):287.
- Prospero, J. M., W. M. Landing, and M. Schulz. 2010. African dust deposition to Florida: Temporal and spatial variability and comparisons to models. *Journal of Geophysical Research: Atmospheres* 115.
- Pushcharovski, I. M. M. 1989. *Mapas geologicas de Cuba*. Moskva, Geologicheskii institut AN SSSR.
- Rad, S. D., C. J. Allegre, and P. Louvat. 2007. Hidden erosion on volcanic islands. *Earth and Planetary Science Letters* 262(1-2):109-124.
- Rea, D. K. 1994. The Paleoclimatic record provided by Eolian deposition in the deep-sea: the geologic history of wind. *Reviews of Geophysics* 32(2):159-195.
- Reed, J. C., J. O. Wheeler, and B. E. Tucholke. Geological Society of America, and Decade of North American Geology Project. 2005. *Geologic map of North America*. Continent-scale map 001. Geological Society of America, Boulder, Colorado, USA.
- Rognon, P., G. CoudeGaussen, M. Revel, F. E. Grousset, and P. Pedemay. 1996. Holocene Saharan dust deposition on the Cape Verde islands: Sedimentological and Nd-Sr isotopic evidence. *Sedimentology* 43(2):359-366.
- Saunders, J. B. and A. W. Snoke. 1998. *Trinidad and Tobago geological map*. Port of Spain, Government of the Republic of Trinidad and Tobago, Ministry of Energy and Energy Industries.
- Schütz, L. and M. Seibert. 1987. Mineral aerosols and source identification. *Journal of Aerosol Science* 18(1):1-10.
- Stallard, R. F. and J. M. Edmond. 1983. Geochemistry of the Amazon 2: The influence of geology and weathering environment on the dissolved load. *Journal of Geophysical Research* 88:9671-9688.
- Stewart, B. W., R. C. Capo, and O. A. Chadwick. 1998. Quantitative strontium isotope models for weathering, pedogenesis and biogeochemical cycling. *Geoderma* 82(1-3):173-195.
- Stewart, B. W., R. C. Capo, and O. A. Chadwick. 2001. Effects of rainfall on weathering rate, base cation provenance, and Sr isotope composition of Hawaiian soils. *Geochimica et Cosmochimica Acta* 65(7):1087-1099.
- Tegen, I., M. Werner, S. P. Harrison, and K. E. Kohfeld. 2004. Relative importance of climate and land use in determining present and future global soil dust emission. *Geophysical Research Letters* 31(5).
- Thornton, E. K. 2011. Reconstructing ancient Maya animal trade through strontium isotope ($^{87}\text{Sr}/^{86}\text{Sr}$) analysis. *Journal of Archaeological Science* 38:3254-3263.
- Trabucco, A. and R. J. Zomer. 2010. *Global soil water balance geospatial database*. CGIAR Consortium for Spatial Information. <http://www.cgiar-csi.org>
- Trapp, J. M., F. J. Millero, and J. M. Prospero. 2010. Temporal variability of the elemental composition of African dust measured in trade wind aerosols at Barbados and Miami. *Marine Chemistry*

- 120(1-4):71–82.
- Vance, D., D. A. H. Teagle, and G. L. Foster. 2009. Variable Quaternary chemical weathering fluxes and imbalances in marine geochemical budgets. *Nature* 458:493–496.
- van Soest, M. C., D. R. Hilton, C. G. Macpherson, and D. P. Matthey. 2002. Resolving sediment subduction and crustal contamination in the Lesser Antilles Island Arc: a combined He–O–Sr isotope approach. *Journal of Petrology* 43(1):143–170.
- Veizer, J., D. Ala, K. Azmy, P. Bruckschen, D. Buhl, F. Bruhn, G. A. F. Carden, A. Diener, S. Ebner, Y. Godderis, T. Jasper, C. Korte, F. Pawellek, O. G. Podlaha, and H. Strauss. 1999. Sr-87/Sr-86, delta C-13 and delta O-18 evolution of Phanerozoic seawater. *Chemical Geology* 161:59–88.
- Vogel, T. A., L. C. Patino, J. K. Eaton, J. W. Valley, W. L. Rose, G. E. Alvarado, and E. L. Viray. 2006. Origin of silicic magmas along the Central American volcanic front: Genetic relationship to mafic melts. *Journal of Volcanology and Geothermal Research* 156(3–4):217–228.
- Vries, A. J. 2000. The semi-arid environment of Curacao: a geochemical soil survey. *Netherlands Journal of Geosciences Geologie en Mijnbouw* 79(4):479–494.
- White, A. F. and A. E. Blum. 1995. Effects of climate on chemical-weathering in watersheds. *Geochimica et Cosmochimica Acta* 59(9):1729–1747.
- White, A. F., A. E. Blum, M. S. Schulz, D. V. Vivit, D. A. Stonestrom, M. Larsen, S. F. Murphy, and D. Eberl. 1998. Chemical weathering in a tropical watershed, Luquillo mountains, Puerto Rico: I. Long-term versus short-term weathering fluxes. *Geochimica et Cosmochimica Acta* 62(2):209–226.
- White, C. D., T. D. Price, and F. J. Longstaffe. 2007. Residential histories of the human sacrifices at the Moon Pyramid, Teotihuacan: Evidence from oxygen and strontium isotopes. *Ancient Mesoamerica* 18:159–172.
- Wright, L. E. 2005. Identifying Immigrants to Tikal, Guatemala: Defining local variability in strontium isotope ratios of human tooth enamel. *Journal of Archaeological Science* 32:555–566.
- Wright, L. E., J. A. Valdés, J. H. Burton, T. D. Price, and H. P. Schwarcz. 2010. The children of Kaminaljuyu: Isotopic insight into diet and long distance interaction in Mesoamerica. *Journal of Anthropological Archaeology* 29:155–178.

SUPPLEMENTAL MATERIAL

APPENDIX A

Table A1. Parameterization of Eqs. 5 and 7 for each lithological descriptor present in the Caribbean geodatabase (French et al. 2004). Sr_ratio is calculated using the analogous descriptor from Bataille and Bowen (2012) and Eq. 1; b and b_0 are obtained from analogous descriptor and calibrations recalculated in Jansen et al. (2010); Sr/SiO₂ ratios is parameterized using median and standard deviation values from 121,253 analyses available through the Earthchem Portal for each descriptor from Bataille and Bowen (2012; www.earthchem.org; Query by “chemistry”: all Sr AND SiO₂, “database”: Georoc results).

Lithological descriptor	Sr_ratio	b_0	b	Sr/SiO ₂ median (SD)	Analogous descriptor	
					From Bataille and Bowen (2012)	From Jansen et al. (2010)
cretaceous amphibolite	0.7067	0.018	0.834	0.0007 (±0.0004)	Amphibolites	Metamorphics
Cretaceous andesitic to silicic volcanic rocks	0.7042	0.018	1.166	0.0007 (±0.0004)	Andesites	Acid and Intermediate Volcanics
Cretaceous granite	0.7114	0.018	0.956	0.0003 (±0.0004)	Granites	Acid Plutonics
Cretaceous marine strata	0.7077	0.028	0.776	0.0150 (±0.015)	Carbonates	Carbonate Sedimentary Rocks
Cretaceous metasedimentary and metaigneous rocks, low to intermediate metamorphism	0.7056	0.018	0.834	0.0005 (±0.0009)	Metamorphic rocks	Metamorphics
Cretaceous plutons, mostly intermediate to silicic	0.7098	0.018	0.956	0.0003 (±0.0004)	Plutonic rocks	Acid Plutonics
Cretaceous quartz diorite	0.7053	0.028	1.010	0.0007 (±0.0004)	Quartz diorites	Basic and Intermediate Plutonics
Cretaceous sedimentary and volcanic rocks	0.7056	0.018	1.031	0.0007 (±0.0004)	Volcanic rocks	Acid and Intermediate Volcanics
Cretaceous volcanic rocks	0.7056	0.018	1.031	0.0007 (±0.0004)	Volcanic rocks	Acid and Intermediate Volcanics

Table A1. Continued.

Lithological descriptor	Sr_ratio	b_0	b	Sr/SiO ₂ median (SD)	Analogous descriptor	
					From Bataille and Bowen (2012)	From Jansen et al. (2010)
Eclogite	0.7040	0.018	1.031	0.0003 (± 0.0004)	Volcanic rocks	Acid and Intermediate Volcanics
Eocene and Paleocene volcanic flows and associated pyroclastic and volcanoge	0.7052	0.018	1.166	0.0007 (± 0.0004)	Volcanic rocks	Basic volcanic and pyroclastics
Eocene and(or) Paleocene marine strata	0.7077	0.028	0.776	0.0150 (± 0.015)	Carbonates	Carbonate Sedimentary Rocks
Eocene strata	0.7080	0.028	0.776	0.0150 (± 0.015)	Carbonates	Carbonate Sedimentary Rocks
Gabbro	0.7041	0.028	1.010	0.0003 (± 0.0003)	Gabbros	Basic and Intermediate Plutonics
Gabbro and related rocks	0.7040	0.028	1.010	0.0003 (± 0.0003)	Gabbros	Basic and Intermediate Plutonics
Granite	0.7114	0.018	0.956	0.0003 (± 0.0004)	Granites	Acid Plutonics
Intrusive rocks, undivided, mostly intermediate to silicic	0.7069	0.018	0.956	0.0003 (± 0.0004)	Plutonic rocks	Acid Plutonics
Jurassic and Triassic marine and continental strata	0.7077	0.028	0.776	0.0150 (± 0.015)	Carbonates	Carbonate Sedimentary Rocks
Jurassic and Triassic sedimentary and volcanic rocks	0.7061	0.018	1.031	0.0007 (± 0.0004)	Volcanic rocks	Acid and Intermediate Volcanics
Jurassic complex of sedimentary, igneous, and metamorphic rocks	0.7058	0.018	0.834	0.0005 (± 0.0009)	Metamorphic rocks	Metamorphics
Jurassic marine and continental strata	0.7075	0.028	0.776	0.0150 (± 0.015)	Carbonates	Carbonate Sedimentary Rocks
Jurassic volcanic rocks, mostly andisitic to silicic	0.7042	0.018	1.031	0.0007 (± 0.0004)	Andesites	Acid and Intermediate Volcanics
Lower Cretaceous flows, breccia, and tuff, partly of marine deposition	0.7073	0.028	0.776	0.0150 (± 0.015)	Carbonates	Carbonate Sedimentary Rocks
Mesozoic amphibolites and associated metasedimentary rocks	0.7067	0.018	0.834	0.0007 (± 0.0004)	Amphibolites	Metamorphics
Mesozoic and Paleozoic marine and continental strata	0.7082	0.028	0.776	0.0150 (± 0.015)	Carbonates	Carbonate Sedimentary Rocks
Mesozoic and Paleozoic metasedimentary and metagneous rocks	0.7061	0.018	0.834	0.0003 (± 0.0004)	Metamorphic rocks	Metamorphics
Mesozoic flows and small plutons, mostly intermediate to silicic	0.7105	0.018	0.956	0.0003 (± 0.0004)	Plutonic rocks	Acid Plutonics
Mesozoic metamorphic rock	0.7061	0.018	0.834	0.0005 (± 0.0009)	Metamorphic rocks	Metamorphics
Mesozoic metasedimentary and metagneous rocks, low to intermediate metamorphic	0.7061	0.018	0.834	0.0005 (± 0.0009)	Metamorphic rocks	Metamorphics
Mesozoic metavolcanic and associated metasedimentary rocks	0.7059	0.018	0.834	0.0005 (± 0.0009)	Metavolcanic rocks	Metamorphics
Mesozoic plutons, mostly intermediate to silicic	0.7105	0.018	0.956	0.0003 (± 0.0004)	Plutonic rocks	Acid Plutonics
Mesozoic sedimentary and volcanic rocks	0.7061	0.018	1.031	0.0007 (± 0.0004)	Volcanic rocks	Acid and Intermediate Volcanics
Mesozoic volcanic and sedimentary rocks	0.7061	0.018	1.031	0.0007 (± 0.0004)	Volcanic rocks	Acid and Intermediate Volcanics
Miocene and Oligocene volcanic rocks	0.7050	0.018	1.031	0.0007 (± 0.0004)	Volcanic rocks	Acid and Intermediate Volcanics
Mylonite or cataclastic zone along major fault (Guyana Shield)	0.7198	0.018	0.834	0.0005 (± 0.0009)	Mylonites	Metamorphics
Oligocene strata	0.7085	0.028	0.776	0.0150 (± 0.015)	Carbonates	Carbonate Sedimentary Rocks
Paleozoic and Precambrian igneous and metamorphic rocks, undivided	0.7143	0.018	0.834	0.0005 (± 0.0009)	Metamorphic rocks	Metamorphics
Paleozoic and Precambrian metamorphic rocks, undivided	0.7143	0.018	0.834	0.0005 (± 0.0009)	Metamorphic rocks	Metamorphics
Paleozoic granite	0.7196	0.018	0.956	0.0003 (± 0.0004)	Granites	Acid Plutonics
Paleozoic plutons, mostly intermediate to silicic	0.7196	0.018	0.956	0.0003 (± 0.0004)	Plutonic rocks	Acid Plutonics

Table A1. Continued.

Lithological descriptor	Sr_ratio	b_0	b	Sr/SiO ₂ median (SD)	Analogous descriptor	
					From Bataille and Bowen (2012)	From Jansen et al. (2010)
Paleozoic strata	0.7082	0.028	0.776	0.0150 (±0.015)	Carbonates	Carbonate Sedimentary Rocks
Paleozoic volcanic rocks	0.7076	0.018	1.031	0.0007 (±0.0004)	Volcanic rocks	Acid and Intermediate Volcanics
Permian granite	0.7124	0.018	0.956	0.0003	Granites	Acid Plutonics
Pliocene and Miocene andesitic flows and associated volcanic rocks	0.7040	0.018	1.031	0.0007 (±0.0004)	Andesites	Acid and Intermediate Volcanics
Pliocene and Miocene strata	0.7088	0.028	0.776	0.0150 (±0.015)	Carbonates	Carbonate Sedimentary Rocks
Pliocene calc-alkaline volcanic rocks	0.7050	0.018	1.031	0.0007 (±0.0004)	Volcanic rocks	Acid and Intermediate Volcanics
Post-Eocene continental strata	0.7085	0.028	0.776	0.0150 (±0.015)	Carbonates	Carbonate Sedimentary Rocks
Post-Eocene marine strata	0.7085	0.028	0.776	0.0150 (±0.015)	Carbonates	Carbonate Sedimentary Rocks
Precambrian amphibolite and associated metasedimentary and metaigneous rocks	0.7076	0.028	1.010	0.0003 (±0.0004)	Amphibolites	Basic and Intermediate Plutonics
Precambrian diabase sills and dikes: Ages 1,500–1,750 my	0.7031	0.028	1.010	0.0003 (±0.0004)	Diabases	Basic and Intermediate Plutonics
Precambrian gneiss	0.7348	0.018	0.956	0.0005 (±0.0009)	Gneisses	Acid Plutonics
Precambrian granitic rocks: Ages 1,000–1,550 my	0.7375	0.018	0.956	0.0003 (±0.0004)	Granites	Acid Plutonics
Precambrian granitic rocks. Ages 1,800–3,140 my	0.7679	0.018	0.956	0.0003 (±0.0004)	Granites	Acid Plutonics
Precambrian igneous and metamorphic rocks, undivided	0.7310	0.018	0.834	0.0005 (±0.0009)	Metamorphic rocks	Metamorphics
Precambrian metamorphic rocks of low grade	0.7310	0.018	0.834	0.0005 (±0.0009)	Metamorphic rocks	Metamorphics
Precambrian metasedimentary and metaigneous rocks, undivided	0.7310	0.018	0.834	0.0005 (±0.0009)	Metamorphic rocks	Metamorphics
Precambrian metasedimentary and metavolcanic rocks	0.7310	0.018	0.834	0.0005 (±0.0009)	Metamorphic rocks	Metamorphics
Precambrian quartzofeldspathic gneiss, ferruginous quartzite, and banded bio	0.7348	0.018	0.834	0.0005 (±0.0009)	Gneisses	Metamorphics
Precambrian silicic flows, tuffs, and ignimbrites	0.7348	0.018	1.166	0.0003 (±0.0004)	Felsic volcanic	Acid and Intermediate Volcanics
Precambrian ultramafic rocks	0.7040	0.028	1.010	0.000002 (±0.0004)	Ultramafic rocks	Basic and Intermediate Plutonics
Quartz diorite	0.7053	0.028	1.010	0.0007 (±0.0004)	Quartz diorites	Basic and Intermediate Plutonics
Quaternary alluvium	0.7080	0.018	1.056	0.0003 (±0.0004)	Alluvium	Unconsolidated Sediments
Quaternary and Tertiary continental deposits	0.7092	0.028	0.776	0.0150 (±0.015)	Carbonates	Carbonate Sedimentary Rocks
Quaternary and Tertiary marine limestone, sandstone, and shale	0.7090	0.028	0.776	0.0150 (±0.015)	Carbonates	Carbonate Sedimentary Rocks
Quaternary and Tertiary volcanic edifices, flows, tuff, silicic pyroclastic	0.7041	0.018	1.166	0.0007 (±0.0004)	Andesites	Basic volcanic and pyroclastics
Quaternary pumice fills and pyroclastic mantles	0.7041	0.018	1.166	0.0007 (±0.0004)	Andesites	Basic volcanic and pyroclastics
Quaternary volcanic edifices, flows, and pyroclastic deposits	0.7041	0.018	1.166	0.0007 (±0.0004)	Andesites	Basic volcanic and pyroclastics
Recent volcanic	0.7051	0.018	1.031	0.0007 (±0.0004)	Volcanic rocks	Acid and Intermediate Volcanics
Tertiary and Cretaceous complex of deformed sedimentary rocks Metamorphics	0.7106	0.018	0.834	0.0003 (±0.0004)		Metasedimentary rocks
Tertiary and Cretaceous continental strata	0.7078	0.028	0.776	0.0150 (±0.015)	Carbonates	Carbonate Sedimentary Rocks
Tertiary and Cretaceous marine strata	0.7077	0.028	0.776	0.0150 (±0.015)	Carbonates	Carbonate Sedimentary Rocks

Table A1. Continued.

Lithological descriptor	Sr_ratio	b_0	b	Sr/SiO ₂ median (SD)	Analogous descriptor	
					From Bataille and Bowen (2012)	From Jansen et al. (2010)
Tertiary and Cretaceous plutons, mostly intermediate to silicic	0.7098	0.018	0.956	0.0003 (± 0.0004)	Plutonic rocks	Acid Plutonics
Tertiary and Cretaceous volcanic rocks	0.7056	0.018	1.031	0.0007 (± 0.0004)	Volcanic rocks	Acid and Intermediate Volcanics
Tertiary continental strata	0.7085	0.028	0.776	0.0150 (± 0.015)	Carbonates	Carbonate Sedimentary Rocks
Tertiary granite	0.7099	0.018	0.956	0.0003 (± 0.0004)	Granites	Acid Plutonics
Tertiary marine strata	0.7085	0.028	0.776	0.0150 (± 0.015)	Carbonates	Carbonate Sedimentary Rocks
Tertiary plutons, mostly intermediate to silicic	0.7092	0.018	0.956	0.0003 (± 0.0004)	Plutonic rocks	Acid Plutonics
Tertiary volcanic rocks	0.7052	0.018	1.031	0.0007 (± 0.0004)	Volcanic rocks	Acid and Intermediate Volcanics
Ultramafic rocks	0.7032	0.028	1.010	0.0009	Ultramafic rocks	Basic and Intermediate Plutonics
Upper Cretaceous marine strata	0.7076	0.028	0.776	0.0150 (± 0.015)	Carbonates	Carbonate Sedimentary Rocks
Volcanic rocks	0.7050	0.018	1.031	0.0007 (± 0.0004)	Volcanic rocks	Acid and Intermediate Volcanics

CHAPTER IV

A GEOSTATISTICAL FRAMEWORK TO PREDICT STRONTIUM ISOTOPES VARIATIONS IN ALASKA RIVERS

Reprinted from *Chemical Geology*, Vol. 389, C.P., Bataille, S.R., Brennan, J., Hartmann, N., Moosdorf, M.J., Wooller, G.J., Bowen, A geostatistical framework for predicting variations in strontium concentrations and isotope ratios in Alaskan rivers, pp. 1-15.
Copyright 2014, with permission from Elsevier.

Abstract

Bataille and Bowen (2012) developed models to predict $^{87}\text{Sr}/^{86}\text{Sr}$ in rocks (bedrock model) and rivers (catchment water model) for regional provenance study. Here, we revisit those models formulation and calibration and we apply them to predict Sr concentrations and $^{87}\text{Sr}/^{86}\text{Sr}$ of Alaska Rivers. In a first step, we add several new components and/or improvements to resolve limitations of the bedrock model, including: 1) an independent siliciclastic sediment submodel, 2) an explicit consideration of $^{87}\text{Sr}/^{86}\text{Sr}$ variability at local scale, and 3) a fully-coupled assessment of prediction uncertainty. Tested against a compilation of 885 $^{87}\text{Sr}/^{86}\text{Sr}$ rock analyses across Alaska, the bedrock model significantly improves $^{87}\text{Sr}/^{86}\text{Sr}$ prediction accuracy in both igneous and sedimentary settings. In a second step, we develop a fully independent Sr chemical weathering model calibrated using a database of 339 Sr concentrations analyses from rivers of North hemisphere high-latitudes and predicting the spatial variations in the rate of Sr release from rocks as a function of lithology, permafrost cover and slope. We combine the bedrock and Sr chemical weathering models to predict Sr concentration and $^{87}\text{Sr}/^{86}\text{Sr}$ in Alaska Rivers. Tested on a dataset of 61 water samples from Alaska Rivers, the resulting catchment water model explains 82% of $^{87}\text{Sr}/^{86}\text{Sr}$ variations. We use the catchment water model to estimate the average Sr concentration and $^{87}\text{Sr}/^{86}\text{Sr}$ of Alaska runoff and compare those predicted values to Sr concentration and $^{87}\text{Sr}/^{86}\text{Sr}$ of the Yukon River. The predicted average Sr concentration and $^{87}\text{Sr}/^{86}\text{Sr}$ of the entire Alaska surface runoff – $104.3 \mu\text{g}\cdot\text{L}^{-1}$ and 0.7098, respectively – differs significantly from those of the Yukon River – $139.3 \mu\text{g}\cdot\text{L}^{-1}$ and 0.7137, respectively. This result questions the assumption that Sr concentration and $^{87}\text{Sr}/^{86}\text{Sr}$ are representative of the entire Earth

surface. The data products from this work can also provide robust baseline $^{87}\text{Sr}/^{86}\text{Sr}$ maps in rocks and rivers for regional provenance studies over Alaska.

Introduction

Variations in the ratio of 87-strontium on 86-strontium ($^{87}\text{Sr}/^{86}\text{Sr}$) in seawater have been used for decades as a proxy to reconstruct the interplay of mantle processes and continental weathering on the Earth's surface at million years' time scale (Brevart and Allegre, 1977; Burke et al., 1982; Chaudhuri and Clauer, 1986; Peterman et al., 1970; Shields, 2007; Veizer, 1989; Veizer and Compston, 1974). However, interpreting the $^{87}\text{Sr}/^{86}\text{Sr}$ variations in seawater remain challenging and a multitude of hypotheses have been advanced to explain diagnostic features of the seawater $^{87}\text{Sr}/^{86}\text{Sr}$ curve. For instance, it has been argued that the rapid increase in $^{87}\text{Sr}/^{86}\text{Sr}$ in seawater over the last 40Ma could be associated to climatic factors such as a shift from greenhouse to icehouse periods enhancing high latitude denudation rates (Armstrong, 1971; Zachos et al., 1999) as well as tectonic factors such as orogenesis rate or change in subduction and seafloor spreading rate (Edmond, 1992; Raymo et al., 1988).

The interpretation of $^{87}\text{Sr}/^{86}\text{Sr}$ variations in seawater relies heavily on our understanding of the modern strontium (Sr) budget in seawater. The modern Sr budget in seawater is thought to be primarily controlled by the input of Sr from two isotopically distinct Sr fluxes: a radiogenic Sr flux from continental runoff and a poorly constrained nonradiogenic Sr flux from the mantle including island arcs weathering (Allègre et al., 2010), ophiolites weathering (Davis et al., 2003), and on and off-axis hydrothermal alteration at oceanic ridges (Coogan and Gillis, 2013; Spooner, 1976). The magnitude

and isotopic signature of each of these fluxes in the modern Sr budget in seawater has been estimated by compiling worldwide dataset of Sr concentrations and $^{87}\text{Sr}/^{86}\text{Sr}$ from rivers and fluid samples recovered from on and off-axis oceanic ridges (Brass, 1976; Palmer and Edmond, 1992; Peucker-Ehrenbrink et al., 2010). However, the observation that the current estimates of the nonradiogenic and radiogenic Sr fluxes do balance each other feeds a vivid debate about the accuracy of the empirically-based estimates of those Sr fluxes. Some scientists argue that the current Sr budget is inaccurate and/or missing some fluxes (Allègre et al., 2010; Beck et al., 2013; Coogan and Gillis, 2013; Jones et al., 2014; Jones et al., 2012); whereas others argue that the modern Sr budget is not at steady-state in postglacial periods (Davis et al., 2003; Vance et al., 2009). Developing models able to predict Sr concentrations and $^{87}\text{Sr}/^{86}\text{Sr}$ in rivers at regional scale could give a more robust framework to improve the estimate of the Sr flux and $^{87}\text{Sr}/^{86}\text{Sr}$ from continental runoff and island arcs and help to resolve this debate.

A prerequisite before developing models predicting $^{87}\text{Sr}/^{86}\text{Sr}$ in rivers is to develop a model to predict $^{87}\text{Sr}/^{86}\text{Sr}$ in rocks because bedrock is the dominant source of Sr in the Earth's surface. In previous work, Bataille and Bowen (2012) developed a bedrock model which predicts $^{87}\text{Sr}/^{86}\text{Sr}$ variations in rocks as a function of rock type and rock age. This model showed promising results when applied to the conterminous US and circum-Caribbean regions (Bataille and Bowen, 2012; Bataille et al., 2012), but suffered from a poor representation of $^{87}\text{Sr}/^{86}\text{Sr}$ heterogeneity within and between rock units across a range of spatial scales as well as a poor formulation of $^{87}\text{Sr}/^{86}\text{Sr}$ variations in siliciclastic sediments.

Another critical step to predict $^{87}\text{Sr}/^{86}\text{Sr}$ in river water is to develop models

predicting the release of Sr by chemical weathering to account for the variable contribution of different rock units to the dissolved Sr in rivers. Bataille and Bowen (2012) developed an initial chemical weathering model accounting for the differential weathering rates and Sr content of different rock types. Bataille et al. (2012) took another approach by applying an adapted version of a multilinear regression model (Hartmann, 2009) predicting solute concentration in rivers as a function of lithological proportion and mean runoff of the catchment. However, this last chemical weathering model is not applicable at high-latitudes and does not account for Sr specific weathering processes.

Here, we add new components and improvements to resolve the limitations of previous versions of the bedrock and chemical weathering models to enhance the predictive power of $^{87}\text{Sr}/^{86}\text{Sr}$ in bedrock and water. We apply those models to predict Sr concentrations and $^{87}\text{Sr}/^{86}\text{Sr}$ in Alaska Rivers (R). Alaska is an ideal area to extend our modeling work because of i) limited human impact on Alaska R, ii) a wealth of geochemical and geological data existing for this region, and iii) a new spatially extensive dataset reporting solute concentrations and $^{87}\text{Sr}/^{86}\text{Sr}$ in 61 Alaska R (Brennan et al., in press). Alaska is also an interesting location to test the sensitivity of the high-latitudes Sr budget to geologic and physiographic factors because Alaska displays a varied geology, large topographic variations and a broad range of climatic conditions. We focus on testing the influence of geology (age and lithology), topography (slope), climate (temperature, runoff), and glacial processes (permafrost and alpine glacier cover) on the Sr concentrations and $^{87}\text{Sr}/^{86}\text{Sr}$ of Alaska R.

Material and methods

Bedrock model

The formulation and calibration of this new bedrock model are standardized to make use of the new global lithological map (GLiM) (Hartmann and Moosdorf, 2012). The GLiM divides rock of the Earth surface into 16 major lithological classes including plutonic and volcanic acid (pa and va), basic (pb and vb), intermediate rocks (pi, py and vi); metamorphic rocks (mt); and siliciclastic (ss), unconsolidated (su), mixed (sm), carbonate (sc) and evaporite sedimentary rocks (ev). The geology of Alaska is represented by 57,714 polygons with an average area of 48 km² and a median age of 57 Myrs.

Igneous submodel

Igneous submodel formulation

For igneous rocks, we keep the model formulation described in Bataille and Bowen (2012) but we develop new calibration steps to assess the uncertainty and overcome the poor representation of high resolution $^{87}\text{Sr}/^{86}\text{Sr}$ variability. Based on the tectonic history of the Earth, Bataille and Bowen (2012) made the simplifying assumption that the modern $^{87}\text{Sr}/^{86}\text{Sr}$ of silicate rocks can be approximated based on a three stage history. Before the onset of plate tectonics and the beginning of recycling and chemical differentiation of crustal material (Dhuime et al., 2012), ^{87}Sr was produced in the chemically quasi-undifferentiated Earth until $^{87}\text{Sr}/^{86}\text{Sr}$ reached 0.701 at 3 Ga (an approximation of the age of the onset of plate tectonics, t_1). After 3 Ga, geochemical differentiation between crust and mantle accelerated and $^{87}\text{Sr}/^{86}\text{Sr}$ evolved independently in the mantle and multiple crustal rock reservoirs having different Rb/Sr ratios. In the

third stage, extant rock units were formed from one of these rock reservoirs at times corresponding to the rock unit ages (t_2), as documented in geological map data. From this theoretical framework, Bataille and Bowen (2012) derived the following equation:

$$\left(\frac{{}^{87}\text{Sr}}{{}^{86}\text{Sr}}\right)_{\text{rock}} = 0.701 + \left(\frac{{}^{87}\text{Rb}}{{}^{86}\text{Sr}}\right)_{\text{parent}} (e^{\lambda(t_1-t_2)} - 1) + \left(\frac{{}^{87}\text{Rb}}{{}^{86}\text{Sr}}\right)_{\text{rock}} (e^{\lambda t_2} - 1), \quad (4.1)$$

where λ is the decay constant of the parent isotope ($1.42 \times 10^{-11} \text{ yr}^{-1}$), $({}^{87}\text{Rb}/{}^{86}\text{Sr})_{\text{parent}}$ is the ${}^{87}\text{Rb}/{}^{86}\text{Sr}$ of the parent material, and $({}^{87}\text{Rb}/{}^{86}\text{Sr})_{\text{rock}}$ is the ${}^{87}\text{Rb}/{}^{86}\text{Sr}$ of the modern rock.

${}^{87}\text{Rb}/{}^{86}\text{Sr}$ can be expressed as:

$$\frac{{}^{87}\text{Rb}}{{}^{86}\text{Sr}} = \frac{\text{Rb}(w^{87}\text{Rb})(m\text{Sr})}{\text{Sr}(w^{86}\text{Sr})(m\text{Rb})} = k \frac{\text{Rb}}{\text{Sr}} \approx 2.8936 \frac{\text{Rb}}{\text{Sr}}, \quad (4.2)$$

where m refers to the atomic mass of an element and w to the abundance (%) of an isotope and k to the conversion factor. $w^{86}\text{Sr}$ and $m\text{Sr}$ depend on the abundance of ${}^{87}\text{Sr}$ and hence on the ${}^{87}\text{Sr}/{}^{86}\text{Sr}$ of each sample. When using the modern abundance of ${}^{87}\text{Rb}$ of 27.8346 % and a ${}^{87}\text{Sr}/{}^{86}\text{Sr}=0.70916$ (seawater), k equals 2.8936 (Faure, 1977). k only increases by a negligible amount when ${}^{87}\text{Sr}/{}^{86}\text{Sr}$ increases from 0.7 to 1. To simplify our calculations, we neglected changes in $w^{86}\text{Sr}$ and $m\text{Sr}$ and assumed a constant k value of 2.8936.

Igneous submodel calibration

In t_2 calibration step (Fig. 4.1), we estimated the numeric minimum and maximum age of each rock unit of Alaska from the age descriptor given in the GLiM

database using the USGS geological time scale (U.S. Geologic Names Committee and Geological Survey, 2007).

In $(^{87}\text{Rb}/^{86}\text{Sr})_{\text{parent}}$ *calibration step* (Fig. 4.1), we proceeded as in Bataille and Bowen (2012), using a $n=31,421$ worldwide dataset downloaded from the Earthchem portal (www.earthchem.org; Query by “chemistry”: $^{87}\text{Sr}/^{86}\text{Sr}$ and Sr and Rb, “Age”=Age exists) containing $^{87}\text{Sr}/^{86}\text{Sr}$, age and Rb/Sr. We grouped samples into 7 subdatasets following their major plutonic, volcanic and metamorphic GLiM lithological classes (mt, pa, pb, pi, va, vb, vi). We then back-calculated $(^{87}\text{Rb}/^{86}\text{Sr})_{\text{parent}}$ for each igneous rock sample by solving equation 4.1. For each GLiM lithological class, the resulting distribution of $(^{87}\text{Rb}/^{86}\text{Sr})_{\text{parent}}$ dataset is strongly positively skewed. To resolve this issue, we power-transformed $(^{87}\text{Rb}/^{86}\text{Sr})_{\text{parent}}$ for each subdataset (R, car package, powerTransform function) to achieve a normal distribution and calculated the mean and standard deviation for each lithological class (Supplementary material and Tables 4S.1 and 4S.2).

In $(^{87}\text{Rb}/^{86}\text{Sr})_{\text{rock}}$ *calibration step* (Fig. 4.1), we overcome the limitations of Bataille and Bowen (2012) by using ordinary kriging to estimate $(^{87}\text{Rb}/^{86}\text{Sr})_{\text{rock}}$. Bataille and Bowen (2012) parameterized $(^{87}\text{Rb}/^{86}\text{Sr})_{\text{rock}}$ using a median approach for each lithological class which did not allow considering Rb/Sr variability within rock units. Ordinary kriging provides a spatially explicit interpolation and variance estimate for a given coordinate location. We obtained a dataset of 18,706 samples of Rb/Sr analyses from igneous rocks across the study area using the Alaska geochemical database (Granitto et al., 2013). We used Rb/Sr data to calculate $(^{87}\text{Rb}/^{86}\text{Sr})_{\text{rock}}$ using equation 4.2. We classified the data following their major igneous GLiM lithological class (pa, pb, pi,

va, vb, vi and mt) and examined the statistical characteristics of each dataset. For each class, the distribution of $^{87}\text{Rb}/^{86}\text{Sr}$ analysis is nonnormal, strongly skewed and contains some outliers. We removed outliers because they can bias statistical results, and because ordinary kriging is optimal when the data has a normal distribution (Saito and Goovaerts, 2000). We power transformed the $^{87}\text{Rb}/^{86}\text{Sr}$ dataset towards normality (R, car package, powerTransform function) (Supplementary material and Tables 4S.3 and 4S.4). For each GLIM lithological class, we fitted the most appropriate semivariogram model on the power transformed datasets and applied ordinary kriging on the resulting datasets to predict mean and standard deviation of $(^{87}\text{Rb}/^{86}\text{Sr})_{rock}$ at each pixel (1km by 1km resolution) across the study area (Supplementary material and Tables 4S.5, 4S.6 and 4S.7).

Carbonate submodel

Bataille and Bowen (2012) also developed an independent model for carbonates and evaporites (sc and ev classes from the GLIM) because $(^{87}\text{Sr}/^{86}\text{Sr})_{rock}$ of carbonates is mostly a function of $^{87}\text{Sr}/^{86}\text{Sr}$ in seawater at the time of deposition:

$$\left(\frac{^{87}\text{Sr}}{^{86}\text{Sr}}\right)_{rock} = \left(\frac{^{87}\text{Sr}}{^{86}\text{Sr}}\right)_{seawater} + \left(\frac{^{87}\text{Rb}}{^{86}\text{Sr}}\right)_{rock} (e^{\lambda t_2} - 1), \quad (4.3)$$

where $(^{87}\text{Sr}/^{86}\text{Sr})_{seawater}$ is the $^{87}\text{Sr}/^{86}\text{Sr}$ of seawater at t_2 the time of deposition.

The formulation of the carbonate submodel here remains identical to that of Bataille and Bowen (2012), and we only modify our approach to parameterization estimation. In t_2 calibration step, we determined the minimum and maximum age of each

rock unit as for the igneous submodel t_2 calibration step. In $^{87}\text{Sr}/^{86}\text{Sr}_{\text{seawater}}$ calibration step, we used the minimum and maximum age of each carbonate rock unit of the GLiM over Alaska to estimate the minimum and maximum $^{87}\text{Sr}/^{86}\text{Sr}_{\text{seawater}}$ from the *Precambrian Marine Carbonate Isotope Database* (Shields and Veizer, 2002). In $(^{87}\text{Rb}/^{86}\text{Sr})_{\text{rock}}$ calibration step, we proceeded similarly as with the igneous submodel $(^{87}\text{Rb}/^{86}\text{Sr})_{\text{rock}}$ calibration step, by applying ordinary kriging on a screened and power-transformed dataset of 358 Rb/Sr analyses from carbonates (used to calculate $^{87}\text{Rb}/^{86}\text{Sr}$ from equation 4.2) gathered from the Alaska geochemical database (Granitto et al., 2013). We developed a spatially explicit parameterization for $(^{87}\text{Rb}/^{86}\text{Sr})_{\text{rock}}$ because Rb/Sr in carbonates display some spatial variability originating primarily from the higher average Rb/Sr of dolomites in comparison with limestones (Simo et al., 2009). Details and results on each of the statistical steps of this work are given in Supplementary material and Tables 4S.3, 4S.4, 4S.5, 4S.6 and 4S.7.

Siliciclastic sedimentary rock submodel

Siliciclastic sedimentary rock submodel formulation

Accurate modeling of siliciclastic sedimentary rocks is crucial because they cover close to 50% of the Earth's surface (Hartmann and Moosdorf, 2012). In Bataille and Bowen (2012), the siliciclastic sedimentary rock submodel formulation and calibration steps are identical to the igneous submodel (equation 4.1). t_2 is estimated using the age of sediment deposition, $(^{87}\text{Rb}/^{86}\text{Sr})_{\text{rock}}$ is estimated using the median modern Rb/Sr value of a given siliciclastic sedimentary rock type, and $(^{87}\text{Rb}/^{86}\text{Sr})_{\text{parent}}$ is back-calculated from equation 4.1. A fundamental inaccuracy in this modeling approach is that up to 95% of

clastic sediments on the Earth's surface are derived from recycling of preexisting sediments and are composed of detrital grains from geologically-distinct parent rocks deposited at different periods (Veizer and Jansen, 1979). Consequently, the actual geological age of siliciclastic sedimentary rocks differs from the age of the sediment deposition (t_2) given by geological maps (Garrels and Mackenzie, 1971; Goldstein, 1988; Veizer and Mackenzie, 2003). The detrital origin of siliciclastic sedimentary rocks lead to a progressive increase of their Rb/Sr during their recycling history because of both the increasing Rb/Sr of their parent rocks associated with magmatic processes and the preferential weathering of nonradiogenic Sr (Bickle, 1994; Garrels and Mackenzie, 1971; Goldstein, 1988; McDermott and Hawkesworth, 1990; Veizer, 1973; Veizer and Mackenzie, 2003). Moreover, in the past 3Ga, the rate of crustal recycling largely exceeded the rate of new crust formation leading to an acceleration of $^{86}\text{Rb}/^{87}\text{Sr}$ increase through time (Cawood et al., 2012).

One solution to overcome these issues is to take terrane (genetically related fragment of continental crust) into account because terranes play an important role in determining the geochemistry of siliciclastic sediments (Veizer and Jansen, 1979). Alaska is composed of a series of autochthonous and allochthonous terranes which accreted to the North American craton (Fig. 4.2) (Nelson et al., 2013). Siliciclastic sedimentary rocks deposited on young outboard and insular terranes display a unimodal age distribution of detrital zircons, centered on the age of the terrane on which they were deposited suggesting that igneous rocks from this terrane were their primary parent rock (Amato and Pavlis, 2010; Gehrels et al., 1996). Siliciclastic sedimentary rocks from older terranes or cratons display much more complex multimodal age distribution reflecting the

different parent rocks and multiple recycling events leading to the formation of those siliciclastic sedimentary units (Bradley et al., 2007; Miller et al., 2006; Nelson and Gehrels, 2007). As a result, the Rb/Sr of siliciclastic sedimentary units lying on older terranes is generally much higher than the Rb/Sr of siliciclastic sedimentary units from younger Phanerozoic terranes, reflecting the higher degree of recycling of older sediments (Goldstein, 1988; McDermott and Hawkesworth, 1990).

We build upon these ideas to develop a new siliciclastic sedimentary rocks submodel formulation. The modern $^{87}\text{Sr}/^{86}\text{Sr}$ of siliciclastic sedimentary rocks can be approximated based on a four-stage history with the first, second and fourth steps identical to the first, second and third calibration steps of the igneous submodel. We add an intermediate third step which accounts for recycling occurring between t_T (age of formation of a given terrane) and t_2 (age of deposition of the modern siliciclastic sedimentary unit). During that time, the Rb/Sr of siliciclastic sediments deposited and recycled on a given terrane increases exponentially with time from the Rb/Sr value of the dominant igneous rocks of the terrane to the modern Rb/Sr value of the siliciclastic sedimentary unit. The $^{87}\text{Sr}/^{86}\text{Sr}$ of siliciclastic sedimentary rocks ($(^{87}\text{Sr}/^{86}\text{Sr})_{ss}$) is predicted following the equation:

$$\left(\frac{^{87}\text{Sr}}{^{86}\text{Sr}}\right)_{ss} = 0.701 + \left(\frac{^{87}\text{Rb}}{^{86}\text{Sr}}\right)_{parent} (e^{\lambda(t_1-t_2)} - 1) + \int_{t=t_T}^{t=t_2} \left(\left(\frac{^{87}\text{Rb}}{^{86}\text{Sr}}\right)_T\right)_t (e^{\lambda(t)} - 1) dt + \left(\frac{^{87}\text{Rb}}{^{86}\text{Sr}}\right)_{rock} (e^{\lambda t_2} - 1), \quad (4.4)$$

where $(^{87}\text{Rb}/^{86}\text{Sr})_{parent}$ is the $^{87}\text{Rb}/^{86}\text{Sr}$ of the parent igneous rock of the terrane, $((^{87}\text{Rb}/^{86}\text{Sr})_T)_t$ is age-dependent $^{87}\text{Rb}/^{86}\text{Sr}$ of siliciclastic sedimentary rocks from the terrane between t_T and t_2 and $(^{87}\text{Rb}/^{86}\text{Sr})_{rock}$ is the $^{87}\text{Rb}/^{86}\text{Sr}$ of the modern siliciclastic

sedimentary units.

$(^{87}\text{Rb}/^{86}\text{Sr})_T$ can be expressed as:

$$\left(\left(\frac{^{87}\text{Rb}}{^{86}\text{Sr}} \right)_T \right)_t = b \exp(at), \quad (4.5)$$

where a and b are parameters calculated from boundary conditions at t_T with

$(^{87}\text{Rb}/^{86}\text{Sr})_T = (^{87}\text{Rb}/^{86}\text{Sr})_{\text{parent}}$ and at t_T with $(^{87}\text{Rb}/^{86}\text{Sr})_T = (^{87}\text{Rb}/^{86}\text{Sr})_{\text{rock}}$. The exponential function represents the progressive increase of $^{87}\text{Rb}/^{86}\text{Sr}$ of siliciclastic sedimentary rocks from $(^{87}\text{Rb}/^{86}\text{Sr})_T$ to $(^{87}\text{Rb}/^{86}\text{Sr})_{\text{rock}}$ as the terrane gets older and increasingly recycled material from multiple parent rocks mixes with siliciclastic sedimentary rocks at the surface of the terrane.

Siliciclastic sedimentary rock submodel calibration

In t_2 calibration step, we determined the minimum and maximum age of each rock unit as for the igneous submodel t_2 calibration step.

In $(^{87}\text{Rb}/^{86}\text{Sr})_{\text{parent}}$ calibration step, we determined the primary igneous lithology and corresponding major igneous GLiM lithological class (pa,pb,pi,va,vb,vi,mt) of each Alaska terrane based on their geological history (Supplementary material and Table 4S.8). We then used the $(^{87}\text{Rb}/^{86}\text{Sr})_{\text{parent}}$ calculated in the igneous submodel $(^{87}\text{Rb}/^{86}\text{Sr})_{\text{rock}}$ calibration step to assign a $(^{87}\text{Rb}/^{86}\text{Sr})_{\text{parent}}$ to each terrane corresponding to its major GLiM lithological class (see “Igneous submodel” section).

In t_T calibration step, we estimated the numeric maximum and minimum age of each Alaska terrane unit present in the digital atlas of terranes for the Northern Cordillera

(Colpron and Nelson, 2011) from the detailed geological history of each individual terrane of Alaska (Nelson et al., 2013) (Supplementary material and Table 4S.8).

In $(^{87}\text{Rb}/^{86}\text{Sr})_{\text{rock}}$ calibration step, we proceeded similarly as with the igneous submodel $(^{87}\text{Rb}/^{86}\text{Sr})_{\text{rock}}$ calibration step. We applied ordinary kriging on a screened and power-transformed dataset of 17,727 Rb/Sr analyses for siliciclastic sedimentary rock analyses from the Alaska geochemical database (Granitto et al., 2013). Details and results on each of the statistical steps of this work are given in Supplementary material and Tables 4S.3, 4S.4, 4S.5, 4S.6 and 4S.7.

Uncertainty assessment for each submodel calibration step

We calculated the distribution of predicted $^{87}\text{Sr}/^{86}\text{Sr}$ values at each pixel given the distribution and uncertainty of each submodel input parameter using Monte Carlo simulation procedures (Fig. 4.1). Input parameters include t_2 , $(^{87}\text{Rb}/^{86}\text{Sr})_{\text{parent}}$ and $(^{87}\text{Rb}/^{86}\text{Sr})_{\text{rock}}$ for the igneous submodel, t_2 , $(^{87}\text{Rb}/^{86}\text{Sr})_{\text{rock}}$ and $(^{87}\text{Sr}/^{86}\text{Sr})_{\text{seawater}}$ for the carbonate submodel and t_2 , t_T , $(^{87}\text{Rb}/^{86}\text{Sr})_{\text{parent}}$ and $(^{87}\text{Rb}/^{86}\text{Sr})_{\text{rock}}$ for the siliciclastic sediment rock submodel. For each submodel, we used the mc2d package in R (Pouillot and Delignette-Muller, 2010) to repeat 10,000 random draws from the distribution of each input parameter with:

- t_2 described using a uniform distribution between the estimated minimum and maximum age at each rock unit derived from the t_2 calibration step of the igneous, carbonate and siliciclastic sedimentary rock submodels
- $(^{87}\text{Rb}/^{86}\text{Sr})_{\text{parent}}$ described using a normal distribution derived from the power-transformed mean and standard deviation calculated in the $(^{87}\text{Rb}/^{86}\text{Sr})_{\text{parent}}$

- calibration step of the igneous and siliciclastic sedimentary rock submodels
- $(Rb/Sr)_{rock}$ described using a normal distribution derived from the power-transformed mean and standard deviation calculated in the $(^{87}Rb/^{86}Sr)_{rock}$ calibration step of the igneous, carbonate and siliciclastic sedimentary rock submodels
 - $(^{87}Sr/^{86}Sr)_{seawater}$ described using a uniform distribution between the minimum and maximum $(^{87}Sr/^{86}Sr)_{seawater}$ derived from $(^{87}Sr/^{86}Sr)_{seawater}$ calibration step of the carbonate submodel
 - t_T described using a uniform distribution between the minimum and maximum age of each Alaska terranes of the t_T .

The R scripts used for the different submodels are available in Supplementary material (Scripts 4S.1, 4S.2 and 4S.3).

Geographic information system processing

The output $^{87}Sr/^{86}Sr$ rasters obtained for each submodel from the Monte Carlo simulations were clipped using the GLiM rock unit polygons of Alaska corresponding to each submodel including igneous rock units (pa, pb, pi, va, vb, vi, mt), carbonate units (sc, ev) and sedimentary rock units (sm, ss, su). Those clipped submodel output $^{87}Sr/^{86}Sr$ rasters were then mosaicked (ArcGIS/Data Management Toolbox) to calculate the minimum, maximum, decile 1, decile 10, quartile 1 and quartile 3, median $^{87}Sr/^{86}Sr$ values across the entire Alaska surface (Fig. 4.3A, 4.3B and 4.3C).

Bedrock model validation dataset

We compiled and georeferenced validation data from the literature, including 97 $^{87}\text{Sr}/^{86}\text{Sr}$ analyses in sedimentary rocks and 788 $^{87}\text{Sr}/^{86}\text{Sr}$ analyses in igneous rocks sampled in Alaska (Fig. 4.4A, Fig. 4.4B and Table 4S.9). Georeferencing was accomplished either by using reported latitude/longitude values given in the publication or by estimating latitude and longitude using other geographical data from the publication (e.g., map) and Google Earth.

Chemical weathering model

We developed a Sr specific chemical weathering model using multiple linear regression model techniques and following the statistical framework described in Hartmann (2009). Detailed steps and limitations associated with the dataset used to develop the Sr chemical weathering model are described in Supplementary material.

Chemical weathering model calibration dataset

An initial step before testing the significance of different predictors on predicting Sr concentrations in rivers using multiple linear regression models consisted in compiling and georeferencing a calibration dataset of Sr concentrations in rivers. Starting from an existing dataset (Peucker-Ehrenbrink et al., 2010), we compiled and georeferenced 405 published Sr concentration and isotope data from major rivers and tributaries from North hemisphere high-latitudes (Fig. 4.5A and Table 4S.10). From this dataset, we selected a chemical weathering model calibration dataset of 339 Sr concentration data (Table 4S.10) excluding 66 samples which shared part of their drainage catchment in common with

another sample in the calibration set. We selected only high-latitude rivers (catchments above 60°N) to limit the range of temperature and its potential effect on chemical weathering. Georeferencing was accomplished either using reported latitude/longitude values given in the publication or by estimating latitude and longitude using other geographical data from the publication (e.g., map) and Google Earth. Each sample point of the calibration dataset was manually snapped on the river network derived from the Hydro1K dataset (Data available from the U.S. Geological Survey) and used to define their catchment feature (Spatial Analyst/Hydrology Toolbox).

Chemical weathering model predictors across the calibration catchments

In a second step, we gathered spatial datasets describing the variations of potential predictors of Sr concentrations in rivers across the North hemisphere high-latitudes. Solute concentration in rivers is primarily determined by major geological properties of the catchment (Goldstein and Jacobsen, 1988; Jeandel et al., 2007; Livingstone, 1963; Mackenzie and Garrels, 1966; Meybeck, 1987; Stallard and Edmond, 1983). We used the global lithological map (GLiM) reprojected and resampled onto an equal area projection (WGS84-EckertIV) and uniform 1 km² grid (ArcGIS/Data Management Tools) (Hartmann and Moosdorf, 2012) to calculate the proportion of each lithology on calibration catchments. It is also well-known that some sparse Sr-rich lithologies such as evaporites or trace calcite can significantly contribute to the Sr flux (Blum et al., 1998; Huh et al., 1998b; White et al., 1999b). To account for the potential influence of those Sr-rich lithologies, we calculated the proportion of evaporite in each calibration catchment from the global distribution of salt basins (Hudec and Jackson, 2007).

While lithology is the primary source of Sr to rivers, other environmental factors can modulate the contribution of different lithologies to the Sr flux to rivers, including runoff amount and rate (Gaillardet et al., 1999; Meybeck, 1987), temperature (Brady, 1991; Huh and Edmond, 1999; White et al., 1999a), and topography (Raymo et al., 1988). For each calibration catchment, we calculated mean annual runoff from the Global Runoff Data Center runoff dataset (Fekete et al., 2002), mean annual temperature from the 30 arc-seconds WorldClim mean annual temperature dataset (Hijmans et al., 2005), and mean slope from the 30 arc-seconds resolution GTOPO30 dataset (USGS, 1996). High-latitudes permafrost and thawing mechanisms (Huh et al., 1998a; Keller et al., 2010) as well as alpine glacier processes (Anderson, 2007; Armstrong, 1971) could be an important control of the Sr budget. We calculated the mean permafrost cover from the global permafrost extent and zonation index (Gruber, 2012). Using the Global Land Ice, we found that only three samples from the chemical weathering model calibration dataset had some alpine glacier cover in their catchments (Kargel et al., 2013), which is not sufficient to test the influence of this parameter on Sr concentrations in rivers. In absence of sufficient data for high-latitudes, we did not consider the potential effect of soil processes (Stewart et al., 2001; White et al., 1996; White and Brantley, 2003) and land cover (Boucot and Gray, 2001) on the rate of Sr release from different rock units.

Multiple linear regression model calibration

We used the summary statistics of each predictor across the catchment of the chemical weathering model calibration dataset to evaluate the statistical significance of different multivariate linear regression models following the method described in

Hartmann (2009). We iteratively tested the potential of different variables as predictors of Sr concentrations in river waters starting with proportion of major lithology and successively testing the addition of other variables to multiple linear regression models, including evaporite proportion, mean permafrost index, mean slope, mean runoff and mean temperature. Scatterplot analyses of trends of each multiple linear regression model residuals with variables not included in the model were used to identify additional predictors of Sr concentrations in river. To include those factors, model equations were adapted (incorporating new parameters) and analyzed again in an iterative process (Hartmann, 2009). Different model forms (linear and nonlinear) were tested and only model forms for which each individual parameter was significant (p-value<0.05) were considered (Hartmann, 2009). The significance of each individual parameter addition to a given model form was tested by looking at the change in variance of the residuals from the model. If the variance of the residuals was significantly decreased (F-test between models) by the parameter addition, we tested the significance (p-value<0.05) of each individual parameter of the new model. At equivalent goodness of fit the simplest model form (equal) was preferred over the more complex (nonlinear) model forms. For more details on the model form selection, see details in Hartmann (2009) method.

Equation 4.6 represents the Sr chemical weathering model that best combines prediction quality and parameter significance for the river Sr calibration dataset:

$$\ln(Sr) = \frac{1}{\sum_i L_i} \left(L_{ssed} b_{ssed} + L_{sc} b_{sc} + L_{sm} b_{sm} + L_{ig} b_{ig} + L_{mt} b_{mt} + L_{salt} b_{salt} \right) + \overline{pfi} b_{pfi} + \overline{slope} b_s \quad (4.6)$$

where $\ln(Sr)$ is the logarithm of Sr concentrations; L_{ssed} , L_{sc} , L_{sm} , L_{ig} , L_{mt} and L_{salt} are,

respectively, the proportion of each lithological class calculated from the GLiM, including siliclastic sedimentary (ss), carbonates (sc), mixed sediments (sm), plutonic and volcanic acid, basic and intermediate rocks (pa, va, pb, vb, pi, vi), metamorphic rocks (mt), and evaporites (ev). The proportion of each lithological class is normalized so that the sum of the i lithologies ($\sum L_i$) within the catchment totals 1; \overline{pfi} and \overline{slope} are the average permafrost zonation index (Gruber, 2012) and slope (in degrees) across each catchment; b_{ssed} , b_{sc} , b_{sm} , b_{ig} , b_{mt} and b_{salt} , b_{pfi} and b_s are the associated chemical weathering model parameters for each variable calculated from the Levenberg-Marquart estimation techniques implemented in Statistica (STATSOFT©) (Table 4.1)

Local water model

We combined the chemical weathering and bedrock models to develop a local water model, which estimates the $^{87}\text{Sr}/^{86}\text{Sr}$ of strontium weathered from local bedrock at each map grid cell ($(^{87}\text{Sr}/^{86}\text{Sr})_{local}$). The $(^{87}\text{Sr}/^{86}\text{Sr})_{local}$ is equal to $^{87}\text{Sr}/^{86}\text{Sr}$ of the bedrock except when the primary lithology is a mixture of lithologies, such as mixed sediments (sm class in the GLiM), or when Sr-rich secondary lithologies are reported in the GLiM, such as evaporites and carbonates (xxev and xxpu classes in the GLiM). In those special cases, $(^{87}\text{Sr}/^{86}\text{Sr})_{local}$ is calculated using the following equations:

$$\left(\frac{^{87}\text{Sr}}{^{86}\text{Sr}}\right)_{local} = \left(\frac{0.75 * Sr_{major}}{Sr_{local}}\right) * \left(\frac{^{87}\text{Sr}}{^{86}\text{Sr}}\right)_{major} + \left(\frac{0.25 * Sr_{minor}}{Sr_{local}}\right) * \left(\frac{^{87}\text{Sr}}{^{86}\text{Sr}}\right)_{minor}, \quad (4.7)$$

$$Sr_{local} = 0.75 * Sr_{major} + 0.25 * Sr_{minor}, \quad (4.8)$$

where 0.75 and 0.25 are the “best guess” estimates of relative major and minor lithology proportions, respectively, used in the absence of reported quantitative proportions in the GLiM ; $(Sr)_{major}$ and $(Sr)_{minor}$ are the predicted Sr concentrations of the major and minor lithologies from the Sr chemical weathering model; $(^{87}Sr/^{86}Sr)_{major}$ and $(^{87}Sr/^{86}Sr)_{minor}$ are the isotopic signature from each lithology calculated from the bedrock model.

In a final step, we calculated the distribution of predicted $(^{87}Sr/^{86}Sr)_{local}$ values at each pixel (Script 4S.4) using Monte Carlo simulation procedures. Input parameters for the local water model includes $(^{87}Sr/^{86}Sr)_{major}$, $(^{87}Sr/^{86}Sr)_{minor}$, $(Sr)_{major}$ and $(Sr)_{minor}$. We used the mc2d package in R (Pouillot and Delignette-Muller, 2010) to repeat 10,000 random draws from the distribution of each input parameter with:

- $(^{87}Sr/^{86}Sr)_{major}$ and $(^{87}Sr/^{86}Sr)_{minor}$ are described using a lognormal distribution (R, mc2d package) derived from the mean and standard deviation predicted by the bedrock model.
- $(Sr)_{major}$ and $(Sr)_{minor}$ are calculated using equation 4.6 and the multiple linear regression model parameters from Table 4.1.

Catchment water model

We combined the chemical weathering and local water models to develop a catchment water model, which estimates the $^{87}Sr/^{86}Sr$ of surface waters flowing through each map location, including all contributions from up-catchment locations. The catchment water map of Alaska was created using the Flow Accumulation tool (Spatial Analyst toolbox) in ArcGIS and 1 km gridded flow direction values (Hydro 1K dataset). We applied equation 4.10 to calculate the annual Sr isotope ratio flux (FSr_{iso}) and

equation 11 to calculate the annual Sr flux (FSr) by accumulating each flux down-stream through the Hydro 1K river network. We divided FSr_{iso} by FSr (equation 4.11) to obtain estimated water $^{87}\text{Sr}/^{86}\text{Sr}$ values that represented an average of the up-stream Sr sources to each map pixel, weighted by the contribution of Sr flux from each pixel in the catchment:

$$FSr_{iso} = \sum Q(Sr)_{local} \left(\frac{^{87}\text{Sr}}{^{86}\text{Sr}} \right)_{local}, \quad (4.9)$$

$$FSr = \sum Q(Sr)_{local}, \quad (4.10)$$

$$\left(\frac{^{87}\text{Sr}}{^{86}\text{Sr}} \right)_{catchment} = \frac{FSr_{iso}}{FSr}, \quad (4.11)$$

where $(Sr)_{local}$ is the Sr concentration calculated from equation 4.8, $(^{87}\text{Sr}/^{86}\text{Sr})_{local}$ is the $^{87}\text{Sr}/^{86}\text{Sr}$ from the local water model calculated from equation 4.7, and Q is the mean annual runoff from the GRDC dataset (Fekete et al., 2002).

Chemical weathering model and catchment water model

validation dataset

To validate the chemical weathering model and catchment water model, we compared the predictions of Sr concentrations and $^{87}\text{Sr}/^{86}\text{Sr}$ in Alaska Rivers from the chemical weathering and catchment water models with the observed Sr concentrations and $^{87}\text{Sr}/^{86}\text{Sr}$ in 61 Alaska R (Fig. 4.6). The sampling strategy, analytical methods, and interpretations related to the generation of this dataset gathering various solute analyzes

in 61 Alaska R are described extensively in a companion paper (Brennan et al. in press).

Results and discussion

Bedrock model

Patterns of $^{87}\text{Sr}/^{86}\text{Sr}$ variations from the bedrock model

On a scale of thousands to hundreds of kilometers, the variations in $^{87}\text{Sr}/^{86}\text{Sr}$ range and median values across Alaska from the bedrock model (Fig. 4.3A, 4.3B and 4.3C) reflect the geological history and successive production and/or accretion of terranes to the Laurentian cratonic core of Ancestral North American (Fig. 4.2). We observe a general trend of decreasing median and range of $^{87}\text{Sr}/^{86}\text{Sr}$ values from Northeast to Southwest. This trend is largely driven by the difference in rock age with older rocks from the Laurentian North American craton in the East and younger rocks associated with newly produced or accreted terranes in the Southwest of Alaska (Fig. 4.2). The dominance of age on the continental scale $^{87}\text{Sr}/^{86}\text{Sr}$ variations is related to the unique geological setting of Alaska, where Precambrian cratonic rocks are juxtaposed with newly-produced mafic terranes (Nelson et al., 2013).

On a scale of tens of kilometers, $^{87}\text{Sr}/^{86}\text{Sr}$ variations display much higher variability than Bataille and Bowen's (2012) bedrock model (Fig. 4.3D) that are driven by changes in rock unit age and/or lithology as well as intra-unit variability. The new bedrock model also represents spatial variation in $^{87}\text{Sr}/^{86}\text{Sr}$ prediction uncertainty (Fig. 4.3A, 4.3B and 4.3C), with the ranges of $^{87}\text{Sr}/^{86}\text{Sr}$ at each pixel reflecting the limits of available constraints on age and lithology resolution from the dataset used to develop the bedrock models. This consideration of $^{87}\text{Sr}/^{86}\text{Sr}$ prediction uncertainty as a function of

model parameters at a particular location is a substantial improvement over Bataille and Bowen's (2012) approach.

Bedrock model validation

We extracted the bedrock model value (ArcGIS/Spatial Analyst Toolbox) for each sample point of the bedrock model validation dataset (Table 4S.9). The igneous and siliciclastic sedimentary rock submodels explain 72% and 51% of the observed $^{87}\text{Sr}/^{86}\text{Sr}$ variations of igneous and siliciclastic sedimentary rocks, respectively (Fig. 4.4A and 4.4B). These new models significantly improved the coefficient of determination (R^2) in comparison with Bataille and Bowen's (2012) bedrock model. Predictions are clustering much closer to the 1:1 relationship (Fig. 4.4A and 4.4B). Other goodness of fit indices less sensitive than R^2 to outliers also suggest large improvements in the predictive power of the new bedrock model (Table 4.2). For the igneous and siliciclastic sedimentary rock data, respectively, the mean absolute errors for model predictions are 0.00176 and 0.00356 for the new bedrock model and 0.00244 and 0.00650 for the Bataille and Bowen's (2012) model applied to Alaska (Table 4.2). For both the igneous and siliciclastic sedimentary rock submodels, the remaining error (Table 4.2) and negative bias (Fig. 4.4A and 4.4B) are likely related to the $(^{87}\text{Rb}/^{86}\text{Sr})_{\text{parent}}$ calibration step, which remains based on a median approach and does not account for spatial variations in rock chemistry and initial $^{87}\text{Sr}/^{86}\text{Sr}$ related to tectonic settings. Further improving the bedrock model will require more detailed geological maps and information on parent rock history for each unit, including constraints on the evolution of magmatic fluids, metamorphic processes, and sediment provenance.

Chemical weathering model

Chemical weathering model calibration results

Significant predictors of Sr concentrations were found to include major lithological proportions – carbonates, siliciclastic and mixed sedimentary rocks, metamorphic rocks, and igneous rocks – proportion of evaporites, mean permafrost zonation index, and mean slope (equation 4.6 and Table 4.1). A multiple linear regression model considering only major lithological proportion as predictors of Sr concentration explains 45% of the variance in Sr concentrations. Substantial improvements were obtained by combining major lithologies with other predictors including proportion of evaporite ($R^2=0.58$), proportion of evaporite and mean permafrost zonation index ($R^2=0.62$), and proportion of evaporite, mean permafrost zonation index and mean slope ($R^2=0.65$; Fig 4.5B). Mean runoff and mean temperatures were not significant predictors of $\ln(\text{Sr})$ on the chemical weathering calibration dataset. For all the tested models, residuals were normally distributed and have a mean close to 0 (e.g., Fig. 4.5C).

Chemical weathering model validation in Alaska Rivers

Indices of goodness of fit demonstrate that the chemical weathering model predicts reasonably well the Sr concentrations of the 61 Alaska Rivers (R) from the chemical weathering model validation dataset (Table 4.3). When removing the five major outliers – South Fork of the Kuskokwim, the Dietrich, the Middle Fork of the Koyukuk, the Nenana and the Canning R (Fig. 4.6 and Fig. 4.7A) – the predicted Sr fluxes explain 40% of the variations of observed Sr concentrations (Fig. 4.7A). However, this prediction accuracy is significantly lower for Alaska R than for the chemical weathering model

calibration dataset (Fig. 4.5B), and we attempt to identify the factors influencing the chemical weathering model residuals.

Spatial patterning and interpretation of chemical weathering model

residuals

A geographic pattern is apparent in the chemical weathering model residuals. The chemical weathering model tends to overpredict Sr concentrations in rivers from Southwest Alaska including the Ahklun Mountains Province and the Alaskan-Aleutian Range and to underpredict Sr concentrations in rivers from South-central Alaska including the Chugach Mountains, the Wrangelia Composite Terrane (Fig. 4.6). Most rivers from Southwest Alaska have observed Sr concentrations ranging from $30 \mu\text{g.L}^{-1}$ to $60 \mu\text{g.L}^{-1}$, whereas rivers from the South-central Alaska have Sr concentrations ranging between $100 \mu\text{g.L}^{-1}$ and $250 \mu\text{g.L}^{-1}$. Southwest and South-central rivers both drain similarly steep mountainous terrains composed primarily of igneous rocks related to Cenozoic Arc and Paleozoic to Mesozoic volcanoclastic sediments. In South-central Alaska marine flysch from the accretionary complex of the Chugach terrane is also present.

We suspect that the overestimation of Sr concentrations in Southwest Alaska R is related to the lithological classification of the GLiM. The geology of this area is primarily constituted of volcanoclastic units but in the GLiM those units are classified within the broad siliciclastic sediments GLiM class (ss). The ss GLiM class encompasses a large variety of sedimentary rocks from marine shales to continental volcanoclastic units (Hartmann and Moosdorf, 2012). Fine-grained marine siliciclastic sediments usually

contain a significant proportion of carbonate and are likely to release more Sr than coarse-grained volcanoclastic sediments. In our Sr chemical weathering model, all ss rocks release Sr at the same rate and we suspect the model overestimates the Sr flux from volcanoclastic units. Separating the ss GLiM class into different subclasses might resolve this issue but will require more detail in the GLiM lithological classification.

By contrast, the underestimation of the Sr concentrations in South-central Alaska is surprising considering that most watersheds from this area also contain large amounts of volcanoclastic units. Rivers of South-central Alaska – the Klutina, Nizina, Chitina, the Little Tonsina and Matanuska R – display high Sr concentrations ranging between 150 $\mu\text{g.L}^{-1}$ to 250 $\mu\text{g.L}^{-1}$. Those rivers display high Ca and Na concentrations (Brennan et al., in press). Some Paleocene marine flysch units are present in those watersheds (Harris et al., 1996) but if marine Sr from those flysch units were the principal source of the high Sr concentrations of the South-central Alaska rivers, we would expect their $^{87}\text{Sr}/^{86}\text{Sr}$ values to converge towards the Paleocene seawater $^{87}\text{Sr}/^{86}\text{Sr}$ values around 0.7076-0.708 (Veizer et al., 1999). The $^{87}\text{Sr}/^{86}\text{Sr}$ of those rivers remain fairly low (~ 0.706) and suggests that marine Sr is not the only contributor to the large Sr concentrations in those rivers. The chemical weathering model also underpredicts the Sr concentrations of five rivers from the Alaska Range and Brook Range regions including the South Fork of the Kuskokwim, the Dietrich, the Middle Fork of the Koyukuk, the Nenana and the Canning R, which all display very high Sr concentrations ($>300 \mu\text{g.L}^{-1}$) (red triangles on Fig. 4.7A). Those rivers also display high Ca and Na concentrations (Brennan et al., in press). Here again, the geology of the watersheds and the varied $^{87}\text{Sr}/^{86}\text{Sr}$ of those rivers indicate that the marine Sr does not appear to be the primary source of the high Sr concentrations in those

watersheds.

We hypothesize that the high Sr of the South-central Alaska R and of the five rivers from the Alaska Range and Brook Range regions are related to the presence of alpine glaciers and periglacial loess in their headwaters (Kargel et al., 2013). Previous studies have shown that the solute flux from glacier-covered basins tends to be dominated by calcite dissolution (trace calcite and/or marine carbonates) regardless of bedrock geology (Anderson, 2007). Even when the watershed is composed of silicate rocks, dissolution of trace calcite from those lithologies leads to very high Sr and Ca concentrations in rivers (Anderson, 2007). Moreover, the enhanced dissolution of trace calcite might explain the nonmarine $^{87}\text{Sr}/^{86}\text{Sr}$ of most of the rivers underpredicted by the chemical weathering model because trace calcite from silicate lithologies has a nonmarine $^{87}\text{Sr}/^{86}\text{Sr}$. This is reinforced by Anderson et al. (2000) who demonstrated that in tributaries draining the Bench glacier in South-central Alaska, the Sr flux and $^{87}\text{Sr}/^{86}\text{Sr}$ of rivers was dominated by a mixing between nonradiogenic trace calcite from silicate lithologies and marine carbonates dissolution with $^{87}\text{Sr}/^{86}\text{Sr}$ of seawater. Enhanced trace calcite and/or marine carbonate dissolution due to alpine glacial processes appears to be an important factor in explaining chemical weathering model residuals in Alaska and was not taken into account in our chemical weathering model calibration.

Catchment model

Patterns of $^{87}\text{Sr}/^{86}\text{Sr}$ variations in Alaska Rivers from the catchment model

$^{87}\text{Sr}/^{86}\text{Sr}$ from the catchment water model applied to Alaska displays a similar pattern to that predicted by the bedrock model (Fig. 4.8A, 4.8B and 4.8C), with a strong influence of terrane age on the regional $^{87}\text{Sr}/^{86}\text{Sr}$ signatures of rivers. Rivers draining the Ancestral North American Craton or old terranes (Fig. 4.2) display high $^{87}\text{Sr}/^{86}\text{Sr}$, whereas rivers draining young arc terranes (Fig. 4.2) display low $^{87}\text{Sr}/^{86}\text{Sr}$. In comparison with the bedrock model, both the variability and median $^{87}\text{Sr}/^{86}\text{Sr}$ value from the catchment water model are strongly buffered by nonradiogenic carbonate units present in most watersheds.

Catchment water model validation

The catchment model predicts $^{87}\text{Sr}/^{86}\text{Sr}$ values of river waters well, with 89% of the observed $^{87}\text{Sr}/^{86}\text{Sr}$ values falling within the interquartile range of the simulated prediction (Fig. 4.7B). Removing the four major outliers – Nenana, Chena, Salcha and Chatanika R. (red squares on Fig. 4.7B) – the catchment model explains 82% of the variance with a mean absolute error equal to 0.0012 (Table 4.4). Other indices of goodness of fit metrics show very good performance of the catchment water model (Table 4.4) and significant improvement in comparison with the Bataille and Bowen's (2012) catchment model.

Interpretations of catchment model outliers

Among the four major outliers, the Nenana River is the only river where the model exhibits a strong positive $^{87}\text{Sr}/^{86}\text{Sr}$ bias as well as underpredicted Sr concentration in the Sr chemical weathering model. The geology of the watershed is highly simplified in the GLiM as most of the watershed is represented as siliclastic sedimentary rocks without any carbonate lithologies reported. We hypothesized that the overestimation of the catchment water model and underestimation of Sr concentration in this catchment is related to the absence of representation of nonradiogenic Sr-rich metalimestones contribution to the river Sr budget in the catchment model. Assuming a $^{87}\text{Sr}/^{86}\text{Sr}$ of 0.708 for the Paleozoic metalimestone units (Veizer, 1989), we calculated that carbonate would have to contribute 66% of the catchment Sr flux to match the observed $^{87}\text{Sr}/^{86}\text{Sr}$ and Sr concentrations. This large contribution from minor carbonate lithologies could be possible given the presence of active glaciers in the catchment which enhance calcite dissolution (Anderson, 2007).

Three rivers draining the Yukon Tanana uplands – the Salcha, Chena and Chatanika R – have observed $^{87}\text{Sr}/^{86}\text{Sr}$ much higher than those predicted by the catchment water model. These rivers are all tributaries of the Tanana River and flow westward draining similar Paleozoic and Precambrian metamorphic units composed of quartzite, amphibolites and rare marble locally intruded by Mesozoic granitoid plutons (Newberry et al., 1996). This geology is well-reproduced by the GLiM and the bedrock model predicts accurately the $^{87}\text{Sr}/^{86}\text{Sr}$ of siliclastic units in this region with predicted $^{87}\text{Sr}/^{86}\text{Sr}$ ranging from 0.714 to 0.740 (median at 0.724) for the metamorphic units and predicted $^{87}\text{Sr}/^{86}\text{Sr}$ ranges from 0.704 to 0.712 (median at 0.707) for the Mesozoic

granitoid plutons. Those values compare well with the observed end-member $^{87}\text{Sr}/^{86}\text{Sr}$ values for water draining those metamorphic and plutonic rocks (Goldfarb et al., 1997). While the bedrock model appears to predict accurately the $^{87}\text{Sr}/^{86}\text{Sr}$ of siliciclastic units, the chemical weathering model predicts that between 40% and 60% of the Sr flux in those catchments originate from nonradiogenic marine carbonate lithologies.

Two hypotheses could explain the mismatch between predicted and observed $^{87}\text{Sr}/^{86}\text{Sr}$ and Sr concentrations in those rivers: 1) the Sr released from the silicate (carbonate) fraction of the metamorphic units is much higher (lower) than predicted by the catchment model and/or, 2) metamorphosed limestones and marbles with $^{87}\text{Sr}/^{86}\text{Sr}$ higher than seawater contribute to the Sr flux. Consistent with the first hypothesis, the marine finely-grained metasedimentary rocks in these watersheds might be expected to release more Sr than predicted by the Sr chemical weathering model (equation 4.6) because the Sr chemical weathering model only gives an average of Sr flux from all types of metamorphic rocks at high-latitudes, which is biased by slowly weathering metaigneous rocks. However, the presence of marble and metalimestone could be taken in support the second hypothesis. Carbonates can exchange Sr with surrounding radiogenic lithologies during metamorphism, thereby inheriting the $^{87}\text{Sr}/^{86}\text{Sr}$ of the more radiogenic siliciclastic lithologies (Bickle et al., 1995; Veizer, 1992). The contribution of radiogenic metamorphic carbonates to the Sr budget of rivers has been identified in the Himalayas (Blum et al., 1998; Quade et al., 2003; Quade et al., 1997) and the Canadian Cordillera (Millot et al., 2003). Based on the evaluation of outlier values presented above, Alaska might represent another occurrence of such radiogenic metamorphosed carbonates.

Sensitivity of the regional Sr budget to geologic and environmental controls

In the hypothetical case that Alaska was a single catchment, we calculated the proportion of each GLiM lithology, the proportion of evaporite, the mean slope and mean permafrost index over Alaska (Table 4.5). We used those values to apply equation 4.6 to estimate the influence of each significant predictor of Sr concentrations in rivers over Alaska (Table 4.5).

Although carbonates are not very abundant over Alaska, they contribute to half the Sr flux in this region and buffer the overall $^{87}\text{Sr}/^{86}\text{Sr}$ toward seawater $^{87}\text{Sr}/^{86}\text{Sr}$. Siliciclastic sedimentary rocks are very abundant and contribute in similar proportion as carbonate to the Sr flux, but because their $^{87}\text{Sr}/^{86}\text{Sr}$ is much more variable, they are the primary control of $^{87}\text{Sr}/^{86}\text{Sr}$ of Alaska R. Despite being fairly abundant and primarily located in regions with high slopes (Table 4.5), igneous rocks and metamorphic rocks contribute little to the Sr flux in Alaska.

We calculated the increase in Sr flux associated with Alaska topography and permafrost cover in comparison with a scenario of “flat” and “nonglaciaded” Alaska. We applied equation 4.6 and inputs from Table 4.5 to calculate the Sr flux associated with slope over Alaska and found that current Alaska topography increases Sr flux by 39% in comparison with a “flat” Alaska scenario. We proceeded similarly to calculate the change in Sr flux associated with permafrost cover and found that current permafrost cover decreased the Sr flux by 14% over Alaska in comparison with a “nonglaciaded” Alaska.

We also demonstrated that the presence of alpine glaciers has a significant impact on Sr concentrations of Alaska R. We compared the Sr concentrations of rivers with

alpine glaciers and rivers without alpine glaciers in their catchment. For catchment underlain by similar lithology, we estimated that catchments with alpine glaciers have Sr concentrations ~3-5 times higher than catchments without alpine glaciers. The current alpine glacier cover represents only 1.3% of the total surface of Alaska (Kargel et al., 2013), which limits the influence of this variable on the total Sr flux. However, the high sensitivity of Sr flux to alpine glaciers indicates that this factor can play a significant role in controlling the Sr budget from high-latitudes in periods of large alpine glacier cover (ice house climate).

Variations in Sr fluxes from the high-latitudes appear controlled by a coupling between climate and tectonics, with a positive feedback on Sr flux due to alpine glacier on steep terrain and a negative feedback on Sr release due to permafrost on flat terrains. This supports the idea that both glacial processes (Armstrong, 1971; Zachos et al., 1999) and orogenesis (Raymo et al., 1988) are primary but coupled controls of $^{87}\text{Sr}/^{86}\text{Sr}$ in seawater (Herman et al., 2013).

Regional Sr budget of Alaska Rivers runoff

In global Sr budget, the Sr flux and $^{87}\text{Sr}/^{86}\text{Sr}$ from Alaska runoff is represented in databases by the Yukon R (Palmer and Edmond, 1992; Peucker-Ehrenbrink et al., 2010). The Yukon R basin covers more than 30% of Alaska and as such its Sr concentrations and $^{87}\text{Sr}/^{86}\text{Sr}$ is thought to be representative of Alaska. The Sr concentrations and $^{87}\text{Sr}/^{86}\text{Sr}$ of the Yukon R are $139.2 \mu\text{g.L}^{-1}$ and 0.7137, respectively, and those values are well-predicted by our catchment water model, $96.74 \mu\text{g.L}^{-1}$ and 0.7127, respectively. However, those values differ significantly from the average Sr concentration of 104.3

$\mu\text{g.L}^{-1}$ and average $^{87}\text{Sr}/^{86}\text{Sr}$ of 0.7098 predicted by our catchment water model for the total runoff of Alaska. The large decrease in $^{87}\text{Sr}/^{86}\text{Sr}$ for the total runoff of Alaska in comparison with the Yukon R is associated with the large flux of nonradiogenic Sr from mafic terranes and island arcs from Southwest Alaska, which are not part of the Yukon R basin.

Conclusion

We developed new process-oriented models predicting $^{87}\text{Sr}/^{86}\text{Sr}$ in bedrock and water across Alaska. The developed catchment water model provides a method to estimate the Sr budget at regional scale and to identify the dominant climatic and tectonic controls of Sr concentrations and $^{87}\text{Sr}/^{86}\text{Sr}$ in rivers. Over Alaska, lithological proportions, topography, and glacial processes (permafrost and alpine glacier cover) are the primary controls on the Sr concentrations in rivers. The average $^{87}\text{Sr}/^{86}\text{Sr}$ of the cumulated Alaska runoff predicted by our model differs significantly from the values of the Yukon River which are traditionally used to constrain the $^{87}\text{Sr}/^{86}\text{Sr}$ of this region in global Sr budget. This difference questions the accuracy of the empirically-constrained Sr budget.

The data products developed from this work can also be used as baseline $^{87}\text{Sr}/^{86}\text{Sr}$ map of Alaska R to interpret provenance of aquatic animals at regional scale. Those baseline $^{87}\text{Sr}/^{86}\text{Sr}$ maps of Alaska R could strongly benefit the fishing industry to trace Pacific salmon natal origins as a tool to better conserve salmon biodiversity and the natural resources they represent.

Acknowledgements

This research was supported by NSF Award EF-01241286. We thank Lisa Stright for help in developing this geostatistical framework, Simon Brewer for his help in using R and Ronny Lauwerald for his help with the ArcGIS model builder. We also thank Michael E. Böttcher (editor-in-chief), two anonymous reviewers and Bernhard Peucker-Ehrenbrink for their suggestions and comments which greatly improved this manuscript.

References

- Allègre, C.J., Louvat, P., Gaillardet, J., Meynadier, L., Rad, S., Capmas, F., 2010. The fundamental role of island arc weathering in the oceanic Sr isotope budget. *Earth and Planetary Science Letters*, 292(1–2): 51-56.
- Amato, J.M., Pavlis, T.L., 2010. Detrital zircon ages from the Chugach terrane, southern Alaska, reveal multiple episodes of accretion and erosion in a subduction complex. *Geology*, 38(5): 459-462.
- Anderson, S.P., 2007. Biogeochemistry of glacial landscape systems. *Annual Review of Earth and Planetary Sciences*, 35(1): 375-399.
- Anderson, S.P., Drever, J.I., Frost, C.D., Holden, P., 2000. Chemical weathering in the foreland of a retreating glacier. *Geochimica et Cosmochimica Acta*, 64(7): 1173-1189.
- Armstrong, R.L., 1971. Glacial erosion and the variable isotopic composition of strontium in sea water. *Nature* (230): 132-133.
- Bataille, C.P., Bowen, G.J., 2012. Mapping $^{87}\text{Sr}/^{86}\text{Sr}$ variations in bedrock and water for large scale provenance studies. *Chemical Geology*, 304–305(0): 39-52.
- Bataille, C.P., Laffoon, J., Bowen, G.J., 2012. Mapping multiple source effects on the strontium isotopic signatures of ecosystems from the circum-Caribbean region. *Ecosphere*, 3(12): art118.
- Beck, A.J., Charette, M.A., Cochran, J.K., Gonnee, M.E., Peucker-Ehrenbrink, B., 2013. Dissolved strontium in the subterranean estuary – Implications for the marine strontium isotope budget. *Geochimica et Cosmochimica Acta*, 117(0): 33-52.
- Bickle, M.J., 1994. The role of metamorphic decarbonation reactions in returning

- strontium to the silicate sediment mass. *Nature*, 367(6465): 699-704.
- Bickle, M.J., Chapman, H.J., Wickham, S.M., Peters, M.T., 1995. Strontium and oxygen isotope profiles across marble-silicate contacts, Lizzies Basin, East Humboldt Range, Nevada: Constraints on metamorphic permeability contrasts and fluid flow. *Contributions to Mineralogy and Petrology*, 121(4): 400-413.
- Blum, J.D., Gazis, C.A., Jacobson, A.D., Page Chamberlain, C., 1998. Carbonate versus silicate weathering in the Raikhot watershed within the High Himalayan Crystalline Series. *Geology*, 26(5): 411-414.
- Boucot, A.J., Gray, J., 2001. A critique of Phanerozoic climatic models involving changes in the CO₂ content of the atmosphere. *Earth-Science Reviews*, 56(1-4): 1-159.
- Bradley, D.C., McClelland, W.C., Wooden, J.L., Till, A.B., Roeske, S.M., Miller, M.L., Karl, S.M., Abbott, J.G., 2007. Detrital zircon geochronology of some Neoproterozoic to Triassic rocks in interior Alaska. *Geological Society of America Special Papers*, 431: 155-189.
- Brady, P.V., 1991. The effect of silicate weathering on global temperature and atmospheric CO₂. *Journal of Geophysical Research: Solid Earth*, 96(B11): 18101-18106.
- Brass, G.W., 1976. The variation of the marine ⁸⁷Sr/⁸⁶Sr ratio during Phanerozoic time: Interpretation using a flux model. *Geochimica et Cosmochimica Acta*, 40(7): 721-730.
- Brennan, S., Fernandez, D.P., Mackey, G., Cerling, T.E., Bataille, C.P., Bowen, G.J., Wooller, M.J. Strontium isotope variation and carbonate versus silicate weathering in rivers from across Alaska: Implications for provenance studies. *Chemical Geology*. To be published.
- Brevart, O., Allegre, C.J., 1977. Strontium isotopic ratios in limestone through geological time as a memory of geodynamic regimes. *Bulletin De La Societe Geologique De France, Series 7, XIX(6)*: 1253-1257.
- Burke, W.H., Denison, R.E., Hetherington, E.A., Koepnick, R.B., Nelson, H.F., Otto, J.B., 1982. Variation of seawater ⁸⁷Sr/⁸⁶Sr throughout Phanerozoic time. *Geology*, 10(10): 516-519.
- Cawood, P.A., Hawkesworth, C.J., Dhuime, B., 2012. The continental record and the generation of continental crust. *Geological Society of America Bulletin*, 125: 14-32
- Chaudhuri, S., Clauer, N., 1986. Fluctuations of isotopic composition of strontium in

- seawater during the Phanerozoic eon. *Chemical Geology*, 59(4): 293-303.
- Colpron, M., Nelson, J.L., 2011. A Digital Atlas of Terranes for the Northern Cordillera. Accessed online from Yukon Geological Survey (www.geology.gov.yk.ca).
- Coogan, L.A., Gillis, K.M., 2013. Evidence that low-temperature oceanic hydrothermal systems play an important role in the silicate-carbonate weathering cycle and long-term climate regulation. *Geochemistry, Geophysics, Geosystems*, 14(6): 1771-1786.
- Davis, A.C., Bickle, M.J., Teagle, D.A.H., 2003. Imbalance in the oceanic strontium budget. *Earth and Planetary Science Letters*, 211(1-2): 173-187.
- Dhuime, B., Hawkesworth, C.J., Cawood, P.A., Storey, C.D., 2012. A change in the geodynamics of continental growth 3 billion years ago. *Science*, 335(6074): 1334-1336.
- Edmond, J.M., 1992. Himalayan tectonics, weathering processes, and the strontium isotope record in marine limestones. *Science*, 258(5088): 1594-1597.
- Faure, G., 1977. *Principles of Isotope Geology*. Second edition, John Wiley and Sons, New York, 589 p.
- Fekete, B.M., Vörösmarty, C.J., Grabs, W., 2002. High-resolution fields of global runoff combining observed river discharge and simulated water balances. *Global Biogeochem. Cycles*, 16(3): 1042.
- Gaillardet, J., Dupré, B., Louvat, P., Allègre, C.J., 1999. Global silicate weathering and CO₂ consumption rates deduced from the chemistry of large rivers. *Chemical Geology*, 159(1-4): 3-30.
- Garrels, R.M., Mackenzie, F.T., 1971. *Evolution of Sedimentary Rocks*. Norton, New York, 397 p.
- Gehrels, G.E., Butler, R.F., Bazard, D.R., 1996. Detrital zircon geochronology of the Alexander terrane, southeastern Alaska. *Geological Society of America Bulletin*, 108(6): 722-734.
- Geological Survey (U.S.). Geologic Names Committee, Geological Survey (U.S.), 2007. Divisions of geologic time--major chronostratigraphic and geochronologic units, Fact sheet 2007-3015. U.S. Geological Survey, [Reston, Va.].
- Goldfarb, R.J., Farmer, G.L., Cieutat, A.C., Meier, A.L., 1997. Major-element, trace-element, and strontium-isotope systematics of natural waters in the Fairbanks mining district: Constraints from local geology. U.S. Geological Survey Professional Paper, 1614: 12.

- Goldstein, S.J., Jacobsen, S.B., 1988. Nd and Sr isotopic systematics of river water suspended material - Implications for crustal evolution. *Earth and Planetary Science Letters*, 87(3): 249-265.
- Goldstein, S.L., 1988. Decoupled evolution of Nd and Sr isotopes in the continental crust and the mantle. *Nature*, 336(6201): 733-738.
- Gruber, S., 2012. Derivation and analysis of a high-resolution estimate of global permafrost zonation. *The Cryosphere*, 6(1): 221-233.
- Harris, N.R., Sisson, V.B., Wright, J.E., Pavlis, T.L., 1996. Evidence for Eocene mafic underplating during fore-arc intrusive activity, eastern Chugach Mountains, Alaska. *Geology*, 24(3): 263-266.
- Hartmann, J., 2009. Bicarbonate-fluxes and CO₂-consumption by chemical weathering on the Japanese archipelago - Application of a multi-lithological model framework. *Chemical Geology*, 265(3-4): 237-271.
- Hartmann, J., Moosdorf, N., 2012. The new global lithological map database GLiM: A representation of rock properties at the Earth surface. *Geochemistry, Geophysics, Geosystems*, 13(12): 1525-2027.
- Herman, F., Seward, D., Valla, P.G., Carter, A., Kohn, B., Willett, S.D., Ehlers, T.A., 2013. Worldwide acceleration of mountain erosion under a cooling climate. *Nature*, 504(7480): 423-426.
- Hijmans, R.J., Cameron, S.E., Parra, J.L., Jones, P.G., Jarvis, A., 2005. Very high resolution interpolated climate surfaces for global land areas. *International Journal of Climatology*, 25(15): 1965-1978.
- Hudec, M.R., Jackson, M.P.A., 2007. Terra infirma: Understanding salt tectonics. *Earth-Science Reviews*, 82(1-2): 1-28.
- Huh, Y., Edmond, J.M., 1999. The fluvial geochemistry of the rivers of Eastern Siberia: III. Tributaries of the Lena and Anabar draining the basement terrain of the Siberian Craton and the Trans-Baikal Highlands. *Geochimica et Cosmochimica Acta*, 63(7-8): 967-987.
- Huh, Y., Panteleyev, G., Babich, D., Zaitsev, A., Edmond, J.M., 1998a. The fluvial geochemistry of the rivers of Eastern Siberia: II. Tributaries of the Lena, Omoloy, Yana, Indigirka, Kolyma, and Anadyr draining the collisional/accretionary zone of the Verkhoyansk and Cherskiy ranges. *Geochimica et Cosmochimica Acta*, 62(12): 2053-2075.
- Huh, Y., Tsoi, M.-Y., Zaitsev, A., Edmond, J.M., 1998b. The fluvial geochemistry of the rivers of Eastern Siberia: I. Tributaries of the Lena River draining the sedimentary

- platform of the Siberian Craton. *Geochimica et Cosmochimica Acta*, 62(10): 1657-1676.
- Jeandel, C., Arsouze, T., Lacan, F., Téchiné, P., Dutay, J.C., 2007. Isotopic Nd compositions and concentrations of the lithogenic inputs into the ocean: A compilation, with an emphasis on the margins. *Chemical Geology*, 239(1–2): 156-164.
- Jones, M.T., Gislason, S.R., Burton, K.W., Pearce, C.R., Mavromatis, V., Pogge von Strandmann, P.A.E., Oelkers, E.H., 2014. Quantifying the impact of riverine particulate dissolution in seawater on ocean chemistry. *Earth and Planetary Science Letters*, 395(0): 91-100.
- Jones, M.T., Pearce, C.R., Jeandel, C., Gislason, S.R., Eiriksdottir, E.S., Mavromatis, V., Oelkers, E.H., 2012. Riverine particulate material dissolution as a significant flux of strontium to the oceans. *Earth and Planetary Science Letters*, 355–356(0): 51-59.
- Kargel, J.S., G.J. Leonard, M.P. Bishop, A. Kaab, B. Raup (Eds), 2013, *Global Land Ice Measurements from Space*. Springer, 876p.
- Keller, K., Blum, J.D., Kling, G.W., 2010. Stream geochemistry as an indicator of increasing permafrost thaw depth in an arctic watershed. *Chemical Geology*, 273(1–2): 76-81.
- Livingstone, D.A., 1963. Chemical composition of rivers and lakes. USGS Professional Paper, 440-G: G1-G64.
- Mackenzie, F.T., Garrels, R.M., 1966. Chemical mass balance between rivers and oceans. *American Journal of Science*, 264(7): 507-525.
- McDermott, F., Hawkesworth, C., 1990. The evolution of strontium isotopes in the upper continental crust. *Nature*, 344(6269): 850-853.
- Meybeck, M., 1987. Global chemical weathering of surficial rocks estimated from river dissolved loads. *American Journal of Science*, 287(5): 401-428.
- Miller, E.L., Toro, J., Gehrels, G., Amato, J.M., Prokopyev, A., Tuchkova, M.I., Akinin, V.V., Dumitru, T.A., Moore, T.E., Cecile, M.P., 2006. New insights into Arctic paleogeography and tectonics from U-Pb detrital zircon geochronology. *Tectonics*, 25(3): TC3013.
- Millot, R., Gaillardet, J.é., Dupré, B., Allègre, C.J., 2003. Northern latitude chemical weathering rates: Clues from the Mackenzie River Basin, Canada. *Geochimica et Cosmochimica Acta*, 67(7): 1305-1329.

- Nelson, J.L., Gehrels, G., 2007. Detrital zircon geochronology and provenance of the southeastern Yukon–Tanana terrane. *Canadian Journal of Earth Sciences*, 44(3): 297-316.
- Nelson, J.L., Colpron, M., Israel, S., 2013. The Cordillera of British Columbia, Yukon, and Alaska: Tectonics and metallogeny. Society of Economic Geologists, Inc., Special Publication(17): 53–109.
- Newberry, R.J., Bundtzen, T.K., Clautice, K.H., Combellick, R.A., Douglas, T., Laird, G.M., Liss, S.A., Pinney, D.S., Reifentstuhl, R.R., Solie, D.N., 1996. Preliminary geologic map of the Fairbanks mining district, Alaska. Alaska Division of Geological & Geophysical Surveys Public Data File 96-16, 17 p., 2 sheets, scale 1:63,360.
- Palmer, M.R., Edmond, J.M., 1992. Controls over the strontium isotope composition of river water. *Geochimica et Cosmochimica Acta*, 56(5): 2099-2111.
- Peterman, Z.E., Hedge, C.E., Tourtelot, H.A., 1970. Isotopic composition of strontium in sea water throughout Phanerozoic time. *Geochimica et Cosmochimica Acta*, 34(1): 105-120.
- Peucker-Ehrenbrink, B., Miller, M.W., Arsouze, T., Jeandel, C., 2010. Continental bedrock and riverine fluxes of strontium and neodymium isotopes to the oceans. *Geochemistry, Geophysics, Geosystems*, 11(3): Q03016.
- Pouillot, R., Delignette-Muller, M.L., 2010. Evaluating variability and uncertainty separately in microbial quantitative risk assessment using two R packages. *International Journal of Food Microbiology*, 142(3): 330-340.
- Quade, J., English, N., DeCelles, P.G., 2003. Silicate versus carbonate weathering in the Himalaya: A comparison of the Arun and Seti River watersheds. *Chemical Geology*, 202(3–4): 275-296.
- Quade, J., Roe, L., DeCelles, P.G., Ojha, T.P., 1997. The late Neogene $^{87}\text{Sr}/^{86}\text{Sr}$ record of lowland Himalayan rivers. *Science*, 276(5320): 1828-1831.
- Raymo, M.E., Ruddiman, W.F., Froelich, P.N., 1988. Influence of late Cenozoic mountain building on ocean geochemical cycles. *Geology*, 16(7): 649-653.
- Saito, H., Goovaerts, P., 2000. Geostatistical interpolation of positively skewed and censored data in a dioxin-contaminated site. *Environmental Science & Technology*, 34(19): 4228-4235.
- Shields, G.A., 2007. A normalised seawater strontium isotope curve: Possible implications for Neoproterozoic-Cambrian weathering rates and the further oxygenation of the Earth. *eEarth*, 2(2): 35-42.

- Simo, J.A., Johnson, C.M., Vandrey, M.R., Brown, P.E., Castrogiovanni, E., Drzewiecki, P.E., Valley, J.W., Boyer, J., 2009. Burial Dolomitization of the Middle Ordovician Glenwood Formation by Evaporitic Brines, Michigan Basin, Dolomites. Blackwell Publishing Ltd., pp. 167-186.
- Spooner, E.T.C., 1976. The strontium isotopic composition of seawater, and seawater-oceanic crust interaction. *Earth and Planetary Science Letters*, 31(1): 167-174.
- Stallard, R.F., Edmond, J.M., 1983. Geochemistry of the Amazon: 2. The influence of geology and weathering environment on the dissolved load. *Journal of Geophysical Research: Oceans*, 88(C14): 9671-9688.
- Stewart, B.W., Capo, R.C., Chadwick, O.A., 2001. Effects of rainfall on weathering rate, base cation provenance, and Sr isotope composition of Hawaiian soils. *Geochimica et Cosmochimica Acta*, 65(7): 1087-1099.
- USGS, 1996. GTOPO30. <http://edc.usgs.gov/products/elevation/gtopo30.html>
- Vance, D., Teagle, D.A.H., Foster, G.L., 2009. Variable Quaternary chemical weathering fluxes and imbalances in marine geochemical budgets. *Nature*, 458(7237): 493-496.
- Veizer, J., 1973. Sedimentation in geologic history: Recycling vs. evolution or recycling with evolution. *Contributions to Mineralogy and Petrology*, 38(4): 261-278.
- Veizer, J., 1989. Strontium isotopes in seawater through time. *Annual Review of Earth and Planetary Sciences*, 17(1): 141-167.
- Veizer, J., 1992. Depositional and Diagenetic History of Limestones: Stable and Radiogenic Isotopes. In: Clauer, N., Chaudhuri, S. (Eds.), *Isotopic Signatures and Sedimentary Records*. Lecture Notes in Earth Sciences. Springer Berlin Heidelberg, pp. 13-48.
- Veizer, J., Ala, D., Azmy, K., Bruckschen, P., Buhl, D., Bruhn, F., Carden, G.A.F., Diener, A., Ebner, S., Godderis, Y., Jasper, T., Korte, C., Pawellek, F., Podlaha, O.G., Strauss, H., 1999. $^{87}\text{Sr}/^{86}\text{Sr}$, $\delta^{13}\text{C}$ and $\delta^{18}\text{O}$ evolution of Phanerozoic seawater. *Chemical Geology*, 161(1-3): 59-88.
- Veizer, J., Compston, W., 1974. $^{87}\text{Sr}/^{86}\text{Sr}$ composition of seawater during the Phanerozoic. *Geochimica et Cosmochimica Acta*, 38(9): 1461-1484.
- Veizer, J., Jansen, S.L., 1979. Basement and sedimentary recycling and continental evolution. *The Journal of Geology*, 87(4): 341-370.
- Veizer, J., Mackenzie, F.T., 2003. 7.15 - Evolution of Sedimentary Rocks. In: Holland, H.D., Turekian, K.K. (Eds.), *Treatise on Geochemistry*. Pergamon, Oxford, pp.

369-407.

- White, A.F., Blum, A.E., Bullen, T.D., Vivit, D.V., Schulz, M., Fitzpatrick, J., 1999a. The effect of temperature on experimental and natural chemical weathering rates of granitoid rocks. *Geochimica et Cosmochimica Acta*, 63(19-20): 3277-3291.
- White, A.F., Blum, A.E., Schulz, M.S., Bullen, T.D., Harden, J.W., Peterson, M.L., 1996. Chemical weathering rates of a soil chronosequence on granitic alluvium .1. Quantification of mineralogical and surface area changes and calculation of primary silicate reaction rates. *Geochimica et Cosmochimica Acta*, 60(14): 2533-2550.
- White, A.F., Brantley, S.L., 2003. The effect of time on the weathering of silicate minerals: Why do weathering rates differ in the laboratory and field? *Chemical Geology*, 202(3-4): 479-506.
- White, A.F., Bullen, T.D., Vivit, D.V., Schulz, M.S., Clow, D.W., 1999b. The role of disseminated calcite in the chemical weathering of granitoid rocks. *Geochimica et Cosmochimica Acta*, 63(13-14): 1939-1953.
- Zachos, J.C., Opdyke, B.N., Quinn, T.M., Jones, C.E., Halliday, A.N., 1999. Early cenozoic glaciation, antarctic weathering, and seawater $^{87}\text{Sr}/^{86}\text{Sr}$: Is there a link? *Chemical Geology*, 161(1-3): 165-180.

Table 4.1 Summary statistics of the chemical weathering model calibration steps. b_{ssed} , b_{sc} , b_{sm} , b_{ig} , b_{mt} and b_{salt} , b_{pfi} and b_s are the parameters for equation 4.6 for siliciclastic sediments (GLiM classes: ss, sm, su), carbonates (GLiM classes: sc, ev), igneous rocks (GLiM classes: pa, pb, pi, va, vb, vi), metamorphic rocks (GLiM class:mt), evaporites, permafrost zonation index and slope, respectively. The b parameters are calculated from the Levenberg-Marquart estimation techniques implemented in Statistica (STATSOFT®).

	Mean estimate	Standard deviation	p-value	Minimum Estimate	Maximum estimate
b_{ssed}	4.55	0.12	<10E-2	4.32	4.78
b_{sm}	4.39	0.15	<10E-2	4.09	4.69
b_{sc}	5.31	0.24	<10E-2	4.83	5.78
b_{mt}	3.16	0.25	<10E-2	2.85	3.47
b_{ig}	3.34	0.12	<10E-2	3.11	3.57
b_{salt}	9.27	0.34	<10E-2	8.61	9.93
b_{pfi}	-0.34	0.094	<10E-2	-0.53	-0.16
b_s	0.074	0.014	<10E-2	0.046	0.10

Table 4.2 Summary of goodness of fit measures for the bedrock model over Alaska. First column: igneous submodel; second column: siliciclastic sedimentary rock submodel. The bedrock validation dataset is compiled from the literature (Table 4S.9). MAE=Mean Absolute Error, RMSE=Root Mean Square Error, nrmse=Normalized Root Mean Square Error, KGE=Kling-Gupta Efficiency (Gupta et al., 2009), md=modified index of agreement (Legates and McCabe, 1999), R^2 =coefficient of determination, ssed submodel=siliciclastic sedimentary rock submodel, BB12=Bataille and Bowen, 2012.

	Sedimentary dataset		Igneous dataset	
	ssed submodel	BB12 bedrock model	Igneous submodel	BB12 bedrock model
MAE	0.0036	0.0065	0.0018	0.0024
RMSE	0.0081	0.010	0.0044	0.0055
NRMSE %	72.70	92.40	65.40	82.20
KGE	0.52	0.087	0.46	0.23
Md	0.69	0.20	0.68	0.47
R^2	0.52	0.44	0.72	0.51

Table 4.3 Summary of goodness of fit measures for the chemical weathering model for Alaska River. Sr concentrations data are from Brennan et al. (in press). First column: all data included (n=61); second column: Some outliers removed including South Fork of the Kuskokwim, Dietrich, Middle Fork of the Koyukuk, Nenana and Canning Rivers (n=56). MAE=Mean Absolute Error, RMSE=Root Mean Square Error, nrmse=Normalized Root Mean Square Error, KGE=Kling-Gupta Efficiency (Gupta et al., 2009), md=modified index of agreement (Legates and McCabe, 1999), R^2 =coefficient of determination.

	n=61	n=56
MAE ($\mu\text{g.L}^{-1}$)	56	33
RMSE ($\mu\text{g.L}^{-1}$)	103	40
NRMSE %	87.80	77.00
KGE	0.17	0.50
Md	0.51	0.54
R^2	0.39	0.41

Table 4.4 Summary of goodness of fit measures for the catchment water model. First column: all data included (n=61); second column: some outliers removed including Salcha, Chena, Chatanika and Nenana Rivers (n=57). $(^{87}\text{Sr}/^{86}\text{Sr})_{\text{catchment}}$ =catchment water model $^{87}\text{Sr}/^{86}\text{Sr}$ prediction, MAE=Mean Absolute Error, RMSE=Root Mean Square Error, nrmse=Normalized Root Mean Square Error, KGE=Kling-Gupta Efficiency (Gupta et al., 2009), md=modified index of agreement (Legates and McCabe, 1999), R^2 =coefficient of determination.

	n=61	n=57
MAE	0.0020	0.0012
RMSE	0.0045	0.0015
NRMSE %	74.3	42.1
KGE	0.50	0.86
Md	0.72	0.78
R^2	0.46	0.82

Table 4.5 Summary of lithological proportion across Alaska and their corresponding mean slope and mean permafrost zonation index (pfi). The contribution to the regional Sr flux from each lithology is calculated applying equation 4.6.

Lithology (GLiM xx)	Area (%)	mean slope (degrees)	mean pfi	Sr flux (%)
Carbonates (sc+0.5sm)	22.3	5.20	0.60	45.7
Siliciclastic sediments (ss+su+0.5sm)	50.1	3.43	0.43	44.6
Metamorphic rocks (mt)	5.7	6.16	0.39	1.55
Igneous rocks (va+vb+vi+pa+pb+pi+py)	21.9	5.78	0.30	7.3
Evaporites (ev)	0.005	12.94	0.87	1.0
Average	X	4.24	0.43	X

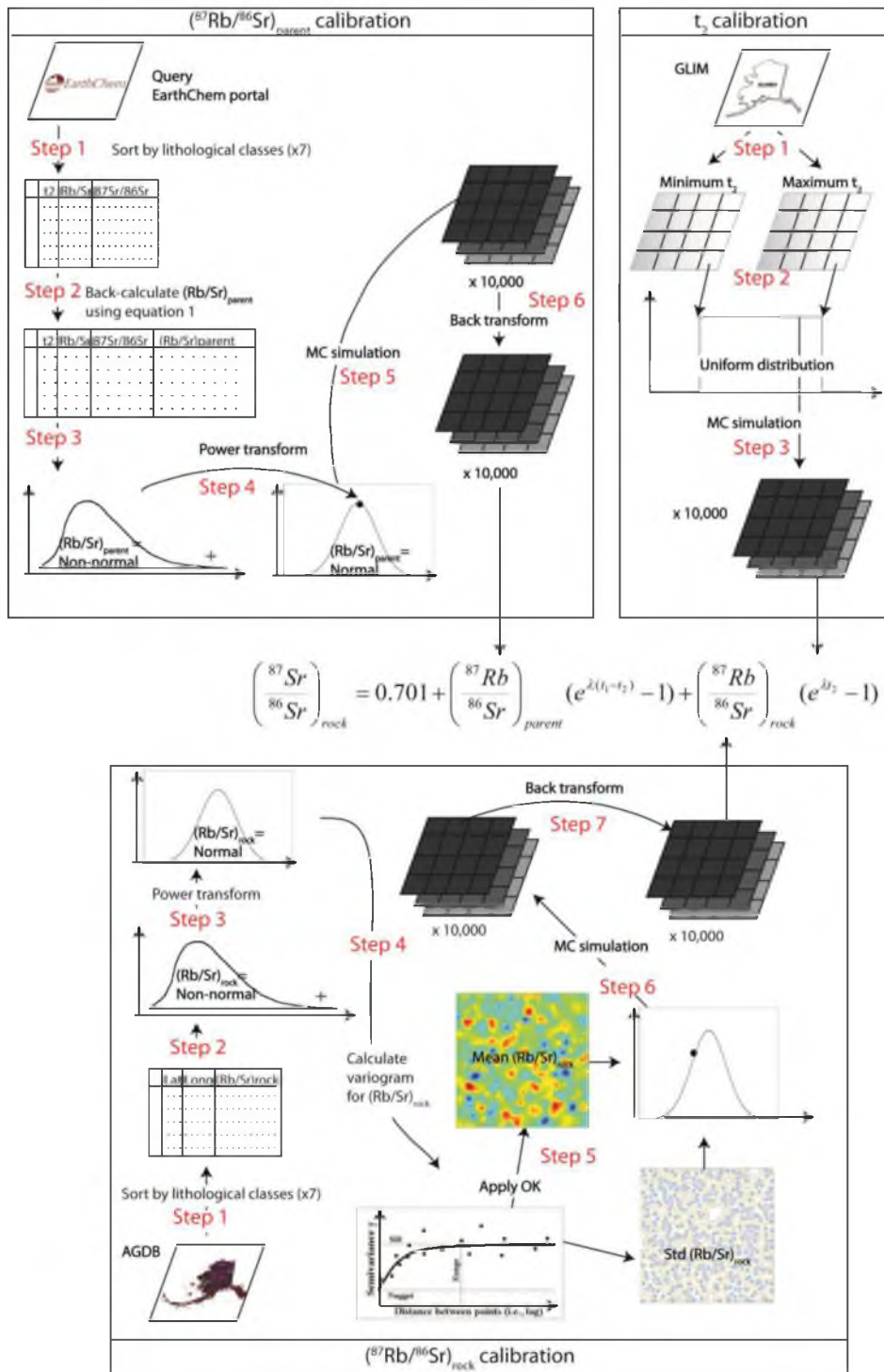


Figure 4.1 Flowchart summarizing the input data, parameterization steps and parameter estimation methods for the igneous submodel.

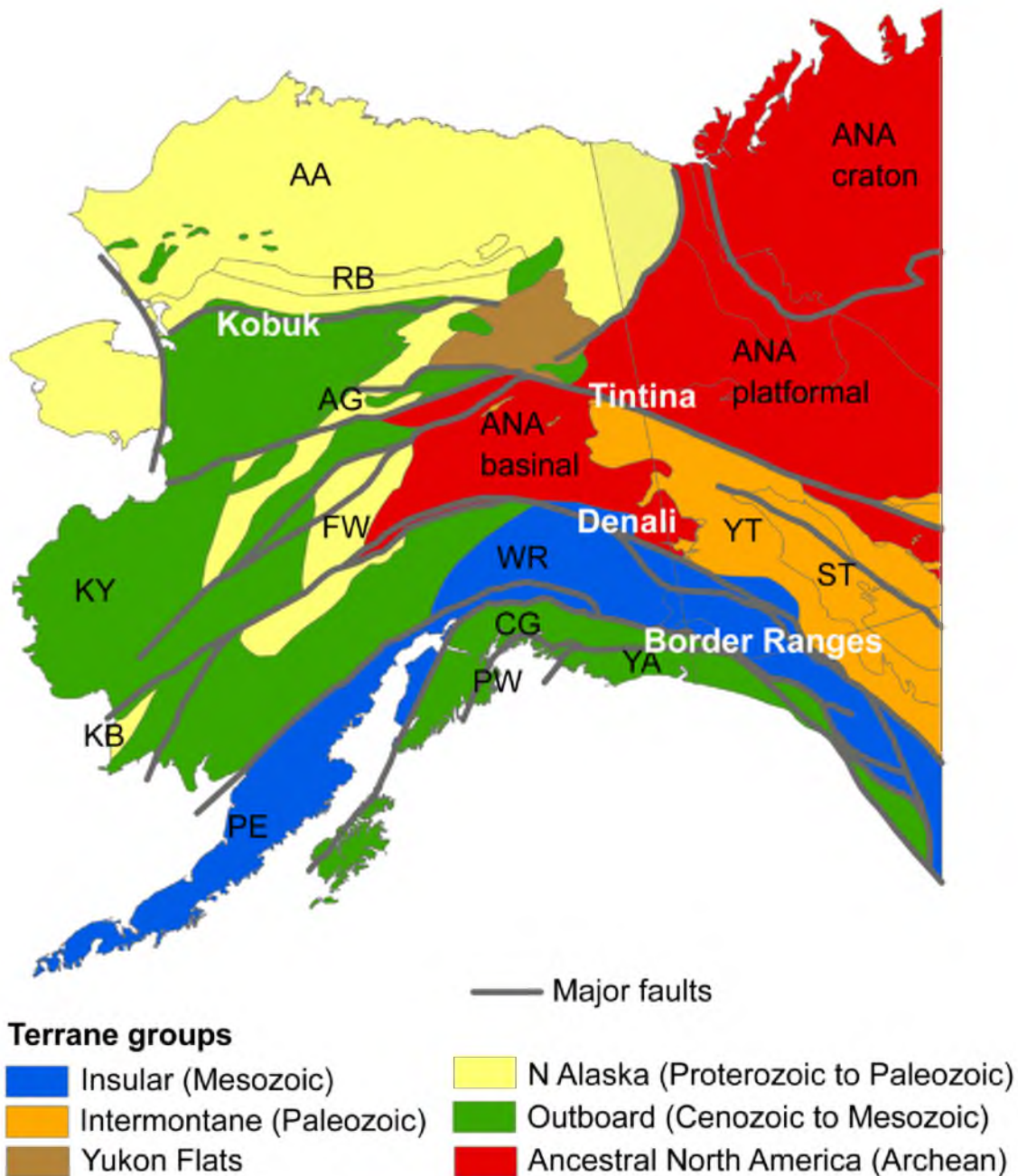


Figure 4.2 Terrane ages and boundaries across Alaska. GIS layer from the digital atlas of terranes for the Northern Cordillera (Colpron and Nelson, 2011). AA=Arctic Alaska; RB=Ruby; AG=Angayucham; FW=Farwell; KY=Koyukuk; WR=Wrangellia; CG=Chugach; PW=Prince-William; YA=Yakutat; PE=Penninsula; YT=Yukon-Tanana; ST=Stikine; ANA=Ancestral North America.

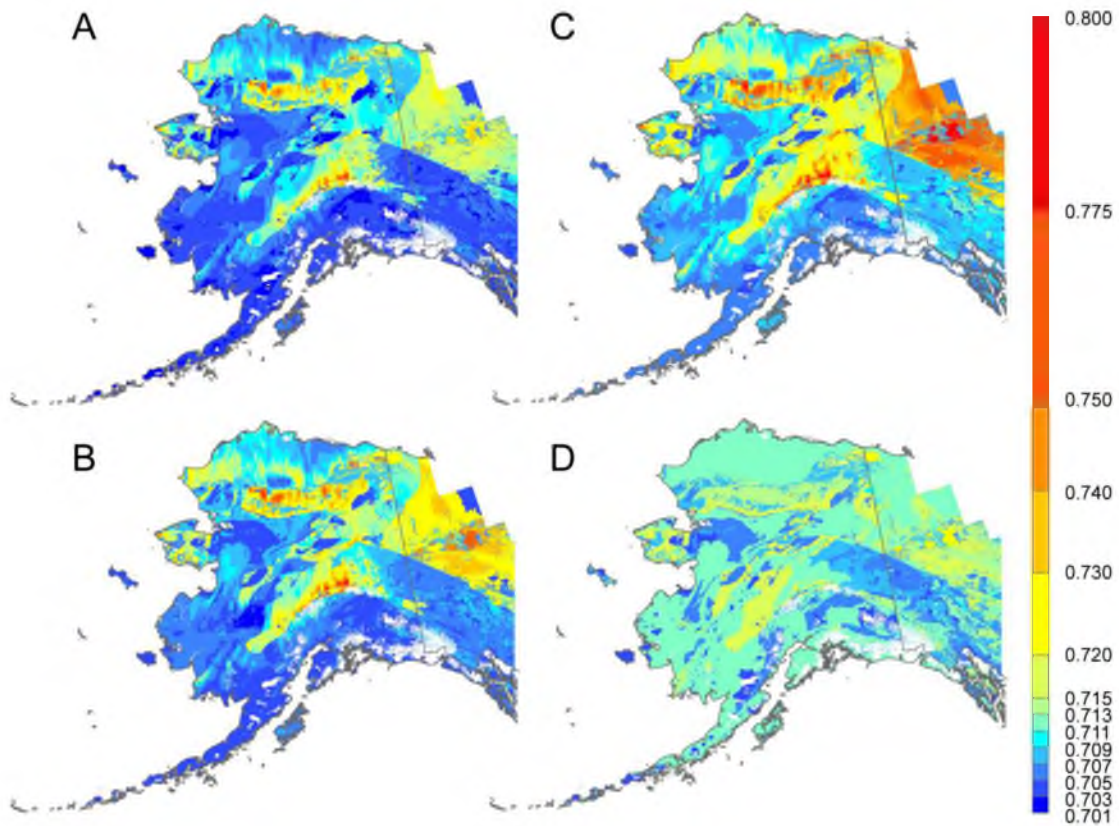


Figure 4.3 Predicted $^{87}\text{Sr}/^{86}\text{Sr}$ in bedrock across Alaska. A. Quartile 1 of $^{87}\text{Sr}/^{86}\text{Sr}$ prediction. B. Median of $^{87}\text{Sr}/^{86}\text{Sr}$ prediction. C. Quartile 3 of $^{87}\text{Sr}/^{86}\text{Sr}$ prediction. D. Mean of $^{87}\text{Sr}/^{86}\text{Sr}$ prediction from Bataille and Bowen's (2012) bedrock model. Political and shoreline vectors corresponds to the Large Scale International Boundary Lines and World Vector Shorelines from the U.S. Department of State, Office of the Geographer.

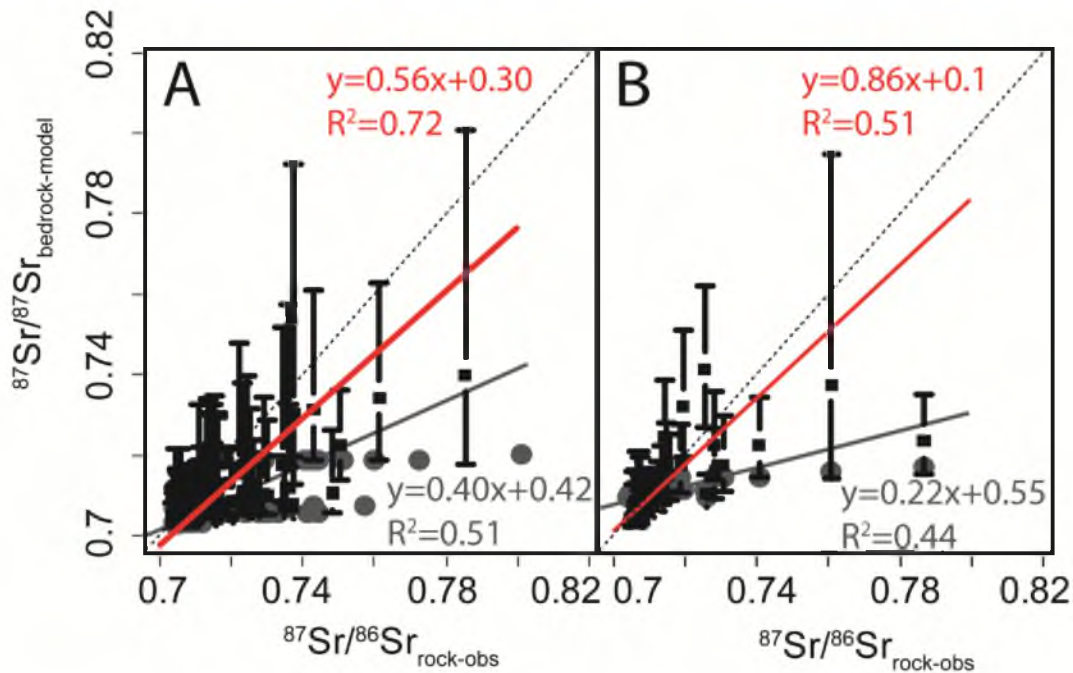


Figure 4.4 Bedrock model validation. A. Scatterplot of observed $^{87}\text{Sr}/^{86}\text{Sr}$ against predicted median $^{87}\text{Sr}/^{86}\text{Sr}$ from the igneous submodel; B. Scatterplot of observed $^{87}\text{Sr}/^{86}\text{Sr}$ against predicted median $^{87}\text{Sr}/^{86}\text{Sr}$ from the siliciclastic sedimentary rock submodel. Observed $^{87}\text{Sr}/^{86}\text{Sr}$ are compiled from the literature (Table 4S.9). Filled gray circles represent the bedrock model prediction from Bataille and Bowen's (2012) model and filled black squares represent the new bedrock model prediction, with error bars representing the interquartile range. Solid lines are least squared regression linear models (grey: Bataille and Bowen's (2012) model, red: new models) and dashed lines represent the 1:1 relationship.

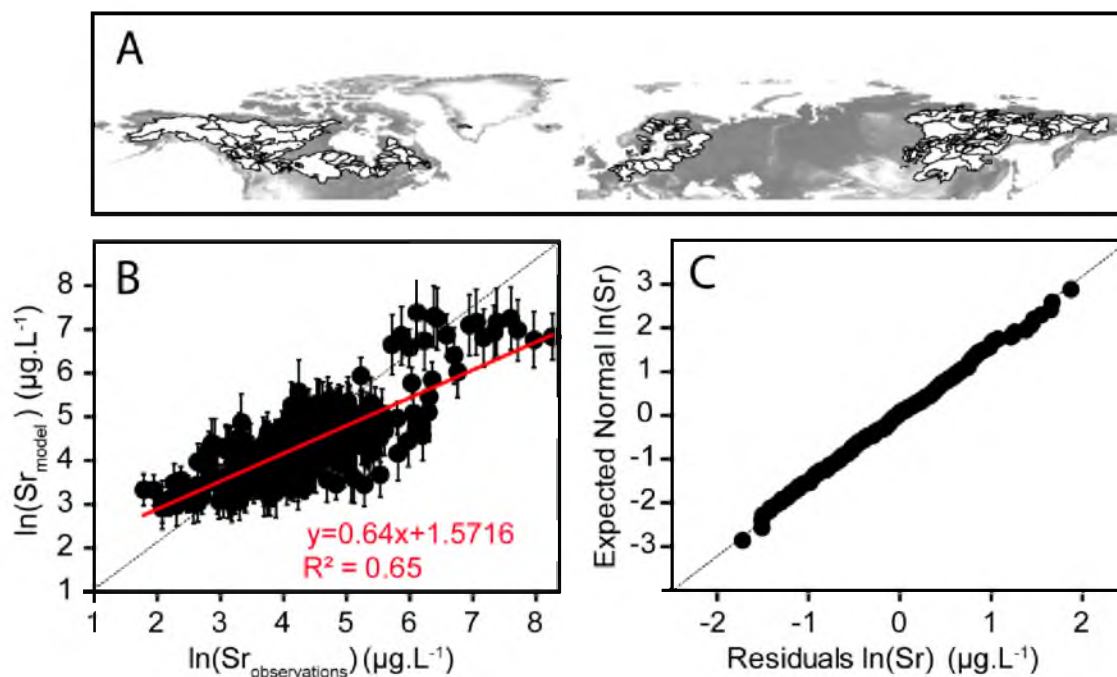


Figure 4.5 Calibration of the Sr chemical weathering model. A. Geographic location of the catchments containing samples used in the chemical weathering model calibration dataset (Table 4S.10). B. Scatterplot between predicted (equation 4.5) and observed logarithm of Sr concentrations on the calibration subset; C. Normal probability plot of logarithm of Sr concentrations residuals on the calibration subset. Error bars in B represent the 95% confidence interval. Solid red line represents linear regression and dashed line corresponds to the 1:1 relationship.

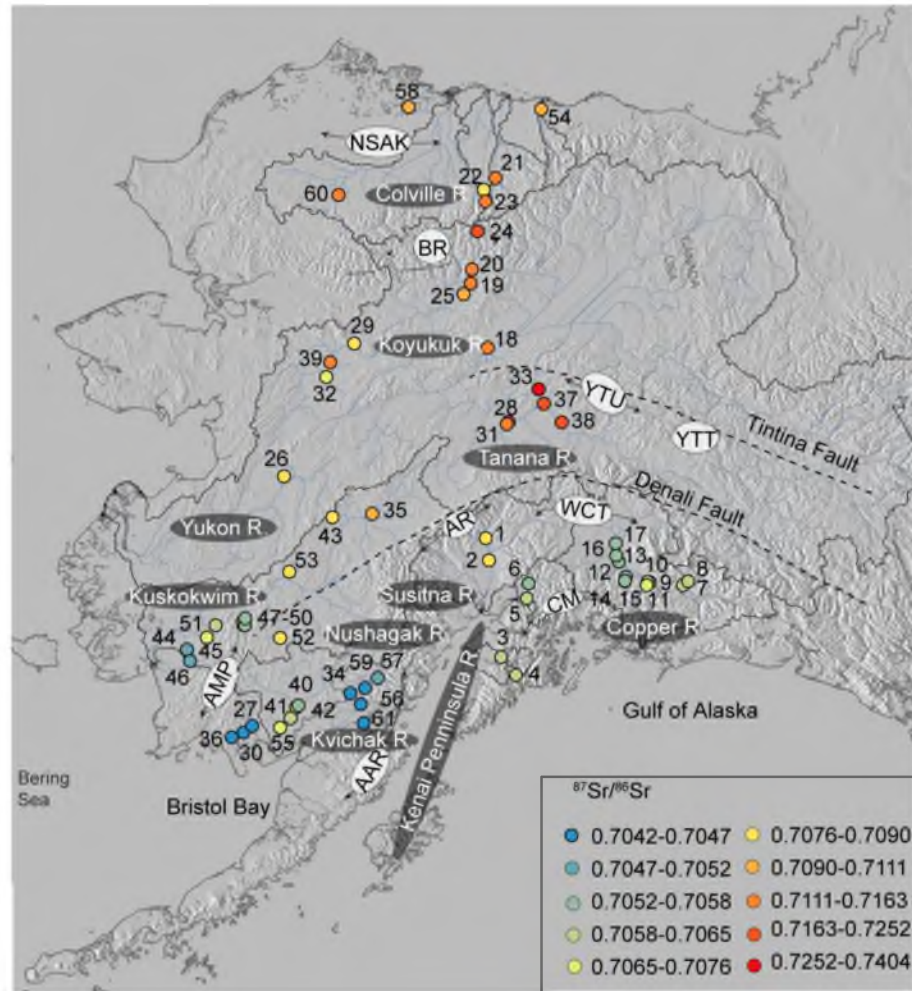


Figure 4.6 Map of sampling sites (with ID numbers) and their associated observed $^{87}\text{Sr}/^{86}\text{Sr}$ (color scale) for the catchment water model validation dataset modified from Brennan et al. (in press). Map also includes the location of major rivers and geographic provinces of Alaska. AAR= Aleutian Alaska Range; CM=Chugach Mountains; WCT=Wrangellia Composite Terrane; AMP= A; AR=Alaska Range; YTT=Yukon-Tanana Terrane; YTU=Yukon-Tanana Uplands; BR=Brook Range; NSAK=North Slope of Alaska.

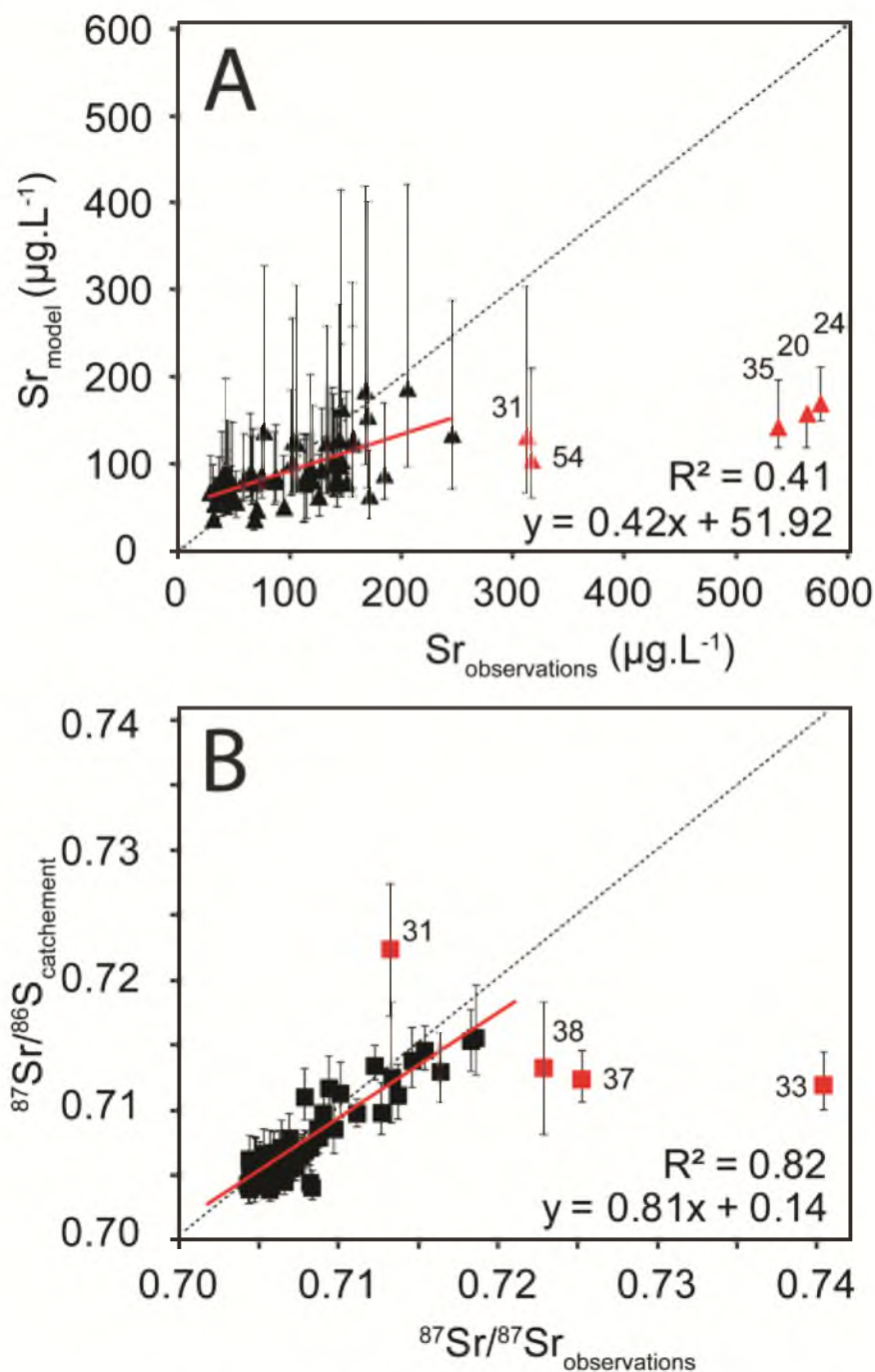


Figure 4.7 Catchment model validation for Alaska Rivers. A. Scatterplot between predicted and observed Sr concentrations in Alaska Rivers with error bars representing 95% confidence intervals; B. Scatterplot between median predicted and observed $^{87}\text{Sr}/^{86}\text{Sr}$ in Alaska Rivers with error bars representing the interquartile range. Red triangles and squares are outliers with their respective ID numbers (Fig. 4.6) and are not considered in the linear regression model. Solid red line represents a linear regression and dashed line corresponds to the 1:1 relationship.

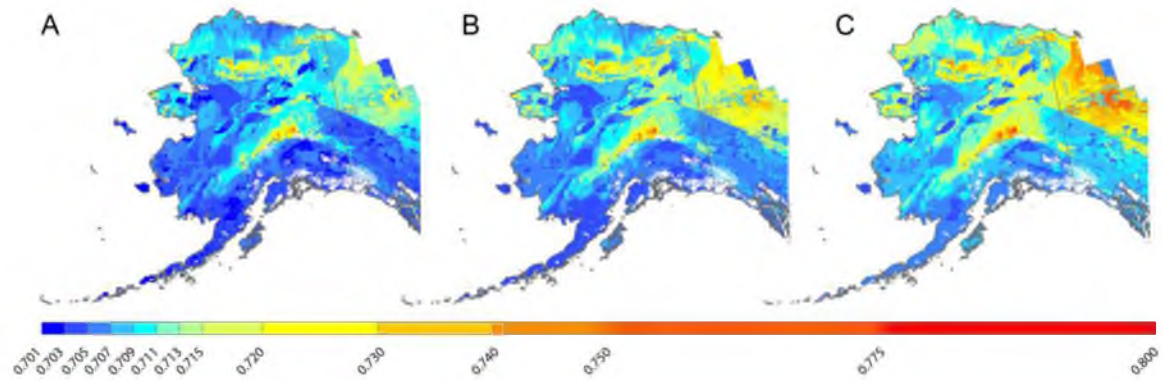


Figure 4.8 Predicted $^{87}\text{Sr}/^{86}\text{Sr}$ from the catchment water model applied across Alaska. A. Quartile 1 of $^{87}\text{Sr}/^{86}\text{Sr}$ prediction; B. Median of $^{87}\text{Sr}/^{86}\text{Sr}$ prediction; C. Quartile 3 of $^{87}\text{Sr}/^{86}\text{Sr}$ predictions. Political and shoreline vectors corresponds to the Large Scale International Boundary Lines and World Vector Shorelines from the US Department of State, Office of the Geographer.

Supplementary material: Statistical methods, tables and scripts for
the bedrock model

1. Igneous submodel parameterization

1.1. $(^{87}\text{Rb}/^{86}\text{Sr})_{\text{parent}}$ parameterization step

1.1.1. We obtained n=31,421 data from the Earthchem portal (www.earthchem.org) using the query:

1.1.1.1. Query by chemistry: Rb content AND Sr content AND $^{87}\text{Sr}/^{86}\text{Sr}$ measurements

1.1.1.2. Query by age: Age “exists”

1.1.1.3. Query by sample type: igneous (all types)

1.1.2. For each sample of the dataset:

1.1.2.1. We back-calculated $(^{87}\text{Rb}/^{86}\text{Sr})_{\text{parent}}$ using equation 4.1 and 4.2 from the manuscript and the given age, Rb and Sr content, and $^{87}\text{Sr}/^{86}\text{Sr}$ data collected from the database query

1.1.2.2. We assigned to each sample a GLiM igneous class (pa, pb, pi, va, vb, vi, mt) corresponding to the lithological description of the sample (Le Bas and Streckeisen, 1991)

1.1.2.3. We sorted and divided the data into 7 subsets following their associated GLiM major lithological class (pa, pb, pi, va, vb, vi, mt), and examined the statistical characteristics of each subset

1.1.3. For each subset:

1.1.3.1. We power transformed the data to approximate a normal distribution (R, Fitting distribution package) (Table 4S.1). The resulting histograms demonstrate that for all GLiM lithological classes, the power transformed $^{87}\text{Rb}/^{86}\text{Sr}$ dataset approximate well a normal distribution.

1.1.3.2. We calculated the mean and standard deviation of $(^{87}\text{Rb}/^{86}\text{Sr})_{\text{parent}}$ (Table 4S.1)

1.1.3.3. We plotted the histograms and Q-Q plots to verify the approximate normal distribution of the data (Table 4S.2)

- 1.2. t_2 parameterization step
 - 1.2.1. We extracted the attribute table of the GLiM database over the study area and converted it into an excel table
 - 1.2.2. For all the “text” age descriptors of the GLiM over the study area (e.g., Cretaceous), we assigned a minimum and maximum numeric age using the USGS geological time scale
 - 1.2.3. We inserted back the modified attribute table and converted the GLiM feature layer into minimum and maximum age rasters (ArcGIS/Geoprocessing tool reference)
- 1.3. $(^{87}\text{Rb}/^{86}\text{Sr})_{\text{rock}}$ parameterization step
 - 1.3.1. We gathered a database of 18,706 samples of Rb/Sr analyses from igneous rocks over the study area using the AK Geochemical Database 2 (AGDB2, Granitto et al., 2013) and the GEOROC database for Yukon and British Columbia
 - 1.3.2. For each sample of the database:
 - 1.3.2.1. We used the given lithological description associated with the sample to assign a GLiM major lithological class (Le Bas and Streckeisen, 1991)
 - 1.3.2.2. We sorted and divided the data into 7 subsets (pa, pb, pi-py, va, vb, vi, mt), and examined the statistical characteristics of each dataset
 - 1.3.3. For each subset:
 - 1.3.3.1. Because the Rb/Sr are strongly positively skewed, we power transformed the $^{87}\text{Rb}/^{86}\text{Sr}$ (R, Fitting distribution package) to approximate a normal distribution and allow the application of nonbiased ordinary kriging algorithms. Ordinary kriging is more efficient on Gaussian distribution (Saito and Goovaerts, 2000) (Tables 4S.1 and 4S.2). The resulting histograms demonstrate that for all GLiM lithological classes, the power transformed $^{87}\text{Rb}/^{86}\text{Sr}$ dataset approximate a normal distribution.
 - 1.3.3.2. We identified and removed outliers by using normal Q-Q plots for the power-transformed data (Table 4S.3). Only those values far away from the majority of samples in the plots were regarded as outliers. This method of outlier identification using graphs is to some extent subjective. Due to the power of the power transformation, this method

of lenient outlier identification is considered adequate. The identified outliers were removed from statistical analyses and spatial structure modeling. They were inserted back for spatial interpolation.

- 1.3.3.3. We checked the univariate distribution and the approximate normal distribution using histograms and Q-Q plots (ArcGIS/geostatistical wizard) (Table 4S.4)
- 1.3.3.4. We checked the presence/absence of trend (ArcGIS/geostatistical wizard)
- 1.3.3.5. We modeled the spatial autocorrelation by building a semi-variogram that quantifies the square of differences between sample pairs as a function of lag distance that separates these sample pairs.
- 1.3.3.6. We fitted the most appropriate semi-variogram model (range, nugget and sill) for each of the power transformed subsets by using the iterative fitting tool (ArcGIS/geostatistical wizard) (Table 4S.5)
- 1.3.3.7. To properly model the theoretical variograms that are applied as the input parameters for spatial interpolation of kriging, we investigated directional features of spatial correlation by creating variogram surface (ArcGIS/geostatistical wizard)
- 1.3.3.8. Based on the created variogram surfaces, directional features were considered for variogram modeling (Table 4S.5).
- 1.3.3.9. For igneous rocks, spatial structures observed in the semivariogram were simple enough to be closely modeled using a single theoretical variogram model (Table 4S.5)
- 1.3.3.10. All igneous rock classes display significant directional features and high nugget effect. For some variables the nugget effect was so high that the OK efficiency highly reduced as shown by the cross-validation (Tables 4S.5 and 4S.6)
- 1.3.3.11. We assessed the efficiency of the variogram model parameters by using cross-validation and comparison tools (ArcGIS/geostatistical wizard) (Table 4S.6)
- 1.3.3.12. We set the semi-variogram parameters as the default neighborhood search with a minimum number of neighbors of 50 and a maximum of 100 to limit the computational time and adjusted the size and shape of the neighborhood by using cross-validation and comparison tools

1.3.3.13. We applied ordinary kriging using the variogram model and search neighborhood parameters to predict mean and standard deviation of $(^{87}\text{Rb}/^{86}\text{Sr})_{\text{rock}}$ at each pixel over the study area at 1km by 1km resolution

1.4. Predicting $^{87}\text{Sr}/^{86}\text{Sr}$ in igneous rocks (Script 4S.1)

1.4.1. We applied a Monte-Carlo simulation procedure to calculate the $^{87}\text{Sr}/^{86}\text{Sr}$ and incorporated uncertainty around model input parameters at each pixel

1.4.2. 10,000 Monte Carlo iterations were performed for each parameter to assure model convergence. Uncertain input parameters for the igneous submodel include t_2 , $(^{87}\text{Rb}/^{86}\text{Sr})_{\text{parent}}$ and $(^{87}\text{Rb}/^{86}\text{Sr})_{\text{rock}}$ with:

1.4.2.1. t_2 described using a uniform distribution (R, mc2d package) derived from the minimum and maximum age from the GLiM rock unit. Using a uniform distribution assume an equal amount of rock formation (either igneous, carbonate or siliciclastic sediments) throughout a given time period. This assumption is likely valid when the range of age is low (<100 million years) but becomes increasingly uncertain when the range of age broaden. This is because geological processes (either sedimentary or magmatic) can be discrete and rate of igneous rocks, carbonates and siliciclastic sediments formation can vary greatly over 100 million years time scales.

1.4.2.2. $(^{87}\text{Rb}/^{86}\text{Sr})_{\text{parent}}$ described using a normal distribution (R, mc2d package) derived from the power-transformed mean and standard deviation calculated in the calibration step 1. Using a normal distribution assume that our power-transformed step led to a normal distribution of $(^{87}\text{Rb}/^{86}\text{Sr})_{\text{parent}}$ which is a good approximation but is not exactly true for all lithological types (Table 4S.2)

1.4.2.3. $(^{87}\text{Rb}/^{86}\text{Sr})_{\text{rock}}$ described using the using a normal distribution (R, mc2d package) derived from the power-transformed mean and standard deviation calculated in the calibration step 2. Using a normal distribution assume that our power-transformed step led to a normal distribution of $(^{87}\text{Rb}/^{86}\text{Sr})_{\text{rock}}$ which is a good approximation but is not exactly true for all lithological types (Table 4S.4)

2. Carbonate submodel parameterization

2.1. $(^{87}\text{Sr}/^{86}\text{Sr})_{\text{seawater}}$ parameterization step

2.1.1. We extracted the attribute table of the GLiM database over the study area

- 2.1.2. We selected all carbonate units (ev, sc) present in the attribute table
- 2.1.3. We used the maximum and minimum age of each carbonate unit and the *Precambrian Marine Carbonate Isotope Database (PMCI)* curve (Shields and Veizer, 2002) to identify the minimum and maximum $(^{87}\text{Sr}/^{86}\text{Sr})_{\text{seawater}}$ within the age range
- 2.1.4. We inserted back the modified attribute table and converted the GLiM feature layer into minimum and maximum $(^{87}\text{Sr}/^{86}\text{Sr})_{\text{seawater}}$ rasters (ArcGIS/Geoprocessing tool reference)
- 2.2. $(^{87}\text{Rb}/^{86}\text{Sr})_{\text{rock}}$ calibration step
 - 2.2.1. We gathered a database of 352 samples of Rb/Sr analyses from carbonates over the study area using the AGDB2 (Granitto et al., 2013)
 - 2.2.1.1. Query by chemistry: Rb and Sr content
 - 2.2.1.2. Query by sample type: carbonates
 - 2.2.2. We followed the same steps as described in section 1.2 above for each sample of the database (Tables 4S.3 and 4S.4)
- 2.3. Predicting $^{87}\text{Sr}/^{86}\text{Sr}$ in carbonates (Script 4S.2)
 - 2.3.1. We applied a Monte-Carlo simulation procedure to calculate the $^{87}\text{Sr}/^{86}\text{Sr}$ and incorporated uncertainty around model input parameters at each pixel
 - 2.3.2. 10,000 Monte Carlo iterations were performed for each parameter to assure model convergence. Uncertain input parameters for the carbonate submodel include t_2 , $(^{87}\text{Sr}/^{86}\text{Sr})_{\text{seawater}}$ and $(^{87}\text{Rb}/^{86}\text{Sr})_{\text{rock}}$ with:
 - 2.3.2.1. t_2 described using a uniform distribution (R, mc2d package) derived from the minimum and maximum age from the GLiM rock unit
 - 2.3.2.2. $(^{87}\text{Sr}/^{86}\text{Sr})_{\text{seawater}}$ described using a uniform distribution (R, mc2d package) derived from the minimum and maximum $(^{87}\text{Sr}/^{86}\text{Sr})_{\text{seawater}}$
 - 2.3.2.3. $(^{87}\text{Rb}/^{86}\text{Sr})_{\text{rock}}$ described using the using a normal distribution (R, mc2d package) derived from the power-transformed mean and standard deviation calculated in the calibration step 2
3. Siliciclastic sedimentary rock submodel parameterization
 - 3.1. $(^{87}\text{Rb}/^{86}\text{Sr})_{\text{parent}}$ parameterization step

- 3.1.1. We downloaded the Digital Atlas of Terranes for the Northern Cordillera (DATNC) (Colpron and Nelson, 2013) and exported the attribute table in excel
 - 3.1.2. We reported the dominant lithology (major GLiM class) of each terrane unit of the DATNC based on their geological history described in Nelson et al. (2013) (Table 4S.8)
 - 3.1.3. Using the GLiM major class assigned to each terrane, we assigned a $(^{87}\text{Rb}/^{86}\text{Sr})_{\text{parent}}$ from the igneous submodel to each terrane unit across Alaska (Table 4S.1)
- 3.2. t_T parameterization step
 - 3.2.1. We extracted the attribute table of the DATNC over the study area and converted it into an excel table
 - 3.2.2. We reported the minimum and maximum numeric age of each terrane unit of the DATNC based on their geological history described in Nelson et al. (2013) (Table 4S.8)
 - 3.2.3. We inserted back the modified attribute table and converted the terrane units into minimum and maximum terrane age rasters (ArcGIS/Geoprocessing tool reference)
- 3.3. $(^{87}\text{Rb}/^{86}\text{Sr})_{\text{terrane}}$ parameterization step (Script 4S.3)
 - 3.3.1. We assumed that the $(^{87}\text{Rb}/^{86}\text{Sr})_{\text{terrane}}$ could be represented by an integral function with $^{87}\text{Rb}/^{86}\text{Sr}$ increasing exponentially from $(^{87}\text{Rb}/^{86}\text{Sr})_{\text{parent}}$ to $(^{87}\text{Rb}/^{86}\text{Sr})_{\text{rock}}$ between t_T and t_2
 - 3.3.2. This formulation assumes that the $^{87}\text{Rb}/^{86}\text{Sr}$ of siliciclastic sediments increases with the exponentially recycled upper continental crust. The exponential formulation accounts for the effect of both magmatic and sedimentary processes in increasing the $^{87}\text{Rb}/^{86}\text{Sr}$ of the upper crust. The exponential formulation is not correct strictly speaking but it may mimic the overall effect of multiple parameters that are affecting the $^{87}\text{Rb}/^{86}\text{Sr}$ reasonably well. This formulation also assumes that recycling rate of the upper crust have been constant in the last 3 billion years (Dhuime et al., 2012)
- 3.4. $(^{87}\text{Rb}/^{86}\text{Sr})_{\text{rock}}$ parameterization step (Tables 4S.4 and 4S.5)
 - 3.4.1. We obtained n=17,727 Rb/Sr data from the AGDB2 (Granitto et al., 2013)

- 3.4.1.1. Query by chemistry: Rb and Sr content
- 3.4.1.2. Query by sample type: siliciclastic sediments (all types)
- 3.4.2. For each subset:
 - 3.4.2.1. Because Rb/Sr data are strongly positively skewed, we power transformed the Rb/Sr (R, Fitting distribution package) to approximate a normal distribution and allow the application of nonbiased ordinary kriging algorithms {Saito, 2000 #2220} (Table 4S.3)
 - 3.4.2.2. We identified and removed outliers by using normal Q-Q plots for the power-transformed data (Table 4S.2). Only those values far away from the majority of samples in the plots were regarded as outliers. This method of outlier identification using graphs is to some extent subjective. Due to the power of the Box-Cox transformation, this method of lenient outlier identification is considered adequate. The $(^{87}\text{Rb}/^{86}\text{Sr})_{\text{parent}}$ identified extreme values were removed from statistical analyses and spatial structure modeling. They were inserted back for spatial interpolation.
 - 3.4.2.3. We checked the univariate distribution and the approximate normal distribution using histograms and Q-Q plots (ArcGIS/geostatistical wizard) (Table 4S.4)
 - 3.4.2.4. We checked the presence/absence of trend (ArcGIS/geostatistical wizard)
 - 3.4.2.5. We modeled the spatial autocorrelation by building a semi-variogram that quantifies the square of differences between sample pairs as a function of lag distance that separates these sample pairs.
 - 3.4.2.6. We fitted the most appropriate variogram model (range, nugget and sill) for each of the power transformed subsets by using the iterative fitting tool (ArcGIS/geostatistical wizard) (Table 4S.5)
 - 3.4.2.7. To properly model the theoretical variograms that are applied as the input parameters for spatial interpolation of kriging, we investigated directional features of spatial correlation by creating variogram surface (ArcGIS/geostatistical wizard)
 - 3.4.2.8. Based on the created variogram surfaces, directional features were considered for variogram modeling (Table 4S.5)
 - 3.4.2.9. For siliciclastic sedimentary rocks, complicated spatial structures

were observed and it was difficult to fit them using a single theoretical variogram model. We used nested models to model the spatial structure (Table 4S.5)

- 3.4.2.10. We assessed the efficiency of the variogram model parameters by using cross-validation and comparison tools (ArcGIS/geostatistical wizard) (Table 4S.6)
- 3.4.2.11. We set the semi-variogram parameters as the default neighborhood search with a minimum number of neighbors of 50 and a maximum of 100 to limit the computational time and adjusted the size and shape of the neighborhood by using cross-validation and comparison tools
- 3.4.2.12. We applied ordinary kriging using the variogram model and search neighborhood parameters to predict mean and standard deviation of $(^{87}\text{Rb}/^{86}\text{Sr})_{\text{rock}}$ at each pixel over the study area at 1km by 1km resolution

3.5. Predicting $^{87}\text{Sr}/^{86}\text{Sr}$ in siliciclastic sediments (Script 4S.3)

- 3.5.1. 10,000 Monte Carlo iterations were performed for each parameter to assure model convergence. Uncertain input parameters for the siliciclastic sedimentary rock submodel t_2 , t_T , $(^{87}\text{Rb}/^{86}\text{Sr})_{\text{terrane}}$ and $(^{87}\text{Rb}/^{86}\text{Sr})_{\text{rock}}$ with:
 - 3.5.1.1. t_2 described using a uniform distribution (R, mc2d package) derived from the minimum and maximum age from the GLiM rock unit. Using a uniform distribution assume an equal amount of rock formation (either igneous, carbonate or siliciclastic sediments) throughout a given time period. This assumption is likely valid when the range of age is low (<100 million years) but becomes increasingly uncertain when the range of age broaden. This is because geological processes (either sedimentary or magmatic) can be discrete and rate of igneous rocks, carbonates and siliciclastic sediments formation can vary greatly over 100 million years time scales.
 - 3.5.1.2. t_T described using a uniform distribution (R, mc2d package) derived from the minimum and maximum age from the DATNC terrane units.
 - 3.5.1.3. $(^{87}\text{Rb}/^{86}\text{Sr})_{\text{parent}}$ described using a normal distribution (R, mc2d package) derived from the power-transformed mean and standard deviation calculated in the calibration step 1. Using a normal distribution assume that our power-transformed stepped to a normal

distribution of $(^{87}\text{Rb}/^{86}\text{Sr})_{\text{parent}}$ which is a good approximation but is not exactly true for all lithological types (Table 4S.2)

3.5.1.4. $(^{87}\text{Rb}/^{86}\text{Sr})_{\text{terrane}}$ described using an integral function (equation 4.5) which parameters are calculated using the calibrated $(^{87}\text{Rb}/^{86}\text{Sr})_{\text{parent}}$ and $(^{87}\text{Rb}/^{86}\text{Sr})_{\text{rock}}$ at t_1 and t_2 respectively

3.5.1.5. $(^{87}\text{Rb}/^{86}\text{Sr})_{\text{rock}}$ described using the using a normal distribution (R, mc2d package) derived from the power-transformed mean and standard deviation calculated in the calibration step 2. Using a normal distribution assume that our power-transformed stepped led to a normal distribution of $(^{87}\text{Rb}/^{86}\text{Sr})_{\text{rock}}$ which is a good approximation but is not exactly true for all lithological types (Table 4S.4)

4. GIS processing

4.1. For each output raster from Monte Carlo simulation:

4.1.1. We sorted the GLiM attribute table by major lithology

4.1.2. We selected iteratively all the units corresponding to one major GLiM lithological class (e.g., va)

4.1.3. We used the selected polygons to clip the output raster from the Monte Carlo simulations (ArcGIS/Analysis toolbox)

4.1.4. We mosaiced the clipped raster from each major GLiM lithological class and obtained the min, max, decile 1, decile 10, quartile 1 and quartile 3, median, mean and standard deviation of $^{87}\text{Sr}/^{86}\text{Sr}$ at each pixel over AK (ArcGIS/Data management toolbox)

Table 4S.1 Summary of power-transformation for $(^{87}\text{Rb}/^{86}\text{Sr})_{\text{parent}}$ dataset of each major GLiM lithological class. n=number of samples in the dataset, n outliers=number of outliers, Power1=the power-transformed coefficient, mean= the mean of the power-transformed $(^{87}\text{Rb}/^{86}\text{Sr})_{\text{rock}}$ dataset and stdev= the standard deviation of the power-transformed $(^{87}\text{Rb}/^{86}\text{Sr})_{\text{rock}}$ dataset.

GLiM class	N	n outliers	Power1	Mean	Stdev
Pa	3127	42	-0.043	1.14	0.021
Pi	3901	51	-0.074	1.19	0.043
Pb	1733	16	-0.23	2.16	0.22
Va	2772	12	-0.50	5.16	1.22
Vb	10731	91	-0.86	24.05	7.37
Vi	9050	74	-0.65	9.85	2.74
Mt	107	2	-0.49	5.00	1.05

Table 4S.2 Q-Q plots and histograms of $(^{87}\text{Rb}/^{86}\text{Sr})_{\text{parent}}$ dataset of each major GLiM lithological class after power-transformation and outliers removal.

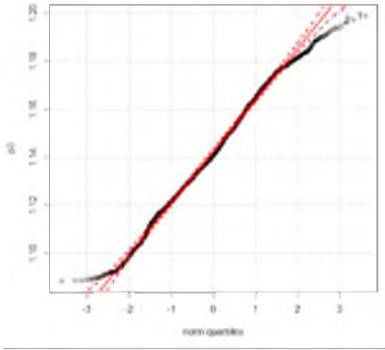
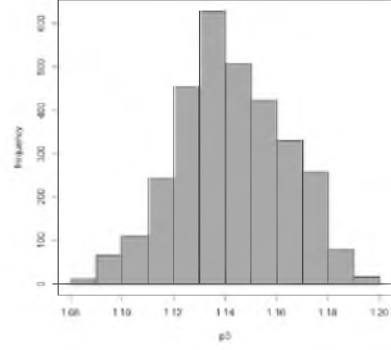
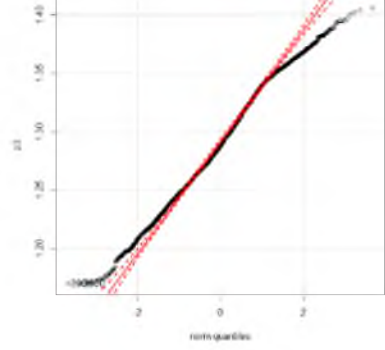
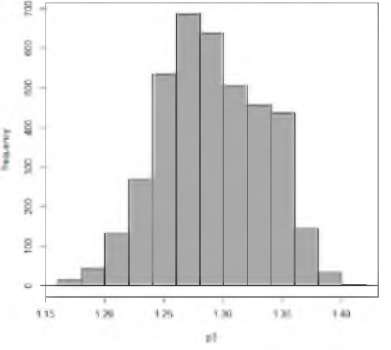
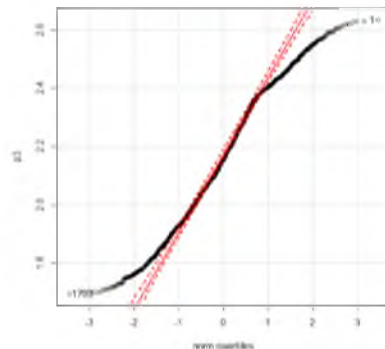
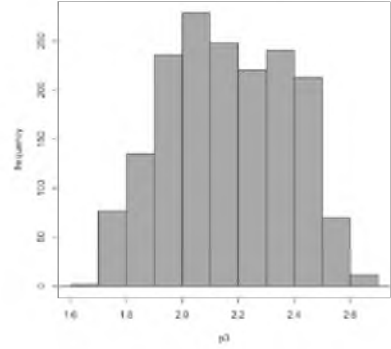
GLiM class	Q-Q plots	Histograms
Pa		
Pi		
Pb		

Table 4S.2 continued

<p>Va</p>		
<p>Vb</p>		
<p>Vi</p>		
<p>Mt</p>		

Table 4S.3 Summary of power-transformation for $(^{87}\text{Rb}/^{86}\text{Sr})_{\text{rock}}$ for each major GLiM lithological class. n=number of samples in the dataset, n outliers=number of outliers, a=the power-transformed coefficient, mean= the mean of the power-transformed $(^{87}\text{Rb}/^{86}\text{Sr})_{\text{rock}}$ dataset and stdev= the standard deviation of the power-transformed $(^{87}\text{Rb}/^{86}\text{Sr})_{\text{rock}}$ dataset.

	N	Outliers	Power2	Mean	Stdev
Pa	3124	76	-0.1427	1.235713	0.2842713
Pi	3252	48	-0.1372	1.398426	0.1959414
Pb	1254	28	-0.2312	0.9318234	0.02128509
Va	1306	46	-0.1429	1.234519	0.225184
Vb	4849	23	-0.05559	1.180985	0.05582446
Vi	2677	27	-0.1579	1.497199	0.186832
Mt	2244	31	-0.1193	1.290058	0.2360382
Ssed	17727	34	0.224	0.8154528	0.2212677
Ca	157	0	-0.4152	4.255055	1.454305

Table 4S.4 Q-Q plots and histograms of $(^{87}\text{Rb}/^{86}\text{Sr})_{\text{rock}}$ datasets for each major GLiM lithological class after power-transformation.

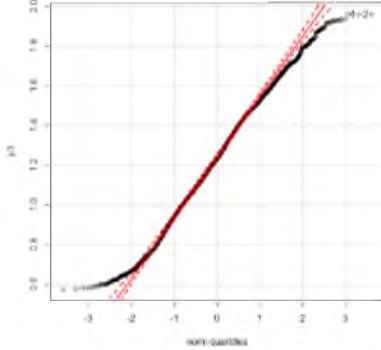
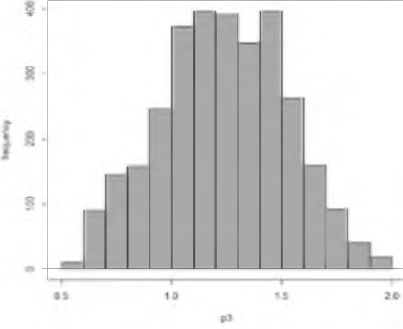
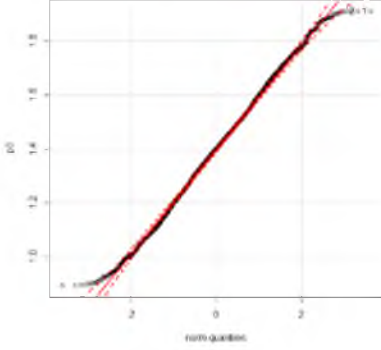
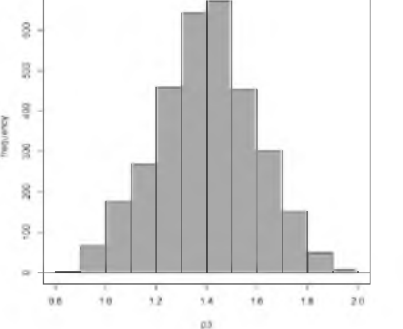
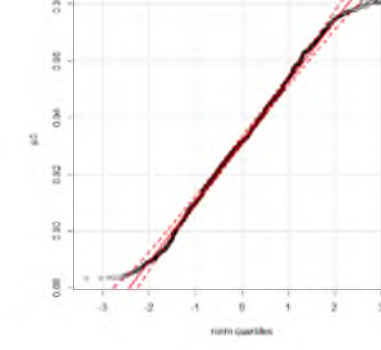
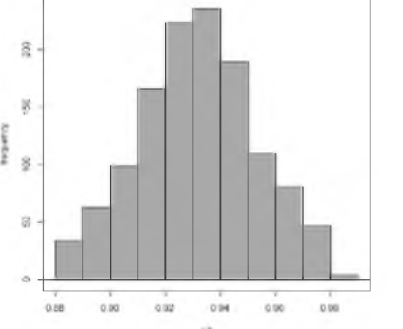
GLiM class	Q-Q plots	Histograms
Pa	 <p>A Q-Q plot for the Pa class. The x-axis is labeled 'norm quantiles' and ranges from -3 to 3. The y-axis is labeled 'p3' and ranges from 0.8 to 2.0. A solid black line represents the data, which closely follows a red dashed normal distribution line. A label 'p3=2.0' is in the top right corner.</p>	 <p>A histogram for the Pa class. The x-axis is labeled 'p3' and ranges from 0.5 to 2.0. The y-axis is labeled 'frequency' and ranges from 0 to 400. The bars show a roughly normal distribution centered around 1.2. A red dashed normal distribution curve is overlaid on the histogram.</p>
Pi	 <p>A Q-Q plot for the Pi class. The x-axis is labeled 'norm quantiles' and ranges from -2 to 2. The y-axis is labeled 'p3' and ranges from 1.0 to 1.8. A solid black line represents the data, which closely follows a red dashed normal distribution line. A label 'p3=1.0' is in the top right corner.</p>	 <p>A histogram for the Pi class. The x-axis is labeled 'p3' and ranges from 0.8 to 2.0. The y-axis is labeled 'frequency' and ranges from 0 to 600. The bars show a roughly normal distribution centered around 1.4. A red dashed normal distribution curve is overlaid on the histogram.</p>
Pb	 <p>A Q-Q plot for the Pb class. The x-axis is labeled 'norm quantiles' and ranges from -3 to 3. The y-axis is labeled 'p3' and ranges from 0.88 to 1.00. A solid black line represents the data, which closely follows a red dashed normal distribution line. A label 'p3=0.95' is in the top right corner.</p>	 <p>A histogram for the Pb class. The x-axis is labeled 'p3' and ranges from 0.88 to 1.00. The y-axis is labeled 'frequency' and ranges from 0 to 200. The bars show a roughly normal distribution centered around 0.95. A red dashed normal distribution curve is overlaid on the histogram.</p>

Table 4S.4 continued

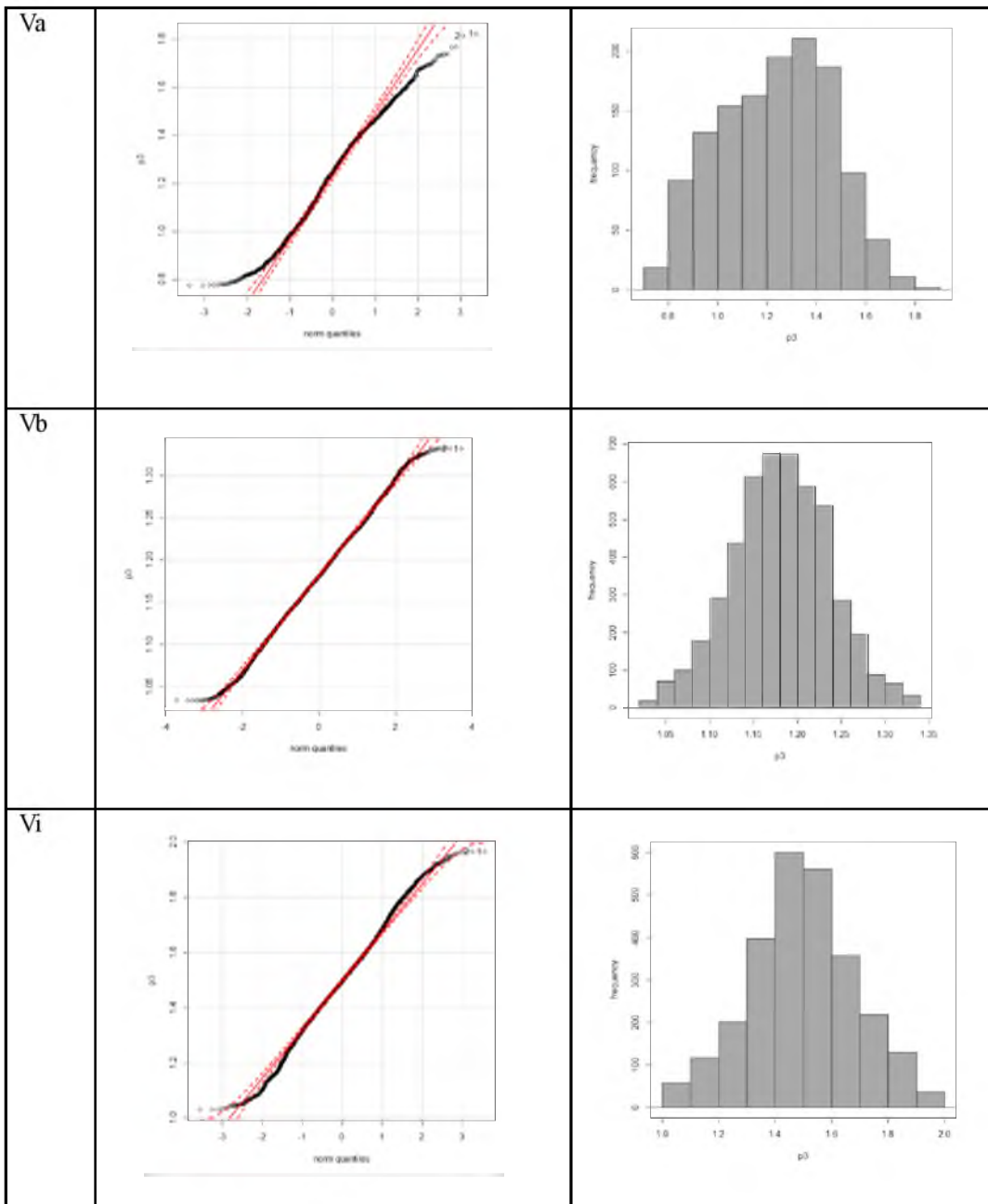


Table 4S.4 continued

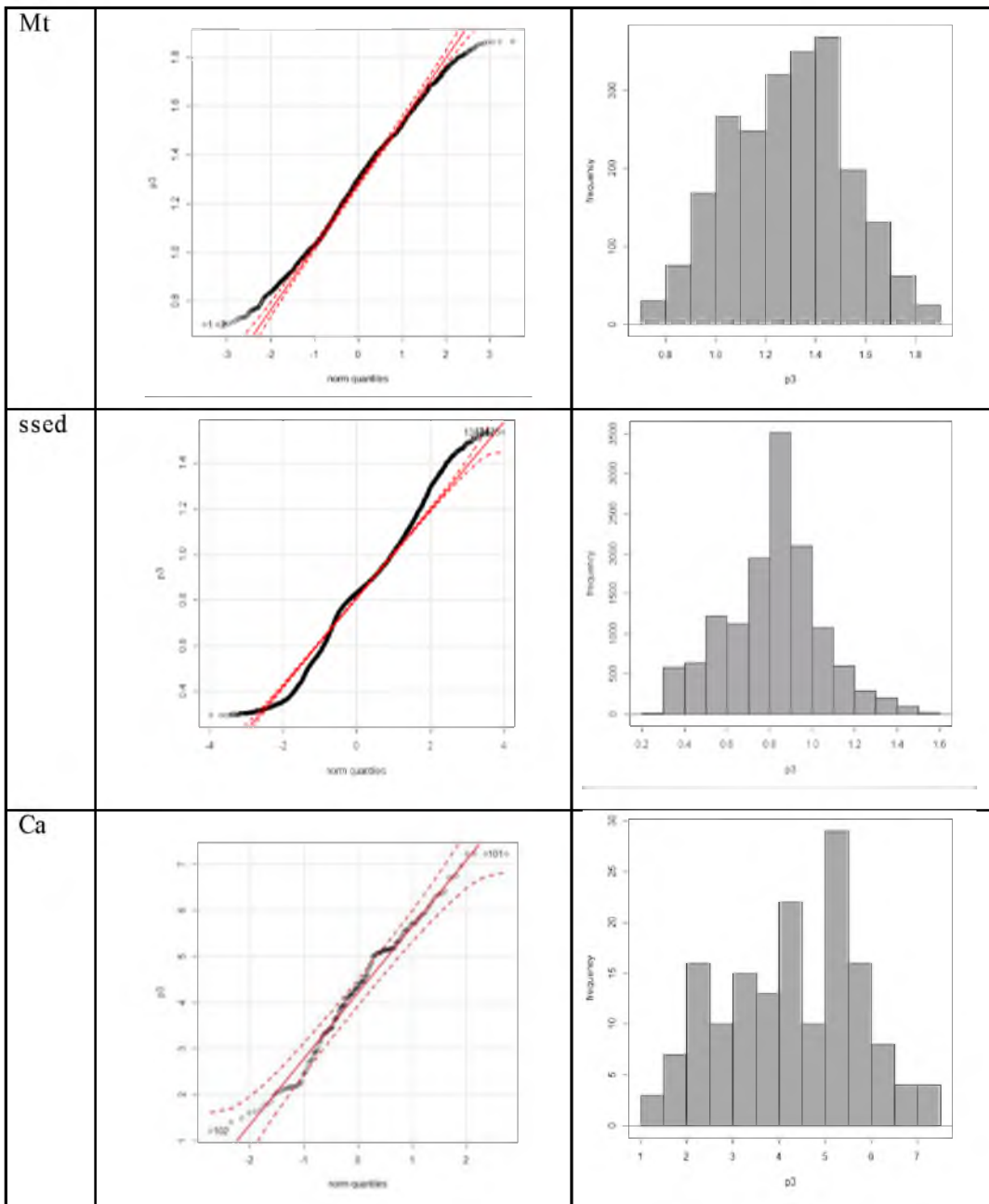


Table 4S.5 Summary of variogram model proprieties used in ordinary krigging of power-transformed $(^{87}\text{Rb}/^{86}\text{Sr})_{\text{rock}}$ of each GLiM class dataset. The specific parameters for the modeled variograms includes the model type (exp=exponential); the nugget effect (a parameter to measure the variation under the current sampling density and measurement errors); the partial sill (the difference between total sill and nugget effect); the major and minor ranges (define the distance at which the samples can be considered as independent in different direction). The direction of the anisotropy is used to model the directional features. The specific fitted variogram plots for selected variables are shown in Table 4S.6.

GLiM classes	Model1/ Model2	Lag size (degree)	Nugget	Major Range	Minor range	Direction (degree)	Neighborhood (neighbours/ ellipse)
Pa	Exp	0.12	0.021	0.96	1.43	24.61	50
Pi	Exp	0.038	0.010	0.30	0.46	22.85	50
Pb	Exp	0.22	0.00028	1.78	2.67	11.43	50
Va	Exp	0.091	0.014	0.73	0.57	111.45	50
Vb	Exp	0.12	0.0020	0.97	0.47	104.94	50
Vi	Exp	0.18	0.022	1.46	0.42	90.18	50
Mt	Exp	0.050	0.024	0.40	0.60	17.93	50
ssed	exp/ gaussian	0.40	0.0077	0.27/ 6.03	2.02	63.50	50
Ca	Exp	0.017	0.45	0.14	x	x	50

Table 4S.6 Plot of empirical variograms and fitted variogram models for each GLiM major lithological class.

GLiM class	Variograms
Pa	
Pi	
Pb	

Table 4S.6 continued

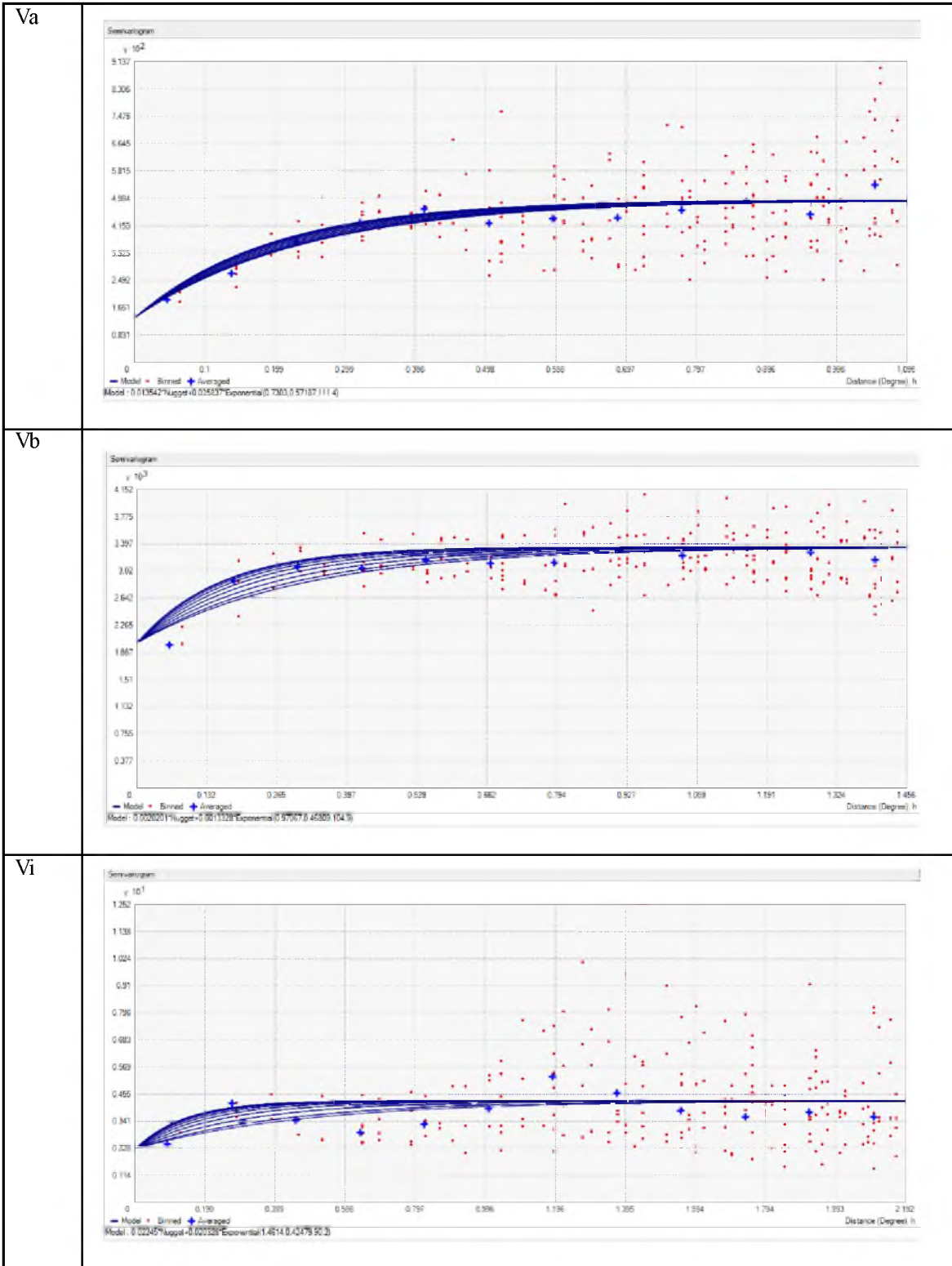


Table 4S.6 continued

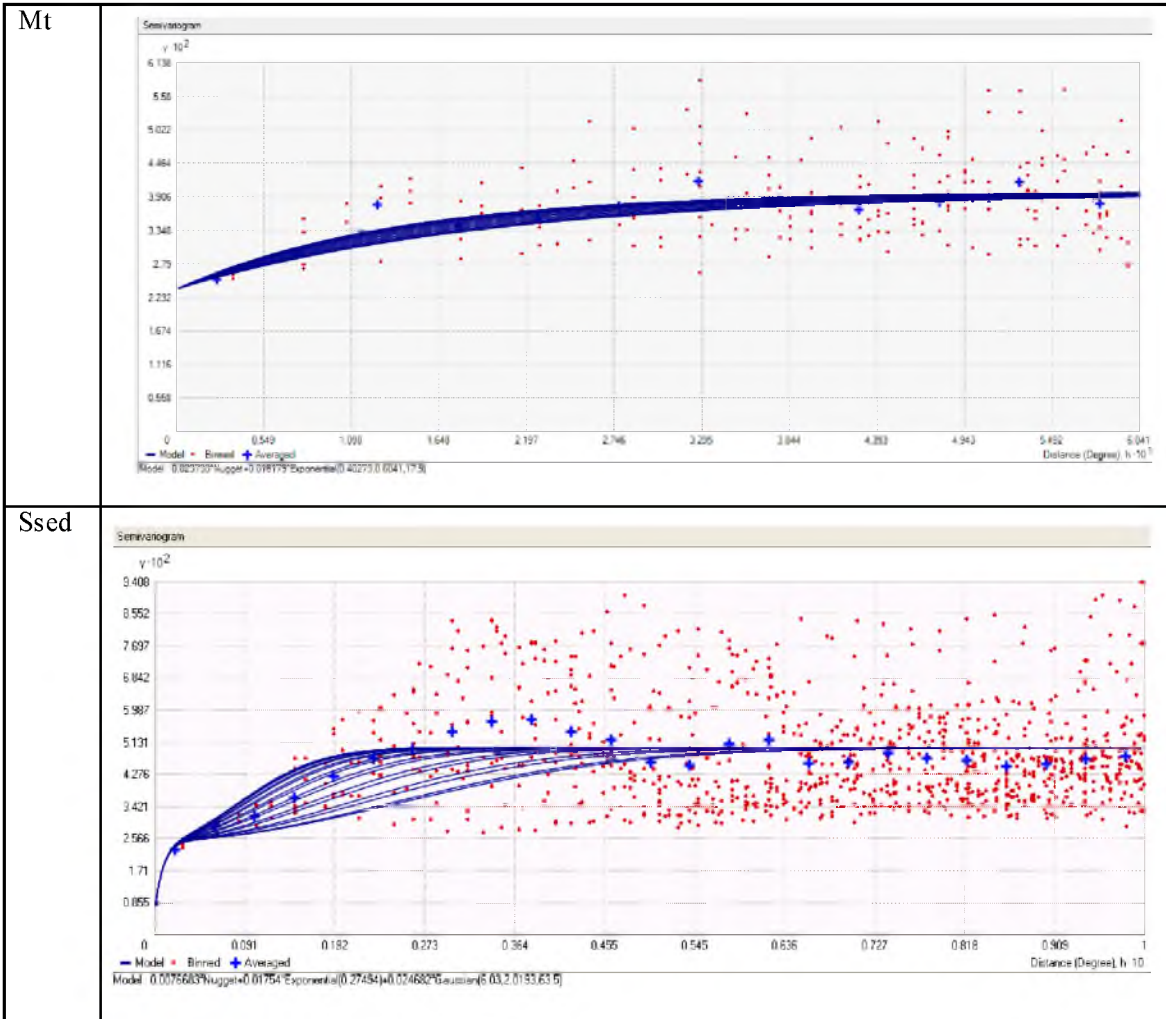


Table 4S.7 Scatterplot of predicted vs. observed power-transformed $(^{87}\text{Rb}/^{86}\text{Sr})_{\text{rock}}$ for each lithological class and summary statistic of model prediction.

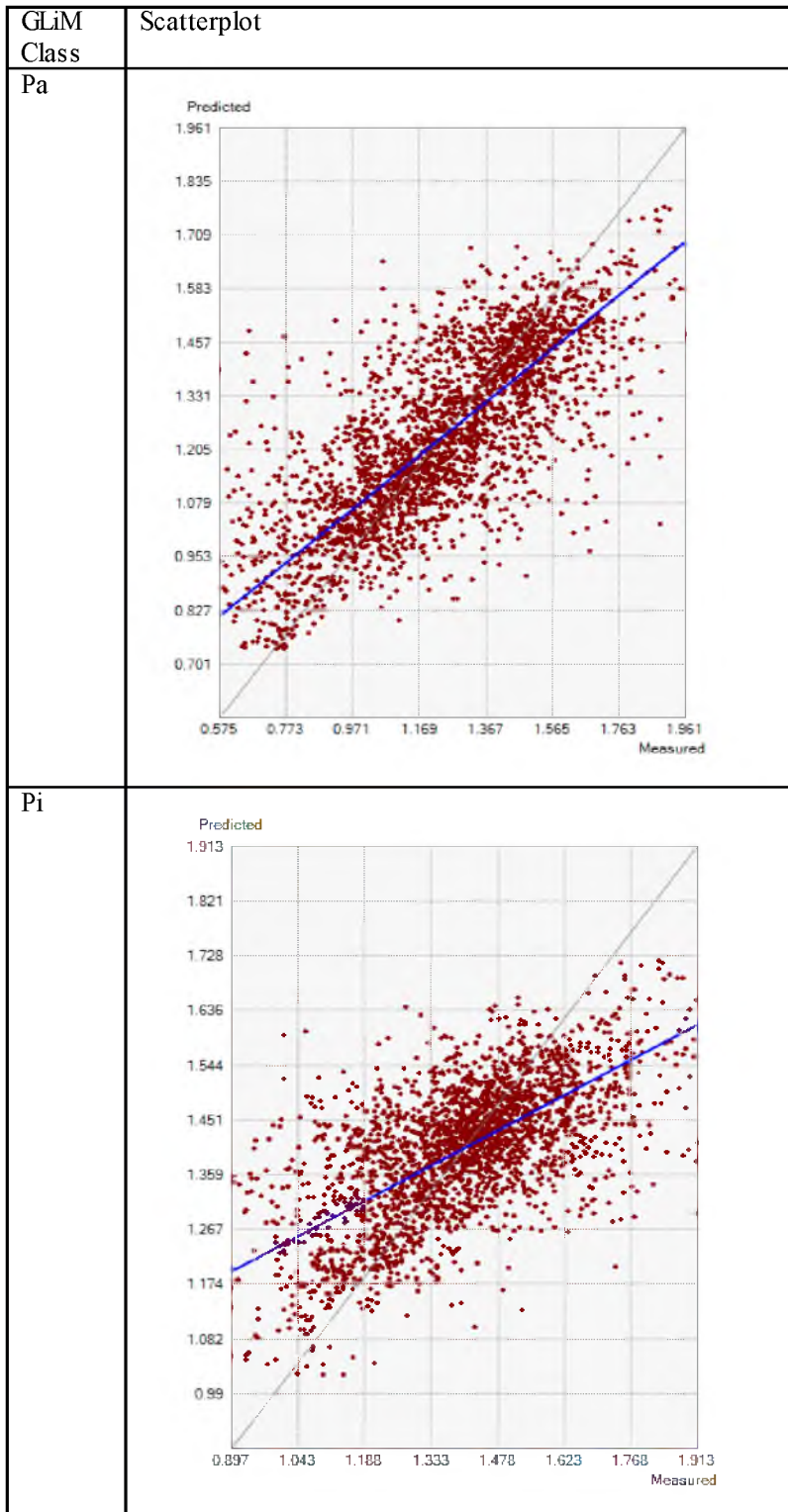


Table 4S.7 continued

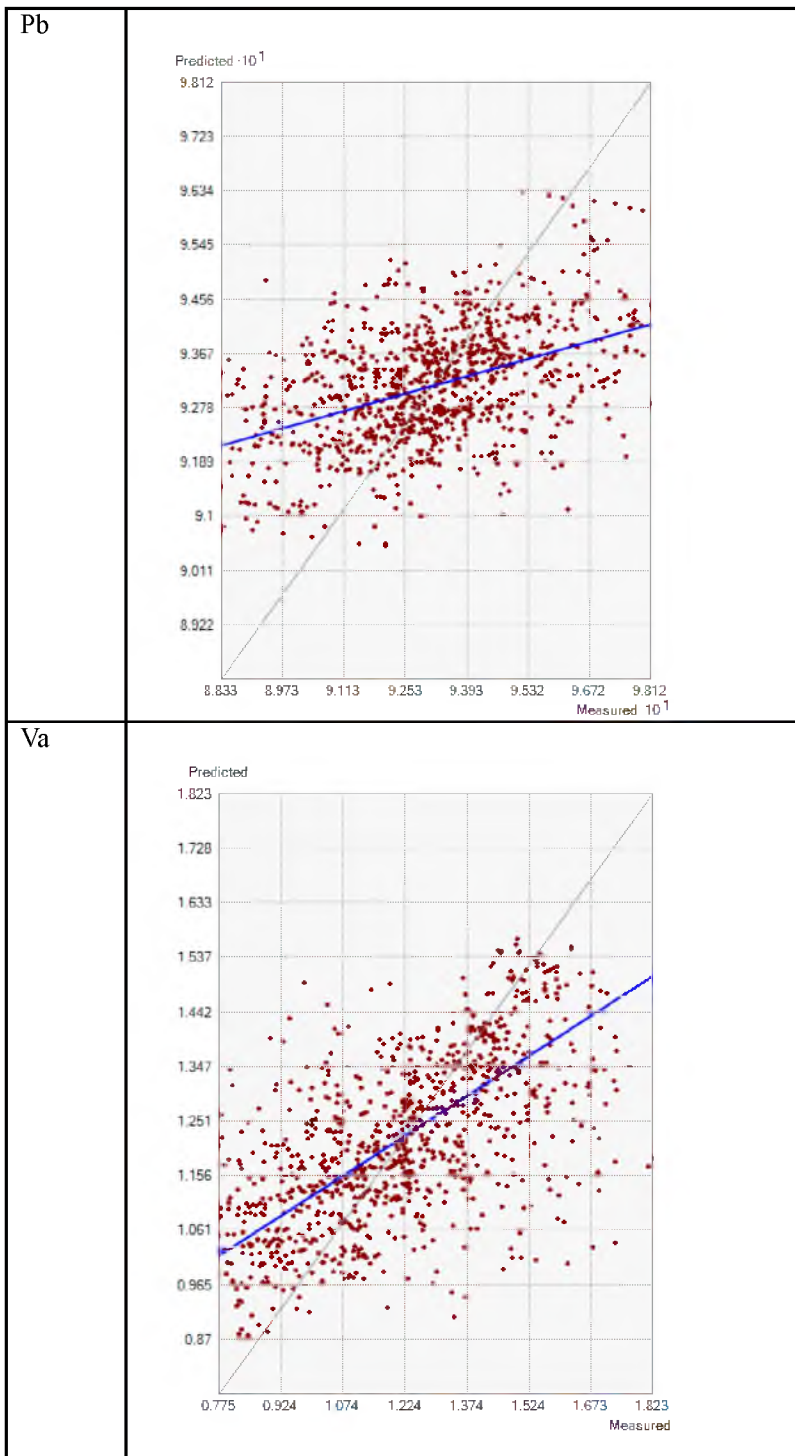


Table 4S.7 continued

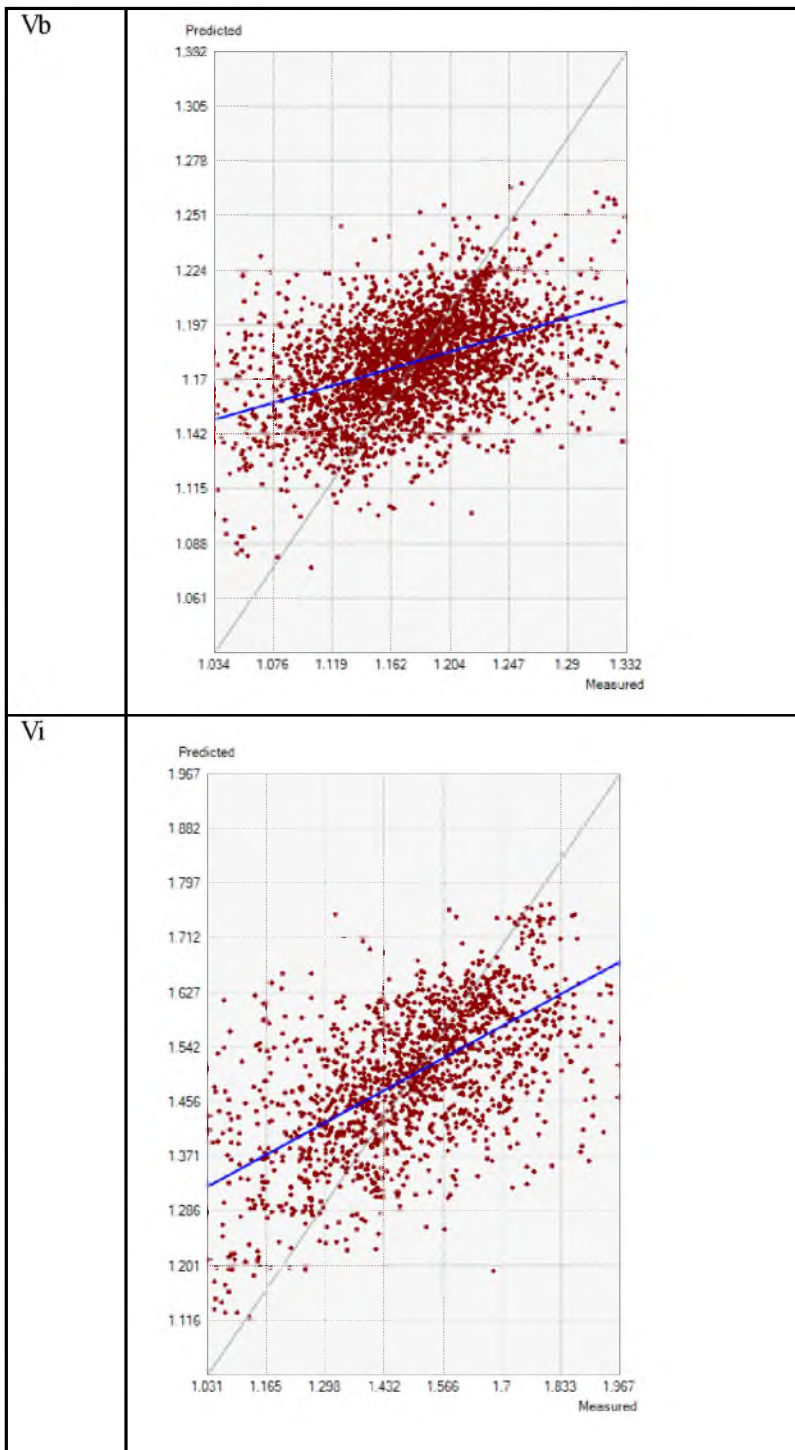


Table 4S.7 continued

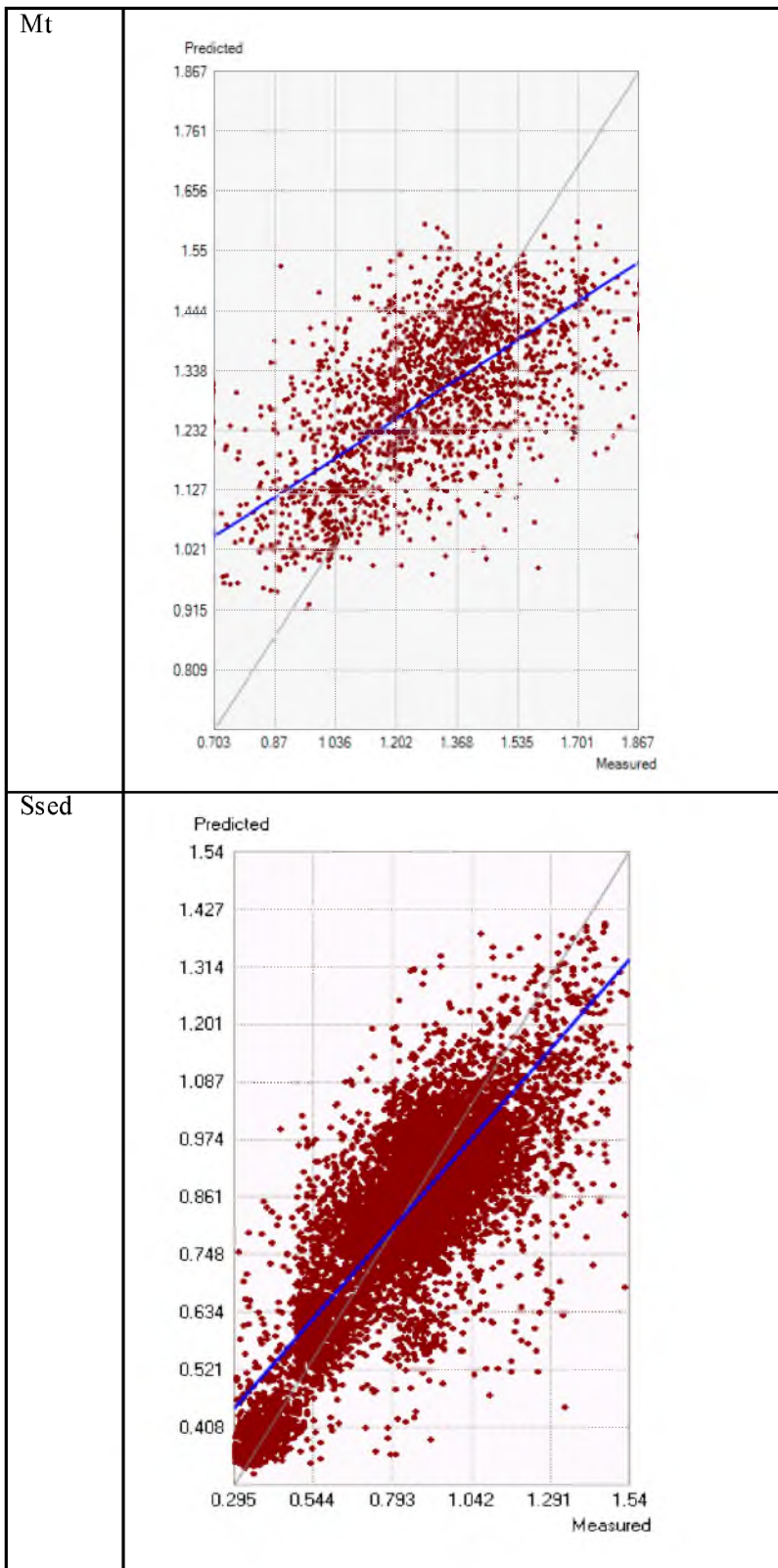


Table 4S.8 Attribute table of the digital Atlas of Terranes from the Northern Cordillera (Colpron and Nelson, 2010) with additional lithological description, min age and max age field based on Nelson et al., 2013.

ID	T_Group	Affinity	GLIM xx	Lithological description	Min age (Ma)	Max age (Ma)
4	Insular	Baltica	vi	pericratonic and arc	350	425
60	Insular	Baltica	vi	pericratonic and arc	350	425
62	Insular	Baltica	vi	pericratonic and arc	350	425
20	Outboard	Siberian- Laurentian	vb	oceanic crust	359	419
21	Outboard	Siberian- Laurentian	vb	oceanic crust	359	419
23	Outboard	Siberian- Laurentian	vb	oceanic crust	359	419
27	Outboard	Siberian- Laurentian	vb	oceanic crust	359	419
29	Outboard	Siberian- Laurentian	vb	oceanic crust	359	419
31	Outboard	Siberian- Laurentian	vb	oceanic crust	359	419
36	Outboard	Siberian- Laurentian	vb	oceanic crust	359	419
37	Outboard	Siberian- Laurentian	vb	oceanic crust	359	419
38	Outboard	Siberian- Laurentian	vb	oceanic crust	359	419
39	Outboard	Siberian- Laurentian	vb	oceanic crust	359	419
40	Outboard	Siberian- Laurentian	vb	oceanic crust	359	419
41	Outboard	Siberian- Laurentian	vb	oceanic crust	359	419
42	Outboard	Siberian- Laurentian	vb	oceanic crust	359	419
43	Outboard	Siberian- Laurentian	vb	oceanic crust	359	419
44	Outboard	Siberian- Laurentian	vb	oceanic crust	359	419
1	N Alaska	Siberian	pi	Pericratonic	542	1000
33	N Alaska	Siberian	pi	Pericratonic	542	1000
34	N Alaska	Siberian	pi	Pericratonic	542	1000
8	Outboard	E Pacific	vi	Accretionary complex	66	146
13	Outboard	E Pacific	vi	Accretionary complex	66	146
59	Outboard	E Pacific	vi	Accretionary complex	66	146
61	Outboard	E Pacific	vi	Accretionary complex	66	146
64	Outboard	E Pacific	vi	Accretionary complex	66	146
65	Outboard	E Pacific	vi	Accretionary complex	66	146
66	Outboard	E Pacific	vi	Accretionary complex	66	146

Table 4S.8 continued

67	Outboard	E Pacific	vi	Accretionary complex	66	146
68	Outboard	E Pacific	vi	Accretionary complex	66	146
69	Outboard	E Pacific	vi	Accretionary complex	66	146
70	Outboard	E Pacific	vi	Accretionary complex	66	146
71	Outboard	E Pacific	vi	Accretionary complex	66	146
72	Outboard	E Pacific	vi	Accretionary complex	66	146
73	Outboard	E Pacific	vi	Accretionary complex	66	146
74	Outboard	E Pacific	vi	Accretionary complex	66	146
75	Outboard	E Pacific	vi	Accretionary complex	66	146
76	Outboard	E Pacific	vi	Accretionary complex	66	146
77	Outboard	E Pacific	vi	Accretionary complex	66	146
78	Outboard	E Pacific	vi	Accretionary complex	66	146
79	Outboard	E Pacific	vi	Accretionary complex	66	146
80	Outboard	E Pacific	vi	Accretionary complex	66	146
81	Outboard	E Pacific	vi	Accretionary complex	66	146
82	Outboard	E Pacific	vi	Accretionary complex	66	146
83	Outboard	E Pacific	vi	Accretionary complex	66	146
84	Outboard	E Pacific	vi	Accretionary complex	66	146
85	Outboard	E Pacific	vi	Accretionary complex	66	146
86	Outboard	E Pacific	vi	Accretionary complex	66	146
87	Outboard	E Pacific	vi	Accretionary complex	66	146
88	Outboard	E Pacific	vi	Accretionary complex	66	146
89	Outboard	E Pacific	vi	Accretionary complex	66	146
90	Outboard	E Pacific	vi	Accretionary complex	66	146
91	Outboard	E Pacific	vi	Accretionary complex	66	146
92	Outboard	E Pacific	vi	Accretionary complex	66	146
93	Outboard	E Pacific	vi	Accretionary complex	66	146
94	Outboard	E Pacific	vi	Accretionary complex	66	146
95	Outboard	E Pacific	vi	Accretionary complex	66	146
96	Outboard	E Pacific	vi	Accretionary complex	66	146
97	Outboard	E Pacific	vi	Accretionary complex	66	146
16	N Alaska	Siberian	pi	Pericratonic and metamorphic	542	1000
30	N Alaska	Siberian	pi	pericratonic to metamorphic	542	1000
17	Outboard	E Pacific	vi	Arc terrane	251	299
25	Outboard	E Pacific	vi	Arc terrane	251	299
2	Ancestral North America	W Laurentia	pi	Pericratonic	2000	3000
22	Ancestral North America	W Laurentia	pi	Pericratonic	2000	3000
63	Ancestral North America	W Laurentia	pi	Pericratonic	2000	3000

Table 4S.8 continued

10 4	Ancestral North America	W Laurentian	pi	Pericratonic	2000	3000
28	Ancestral North America	W Laurentia	pi	Cratonic	2000	3000
9	Insular	Panthalassa	vi	pericratonic and arc	350	425
10	Insular	Panthalassa	vi	pericratonic and arc	350	425
11	Insular	Panthalassa	vi	pericratonic and arc	350	425
12	Insular	Panthalassa	vi	pericratonic and arc	350	425
14	Insular	Panthalassa	vi	pericratonic and arc	350	425
45	Outboard	E Pacific	vi	Accretionary complex	66	146
46	Outboard	E Pacific	vi	Accretionary complex	66	146
47	Outboard	E Pacific	vi	Accretionary complex	66	146
48	Outboard	E Pacific	vi	Accretionary complex	66	146
49	Outboard	E Pacific	vi	Accretionary complex	66	146
50	Outboard	E Pacific	vi	Accretionary complex	66	146
51	Outboard	E Pacific	vi	Accretionary complex	66	146
52	Outboard	E Pacific	vi	Accretionary complex	66	146
53	Outboard	E Pacific	vi	Accretionary complex	66	146
54	Outboard	E Pacific	vi	Accretionary complex	66	146
55	Outboard	E Pacific	vi	Accretionary complex	66	146
57	Outboard	E Pacific	vi	Accretionary complex	66	146
18	N Alaska	Siberian	pi	Pericratonic	542	1000
19	N Alaska	Siberian	pi	Pericratonic	542	1000
24	N Alaska	Siberian	pi	Pericratonic	542	1000
26	N Alaska	Siberian	pi	Pericratonic	542	1000
32	N Alaska	Siberian	pi	Pericratonic	542	1000
99	Intermontane	W Laurentia	vb	Ophiolitic assemblage	359	416
10 0	Intermontane	W Laurentia	vb	Ophiolitic assemblage	359	416
10 3	Intermontane	W Laurentia	vb	Ophiolitic assemblage	359	416
98	Intermontane	W Laurentian	vb	Oceanic assemblage	359	416
3	Insular	E Pacific	vi	rift filled and volcanic strata	359	416
5	Insular	NE Panthalassa	pi	Pericratonic	350	425
15	Insular	NE Panthalassa	pi	Pericratonic	350	425
56	Outboard	E Pacific	vi	Accretionary complex	66	146
58	Outboard	E Pacific	vi	Accretionary complex	66	146
7	Intermontane	W Laurentia	vi	Arc terrane	359	416
10 2	Intermontane	W Laurentia	vi	Arc terrane	359	416
29	Insular	Baltica	vi	pericratonic and arc	350	425

Table 4S.8 continued

41	Intermontane	W Panthalassa	vi	Arc terrane	146	201
42	Intermontane	W Panthalassa	vi	Arc terrane	146	201
45	Intermontane	W Panthalassa	vi	Arc terrane	146	201
2	Ancestral North America	W Laurentia	pi	periocratonic	542	1000
13	Ancestral North America	W Laurentia	pi	periocratonic	542	1000
10	Intermontane	W Panthalassa	vi	Arc terrane	251	298
21	Intermontane	W Panthalassa	vi	Arc terrane	251	298
43	Intermontane	W Laurentia	vi	Arc terrane	201	251
48	Intermontane	W Laurentia	vi	Arc terrane (piece of the ST terrane)	359	416
59	Outboard	E Pacific	vi	Accreted seamounts	66	146
47	Intermontane	W Laurentia	vi	pericratonic and arc	201	251
49	Intermontane	W Laurentia	vi	pericratonic and arc	201	251
50	Intermontane	W Laurentia	vi	pericratonic and arc	201	251
51	Intermontane	W Laurentia	vi	pericratonic and arc	201	251
56	Intermontane-Insular arc overlap	W Laurentia	pi	plutonic	146	251
40	Intermontane	W Laurentia	vi	Arc terrane	146	201
44	Intermontane	W Laurentia	vi	Arc terrane	146	201
15	Ancestral North America	W Laurentia	pi	pericratonic	2500	3000
52	Ancestral North America	W Laurentia	pi	pericratonic	2000	3000
54	Ancestral North America	W Laurentia	pi	pericratonic	2000	3000
38	Ancestral North America	W Laurentia	pi	cratonic	2000	3000
57	Ancestral North America	W Laurentia	pi	cratonic	2000	3000
1	Ancestral North America	W Laurentia	pi	cratonic	2000	3000
39	Ancestral North America	W Laurentia	pi	cratonic	2000	3000
53	Ancestral North America	W Laurentia	pi	cratonic	2000	3000
55	Ancestral North America	W Laurentia	pi	cratonic	2000	3000
20	Intermontane	Caledonian?	pi	pericratonic	542	1500
58	Outboard	E Pacific	vi	Accretionary complex	66	146
9	Intermontane	W Laurentia	vi	Arc terrane	201	251
12	Intermontane	W Laurentia	vi	Arc terrane	201	251
6	Intermontane	W Laurentia	vb	Oceanic assemblage	542	1500
14	Intermontane	W Laurentia	vb	Oceanic assemblage	359	416
16	Intermontane	W Laurentia	vb	Oceanic assemblage	359	416

Table 4S.8 continued

17	Intermontane	W Laurentia	vb	Oceanic assemblage	359	416
18	Intermontane	W Laurentia	vb	Oceanic assemblage	359	416
19	Intermontane	W Laurentia	vb	Oceanic assemblage	359	416
11	Intermontane	W Laurentia	vi	Arc terrane	359	416
24	Intermontane	W Laurentia	vi	Arc terrane	359	416
28	Intermontane	W Laurentia	vi	Arc terrane	359	416
46	Intermontane	W Laurentia	vi	Arc terrane	359	416
22	Insular	NE Panthalassa	pi	pericratonic	350	425
30	Insular	NE Panthalassa	pi	pericratonic	350	425
31	Insular	NE Panthalassa	pi	pericratonic	350	425
32	Insular	NE Panthalassa	pi	pericratonic	350	425
33	Insular	NE Panthalassa	pi	pericratonic	350	425
34	Insular	NE Panthalassa	pi	pericratonic	350	425
35	Insular	NE Panthalassa	pi	pericratonic	350	425
36	Insular	NE Panthalassa	pi	pericratonic	350	425
37	Insular	NE Panthalassa	pi	pericratonic	350	425
3	Intermontane	W Laurentia	vi	Arc terrane	359	416
4	Intermontane	W Laurentia	vi	Arc terrane	359	416
5	Intermontane	W Laurentia	vi	Arc terrane	359	416
7	Intermontane	W Laurentia	vi	Arc terrane	359	416
8	Intermontane	W Laurentia	vi	Arc terrane	359	416
23	Intermontane	W Laurentia	vi	Arc terrane	359	416
25	Intermontane	W Laurentia	vi	Arc terrane	359	416
26	Intermontane	W Laurentia	vi	Arc terrane	359	416
27	Intermontane	W Laurentia	vi	Arc terrane	359	416
29	Baltica	Arctic Alaska	vi	pericratonic and arc	542	1000
26	Baltica	Alexander	vi	pericratonic and arc	350	425
4	W Laurentia	Cassiar	pi	pericratonic	542	1000
21	W Laurentia	Cassiar	pi	pericratonic	542	1000
18	W Panthalassa	Cache Creek	vi	Arc	359	416
2	E Pacific	Chugach	vi	Accretionary complex	66	146
34	E Pacific	Chugach	vi	Accretionary complex	66	146
24	E Pacific	Kluane schist	mt	metamorphic	66	146
11	W Laurentia	North America - basinal strata	pi	pericratonic	2000	3000
23	W Laurentia	North America - basinal strata	pi	pericratonic	2000	3000

Table 4S.8 continued

28	W Laurentia	North America - basinal strata	pi	pericratonic	2000	3000
31	W Laurentia	North America - basinal strata	pi	pericratonic	2000	3000
36	W Laurentia	North America - basinal strata	pi	pericratonic	2000	3000
38	W Laurentia	North America - basinal strata	pi	pericratonic	2000	3000
41	W Laurentia	North America - basinal strata	pi	pericratonic	2000	3000
35	W Laurentia	North America - craton and cover	pi	cratonic	2000	3000
37	N Laurentia	North America - craton and cover	pi	cratonic	2000	3000
1	W Laurentia	North America - platformal strata	pi	cratonic	2000	3000
13	W Laurentia	North America - platformal strata	pi	cratonic	2000	3000
14	W Laurentia	North America - platformal strata	pi	cratonic	2000	3000
16	W Laurentia	Quesnellia	vi	Arc	359	416
17	W Laurentia	Quesnellia	vi	Arc	359	416
5	W Laurentian	Slide Mountain	vb	Oceanic assemblage	359	416
6	W Laurentian	Slide Mountain	vb	Oceanic assemblage	359	416
7	W Laurentian	Slide Mountain	vb	Oceanic assemblage	359	416
8	W Laurentian	Slide Mountain	vb	Oceanic assemblage	359	416
9	W Laurentian	Slide Mountain	vb	Oceanic assemblage	359	416
19	W Laurentian	Slide Mountain	vb	Oceanic assemblage	359	416
20	W Laurentian	Slide Mountain	vb	Oceanic assemblage	359	416
30	W Laurentian	Slide Mountain	vb	Oceanic assemblage	359	416
40	W Laurentia	Slide Mountain	vb	Oceanic assemblage	359	416
15	W Laurentia	ST	vi	Arc	359	416
3	NE Panthalassa	Wrangellia	vi	pericratonic and arc	201	251
25	NE Panthalassa	Wrangellia	vi	pericratonic and arc	359	416
33	E Pacific	Yakutat	vi	Accretionary complex	66	146
10	W Laurentia	Yukon-Tanana	vi	Arc	359	416
12	W Laurentia	Yukon-Tanana	vi	Arc	359	416

Table 4S.8 continued

22	W Laurentia	Yukon-Tanana	vi	Arc	359	416
----	-------------	--------------	----	-----	-----	-----

Script 4S.1 Igneous submodel R script.

```

#load package
library(raster)
library(rgdal)
library(mc2d) #load package

# reads in the input grids for each parameter
# input power-transformed ( $^{87}\text{Rb}/^{86}\text{Sr}$ )rock mean and standard deviation grid from ordinary kriging
Rb_Srock <- raster("drive/input.asc", package="raster")
sd_Rb_Srock <- raster("drive/input.asc", package="raster")
# input power-transformed ( $^{87}\text{Rb}/^{86}\text{Sr}$ )parent from table.1
Rb_Srparent <- raster("drive/input.asc", package="raster")
sd_Rb_Srparent <- raster("drive/input.asc", package="raster")
# input minimum and maximum rock age from GLiM database
min_Age_d <- raster("drive/input.asc", package="raster")
max_Age_d <- raster("drive/input.asc", package="raster")

# combine the RasterLayer objects into a RasterStack
s <- stack(Rb_Srock, sd_Rb_Srock, Rb_Srparent, sd_Rb_Srparent, min_Age_d, max_Age_d)

# Get stack dimensions
sdims = dim(s)
# Set Monte Carlo iterations
ndunc(10001)
fun <- function(x) {
  ## Function to calculate SD ratio + uncertainty using Monte Carlo resampling
  if (length(x) != 6) {stop("Ratio function: vector x!= 6")}
  d_Rb_Srock <- mclmdata(x[1], type="0")
  d_sd_Rb_Srock <- mclmdata(x[2], type="0")
  d_Rb_Srparent <- mclmdata(x[3], type="0")
  d_sd_Rb_Srparent <- mclmdata(x[4], type="0")
  d_min_Age_d <- mclmdata(x[5], type="0")
  d_max_Age_d <- mclmdata(x[6], type="0")
  ## draw a random power-transformed ( $^{87}\text{Rb}/^{86}\text{Sr}$ )rock from a normal distribution
  stRb_Srock <- mcstoc(rnorm, type="U", d_Rb_Srock, d_sd_Rb_Srock, rtrunc=TRUE, lmf=0)
  ## back transform power-transformed ( $^{87}\text{Rb}/^{86}\text{Sr}$ )rock using power transform parameter from table. 3
  stRb_Srock <- exp(log(stRb_Srock)/power2)
  ## draw a random power-transformed ( $^{87}\text{Rb}/^{86}\text{Sr}$ )parent from a normal distribution
  stRb_Srparent <- mcstoc(rnorm, type="U", d_Rb_Srparent, d_sd_Rb_Srparent, rtrunc=TRUE,
lmf=0)
  ## back transform power-transformed ( $^{87}\text{Rb}/^{86}\text{Sr}$ )parent using power transform parameter from table. 1
  stRb_Srparent <- exp(log(stRb_Srparent)/power1)
  ## draw a random  $t_2$  from a uniform distribution
  stAge_d <- mcstoc(runif, type="U", min=d_min_Age_d, max=d_max_Age_d)
  ## input all the randomly drawn parameters into the equation 4.1 to calculate  $^{87}\text{Sr}/^{86}\text{Sr}$  in igneous rock
  Sr_ratio <- 0.701+stRb_Srparent*2.8936*(exp(1.42*10^-11*(3*10^9-stAge_d*10^6))-
1)+stRb_Srock*2.8936*(exp(1.42*10^-11*stAge_d*10^6)-1)
  quantile(Sr_ratio[,c(0.025,0.1,0.25,0.5,0.75,0.9,0.975)],na.rm=TRUE)
}

## Replace the loop below by the calc function much faster on R
x<-calc(s,fun)
plot(x)

```

Script 4S.1 continued

```
x <- writeRaster(x, "drive/output.tif", overwrite=TRUE)
```

Script 4S.2 Carbonates submodel R script.

```

#load package
library(raster)
library(rgdal)
library(mc2d) #load package

# reads in the input grids for each parameter
# input power-transformed ( $^{87}\text{Rb}/^{86}\text{Sr}$ )rock mean and standard deviation grid from ordinary kriging
Rb_Srrock <- raster("drive/input.asc", package="raster")
sd_Rb_Srrock <- raster("drive/input.asc", package="raster")
# input minimum and maximum ( $^{87}\text{Sr}/^{86}\text{Sr}$ )seawater}
min_ca_srparent <- raster("drive/input.asc", package="raster")
max_ca_srparent <- raster("drive/input.asc", package="raster")
#input minimum and maximum rock age from GLiM database
min_Age_d <- raster("drive/input.asc", package="raster")
max_Age_d <- raster("drive/input.asc", package="raster")

# combine the RasterLayer objects into a RasterStack
s <- stack(Rb_Srrock, sd_Rb_Srrock, min_ca_srparent, max_ca_srparent, min_Age_d, max_Age_d)

# Get stack dimensions
sdims = dim(s)

# Set Monte Carlo iterations
ndunc(10001)
fun <- function(x) {
  ## Function to calculate SD ratio + uncertainty using Monte Carlo resampling
  if (length(x) != 6) {stop("Ratio function: vector x!= 6")}
  d_Rb_Srrock <- mcdata(x[1], type="0")
  d_sd_Rb_Srrock <- mcdata(x[2], type="0")
  d_min_ca_srparent <- mcdata(x[3], type="0")
  d_max_ca_srparent <- mcdata(x[4], type="0")
  d_min_Age_d <- mcdata(x[5], type="0")
  d_max_Age_d <- mcdata(x[6], type="0")
  ## draw a random power-transformed ( $^{87}\text{Rb}/^{86}\text{Sr}$ )rock} from a normal distribution
  stRb_Srrock <- mcstoc(rnorm, type="U", d_Rb_Srrock, d_sd_Rb_Srrock, rtrunc=TRUE, lmf=0)
  ## back transform power-transformed ( $^{87}\text{Rb}/^{86}\text{Sr}$ )rock} using power transform parameter from table. 3
  stRb_Srrock <- exp(log(stRb_Srrock)/power1)
  ## draw a random ( $^{87}\text{Sr}/^{86}\text{Sr}$ )seawater} from a uniform distribution
  stca_srparent <- mcstoc(runif, type="U", min=d_min_ca_srparent, max=d_max_ca_srparent,
rtrunc=TRUE, lmf=0)
  ## draw a random rock age t2 from a uniform distribution
  stAge_d <- mcstoc(runif, type="U", min=d_min_ca_srparent, max=d_max_ca_srparent)
  ## input all the randomly drawn parameters into the equation 4.3 to calculate  $^{87}\text{Sr}/^{86}\text{Sr}$  in carbonates
  Sr_ratio <- stca_srparent + stRb_Srrock * 2.8936 * (exp(1.42 * 10^-11 * stAge_d * 10^6) - 1)
  quantile(Sr_ratio[,c(0.025, 0.1, 0.25, 0.5, 0.75, 0.9, 0.975)], na.rm=TRUE)
}

x <- calc(s, fun)
plot(x)
x <- writeRaster(x, "drive/output.tif", overwrite=TRUE)

```

Script 4S.3 Siliciclastic sedimentary rock submodel R script.

```

#load package
library(raster)
library(rgdal)
library(mc2d)
library(stats)

# reads in the input grids for each parameter
# input power-transformed ( $^{87}\text{Rb}/^{86}\text{Sr}$ )rock mean and standard deviation grid from ordinary kriging
Rb_Srock <- raster("drive/input.asc", package="raster")
sd_Rb_Srock <- raster("drive/input.asc", package="raster")
# input power-transformed ( $^{87}\text{Rb}/^{86}\text{Sr}$ )parent from table. 1
Rb_Srparent <- raster("drive/input.asc", package="raster")
sd_Rb_Srparent <- raster("drive/input.asc", package="raster")
#input minimum and maximum rock age from GLiM database
min_Age_d <- raster("drive/input.asc", package="raster")
max_Age_d <- raster("drive/input.asc", package="raster")
# input minimum and maximum terrane age
min_Age_t <- raster("drive/input.asc", package="raster")
max_Age_t <- raster("drive/input.asc", package="raster")

# combine the RasterLayer objects into a RasterStack

s <- stack(Rb_Srock, sd_Rb_Srock, Rb_Srparent, sd_Rb_Srparent, min_Age_d, max_Age_d,
min_Age_t, max_Age_t)

# Get stack dimensions
sdims = dim(s)

## Functions to do integration over a dataframe of Monte Carlo output
newf <- function(my df) {
  a=my df[1]
  b=my df[2]
  t1=my df[3]
  t2=my df[4]
  Rb_Srt <- function(t) {b*exp(a*t)}
  stRb_Srock_int <- integrate(Rb_Srt, t1,t2, subdivisions=500, stop.on.error = FALSE)
  return(stRb_Srock_int$value/(t2-t1))
}

# Set Monte Carlo iterations
ndunc(10001)
fun <- function(x) {
  ## Function to calculate SD ratio + uncertainty using Monte Carlo resampling
  if (length(x) != 8) {stop("Ratio function: vector x != 8")}
  d_Rb_Srock <- mcdata(x[1], type="0")
  d_sd_Rb_Srock <- mcdata(x[2], type="0")
  d_Rb_Srparent <- mcdata(x[3], type="0")
  d_sd_Rb_Srparent <- mcdata(x[4], type="0")
  d_min_Age_d <- mcdata(x[5], type="0")
  d_max_Age_d <- mcdata(x[6], type="0")
  d_min_Age_t <- mcdata(x[7], type="0")
  d_max_Age_t <- mcdata(x[8], type="0")
  ## draw a random power-transformed ( $^{87}\text{Rb}/^{86}\text{Sr}$ )parent from a normal distribution

```

Script 4S.3 continued

```

stRb_Srparent <- mcstoc(rnorm, type="U", d_Rb_Srparent, d_sd_Rb_Srparent, rtrunc=TRUE,
linf=0)
## back transform power-transformed (87Rb/86Sr)parent using power transform parameter from table. 1
stRb_Srparent <- exp(log(stRb_Srparent)/power1)
## draw a random rock age t2 from a uniform distribution
stAge_d <- mcstoc(runif, type="U", min=d_min_Age_d, max=d_max_Age_d)
## draw a random terrane age t1 from a uniform distribution
stAge_t <- mcstoc(runif, type="U", min=d_min_Age_t, max=d_max_Age_t)
## draw a random power-transformed (87Rb/86Sr)rock from a normal distribution
stRb_Srrock <- mcstoc(rnorm, type="U", d_Rb_Srrock, d_sd_Rb_Srrock, rtrunc=TRUE, linf=0)
## back transform power-transformed (87Rb/86Sr)rock using power transform parameter from table. 3
stRb_Srrock <- exp(log(stRb_Srrock)/power2)
#a and b parameters of the fitted model b*exp(a*t) from equation 4.4 calculated using boundary
conditions at t1=3Ga and t2=t2
a = log(stRb_Srrock/stRb_Srparent)/(stAge_d-stAge_t)
b = stRb_Srparent/(exp(log(stRb_Srrock/stRb_Srparent)/(stAge_d-stAge_t)*stAge_t))
## Make up dataframe of Monte Carlo output
mydf = data.frame(a=as.numeric(a), b=as.numeric(b),
                 t1=as.numeric(stAge_d), t2=as.numeric(stAge_t))
## Apply integrate function over data frame
stRb_Srrock_int = apply(mydf, 1, newf)
## input all the randomly drawn parameters into the equation 4.4 to calculate 87Sr/86Sr in siliciclastic
sediments
Sr_ratio <- 0.701+stRb_Srrock_int*2.8936*(exp(1.42*10^-11*(stAge_t*10^6-stAge_d*10^6))-1) +
stRb_Srrock*2.8936*(exp(1.42*10^-11*(stAge_d*10^6))-1)+stRb_Srparent*2.8936*(exp(1.42*10^-
11*(3*10^9-stAge_d*10^6))-1)
quantile(Sr_ratio[,c(0.025,0.1,0.25,0.5,0.75,0.9,0.975),na.rm=TRUE)
}

x<-calc(s,fun)
plot(x)
x <- writeRaster(x, "drive/output.tif", overwrite=TRUE)

```

Script 4S.4 R script for the Monte-Carlo simulation step to calculate back-transform
 $(^{87}\text{Sr}/^{86}\text{Sr})_{\text{local}}$.

```

library(raster)
library(rgdal)
library(mc2d) #load package

# reads in the whole raster for each input variables
#input log-transformed bedrock strontium isotope ratio raster for major bedrock
mn_lnSr_ratio_maj <- raster("drive/input.asc", package="raster")
sd_lnSr_ratio_maj <- raster("drive/input.asc", package="raster")
#input log-transformed bedrock strontium isotope ratio raster for minor bedrock
mn_lnSr_ratio_min <- raster("drive/input.asc", package="raster")
sd_lnSr_ratio_min <- raster("drive/input.asc", package="raster")

#input lithology bi (Table 3) rasters based on the GLiM lithological map for major bedrock
mn_bi_maj <- raster("drive/input.asc", package="raster")
sd_bi_maj <- raster("drive/input.asc", package="raster")
#input lithology bi (Table 3) rasters based on the GLiM lithological map for minor bedrock
mn_bi_min <- raster("drive/input.asc", package="raster")
sd_bi_min <- raster("drive/input.asc", package="raster")

#input global permafrost extent and cover raster
pfi <- raster("drive/input.asc", package="raster")
#input global slope raster
slope <- raster("drive/input.asc", package="raster")

# combine the RasterLayer objects into a RasterStack

s <- stack(mn_lnSr_ratio_maj, sd_lnSr_ratio_maj, mn_lnSr_ratio_min, sd_lnSr_ratio_min,
mn_bi_maj, sd_bi_maj, mn_bi_min, sd_bi_min, pfi, slope)

# Set Monte Carlo iterations
ndunc(1001)
fun <- function(x) {
  ## Function to calculate SD ratio + uncertainty using Monte Carlo resampling
  ## Changed to expect a vector of six values, rather than a raster stack
  if (length(x) != 10) {stop("Ratio function: vector x != 10")}
  d_mn_Sr_ratio_maj <- mcdata(x[1], type="0")
  d_sd_Sr_ratio_maj <- mcdata(x[2], type="0")
  d_mn_Sr_ratio_min <- mcdata(x[3], type="0")
  d_sd_Sr_ratio_min <- mcdata(x[4], type="0")
  d_mn_bi_maj <- mcdata(x[5], type="0")
  d_sd_bi_maj <- mcdata(x[6], type="0")
  d_mn_bi_min <- mcdata(x[7], type="0")
  d_sd_bi_min <- mcdata(x[8], type="0")
  d_pfi <- mcdata(x[9], type="0")
  d_slope <- mcdata(x[10], type="0")
  ## draw a random log-transformed  $^{87}\text{Sr}/^{86}\text{Sr}$  major bedrock from a normal distribution
  stSr_ratio_maj <- mcstoc(mnorm, type="U", d_mn_lnSr_ratio_maj, d_sd_lnSr_ratio_maj,
rtrunc=TRUE, lmf=0)
  ## back-transform  $^{87}\text{Sr}/^{86}\text{Sr}$  major bedrock
  stSr_ratio_maj <- exp(stSr_ratio_maj)
  ## draw a random log-transformed  $^{87}\text{Sr}/^{86}\text{Sr}$  minor bedrock from a normal distribution

```

Script 4S.4 continued

```

stSr_ratio_min <- mcstoc(mnorm, type="U", d_mn_lnSr_ratio_min, d_sd_lnSr_ratio_min,
rtrunc=TRUE, linf=0)
## back-transform 87Sr/86Sr minor bedrock
stSr_ratio_min <- exp(stSr_ratio_min)

## draw a random bi number from each pixel from a normal distribution for major lithology
Stbi_maj <- mcstoc(rnorm, type="U", d_mn_bi_maj, d_sd_bi_maj, rtrunc=TRUE, linf=0)
## draw a random bi number from each pixel from a normal distribution for minor lithology
Stbi_min <- mcstoc(rnorm, type="U", d_mn_bi_min, d_sd_bi_min, rtrunc=TRUE, linf=0)

## draw a random bpfi (Table 3) number from each pixel from a normal distribution
st_b_pfi <- mcstoc(mnorm, type="U", -0.34, 0.094, rtrunc=TRUE, linf=0)
## draw a random bs (Table 3) number from each pixel from a normal distribution
st_b_s <- mcstoc(mnorm, type="U", 0.074, 0.014, rtrunc=TRUE, linf=0)

## apply equation 4.6 with each random parameter drawn for major lithology
lnSr_major <- stbi_maj + st_b_pfi * d_pfi + st_b_s * d_slope
back-transform Sr flux
Sr_major <- exp(lnSr)
## apply equation 4.6 with each random parameter drawn for minor lithology
lnSr_minor <- stbi_min + st_b_pfi * d_pfi + st_b_s * d_slope
back-transform Sr flux
Sr_minor <- exp(lnSr)
## apply equation 4.7
Sr_ratio_local <- (0.75 * Sr_major * stSr_ratio_maj + 0.25 * Sr_minor * stSr_ratio_min) /
(0.75 * Sr_major + 0.25 * Sr_minor)
quantile(Sr_ratio_local[,c(0.025, 0.1, 0.25, 0.5, 0.75, 0.9, 0.975)], na.rm=TRUE)
}

x <- calc(s, fun)
x <- writeRaster(x, "drive/output.tif", overwrite=TRUE)

```


Supplementary dataset 1: Bedrock model validation dataset

Dataset description

We compiled and georeferenced data from the literature including 97 $^{87}\text{Sr}/^{86}\text{Sr}$ analyses in sedimentary rocks and 788 $^{87}\text{Sr}/^{86}\text{Sr}$ analyses in igneous rocks sampled in AK (Table 4S.9). We georeferenced all the samples compiled by reporting latitude/longitude given in the publication or estimating geolocation using other available geographical data from the publication (e.g., map) and Google Earth. The dataset also indicates the major rock type and a lithological descriptor for each sample. We used this dataset to test the accuracy of the bedrock model over AK by extracting the bedrock model value at each sample point of the database (ArcGIS/Spatial Analyst Toolbox). Due to its large size Table 4S.9 is not included in this thesis and is available upon request at:

clement.bataille@gmail.com.

Dataset uncertainty and biases

This dataset present a broad variety of lithologies and ages but are not comprehensive and thus hamper proper validation of the bedrock model because: 1) analyses gathered in these databases are biased toward rocks from active tectonic and volcanic areas, 2) $^{87}\text{Sr}/^{86}\text{Sr}$ values for continental sedimentary samples are under-represented in comparison with igneous rocks, and 3) Mesozoic and Cenozoic rocks are over-represented in the dataset.

Supplementary dataset 2: Chemical weathering model calibration dataset

Dataset description

We compiled and georeferenced 405 published Sr concentration and isotope data from major rivers and tributaries from North hemisphere high-latitudes (Fig. 4.4A and Table 4S.10). From this dataset, we selected a chemical weathering model calibration dataset of 339 Sr concentration data (Table 4S.10) excluding 66 samples which shared part of their drainage catchment in common with another sample in the calibration set. We selected only high-latitude rivers (catchments above 60°N) to limit the range of temperature and its potential effect on chemical weathering. We georeferenced all the samples compiled by reporting latitude/longitude given in the publication or estimating geolocation using other available geographical data from the publication (e.g., map) and Google Earth. Each sample point of the calibration dataset was manually snapped on the river network derived from the Hydro1K dataset (data available from the U.S. Geological Survey) and used to define their catchment feature (Spatial Analyst/Hydrology Toolbox). Due to its large size the Table 4S.10 is not included in this thesis and is available upon request at: clement.bataille@gmail.com.

Dataset biases

The main limitation of this database is that we could not calculate discharge-weighted annual average Sr concentrations and $^{87}\text{Sr}/^{86}\text{Sr}$ because most of the Sr concentration and $^{87}\text{Sr}/^{86}\text{Sr}$ data are derived from a single point sample. In high-latitude catchment, discharge and solute concentrations are highly seasonal and in the Northern high latitudes most of the water discharge and solute export occur during the late spring

and summer. The great majority of the samples from the compiled database were collected during spring (n=93), summer (n=326) and early fall (n=64). We assume that those Sr concentrations are representative of the high flow period and as such they can be used to estimate the annual Sr concentration in the sampled rivers. Flux calculated on the basis of a single sample could differ from the annual mean by more than 50%. $^{87}\text{Sr}/^{86}\text{Sr}$ can also vary seasonally due to the relative contributions of Sr from the subbasins with different lithologies within the drainage. Uncertainty associated with seasonal variations in the high-latitudes can be estimated using published time series of Sr concentrations and $^{87}\text{Sr}/^{86}\text{Sr}$ data, and comparing the range of $^{87}\text{Sr}/^{86}\text{Sr}$ values with the flow and flow and concentration weighted $^{87}\text{Sr}/^{86}\text{Sr}$ values. Using two high-latitude studies reporting time series of Sr concentrations and $^{87}\text{Sr}/^{86}\text{Sr}$ values (Douglas et al., 2013; Voss et al., 2014), we calculated an average difference less than 10% between annual discharge-weighted Sr flux and annual Sr flux derived from single point measurements. Similarly, the average difference for $^{87}\text{Sr}/^{86}\text{Sr}$ values was less than 0.001 in both cases indicating that seasonal variations are only a minor factor in controlling Sr concentrations and $^{87}\text{Sr}/^{86}\text{Sr}$ in high-latitudes rivers. However, heterogeneous glacial and permafrost cover associated with rapid lithological changes are fairly ubiquitous conditions in Alaska and we cannot rule out the possibility of significant seasonal bias in our dataset.

References

- Douglas, T.A., Blum, J.D., Guo, L., Keller, K., Gleason, J.D., 2013. Hydrogeochemistry of seasonal flow regimes in the Chena River, a subarctic watershed draining discontinuous permafrost in interior Alaska (USA). *Chemical Geology*, 335(0): 48-62.
- Saito, H., Goovaerts, P., 2000. Geostatistical interpolation of positively skewed and

censored data in a dioxin-contaminated site. *Environmental Science & Technology*, 34(19): 4228-4235.

Voss, B.M., Peucker-Ehrenbrink, B., Eglinton, T.I., Fiske, G., Wang, Z.A., Hoering, K.A., Montuçon, D.B., LeCroy, C., Pal, S., Marsh, S., Gillies, S.L., Janmaat, A., Bennett, M., Downey, B., Fanslau, J., Fraser, H., Macklam-Harron, G., Martinec, M., Wiebe, B., 2014. Tracing river chemistry in space and time: Dissolved inorganic constituents of the Fraser River, Canada. *Geochimica et Cosmochimica Acta*, 124(0): 283-308.

CHAPTER V

CONCLUSION

Summary

In this dissertation, we presented the results of different modeling efforts allowing the development of models predicting $^{87}\text{Sr}/^{86}\text{Sr}$ in bedrock, river water and soil water for regional scale provenance studies. In Chapter I, we emphasized the interest and necessity of developing predictive $^{87}\text{Sr}/^{86}\text{Sr}$ models to assist provenance interpretation at the regional scale and we reviewed existing approaches to developing such models. In Chapter II, we developed initial model formulations and associated calibration steps to predict $^{87}\text{Sr}/^{86}\text{Sr}$ in bedrock and river water. We applied those models to predict $^{87}\text{Sr}/^{86}\text{Sr}$ over the conterminous USA. Tested against compiled dataset of rock and water $^{87}\text{Sr}/^{86}\text{Sr}$, the bedrock and the water model explained a large portion of $^{87}\text{Sr}/^{86}\text{Sr}$ variations. In Chapter III, we highlighted the limitations of the bedrock and water models in predicting $^{87}\text{Sr}/^{86}\text{Sr}$ of ecosystems in areas where multiple sources of Sr contribute to the $^{87}\text{Sr}/^{86}\text{Sr}$ signature. To address this issue, we developed a model accounting for the mixing of distinct Sr inputs (bedrock, aerosols) into soils and predicting the resulting $^{87}\text{Sr}/^{86}\text{Sr}$ in soil water. This model performed significantly better than the bedrock or water models in predicting $^{87}\text{Sr}/^{86}\text{Sr}$ of biological material, demonstrating the importance of developing substrate-specific $^{87}\text{Sr}/^{86}\text{Sr}$ isoscapes. In Chapter IV, we renewed the bedrock and water model formulation and calibration to enhance the model's predictive power and to assess prediction uncertainty. These new models were applied to predict $^{87}\text{Sr}/^{86}\text{Sr}$ in Alaska Rivers and demonstrated robust predictive power to identify the geographic origin of waters and fish, explaining around 80% of the variance with an uncertainty around ± 0.001 .

Perspectives

Resolving provenance using multi-isotope framework

Predictive $^{87}\text{Sr}/^{86}\text{Sr}$ models are powerful additions to other existing isoscapes (H and O) because of the fine scale and geology-controlled discrete pattern of $^{87}\text{Sr}/^{86}\text{Sr}$ variations they represent. The future integration of $^{87}\text{Sr}/^{86}\text{Sr}$ into a multi-isotope framework with H and O isotopes should considerably increase the probabilistic power and spatial resolution of provenance predictions at local to continental scales. An increase in resolution and accuracy of provenance assessments will likely open the door to new applications and renewed interpretation of existing datasets. Adding Sr isotopes to the routine geochemical provenance toolbox will also enhance the interdisciplinary characteristic of the “isoscape” field by building bridges between traditional and nontraditional isotope geochemistry techniques and applications. For instance, the paleoenvironmental research community could benefit strongly from the development of multi-isotope isoscapes from past geological periods (“paleoisoscapes”) because their combined information can help resolve problems at multiple time scales. $^{87}\text{Sr}/^{86}\text{Sr}$ has been applied in a variety of Quaternary paleoenvironmental studies (Balasse et al., 2002; Hoppe et al., 1999; Koch et al., 1992), but ongoing work and advances in reconstituting Earth paleogeography and paleogeology of the Paleozoic could lead to the development of $^{87}\text{Sr}/^{86}\text{Sr}$ isoscape for older geological periods. Combined paleoisoscapes of H, O and $^{87}\text{Sr}/^{86}\text{Sr}$ could ultimately become powerful tools to study paleoclimate, to reconstruct ancient biogeochemical cycles or to track movements and provenance of animals (e.g., dinosaurs) and materials (e.g., dust) from the Earth’s deep past.

Predictive $^{87}\text{Sr}/^{86}\text{Sr}$ models to identify mechanistic process of
 $^{87}\text{Sr}/^{86}\text{Sr}$ variations

Throughout this dissertation, we demonstrated that map products derived from our model are powerful templates for data analysis and visualization for a variety of fields. Isoscapes-based research can play a fundamental role in identifying mechanistic processes influencing isotope variations. For instance, our predictive $^{87}\text{Sr}/^{86}\text{Sr}$ models applied to Alaska Rivers (Chapter IV) allowed direct visualization of spatial pattern of $^{87}\text{Sr}/^{86}\text{Sr}$ variations and helped to quantify the effect of local (e.g., glacial processes) vs. global (e.g., temperature) factors in controlling $^{87}\text{Sr}/^{86}\text{Sr}$ variations in continental surface waters. Applied to global scale, our model could be used to test the sensitivity of the Sr and $^{87}\text{Sr}/^{86}\text{Sr}$ flux in rivers to varied geological (bedrock model and surface of exposed continents), climatic (precipitation and temperature) and/or environmental (topography and soil types) factors reflecting past Earth surface conditions.

Broader interest of this geostatistical framework

The geostatistics and geospatial data analysis derived from this work could also provide powerful methods for the interpretation and integration of geochemical data and the production of base layers supporting the visualization and widespread scientific application of geochemical and isotopic data. This geostatistical framework contributes to an ongoing effort to integrate the growing amount of publically available geological and geochemical data within a spatial platform. This framework, combined with recent advances in geostatistics, could further help to combine discrete (geological maps, soil maps, geochemical samples) and continuous (aerial and satellite data) data to predict the

concentration of geologically-derived elements and isotopes in various Earth surface reservoirs at a global scale. High resolution global elemental and isotope maps have vast potential for better understanding Earth surface processes in various fields. For instance, those spatial models could offer a unique opportunity to better understand the spatial distribution of life-sustaining nutrients (e.g., phosphorus, iron) at a global scale for land-surface models.

Limitations and future improvements

Improving the geostatistical framework

The main challenge in developing accurate predictive $^{87}\text{Sr}/^{86}\text{Sr}$ models is associated with the type of $^{87}\text{Sr}/^{86}\text{Sr}$ spatial patterning. Isoscape modeling theory has been initially formulated around atmospherically derived H and O isotopes which display spatially continuous variations with smooth isotopic gradient along map transects. This continuous pattern of variation greatly simplifies the application of interpolation algorithms and the assessment of prediction uncertainty. Developing predictive models of $^{87}\text{Sr}/^{86}\text{Sr}$ variations in bedrock requires a completely different mindset because at the regional scale, $^{87}\text{Sr}/^{86}\text{Sr}$ variations in rocks are dominated by discrete patterning associated with geological regime. This discrete patterning is further overprinted by continuous, multiscale $^{87}\text{Sr}/^{86}\text{Sr}$ variability associated with local and regional heterogeneity. In the final approach, presented in Chapter IV of this dissertation, both pattern types (discrete and continuous) are treated separately before being combined to predict $^{87}\text{Sr}/^{86}\text{Sr}$. The discrete pattern is modeled using geological maps, whereas the multiscale continuous patterns are modeled by ordinary kriging. Improving prediction

accuracy and uncertainty assessment will require the integration of those different levels and types of spatial variability into a unified geostatistical framework. Ongoing research aiming to develop kriging algorithms combining discrete and continuous data might strongly benefit the performance of our model in the future (Goovaerts, 2010; Kerry et al., 2012).

Improving spatial resolution of $^{87}\text{Sr}/^{86}\text{Sr}$ isoscape

Increasing the resolution of $^{87}\text{Sr}/^{86}\text{Sr}$ predictive models is critical to improve provenance assessment because of the fine scale $^{87}\text{Sr}/^{86}\text{Sr}$ variations in natural systems. The resolution of our $^{87}\text{Sr}/^{86}\text{Sr}$ predictive models is limited by both the resolution of geological maps and the density and quality of point data ($^{87}\text{Sr}/^{86}\text{Sr}$, Rb and Sr) used in the parameterization steps of our model. While the accuracy and resolution of global geological maps will improve rapidly with ongoing efforts (Hartmann and Moosdorf, 2012), there is little chance that the types of high resolution point sample datasets necessary for representing the fine scale $^{87}\text{Sr}/^{86}\text{Sr}$ variations will exist at global scale in the near future. A solution to reduce the dependence of our parameterization methods on the density and quality of point data, while representing the fine-scale $^{87}\text{Sr}/^{86}\text{Sr}$ variations will consist in identifying continuous spatial datasets derived from satellite/aerial observations that could be correlated with the observations of model variables (e.g., radiometric surveys correlate well with K and Rb content in rocks). Using those continuous datasets in co-kriging procedures should allow representing the fine-scale $^{87}\text{Sr}/^{86}\text{Sr}$ variations at global scale without losing accuracy.

Developing substrate specific $^{87}\text{Sr}/^{86}\text{Sr}$ isoscapes

In this dissertation, we have presented models predicting $^{87}\text{Sr}/^{86}\text{Sr}$ in bedrock, surface water and soil water. However, as Sr is cycled and mixed on the Earth surface, physical and biological processes tend to lead to more and more variable $^{87}\text{Sr}/^{86}\text{Sr}$ in biological reservoirs (Capo et al., 1998). Consequently, depending on the study, substrate-specific isoscapes of accessible water, tap water, plants or food might be required to predict the $^{87}\text{Sr}/^{86}\text{Sr}$ of humans or animals. Estimating the $^{87}\text{Sr}/^{86}\text{Sr}$ of those Sr sources becomes more and more complicated as the source becomes more specific, due to the absence of data to test and validate the isoscapes. In those cases, finding a good compromise between specificity and generality will be required when developing predictive $^{87}\text{Sr}/^{86}\text{Sr}$ models. Such compromises could be permitted if a representative substrate that integrates $^{87}\text{Sr}/^{86}\text{Sr}$ from the Sr sources is found. There is still debate in the archeological/ecological community on which substrates best reflect the integrated $^{87}\text{Sr}/^{86}\text{Sr}$ of animal or human diets (e.g., migratory bird, large mammals, humans) because the substrate might be specie-specific (Copeland et al., 2011; Evans et al., 2010; Frei and Frei, 2011; Hodell et al., 2004; Price et al., 2002; Sillen et al., 1998). Additional data compilations and experiments are required to identify which substrates are the most appropriate and to develop, test and validate substrate-specific $^{87}\text{Sr}/^{86}\text{Sr}$ isoscape.

Toward time-dependent $^{87}\text{Sr}/^{86}\text{Sr}$ isoscapes?

One main advantage in using $^{87}\text{Sr}/^{86}\text{Sr}$ in provenance studies is the limited temporal variations of $^{87}\text{Sr}/^{86}\text{Sr}$ in reservoirs of the Earth surface in comparison with other traditional stable isotopes. Even when large inputs of Sr from seasonal sources

occur (e.g., atmospheric deposition), soil $^{87}\text{Sr}/^{86}\text{Sr}$ will only vary at a temporal scale of hundreds to thousands of years (Bern et al., 2005; Chadwick et al., 2009; Kennedy et al., 1998; Pett-Ridge et al., 2009). As such, $^{87}\text{Sr}/^{86}\text{Sr}$ in bedrock and soils and their associated isoscape can be reasonably assumed constant at human timescale. However, Sr residence time decreases significantly in the hydrosphere and the biosphere leading to temporal $^{87}\text{Sr}/^{86}\text{Sr}$ variability in those reservoirs. Those variations could be considered when modeling substrate specific $^{87}\text{Sr}/^{86}\text{Sr}$ such as river water, plants or food because they bring an additional dimension to constrain geographic provenance. Recent work has demonstrated that temporal $^{87}\text{Sr}/^{86}\text{Sr}$ variations in river water are more common than initially thought, and is encountered in many areas where river discharge is highly seasonal (Douglas et al., 2013; Voss et al., 2014). Rapid flushing of Sr that has accumulated from atmospheric deposition during peak flow (e.g., meltwater, flashflood, permafrost) can temporally dominate the river water Sr export and induce seasonal $^{87}\text{Sr}/^{86}\text{Sr}$ variations in rivers.

References

- Balasse, M., Ambrose, S.H., Smith, A.B., Price, T.D., 2002. The seasonal mobility model for prehistoric herders in the South-western Cape of South Africa assessed by isotopic analysis of sheep tooth enamel. *Journal of Archaeological Science*, 29(9): 917-932.
- Bern, C.R., Townsend, A.R., Farmer, G.L., 2005. Unexpected dominance of parent-material strontium in a tropical forest on highly weathered soils. *Ecology*, 86(3): 626-632.
- Capo, R.C., Stewart, B.W., Chadwick, O.A., 1998. Strontium isotopes as tracers of ecosystem processes: theory and methods. *Geoderma*, 82(1-3): 197-225.
- Chadwick, O.A., Derry, L.A., Bern, C.R., Vitousek, P.M., 2009. Changing sources of strontium to soils and ecosystems across the Hawaiian Islands. *Chemical*

- Geology, 267(1–2): 64-76.
- Copeland, S.R. et al., 2011. Strontium isotope evidence for landscape use by early hominins. *Nature*, 474(7349): 76-78.
- Douglas, T.A., Blum, J.D., Guo, L., Keller, K., Gleason, J.D., 2013. Hydrogeochemistry of seasonal flow regimes in the Chena River, a subarctic watershed draining discontinuous permafrost in interior Alaska (USA). *Chemical Geology*, 335(0): 48-62.
- Evans, J.A., Montgomery, J., Wildman, G., Boulton, N., 2010. Spatial variations in biosphere $^{87}\text{Sr}/^{86}\text{Sr}$ in Britain. *Journal of the Geological Society*, 167(1): 1-4.
- Frei, K.M., Frei, R., 2011. The geographic distribution of strontium isotopes in Danish surface waters – A base for provenance studies in archaeology, hydrology and agriculture. *Applied Geochemistry*, 26(3): 326-340.
- Goovaerts, P., 2010. Combining areal and point data in geostatistical interpolation: Applications to soil science and medical geography. *Mathematical Geosciences*, 42(5): 535-554.
- Hartmann, J., Moosdorf, N., 2012. The new global lithological map database GLiM: A representation of rock properties at the Earth surface. *Geochemistry, Geophysics, Geosystems*, 13(12): 1525-2027.
- Hodell, D.A., Quinn, R.L., Brenner, M., Kamenov, G., 2004. Spatial variation of strontium isotopes ($\text{Sr-}^{87}/\text{Sr-}^{86}$) in the Maya region: A tool for tracking ancient human migration. *Journal of Archaeological Science*, 31(5): 585-601.
- Hoppe, K.A., Koch, P.L., Carlson, R.W., Webb, S.D., 1999. Tracking mammoths and mastodons: Reconstruction of migratory behavior using strontium isotope ratios. *Geology*, 27(5): 439-442.
- Kennedy, M.J., Chadwick, O.A., Vitousek, P.M., Derry, L.A., Hendricks, D.M., 1998. Changing sources of base cations during ecosystem development, Hawaiian Islands. *Geology*, 26(11): 1015-1018.
- Kerry, R., Goovaerts, P., Rawlins, B.G., Marchant, B.P., 2012. Disaggregation of legacy soil data using area to point kriging for mapping soil organic carbon at the regional scale. *Geoderma*, 170(0): 347-358.
- Koch, P.L., Halliday, A.N., Walter, L.M., Stearley, R.F., Huston, T.J., Smith, G.R., 1992. Sr isotopic composition of hydroxyapatite from recent and fossil salmon: The record of lifetime migration and diagenesis. *Earth and Planetary Science Letters*, 108(4): 277-287.

- Pett-Ridge, J.C., Derry, L.A., Kurtz, A.C., 2009. Sr isotopes as a tracer of weathering processes and dust inputs in a tropical granitoid watershed, Luquillo Mountains, Puerto Rico. *Geochimica Et Cosmochimica Acta*, 73(1): 25-43.
- Price, T.D., Burton, J.H., Bentley, R.A., 2002. The characterization of biologically available strontium isotope ratios for the study of prehistoric migration. *Archaeometry*, 44(1): 117-135.
- Sillen, A., Hall, G., Richardson, S., Armstrong, R., 1998. $^{87}\text{Sr}/^{86}\text{Sr}$ ratios in modern and fossil food-webs of the Sterkfontein Valley: Implications for early hominid habitat preference. *Geochimica et Cosmochimica Acta*, 62(14): 2463-2473.
- Voss, B.M. et al., 2014. Tracing river chemistry in space and time: Dissolved inorganic constituents of the Fraser River, Canada. *Geochimica et Cosmochimica Acta*, 124(0): 283-308.